

(2)

NAVAL POSTGRADUATE SCHOOL Monterey, California

AD-A274 903



3



DTIC
ELECTE
JAN 26 1994
S C D

THESIS

A SURVEY OF UNCONTROLLED SATELLITE
REENTRY AND IMPACT PREDICTION

by

Brian D. Neuenfeldt

and

William K. Henderson

September, 1993

Co-Thesis Advisor:

Co-Thesis Advisor:

I. Michael Ross

Joseph J. F. Liu

Approved for public release; distribution is unlimited.

94 1 25 074

4887 94-02283

REPORT DOCUMENTATION PAGE

Form Approved OMB No. 0704

Public reporting burden for this collection of information is estimated to average 1 hour per response, including the time for reviewing instruction, searching existing data sources, gathering and maintaining the data needed, and completing and reviewing the collection of information. Send comments regarding this burden estimate or any other aspect of this collection of information, including suggestions for reducing this burden, to Washington Headquarters Services, Directorate for Information Operations and Reports, 1215 Jefferson Davis Highway, Suite 1204, Arlington, VA 22202-4302, and to the Office of Management and Budget, Paperwork Reduction Project (0704-0188) Washington DC 20503.

1. AGENCY USE ONLY (Leave blank)	2. REPORT DATE 23Sep93	3. REPORT TYPE AND DATES COVERED Master's Thesis
----------------------------------	---------------------------	---

4. TITLE AND SUBTITLE : A Survey of Uncontrolled Satellite Reentry and Impact Prediction	5. FUNDING NUMBERS
--	--------------------

5. AUTHORS: Neuenfeldt, Brian D. and Henderson, William K.
--

7. PERFORMING ORGANIZATION NAME(S) AND ADDRESS(ES) Naval Postgraduate School Monterey CA 93943-5000	8. PERFORMING ORGANIZATION REPORT NUMBER
---	--

9. SPONSORING/MONITORING AGENCY NAME(S) AND ADDRESS(ES) Director, Navy Space Systems Division (N63) Space and Electronic Warfare Directorate Chief of Naval Operations Washington DC 20350-2000	10. SPONSORING/MONITORING AGENCY REPORT NUMBER Naval Space Command Code N4/6T Dahlgren VA 22448-5170
---	--

11. SUPPLEMENTARY NOTES The views expressed in this thesis are those of the author and do not reflect the official policy or position of the Department of Defense or the U.S. Government.

12a. DISTRIBUTION/AVAILABILITY STATEMENT Approved for public release; distribution is unlimited.	12b. DISTRIBUTION CODE A
---	-----------------------------

13. ABSTRACT (maximum 200 words)
The primary goal of this thesis is to identify the "state-of-the-art" in orbit-decay-induced uncontrolled reentry/impact prediction methods, with an emphasis on the physics of the final few revolutions to impact. This was accomplished through a comprehensive literature survey from the 1950's to the present of unclassified military and civil databases. The results of the survey show that the current U.S. and international reentry/impact prediction methodologies are based on analysis which is over 30 years old. Of the various "extensions" to the current reentry theory, of which the NORAD method is recognized as the international standard, there does not appear to be any one method which is singularly superior to the others. It has also been shown that numerous reentry investigations made simplifying assumptions due to insufficient data needed to accurately model reentry and also because of computing limitations of their day. Also, current deterministic dynamic models appear to inadequately describe the actual uncontrolled reentry process, due to a lack of observational data, uncertainty in determining aerodynamic coefficients, atmospheric density, and point mass modeling where changes in vehicle configuration, attitude and lift are neglected. Stochastic and statistical methods could be applied to the current methodology, to better analyze the various uncertainties, which could help to improve the overall predicted impact time and location; however, further research into these methods along with the physics of uncontrolled reentry is necessary.

14. SUBJECT TERMS: reentry, uncontrolled reentry, reentry effects, reentry prediction, impact prediction, reentry motion, reentry aerothermodynamics, satellite breakup, atmospheric density models, reentry/impact models	15. NUMBER OF PAGES 269
--	----------------------------

16. PRICE CODE

17. SECURITY CLASSIFICATION OF REPORT Unclassified	18. SECURITY CLASSIFICATION OF THIS PAGE Unclassified	19. SECURITY CLASSIFICATION OF ABSTRACT Unclassified	20. LIMITATION OF ABSTRACT UL
---	--	---	----------------------------------

Approved for public release; distribution is unlimited.

A SURVEY OF UNCONTROLLED SATELLITE REENTRY AND IMPACT
PREDICTION

by

Brian D. Neuenfeldt
Lieutenant Commander (sel), United States Navy
B.S., University of Texas at San Antonio, 1982

and

William K. Henderson
Lieutenant, United States Navy
B.A., Western State College of Gunnison Colorado, 1984

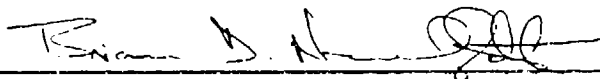
Submitted in partial fulfillment
of the requirements for the degree of

MASTER OF SCIENCE IN SYSTEMS TECHNOLOGY
(SPACE SYSTEMS OPERATIONS)

from the

NAVAL POSTGRADUATE SCHOOL
September 1993

Authors:



Brian D. Neuenfeldt

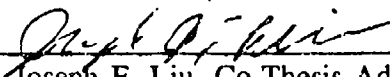


William K. Henderson

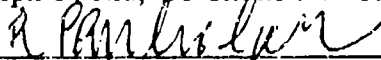
Approved by:



I. Michäel Ross, Co-Thesis Advisor



Joseph F. Liu, Co-Thesis Advisor



Rudolph Panholzer, Chairman
Space Systems Academic Group

TABLE OF CONTENTS

I. INTRODUCTION	1
A. HISTORY	1
1. Case Studies	2
a. Sputnik IV	3
b. Skylab	4
c. Cosmos 954	8
B. PROBLEM STATEMENT	12
C. PURPOSE	14
D. METHODOLOGY	15
II. FUNDAMENTALS OF ATMOSPHERIC REENTRY	18
A. TYPES OF REENTRY	18
1. Uncontrolled Reentry	18
2. Controlled Reentry	18
a. Ballistic Reentry	20
b. Gliding Reentry	20
c. Skip Reentry	20

B. MAJOR FACTORS INFLUENCING UNCONTROLLED	
REENTRY	21
1. Modeling Reentry Equations Of Motion	22
a. Basic Equations of a Rigid Body	22
b. Modeling Gravity	23
c. Modeling Atmospheric Drag	24
(1) Modeling Atmospheric Density	28
(2) Modeling Aerodynamic Coefficients.	33
(3) Rarified Gas Dynamics	33
(4) Vehicle Profile Area.	36
(5) Vehicle Mass.	37
(6) Vehicle Velocity	37
d. Modeling Aerodynamic Lift	37
e. Reentry Equations of Motion	38
(1) Fundamental Equations of Entry Dynamics	39
2. Modeling Breakup	43
a. Reentry Body Structural Mechanics	43
b. Modeling Reentry Heating Effects	44
(1) Reentry Heat Input	46
(2) Reentry Heating Rate	51
(3) Ablation.	51
C. GENERAL DESCRIPTION OF THE REENTRY PHASE	52

D.	CURRENT REENTRY THEORIES	55
1.	Physical Modeling Theory	57
2.	Mean Motion Theory	62
III.	FORMULATIONS AND SOLUTIONS OF REENTRY	66
A.	ANALYTICAL REENTRY EQUATIONS OF MOTION	66
1.	Chapman's Approximate Analytical Entry Equations of Motion	66
2.	Loh's Second Order Unified Solution of Entry Dynamics	71
3.	Yaroshevskii's Entry Theory	74
4.	Universal Equations for Orbit Decay and Reentry	78
5.	Attitude Dynamics of Uncontrolled Motion During Reentry	86
a.	Equations of Perturbed Motion	93
b.	Effect of Motion Relative to the Center of Mass on the Motion of the Center of Mass	103
c.	Follow-on Investigations of Uncontrolled Reentry Body Motion	106
B.	SIX-DEGREE-OF-FREEDOM SIMULATIONS	107
C.	RAREFIED GAS DYNAMICS	111
1.	Newtonian Aerodynamics for Hypersonic Continuum Flow	117
2.	Free Molecular Flow Model	123
3.	Bridging Free Molecular and Continuum Flow	126
a.	Shape Element Bridging Method.	126

b.	Local Bridging Method	131
4.	Gas-Surface/Gas-Gas Interactions	132
D.	SURFACE ROUGHNESS EFFECTS	136
E.	REENTRY HEATING EQUATIONS	144
F.	STRUCTURAL BREAKUP OF A REENTRY BODY	146
IV.	DETERMINISTIC REENTRY/IMPACT PREDICTION METHODS	153
A.	CURRENT REENTRY/IMPACT PREDICTION METHOD	153
B.	ALTERNATE REENTRY/IMPACT PREDICTION METHODS	156
1.	Reentry Prediction Methods At ESOC	156
2.	The LIFETIME Model	162
3.	Modeling Ballistic Coefficient	171
C.	FACTORS INFLUENCING REENTRY/IMPACT DISPERSION	182
V.	STOCHASTIC AND STATISTICAL PREDICTION METHODS	190
A.	EXTENSIONS OF THE PHYSICAL MODELING REENTRY THEORY	190
1.	Estimation of Reentry Trajectories	190
2.	Analysis of Tracking and Impact Prediction (TIP)	202
B.	MONTE CARLO ANALYSIS OF SKYLAB'S IMPACT AREA	214
1.	Simulation Results	221

VI. CONCLUSIONS AND RECOMMENDATIONS 233

 A. CONCLUSIONS 233

 B. RECOMMENDATIONS 238

LIST OF REFERENCES 240

INITIAL DISTRIBUTION LIST 249

LIST OF FIGURES

Figure 1: Sputnik IV Final Revolution [Ref. 9]	5
Figure 2: Sputnik IV Impact Area/Debris Location [Ref. 9]	6
Figure 3: Sputnik IV Impact Area Ground Trace [Ref. 9]	7
Figure 4: Cosmos 954 Impact Area / Debris Dispersion [Ref. 10]	9
Figure 5: Skylab Final One-Quarter Revolution [Ref. 11]	11
Figure 6: Types Of Reentry [Ref. 14]	19
Figure 7: Earth Geopotential Model [Ref. 17]	25
Figure 8: Drag Effect On High Eccentricity Orbits [Ref. 17]	27
Figure 9: Flow Regimes [Ref. 20]	35
Figure 10: Inertial Coordinate System [Ref. 40]	40
Figure 11: Relationship Between Relative And Inertial Velocity [Ref. 40]	41
Figure 12: Changes During Atmospheric Reentry [Ref. 43]	54
Figure 13: Maximum Deceleration vs Initial Flight Path Angle [Ref. 14]	56

Figure 14: Differential Corrections Display [Ref. 49]	60
Figure 15: Tracking And Impact Prediction (TIP) Display [Ref. 49]	61
Figure 16: Z Function Solution Graph For $L/D=0$ [Ref. 14]	69
Figure 17: Z Function Solution Graph For Various L/D 's [Ref. 14]	70
Figure 18: Loh's Second-Order Range Of Applicability [Ref. 40]	72
Figure 19: Loh's Second-Order vs Chapman's First-Order [Ref. 40]	75
Figure 20: Coordinate System And Nomenclature [Ref. 41]	79
Figure 21: Aerodynamic Force Diagram [Ref. 41]	80
Figure 22: Variations Of $-\gamma$ vs The Nondimensional Velocity (v) [Ref. 41]	87
Figure 23: Variations Of $\ln(Z/Z_c)$ vs The Nondimensional Velocity (v) [Ref. 41]	88
Figure 24: Variations Of G vs The Nondimensional Velocity (v) [Ref. 41]	89
Figure 25: Attitude Dynamics Coordinate System [Ref. 57]	92
Figure 26: Trajectory Of The Reentry Body [Ref. 56]	95
Figure 27: Reentry Body Coordinate System [Ref. 56]	97

Figure 28: Six-Degree-Of-Freedom Simulation Flowchart [Ref. 62]	108
Figure 29: Simulated Generic Spacecraft And Reactor Sub-Element [Ref. 64]	110
Figure 30: Flow Regimes - Altitude vs Velocity [Ref. 76]	112
Figure 31: Aerodynamic Coefficients In The Flow Regimes [Ref. 76]	114
Figure 32: Shape Elements And Composed Bodies [Ref. 76]	116
Figure 33: Shape Factor As A Function Of (d/r_N) [Ref. 76]	119
Figure 34: Newtonian Lift And Drag Functions [Ref. 76]	120
Figure 35: Sphere Drag Coefficient In Rarefied Flow [Ref. 76]	127
Figure 36: Disk Drag Coefficient In Rarefied Flow [Ref. 76]	128
Figure 37: Molecular Velocity Distribution [Ref. 80]	133
Figure 38: Average Translational Energy [Ref. 80]	137
Figure 39: Boundary Layer Types [Ref. 22]	140
Figure 40: Boundary-Layer Velocity-Distance Profiles [Ref. 22]	141
Figure 41: Altitude-Air Speed-Dynamic Pressure Relationship [Ref. 22]	142

Figure 42: Structural Breakup - Heating Rate vs Altitude [Ref. 86]	148
Figure 43: Breakup Altitudes For Corrected Heating Rates [Ref. 64]	150
Figure 44: Salyut-7/Cosmos-1686 Final Descent Altitude Profile [Ref. 94]	163
Figure 45: LIFETIME Debris Dispersion Footprint [Ref. 95]	168
Figure 46: LIFETIME Groundtrack And Altitude Decay History [Ref. 95]	169
Figure 47: Best Fit DC RMS For Cosmos-954/1402 [Ref. 92]	177
Figure 48: Dependence Of \dot{h} , Latitude And Longitude On B [Ref. 47]	181
Figure 49: Near-Earth View Of All Cataloged Space Objects (1987) [Ref. 100]	186
Figure 50: U.S. Radar And Electro-Optical Assets [Ref. 100]	187
Figure 51: Orbital Plane Rotation Due To A Rotating Atmosphere [Ref. 101]	189
Figure 52: Tangent Plane Projection Of Earth Impact Location [Ref. 102]	200
Figure 53: Decay Predicted Accuracy (By Year) [Ref. 48]	203
Figure 54: Final Run vs <i>Vis Obs</i> Mean Time Error [Ref. 48]	205
Figure 55: Final Time Error Standard Deviation [Ref. 48]	206

Figure 56: Mean Time Error And Standard Deviation (1987-1990) [Ref. 48]	208
Figure 57: Mean Location Error And Standard Deviation (1987-1990) [Ref. 48]	210
Figure 58: Regression Model Mean Approximate Error (1987-1990) [Ref. 48]	213
Figure 59: Numerical Stability Region [Ref. 45]	219
Figure 60: Relative Entry Flight Path Angle Scattergram [Ref. 45]	223
Figure 61: Skylab Nominal Flight Characteristics [Ref. 45]	224
Figure 62: Downrange Impact Point Variations [Ref. 45]	225
Figure 63: Latitude Histogram / Cumulative Probability Distribution [Ref. 45]	227
Figure 64: Longitude Histogram / Cumulative Probability Distribution [Ref. 45]	228
Figure 65: Down Range And Crossrange Dispersions [Ref. 45]	231
Figure 66: Downrange And Uprange Dispersions Three-Sigma Limits [Ref. 45]	232

LIST OF TABLES

Table I: SKYLAB RECOVERED DEBRIS (PARTIAL LISTING) [Ref. 10]	10
Table II: OBSERVATIONAL DATA FORMAT [Ref. 49]	59
Table III: BRIDGING DEPENDENCIES [Ref. 76]	115
Table IV: TRANSITIONAL BRIDGING FUNCTIONS [Ref. 76]	115
Table V: NEWTONIAN LOCAL PRESSURE LAW [Ref. 76]	117
Table VI: SHAPE FACTOR VALUES [Ref. 76]	121
Table VII: BODY SHAPE AND LIFT SLOPE [Ref. 76]	123
Table VIII: LOCAL SURFACE PRESSURE AND SHEAR STRESS [Ref. 76]	124
Table IX: AERODYNAMIC FORCE COEFFICIENTS [Ref. 76]	124
Table X: SHAPE DEPENDENT BOUNDARIES [Ref. 76]	130
Table XI: FREESTREAM CONDITIONS [Ref. 80]	136
Table XII: RESULTS OF BREAKUP ANALYSIS [Ref. 6 ^d]	151
Table XIII: SALYUT-7/COSMOS-1686 FINAL DECAY PREDICTIONS [Ref. 94]	164

Table XIV: DISTRIBUTION OF DECAYED ORBITAL OBJECTS
[Ref. 92] 173

Table XV: DECAY TIME ERROR RMS
[Ref. 92] 178

Table XVI: ENTRY STATE VECTOR / ERROR COVARIANCE MATRIX
[Ref. 45] 222

ACKNOWLEDGEMENTS

I would like to thank some of the many people who helped make my time at the Naval Postgraduate School one of the most rewarding tours of my naval career as well as personally fulfilling. First, there could be no better co-thesis advisors than Dr. I. M. Ross and Dr. J. J. F. Liu. Without the tireless efforts of these two scholars and subject matter experts, this thesis would have been nearly impossible to complete. Secondly, I would like to thank the Space Systems Operations academic advisor, Dr. D. C. Boger. I will never forget his advice to me at the beginning of my postgraduate education, "...take all the math you can, it can't hurt you," he was right! Next, I would like to acknowledge the superb academic staff of the Naval Postgraduate School without whom an undergraduate biology major could never have been transformed into a space systems operations major. And of course, this thesis is only half my work.. Without the daily exchange of ideas and suggestions of my thesis partner and good friend, LT Kelly Henderson, this would never have happened. Finally, I must thank my family. I could never have made it this far in my career without the constant support of my parents and parents-in-law, especially when I was at sea and my wife was alone with the boys. And so it goes without saying that my wife, Mary, is my driving force and my children (Matthew, Christopher, Timothy and Mark) are my inspiration. I could not have completed this course of study or the thesis without their endless support and love.

Brian D. Neuenfeldt

ACKNOWLEDGEMENTS

I would like to sincerely thank all of those individuals who have helped in my efforts. Since the beginning of my academic career at the Naval Postgraduate School, many prominent people have given their valuable time and expertise which has made this tour, both professionally and personally, one of the most meaningful and rewarding tours in my Naval career. I owe a great deal of gratitude to my co-thesis advisors, Dr. I. Michael Ross and Dr. Joseph J. F. Liu, for their expert guidance and wisdom. Their willingness to invest a significant amount of time and effort into making this a meaningful thesis is truly appreciated. Also, I would again like to thank Dr. John Darrah and Dr. Liu's staff at the Air Force Space Command, Dr. Steve Knowles and his staff at the Naval Space Command, Mr. Frank Marcos at the Air Force Geophysics Laboratory and Dr. George Chao at The Aerospace Corporation for their technical support. To my partner and good friend, LCDR Brian Neuenfeldt, it has been a pleasure working with you. Your suggestions, ideas and unique approach have greatly contributed to strengths of this thesis. I would also like to thank my parents and parents-in-laws for supporting my family and I throughout my career. Finally, my greatest thanks goes to my wife and life long partner, Monica, and my children, Zeb and Jeremiah. Without their unselfish love and support, this academic and final endeavor would not have been possible.

William K. Henderson

I. INTRODUCTION

A. HISTORY

Satellite or spacecraft reentry related work has been done in this country for nearly five decades. With the advent of the rocket in World War II, the military saw the first application of spacecraft reentry prediction as the ballistic trajectory calculation of the target aimpoint. Prior to this, several nations had "rocket societies," however, none had actually applied the use of "space" to a technology or an industry. Thus, the first application of space was by the military for the purpose of war. [Ref. 1:p. 13]

On October 4, 1957, the former Soviet Union changed the perception of space held by most Americans and possibly the world. It was the launch of Sputnik I that caused, then Senator, Lyndon B. Johnson to remark:

That sky had always been so friendly, and had brought us beautiful stars and moonlight and comfort; all at once it seemed to have some question marks all over it. [Ref. 2:p. 13]

When the former Soviets again launched another rocket barely one month later and sent a dog into space, onboard Sputnik II, the world now saw the first space traveler and the dream of humans in space became more real than dream [Ref. 1:p. 20].

After a dismal failure of the United States' first attempt to launch a satellite into orbit with Vanguard I, which was dubbed by some reporters as "Kaputnik" after it exploded on the launch pad on December 16, 1957, Explorer I was successfully launched

on January 31, 1958. The space race had begun, and both countries were pushing to have the first human in space. [Ref. 1:p. 20], [Ref. 2:p. 16]

With the goal of putting humans into space came the necessary requirement of providing for the safe return of those humans back to Earth, unlike the first dog in space which perished after about a week when the oxygen supply was exhausted [Ref. 2:p. 16]. This was the beginning of the most intense research period into the reentry process over the entire history of space exploration.

By April 1972, there were at least 44 reported instances where man-made space objects had impacted on the Earth [Ref. 3:p. 383]. By March 1978, the total count of man-made objects placed into Earth orbit was 10,791 [Ref. 4:p. 107]. By Aug 1991, the cumulative count of objects ever placed into space was 21,231 with 14,417 decays/reentries, leaving 6,814 objects in Earth orbit [Ref. 5:p. v].

The return or reentry of manned spaceflights has been covered by the various media sources with varying degrees of intensity based upon the "newsworthiness" of the event and sensed public interest:

Solar Max satellite plunges to Earth. [Ref. 6:p. 21(N)]

Spacecraft's study of sun ends today: Solar Max heads for fiery reentry. [Ref. 7:p. A3]

If you see a shooting star Dec. 8, make a fast wish for a deep cave. [Ref. 8:p. B1]

1. Case Studies

It is useful for the reader to understand the motivation for studying the reentry process. Obviously, the routine recovery of numerous U.S. and Soviet spacecraft

must imply that the reentry process is adequately understood. In the case of controlled reentry and space vehicles designed for reentry, this may well be the case; however, in the uncontrolled reentry case, this is not as easy to conclude.

a. Sputnik IV

September 5, 1962, the first recorded impact of a man-made space object in the United States was satellite number, 1960 ϵ 1, Sputnik IV. This satellite reentered the Earth's atmosphere over North America and many fragments of the reentering debris ended their orbit over the state of Wisconsin. The largest fragment of which was found to weigh approximately 21 pounds (9.49 kg) impacted in the city of Manitowoc, Wisconsin at approximately 0530 local time. [Ref. 9:p. 1]

Sputnik IV, which had been launched on May 14, 1960, was designed to test life-support systems for Soviet manned space flight. On May 19, a planned deorbit maneuver failed and the pressure vessel separated from the cabin, leaving the cabin in a "lopsided" orbit. [Ref. 9:p. 2] There were a total of nine separate orbiting objects associated with satellite 1960 ϵ 1. The first of these objects to reenter was the last stage rocket body, which reentered on July 17, 1960. By July 1, 1961, six of the nine pieces had reentered. The payload reentered on September 5, 1962 leaving only one other object in orbit. [Ref. 9:p. 3]

The U.S. Space Detection and Tracking System (SPADATS) predicted Sputnik IV would reenter on or about September 6, 1962. Moonwatch observers, teams of volunteers who attempted to observe reentry events with either the naked eye or telescopes, were notified of the SPADATS prediction on August 29, 1962. [Ref. 9:p. 10]

It was based on these observations that the fragments of Sputnik IV were eventually located, with the exception of the largest fragment, which was found by a routine police patrol of the city of Manitowoc. Figure 1 shows the satellite ground trace over the last one-half revolution [Ref. 9:p. 20]. Figure 2 shows the ground trace of the last one hundred nautical miles [Ref. 9:p. 12]. Figure 3 shows the impact location of objects recovered in Manitowoc [Ref. 9:p. 17]. The objects found on the roof of the church annex, noted in Figure 3, consisted of 15 small spherules approximately 1/8 inch in diameter. These were about 325 feet further downrange from the initial mass which impacted near the intersection of Park St. and 8th St.

There was no loss of life and the only reported property damage was the impact impression left in the street.

b. Skylab

In May 1973, the last U.S. Saturn V rocket launched Skylab into orbit approximately 270 nautical miles (nm) above the Earth. Skylab was the first U.S. space station and the centerpiece of the U.S. space program since the last U.S. moon mission. Skylab would remain in orbit until July 11, 1979. [Ref. 10:p. 1]

Knowing the inevitability of decay and reentry of low Earth orbits, NASA contracted the Lockheed Missile and Space Company (LMSC) to investigate the predicted reentry and breakup of Skylab three years prior to its launch. This initial report predicted that Skylab would begin to breakup at an altitude of 65 nm (120 km) and that debris would fall 3600 nm downrange from the initial breakup. [Ref. 10:p. 2]

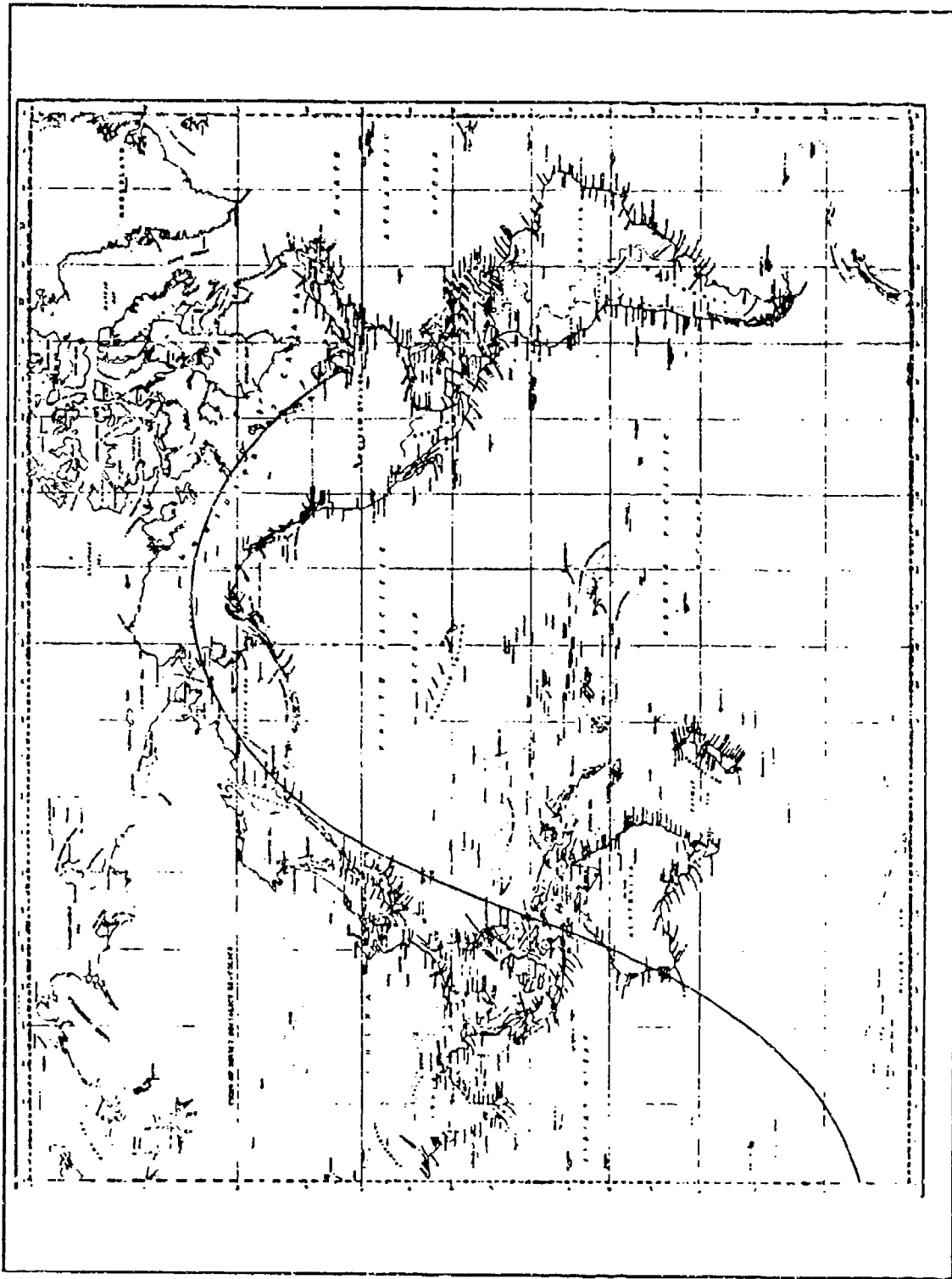


Figure 1: Sputnik IV Final Revolution
[Ref. 9]

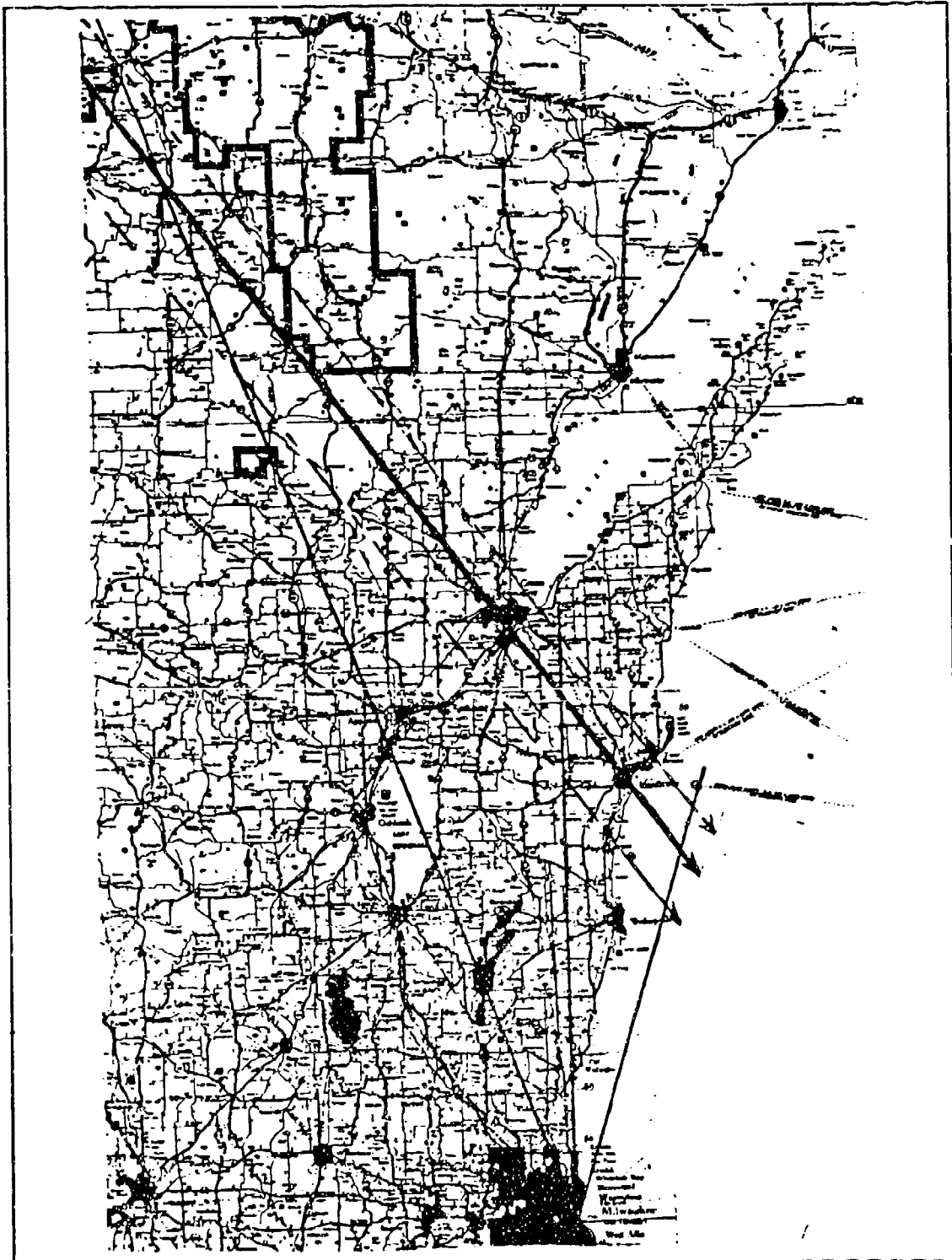


Figure 2: Sputnik IV Impact Area/Debris Location
[Ref. 9]

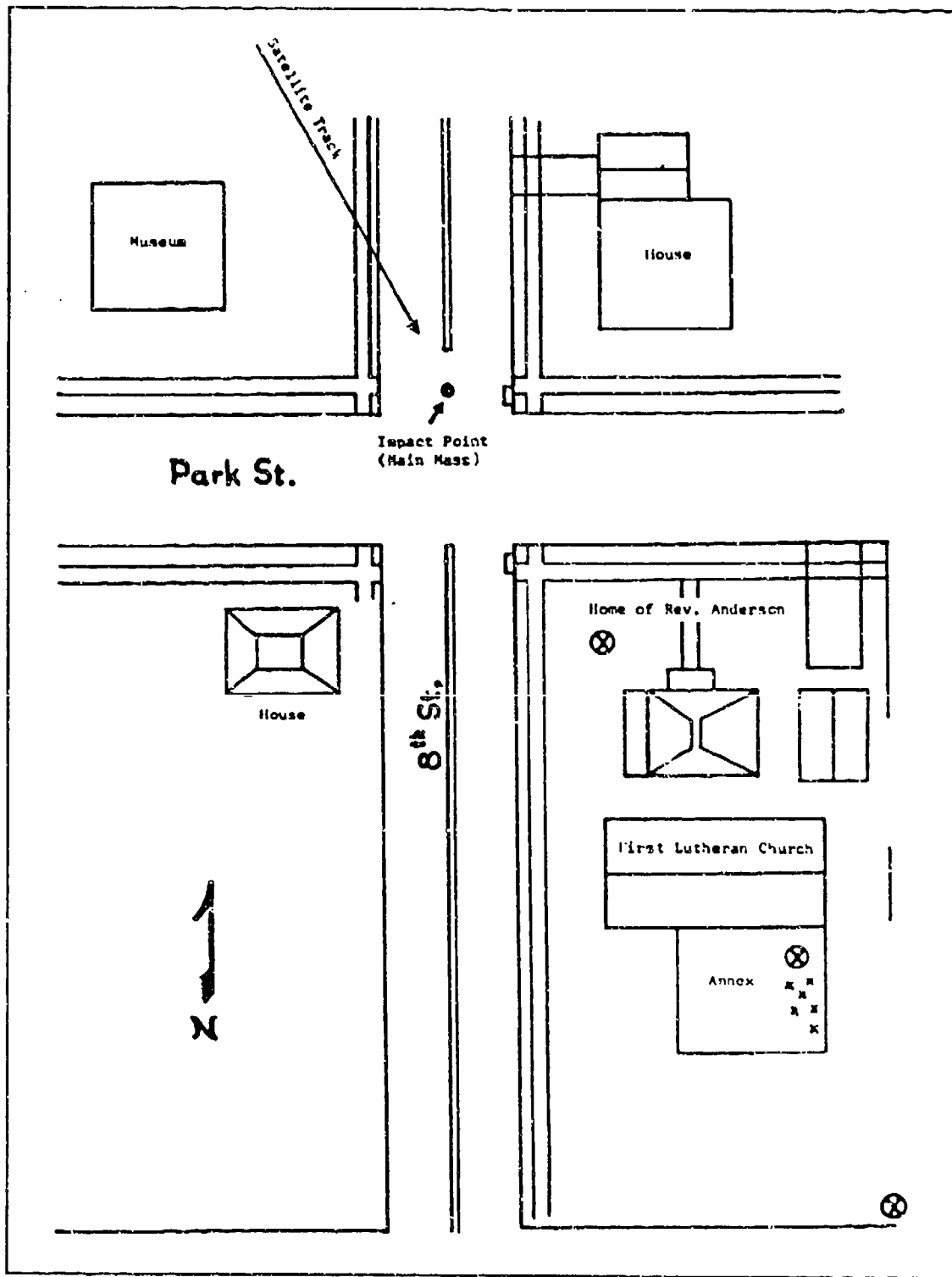


Figure 3: Sputnik IV Impact Area Ground Trace
 [Ref. 9]

Based on the post-flight reconstruction of the reentry of Skylab, Marshall Space Flight Center (MSFC) was able to conclude that telemetry signals were still being sent from Skylab as it passed over Bermuda and Ascension Islands. Also, each of these tracking stations reported only one radar contact. It was therefore concluded that Skylab was intact and breakup had not begun, although the altitude had decreased to 57 nm. [Ref. 10:p. 5] Survivability underestimation has been typical of past analysis as will be discussed in Chapter III.

Figure 4 shows the ground trace of Skylab over the last one-quarter revolution and denotes the impact footprint (debris dispersion area) [Ref. 10:p. 18]. Table 1 is a partial listing of recovered debris from Skylab and the recovery location [Ref. 10:p. 10].

Again, there was no loss of life, no human injury and no property damage as a result of this uncontrolled reentry.

c. Cosmos 954

January 24, 1978 marked the first uncontrolled reentry and Earth impact of a nuclear powered artificial satellite [Ref. 3:p. 384]. This was also the first case of "significant" property damage due to an artificial Earth satellite impact. It was reported that Canada spent over 11 million dollars and the United States spent nearly 3 million dollars in the location and recovery of radioactive debris [Ref. 3:p. 386]. Figure 5 shows the reentry ground trace and impact dispersion area of Cosmos 954 [Ref. 11:p. 303].

Table I: SKYLAB RECOVERED DEBRIS (PARTIAL LISTING)
 [Ref. 10]

ITEMS	PROBABLE SOURCE	LOCATION
Charred Fragments	OWS	33.9S, 121.9E (In Esperance)
Burned Material	OWS	33.9S, 121.9E (In Esperance)
Aluminum 356 Casting	OWS	33.7S, 122.1E (20 mi NE of Esperance)
Foam Fiberglass Beam Section	OWS	33.9S, 122.0E (9 mi E of Esperance)
H ₂ O Tank Aft End	OWS	33.8S, 122.0E (9 mi NE of Esperance)
H ₂ O Tank	OWS	33.9S, 122.1E (10 mi E. of Esperance)
10' Steel Strip	OWS (H ₂ O Tank)	33.9S, 122.3E (25 mi E of Esperance)
Heat Exchanger	OWS (H ₂ O Cooler)	33.9S, 122.1E (12 mi E. of Esperance)
Segment of Fiberglass Sphere	OWS	33.9S, 122.1E (11 mi E of Esperance)
Insulation	OWS (Bulkhead)	33.9S, 122.1E (11 mi E of Esperance)
Aluminum Gear and Housing	OWS (Urine Separator)	33.7S, 122.5E (40 mi NE of Esperance)
N ₂ Tank	AM	33.2S, 122.6E (60 mi NE of Esperance)
Electronics Module	AM	33.5S, 122.3E (35 mi NE of Esperance)
N ₂ Sphere	AM	33.5S, 122.8E (49 mi ENE of Esperance in Neridup area)
Pressure Tank	IU	33.2S, 122.6E (60 mi NE of Esperance)

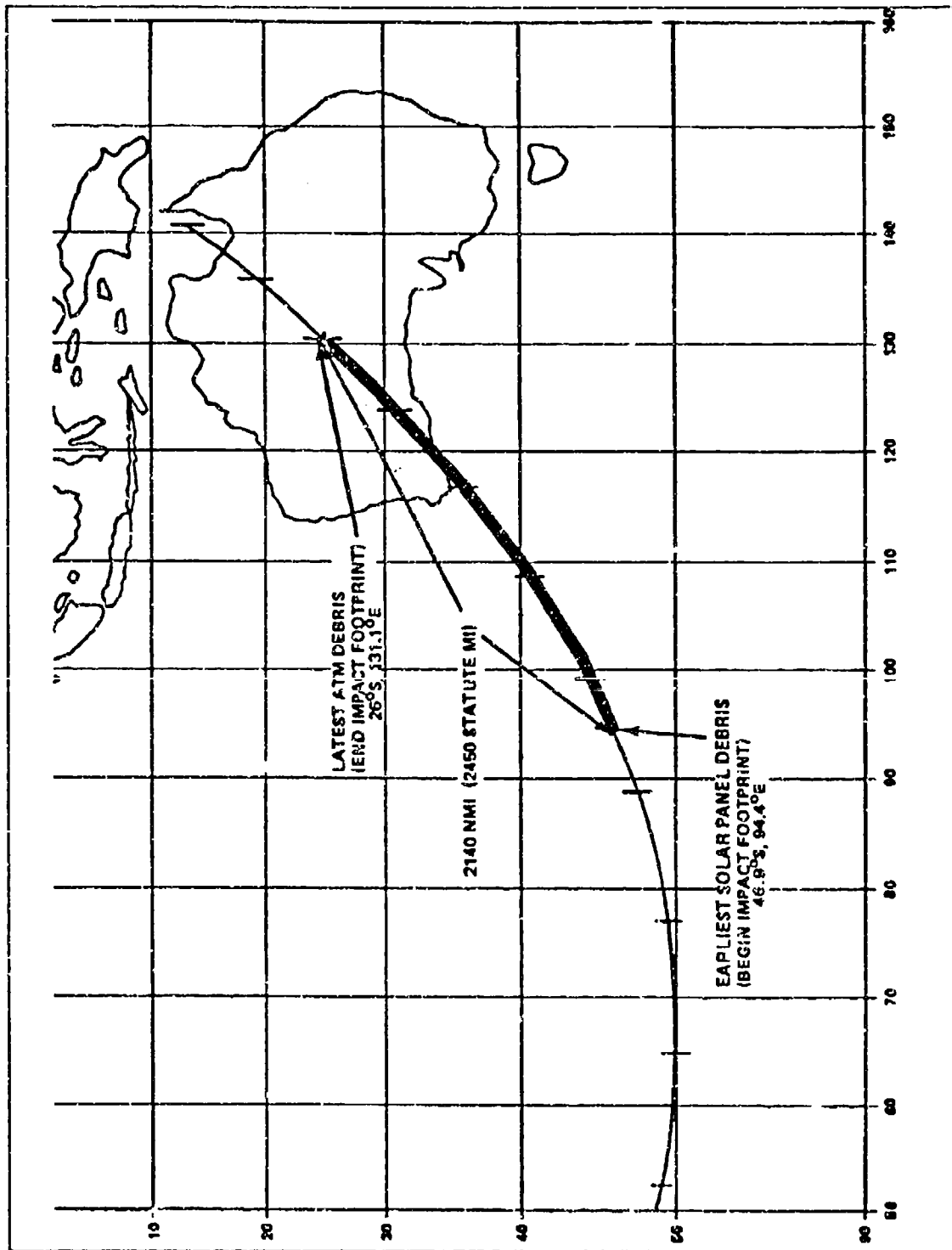


Figure 5: Skylab Final One-Quarter Revolution
 [Ref. 11]

The Outer Space Treaty of 1967, the Liability Convention of 1972 and the Registration Convention of 1976 are the three principal documents, drafted by the United Nations Committee on the Peaceful Uses of Outer Space and its Legal Subcommittee, which define ownership responsibilities of space objects [Ref. 12:p. 457]. Although the Outer Space Treaty, Article VIII, provides in explicit terms the requirements that the registry state (country of origin) retains jurisdiction and control over its satellites while in space or on a celestial body, [Ref. 3:p. 389] there may be no legal requirement under the Liability Convention or the Rescue and Return Agreement for the former Soviet Union to reimburse either the U.S. or Canada for the cleanup cost of Cosmos 954 [Ref. 3:p. 387].

It is because of the potential for the loss of human life, significant property damage and legal responsibility based in international law that the reentry of uncontrolled artificial satellites must be further investigated. In the case of Cosmos 954, on the morning of reentry, the Soviets predicted reentry impact near the Aleutian Islands (52°N,173°W) and the North American Air Defense Command (NORAD) predicted reentry impact near Hawaii (19°N,156°W) [Ref. 4:p. 110]. The physics of uncontrolled reentry and the modeling of the reentry process must be better understood in order to improve the accuracy of reentry predictions.

B. PROBLEM STATEMENT

The probability of space objects reentering the Earth's atmosphere and surviving to impact is relatively small; most artificial objects burn up in the atmosphere before they

impact [Ref. 13:p. 1]. Falling debris nonetheless presents a potential hazard to people and property. The most difficult problem associated with reentry impact prediction is not to determine what will survive to impact in as much as where impact will occur. [Ref. 5:p. v]

The significant factors related to the prediction of time to impact and location of the reentry are a lack of observational data over the entire orbit and a lack of "precise" mathematical models which accurately describe the physical processes occurring during reentry. The major parameters which contribute to the uncertainties of the reentry prediction are: [Ref. 5:p. v]

1. Atmospheric density variations--atmospheric density is strongly influenced by solar and geomagnetic activity, both of which are difficult to forecast.
2. Aerodynamic force models--aerodynamic forces are a function of attitude, lift and drag coefficients, gas-surface interactions and gas dynamics such as continuum flow or free-flow regimes.
3. Spacecraft attitude motion--the attitude of the object and how it changes with time is an important factor in estimating the aerodynamic forces encountered during reentry.
4. Changes in configuration--ablation and fragmentation cause changes in configuration (profile area and mass/area loss) which can change the aerodynamic forces experienced either as an increase or decrease in net force.

The lack of regularly spaced observational data over the entire orbit can severely handicap the efforts to predict reentry, especially in the final phase. Since most observational data is from radar tracking stations and the object is in a very low orbit, the time in view is of short duration as well as limited by the geographic location of the

tracking stations. The availability of good quality tracking data is required for accurate reentry predictions and could compensate for inherent deficiencies in the models. [Ref. 5:p. vi]

C. PURPOSE

This research was initiated by the Air Force Space Command. The purpose of this thesis is threefold:

1. Conduct a comprehensive literature survey in the area of artificial satellite reentry specifically, uncontrolled orbit decay and reentry into the Earth's atmosphere.
2. Describe the "state-of-the-art" of reentry/impact prediction techniques.
3. Define critical areas of research where increased emphasis is required in order to improve the accuracy of the reentry prediction.

The focus of this thesis is the physical processes of the uncontrolled reentry from the final few revolutions to impact. It is not the intended purpose of this thesis to examine in detail or focus on the following aspects of the reentry prediction problem:

1. Atmospheric density models
 - a. Solar activity and influence on reentry
 - b. Geomagnetic influence on reentry
2. Long-term orbital lifetime prediction

It is necessary, however, to discuss these aspects of the reentry process in order to completely study the physical phenomena associated with reentry. These topics are the subject matter of Chapter II and are considered the fundamental background material required for a further, more detailed study of the reentry process.

D. METHODOLOGY

The primary research methodology of this thesis was a comprehensive literature survey of military and civil aerospace data bases. The literature search of Department of Defense (DoD) data bases was restricted to unclassified work. The literature search was conducted at or through the following activities:

1. Naval Postgraduate School, Dudley Knox Library
2. Hanscom Air Force Base Research Library
3. University of Colorado at Boulder, Astrophysics and Engineering libraries
4. AFSPACCOM Astrodynamics Division (CNY) technical library
5. United States Air Force Academy Library

The secondary research methodology of this thesis was personal interviews with "experts" in the study of reentry or reentry related fields. The activities which were contacted or visited personally include:

1. TRW Corporation
2. The Aerospace Corporation

3. Phillips Laboratories
4. Air Force Geophysics Laboratory (AFGL)
5. Naval Space Surveillance Center (NAVSPASUR)
6. Air Force Space Command (AFSPACECOM)
7. United States Space Command (USSPACECOM)

The primary data bases and periods over which the literature survey was conducted include:

- | | |
|-----------|-------------|
| 1. NASA | 1940 - 1993 |
| 2. DTIC | 1950 - 1993 |
| 3. IAA | 1960 - 1993 |
| 4. STAR | 1960 - 1993 |
| 5. DIALOG | 1970 - 1993 |

These data bases were searched with similar strategies in an effort to pull as many "original" articles as possible, while concurrently verifying the search process by producing numerous "duplicate" articles found in other data bases. The primary search terms included: reentry, reentry prediction, satellite reentry, atmosphere reentry, spacecraft, spacecraft reentry, uncontrolled reentry, reentry impact prediction, satellite,

descent trajectory, atmosphere drag, atmospheric density models, satellite orbit decay, reentry heating, reentry dynamics and reentry effects.

In order to prevent confusion of common variables when derived in multiple sources, the equations and variable nomenclature presented throughout this thesis are as presented in the original works, with the exception of minor changes made as noted. An example of such a change is the flight path angle, γ , presented in Chapter II. Since this is a survey of the literature, which dates back to the 1950's, the authors have made a conscious effort to preserve the flavor of the individual works and no attempt has been made to standardize the nomenclature. However, this is an object for further study as indicated in Chapter VI.

II. FUNDAMENTALS OF ATMOSPHERIC REENTRY

A. TYPES OF REENTRY

The reentry trajectories of space vehicles can be classified into two types, either uncontrolled or controlled. The focus of this thesis is to investigate the uncontrolled reentry of satellites, however, three major types of controlled reentry, ballistic, gliding and skip, as shown in Figure 6, will be described for completeness [Ref. 14:p. 6].

1. Uncontrolled Reentry

Uncontrolled reentry may be the result of an unrecoverable satellite subsystem failure or the end of the satellite's operational life. The flight path angle is usually much less than one degree and lift is considered negligible. Typically, very large uncertainties in impact point predictions are created by decay-induced uncontrolled reentries. [Ref. 15:p. 44]

2. Controlled Reentry

During a controlled reentry, the vehicle's aerodynamic and heating loads are maintained within acceptable limits by controlling the effects of lift and drag forces on the vehicle throughout the flight. This is accomplished through a carefully designed space vehicle, flight trajectory and possibly a precision guidance system. Controlled reentry spans an aerodynamic flight regime from subsonic to Mach 25 and beyond for hyperbolic reentry. [Ref. 16:p. 231]

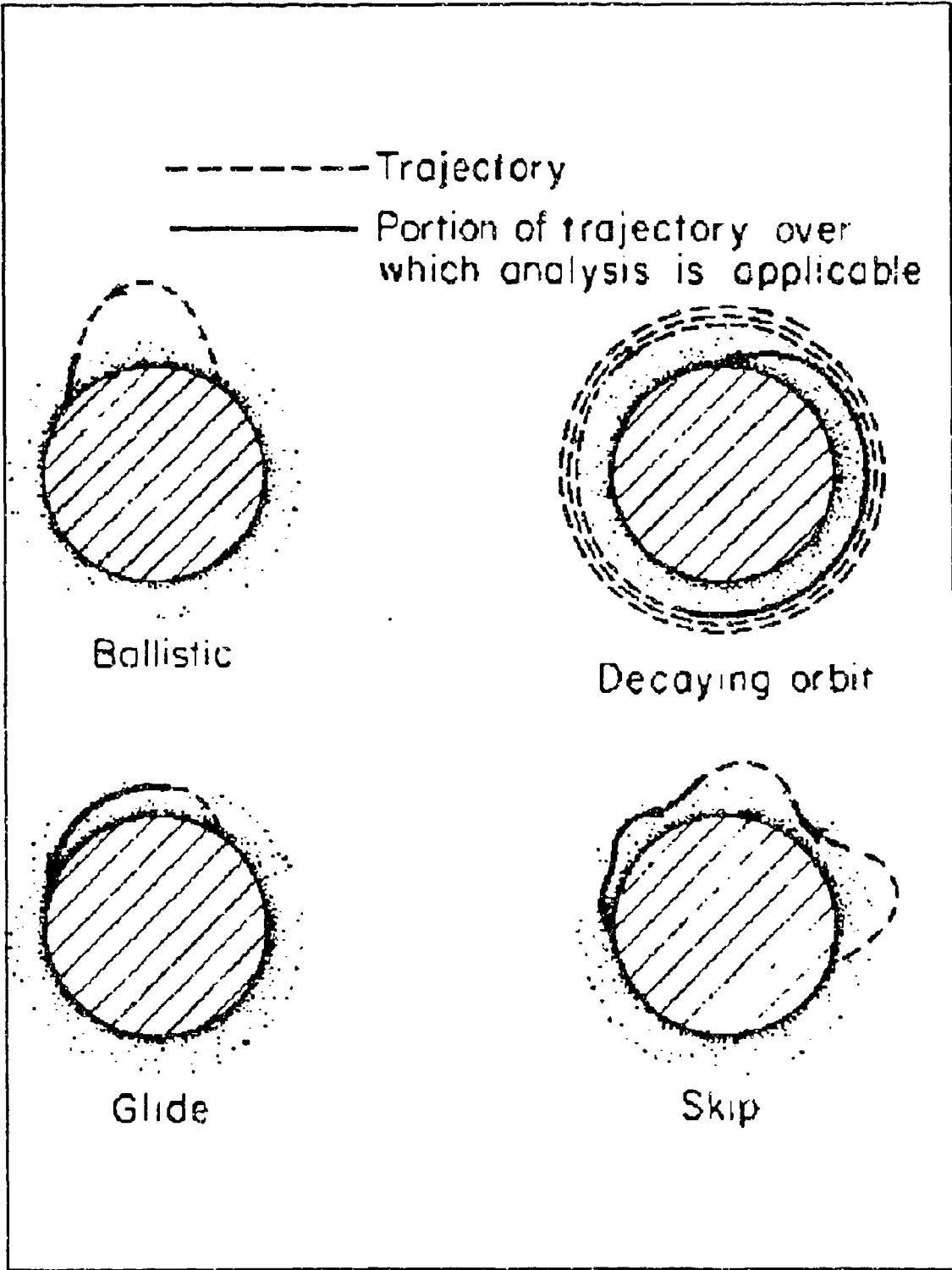


Figure 6: Types Of Reentry
 [Ref. 14]

a. Ballistic Reentry

A ballistic reentry is characterized by sufficiently steep reentry angles where the force of lift is assumed to be negligible [Ref. 14:p. 2]. The ability to control the reentry velocity, flight path angle, ballistic coefficient and atmospheric properties determines the accuracy of ballistic reentry vehicles. Impact accuracies within the intended target vary from 20 km for shallow angle reentries, such as Mercury type vehicles, to an accuracy of a few hundred meters for a steep angle reentry of an intercontinental ballistic missile type vehicle. [Ref. 16:pp. 237-242]

b. Gliding Reentry

A gliding reentry is characterized by a glide slope rather than a reentry trajectory. During a gliding reentry, a vehicle such as the space shuttle creates enough lift to maintain a long hypersonic glide at a small flight path angle [Ref. 16:p. 242]. A measure of the vehicle's lift that influences the descent path and cross range capability of a vehicle is the lift-to-drag (L/D) ratio [Ref. 15:p. 47]. By adjusting the vehicle L/D ratio or bank angle, σ , (the angle between the vehicle lift vector and the plane containing the vehicle position and velocity vectors), the extent of the range and cross-range can be controlled [Ref. 15:p. 44].

c. Skip Reentry

A skip reentry is characterized by a vehicle whose L/D is greater than zero. Sufficient lift is produced to dominate the gravitational and centrifugal forces. If this lift is combined with a large enough initial angle of descent, a reentry trajectory with

one or more skips may be produced. As the vehicle begins to reenter, it reaches a minimum altitude where it begins to "pull-up" due to the lift force dominating over gravity. Eventually, the vehicle will exit the atmosphere at a reduced velocity. If the exit velocity and flight path angle are correctly controlled, the vehicle will achieve a brief orbital phase followed by a second reentry downrange from the first. [Ref. 16:pp. 245-246]

B. MAJOR FACTORS INFLUENCING UNCONTROLLED REENTRY

It is the focus of this thesis to describe the physical processes of the final few revolutions of a reentry body's orbit and the reentry phase to impact. Reentry trajectory techniques differ from orbit determination techniques. The reentry phase is very dynamic as opposed to the exoatmospheric phase of orbital motion. Specifically, the reentry phase is characterized by:

1. Rapidly decreasing altitude
2. Rapidly increasing aerodynamic heating effects
3. Rapidly changing aerodynamic load effects

The reentry phase can be characterized by that portion of the trajectory prior to breakup and after breakup. Prior to breakup, the reentry trajectory equations of motion include parameters such as gravity, atmospheric density, ballistic coefficient, position and velocity. Solutions to the reentry equations of motion can be found using analytical,

semi-analytical and numerical techniques. Breakup can be described as that point in the trajectory where heating effects and load effects cause the reentry body to lose its structural integrity.

1. Modeling Reentry Equations Of Motion

a. Basic Equations of a Rigid Body

The three basic equations of a rigid body are

$$\frac{dr}{dt} = V \quad (1)$$

$$\frac{dK}{dt} = F \quad (2)$$

$$\frac{dH}{dt} = M \quad (3)$$

where

H = reentry body's angular momentum vector relative to its center of mass

K = reentry body's linear momentum vector

M = total moment force vector relative to the center of mass

F = total force vector acting on the body

r = position vector of the body

V = velocity vector of the center of mass

Equations (1) and (2) are the kinematic and force equations, respectively.

When these equations are coupled, they yield one second-order, non-linear, vector

differential equation which describes three-dimensional motion of the reentry body's center of mass, given by

$$\frac{d^2 \mathbf{r}}{dt^2} = \mathbf{g} + \mathbf{a}_{\text{drag}} \quad (4)$$

where \mathbf{g} is the gravitational field and \mathbf{a}_{drag} represents the atmospheric drag acceleration. It is atmospheric drag that causes an artificial satellite to decay and reenter.

Equation (3) describes the motion of a body about its center of mass, commonly referred to as attitude motion. The reentry body's attitude is related to angle of attack, α , and is an important parameter which will be discussed in the next section.

When the system of equations (1) through (3) are coupled along with the attitude parameters, it yields two second-order, non-linear, vector differential equations or six second-order scalar differential equations. These six differential equations completely describe the six-dimensional motion of and about the center of mass. This system of equations is commonly referred to as the six-degree-of-freedom model which will be described further in Chapter III.

b. Modeling Gravity

In equation (4) the gravitational field, \mathbf{g} , may be written as an inverse square relationship

$$\mathbf{g} = -\frac{\mu}{r^3} \mathbf{r} \quad (5)$$

where

$$\mu = \text{gravitational constant (Earth} = 3.9865 \times 10^5 \text{ km}^3/\text{sec}^2)$$

or more accurately via the geopotential model. The geopotential model divides the Earth into three sets of geographically divided regions described by latitude and longitude as shown in Figure 7 [Ref. 17:p. 233]. The significance of the geopotential model is its ability to describe the gravitational field more accurately than a point mass model for the Earth. For example, in the region of reentry below 120 km, the first-order zonal harmonic J_2 , may attain a magnitude approaching that of atmospheric drag [Ref. 18:p. 40].

c. Modeling Atmospheric Drag

As previously mentioned, the force that causes an artificial satellite's orbit to decay is atmospheric drag. The atmospheric drag acceleration vector, in equation (4), acts in the direction opposite of the satellite's relative velocity vector and is given by [Ref. 17:p. 258]

$$\mathbf{a}_{drag} = -\frac{1}{2} \frac{C_D A}{m} \rho V_{AV}^2 \mathbf{v} \quad (6)$$

where

C_D = satellite drag coefficient

A = aerodynamic effective cross-section area

m = satellite mass

ρ = local neutral density of the atmosphere

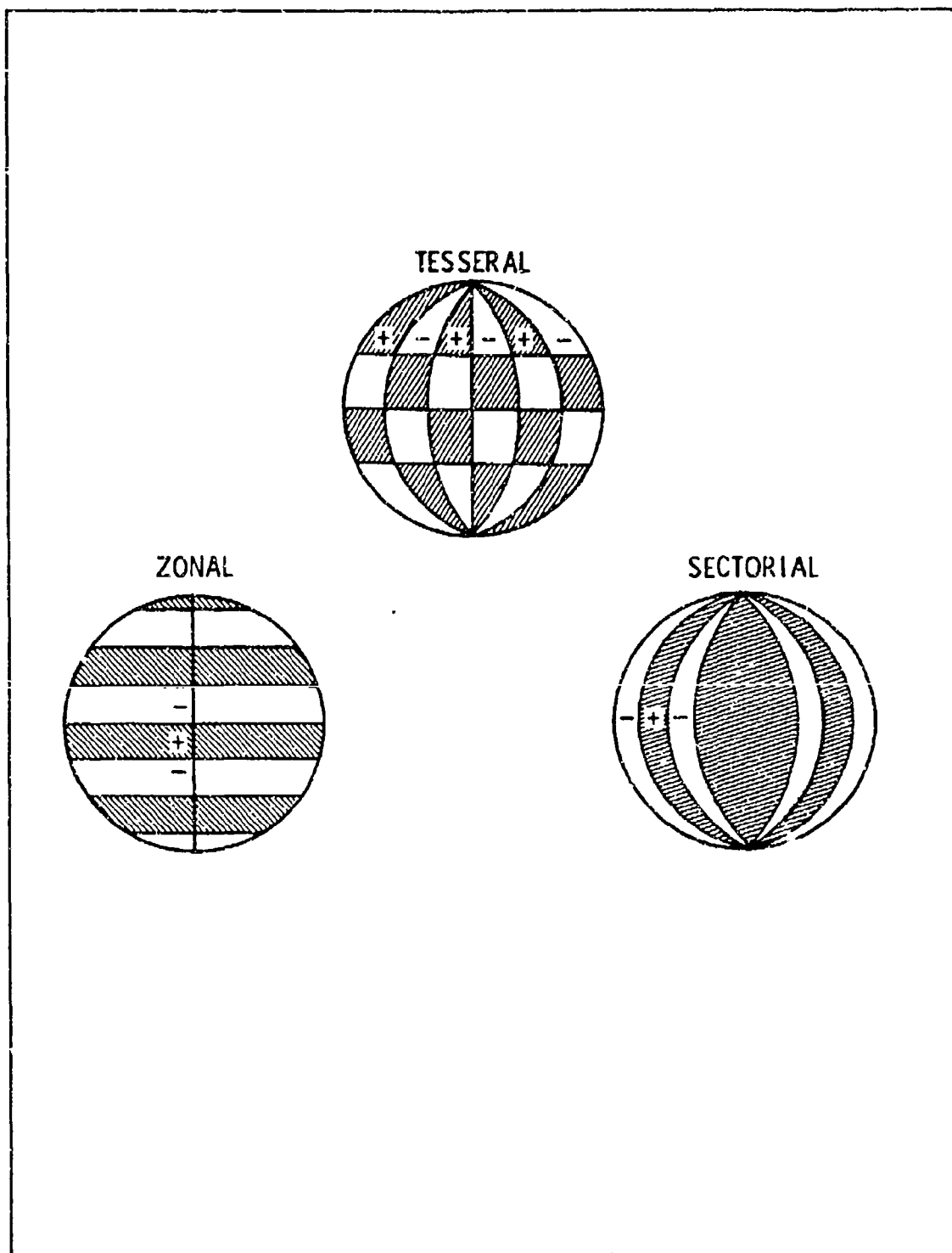


Figure 7: Earth Geopotential Model
[Ref. 17]

$$V_A = |V - \omega_e \times r| \quad (\text{satellite's airspeed})$$

$$v = \text{unit vector in direction of } (V - \omega_e \times r)$$

$$\omega_e = 2\pi \text{ rad/day}$$

$$V = \text{satellite's inertial velocity vector}$$

The ballistic coefficient, from equation (6), is defined as

$$B = \frac{C_D A}{m} \quad (7)$$

Atmospheric drag dissipates the satellite's energy which in turn causes a decrease in the semi-major axis. Drag affects high eccentricity orbits by gradually decreasing the apogee altitude, while maintaining a nearly constant perigee altitude, resulting in circularizing the orbit as shown in Figure 8 [Ref. 17:p. 258]. This contraction will continue until the satellite begins the reentry phase. Under certain simplifying assumptions, such as ignoring the rotation of the atmosphere, the analytical results describing the change per one revolution in semi-major axis and eccentricity for orbital decay are given by [Ref. 19:p. 230]

$$\Delta a = -\frac{C_D A}{m} a^2 \int_0^{2\pi} \rho \frac{(1+e\cos E)^{\frac{3}{2}}}{(1-e\cos E)^{\frac{1}{2}}} dE \quad (8)$$

$$\Delta e = -\frac{C_D A}{m} a \int_0^{2\pi} \rho \left(\frac{1+e\cos E}{1-e\cos E} \right)^{\frac{1}{2}} (\cos E + e) dE \quad (9)$$

where

$$a = \text{semi-major axis}$$

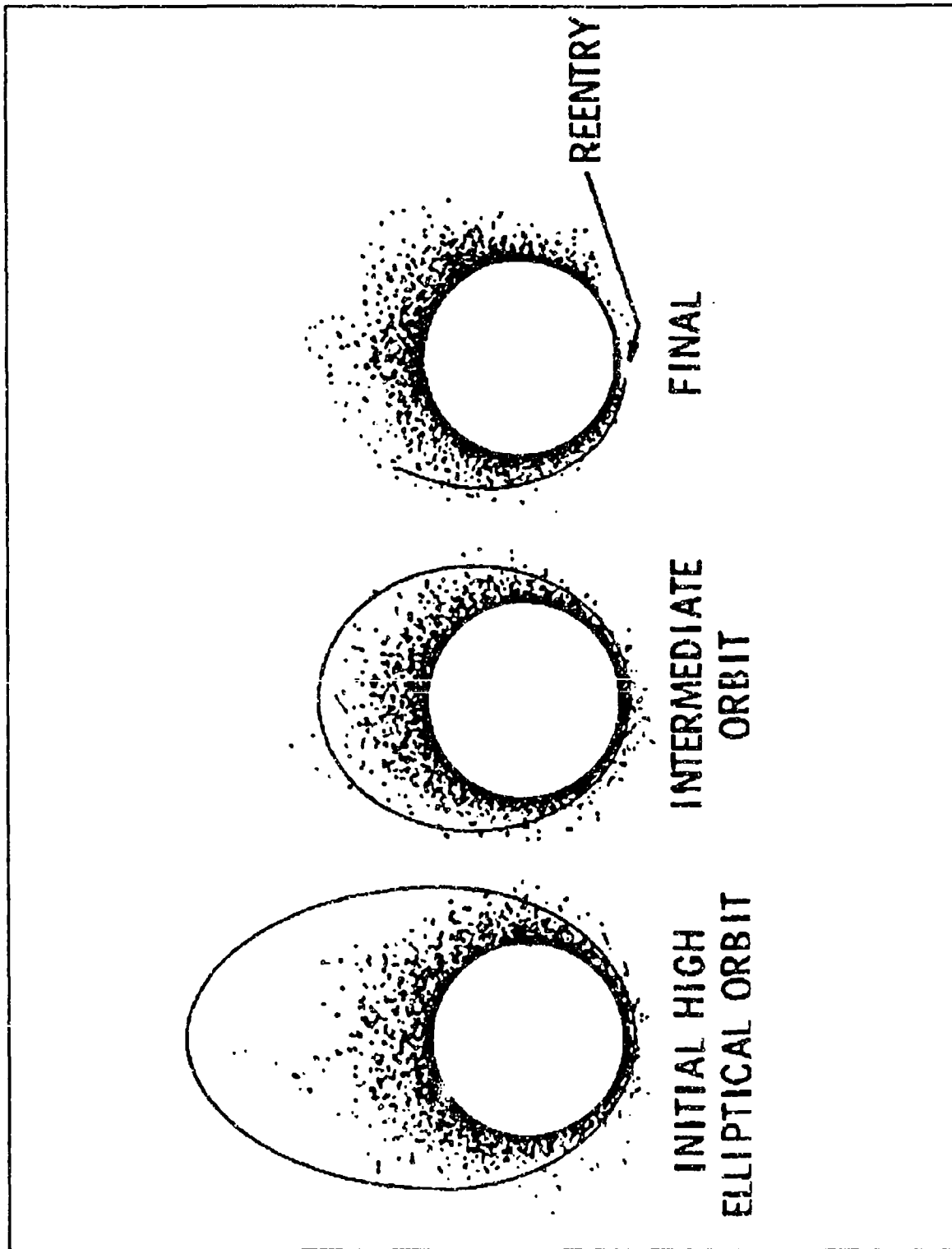


Figure 8: Drag Effect On High Eccentricity Orbits
[Ref. 17]

e = eccentricity

E = eccentric anomaly

(1) *Modeling Atmospheric Density.* The Earth's atmosphere is primarily composed of nitrogen and oxygen. Solar radiation affects the dynamic properties of this medium by constantly changing the temperature, pressure, chemical constituents, particulate presence and electrical properties [Ref. 20:p. 5]. The inability to model the atmospheric neutral density is an integral part of the satellite reentry problem. Neutral density is defined as the density of the neutrally charged constituents of the atmosphere. The atmospheric density is not precisely known along the satellite path because it varies with geographic location, solar and geomagnetic conditions, altitude and time [Ref. 17:p. 257].

Atmospheric density models are categorized as either "theoretical," or "empirical" models. Empirical models describe the phenomena of the Earth's atmosphere, based on a summary of observed data and are constructed independently of the laws of physics. Theoretical models apply the laws of physics. Empirical and theoretical models may have overlapping domains. For instance, data used to construct a particular empirical model may be smoothed and/or extrapolated based on theoretical considerations. Likewise, theoretical models must be compared to empirical data in order to define empirical parameters such as average sea level values of pressure and temperature and to establish assumption limits. [Ref. 21:pp. B-1,B-2] For example, the well known Jacchia models and the global dynamic models are semi-theoretical and semi-empirical in nature. The global dynamic models describe the physical and chemical

processes of the Earth's coupled thermosphere-ionosphere system. Solar radiation and auroral input measurements are used in the physical model to predict the time-dependent density response. [Ref. 22:p. 1]

A simplified analytical atmospheric model demonstrates the relationships between temperature, altitude and density

$$\rho = \rho_0 e^{\left(-\frac{z}{H}\right)} \quad (10)$$

where

ρ_0 = sea level air density

z = altitude

H = atmospheric scale height (RT_0 / g)

T_0 = atmospheric temperature at sea level

R = gas constant (air)

Equation (10) is a simple analytic relationship where the atmospheric density decreases exponentially with altitude when gravity, temperature and chemical composition are assumed to be constant at all altitudes. This model represents a rough approximation of the atmospheric density. Additional physical properties and levels of sophistication can be incorporated into this simplified model in order to better describe the actual atmosphere.

Empirical atmospheric density models use a variety of functions to describe the atmosphere. Some of these functions are common to most models. The

following list provides a brief description of these common functions: [Ref. 21:pp. B-13--17]

1. Altitude--density decreases with increasing altitude.
2. Early afternoon bulge--maximum daytime temperatures cause the density to increase at satellite altitudes.
3. Average 10.7 cm ($F_{10.7}$) flux--the average solar power per unit area at a frequency of 2800 MHz ($\lambda = 10.7$ cm) measured at various Earth locations. The 10.7 cm flux is closely correlated to the extreme ultra-violet (EUV) radiation which heats up the upper atmosphere and is used as an indicator of the EUV flux, since EUV flux is absorbed at higher altitudes and is converted to heat.
4. Daily 10.7 cm flux--accounts for the rapidly changing values of the $F_{10.7}$ measurement.
5. Geomagnetic index (A_p)--related to the activity of charged particles. Usually modeled as a correction to the atmospheric temperature.
6. Winds--speeds up to 300 m/s have been observed in the upper atmosphere. Wind can significantly change the drag experienced by the satellite since drag is proportional to the square of the velocity with respect to the surrounding air.

Numerous empirical atmospheric density models have been developed since the launch of Sputnik I [Refs. 23-31]. Early models such as the Jacchia 70 and 71 were derived from the analysis of satellite drag. These models identified the upper atmosphere as dependent on solar flux, geomagnetic index, diurnal, monthly and seasonal variations. A later model, the Jacchia 77 model incorporated composition data of nitrogen (N_2) and mono-atomic oxygen (O) which was observed from satellite mass spectrometers. The mass spectrometer and incoherent backscatter (MSIS) model was

constructed using composition data derived from satellite mass spectrometers, accelerometers and ground based incoherent backscatter measurements.

Several comparison studies have been conducted with various empirical atmospheric density models to determine their overall accuracy and efficiency. These studies indicate the following limitations and deficiencies of empirical models [Refs. 21, 32-34]

1. Accuracies of models have remained relatively unchanged for the past two decades.
2. Statistical analysis of measured satellite accelerometer density data as compared with atmospheric density model mean values and standard deviations, indicate mean value accuracies of approximately $\pm 10\%$ with standard deviations of approximately $\pm 15\%$.
3. Some models are significantly less efficient in terms of computational time.
4. The $F_{10.7}$ cm measurement does not adequately represent the complex interaction between the EUV flux and the thermosphere.
5. The geomagnetic index, A_p , or 3 hour K_p does not necessarily represent the physical mechanism that causes the variation in atmospheric density.
6. New model parameters such as the precipitation index (used as an indicator of magnetospheric activity), are needed to model the real physical variations in the atmosphere.

Additionally, our ability to predict the solar flux and the geomagnetic field is usually difficult and unreliable at best. As a consequence, accurate forecasting of atmospheric density into the future is limited. This affects the

determination of the predicted orbital decay rates because of the dynamic dependence on the variations of the $F_{10.7}$ and A_p indices. [Ref. 35:p. 1]

Considerable progress has been made over the past decade in the development of a dynamic atmospheric model of the coupled thermosphere-ionosphere system. The National Center for Atmospheric Research (NCAR) has developed a model as the thermosphere/ionosphere general circulation model (TIGCM). The pressure coordinate primitive equations of the lower atmospheric meteorology are the foundation of the TIGCM. TIGCM uses 20 minutes of CRAY-Y-MP 8/64 computer time per simulated model day to compute the prognostic thermodynamic, eastward and northward momentum equations and diagnostic equations of state and continuity. The model utilizes a 5° lat-long grid with 24 constant pressure surfaces distributed from an altitude of 95 to 500 km. Density data collected from a 200 km altitude satellite was compared with the TIGCM calculated density and the results showed that the TIGCM calculations were within $\pm 9-12\%$ on a point by point basis along the satellite's track. A new version, TIE-GCM, added an interactive dynamo model to calculate electrodynamic interactions between the thermosphere and the ionosphere. Results indicate this version model is able to provide improved determination of thermospheric density, especially during disturbed geomagnetic conditions. [Ref. 22:pp. 1-6] An operational version of this model, using a vector spherical harmonic (VSH) technique is under development at the University of Michigan. With further development, this dynamic atmospheric model may be able to forecast global atmospheric density values with errors less than 10%. [Ref. 36]

(2) *Modeling Aerodynamic Coefficients.* The aerodynamic coefficients, depend upon the following factors:

1. The shape and dimensions of the vehicle
2. The vehicle orientation to the on-coming air flow (angle of attack)
3. The temperature and composition of the neutral atmosphere
4. The gas-surface interaction phenomenon

The flow phenomena encountered around complex shapes further complicates and varies this parameter in the aerodynamic regimes: free molecular flow, transitional flow, and continuum flow [Ref. 37:p. 5]. A C_D of 2.2 is typically used as a constant value in the free molecular flow region above 120 km. However, C_D is a function of angle of attack, shape and flow regime. Therefore, knowing the vehicle's motion about its center of mass is a critical factor in determining the aerodynamic forces acting on the vehicle. These forces dictate the orbit decay rate, reentry and impact location. C_D can vary from 2 in the free molecular flow regime to a value much less than 1 in the continuum flow regime.

(3) *Rarified Gas Dynamics.* The pressure distribution and subsequent forces imparted by the near flowfield on a reentry body determines the forces and moments acting on the body via the aerodynamic coefficients [Ref. 20:p. 203]. There are basically five flow regimes which have distinguishable characteristics. These five flow regimes may be given quantitative definition using the Knudsen number (Kn). The Knudsen number is defined as the ratio of molecular mean free path to a characteristic

vehicle dimension, usually nose radius. The Knudsen number is indexed according to its reference mean free path, either after collision or in the oncoming flow.

The boundary layer may be characterized by the Reynolds number (Re). Flow is said to be laminar when the viscous forces are sufficiently large to damp out oscillations caused by the dynamic forces. A low Reynolds number is characteristic of laminar flow. Turbulent flow is said to occur when the dynamic forces overcome the viscous forces, there is random mixing of particles and large momentum exchanges between fluid particles. When flow over a solid body reaches a critical Reynolds number the initial laminar flow transitions to turbulent flow. Turbulent flow is a critical factor in reentry since there is much more energy near the vehicle's surface than in laminar flow conditions. In turn, under turbulent flow conditions, more heat is transferred to the surface of the vehicle. The five flow regimes are shown graphically in Figure 9 and described as follows: [Ref. 20;pp. 203-206]

1. Free Molecule Regime--this region is where the molecular mean free path (λ) is relatively large compared to a characteristic vehicle dimension such as nose radius. When molecules collide with a boundary layer they attain the state of that boundary after a single collision. This flow regime is characteristic of the uppermost portion of the atmosphere.
2. Near Free Molecular Flow--frequently referred to as the "slip region" because gas molecules will acquire the momentum of the moving boundary only after several collisions. If, on the average, a molecule fails to acquire the momentum of the moving boundary after a single collision, then it is said to lack "accommodation." This lack of accommodation means that the temperature is a nearly discontinuous function of distance away from the moving surface.

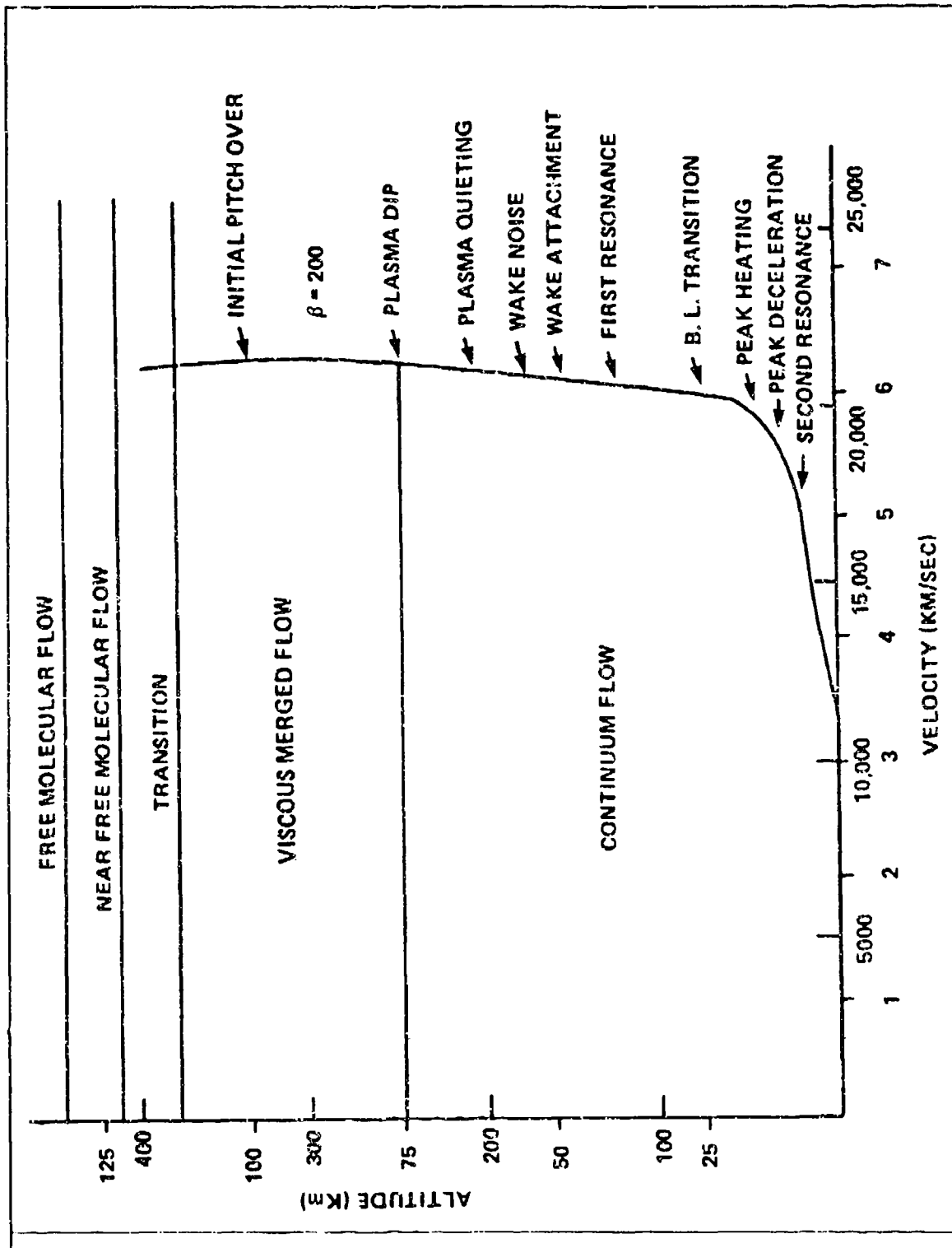


Figure 9: Flow Regimes
[Ref. 20]

3. Transition Regime--little is known about aerodynamic quantities such as lift, drag or heat transfer. This region is not treated very well analytically.
4. Viscous Merged Layer Regime--essentially that region consisting of dynamically coupled shock-wave, boundary-layer interactions. The presence of a boundary layer on the wall alters the boundary conditions for the shock wave, simultaneously, the large pressure gradients due to the shock wave strongly alter the boundary-layer flow. Neither the shock wave nor the boundary layer may be treated as discontinuities. This is the region from approximately 110 km to 75 km; this is where the "initial pitch over" occurs and reentry "starts."
5. Continuous Regime--the region where classical fluid mechanics of high Reynolds number applies, here the shock wave and boundary layers are again treated as discontinuities. Often this regime is subdivided into four categories (subsonic, transonic, supersonic, hypersonic) with lines of demarcation established by Mach numbers.

(4) *Vehicle Profile Area.* The profile area, or aerodynamically effective cross-section of the vehicle, is the area presented to the oncoming flow of the atmosphere and is a function of the vehicle's attitude and configuration. A spherical satellite maintains a constant profile area. More complex vehicles that have various design shapes and deployed solar panels can have highly variable areas. The ability to model the area depends on the known dimensions and orientation of the vehicle. Since an uncontrolled satellite reentry is characterized by a critical system failure or the end of its operational lifetime, communications with the vehicle may have been lost. Under this condition, information on the satellite's attitude will not be directly available [Ref. 37:p. 4]. Additionally, the vehicle will experience increasing aerodynamic and thermal loads as the altitude decreases. These forces will act to change the vehicle configuration by deformation and removal of structures (mass) [Ref. 5:p. iv].

(5) *Vehicle Mass.* Knowing the mass of a satellite accurately assumes a comprehensive knowledge of the vehicle. This information may be available for some U.S. satellites, however, for foreign systems this may pose a problem. As mentioned in the previous paragraph, aerodynamic and thermal loads can change the satellite mass. The ability to model changes in mass also assumes an accurate knowledge of the environment and how it affects the forces and subsequent motion of the vehicle about its center of mass. In order to develop a model capable of predicting this motion, the vehicle's moments of inertia must be known. [Ref. 37:p. 4]

(6) *Vehicle Velocity.* The relative velocity of the vehicle with respect to the Earth's rotating atmosphere in equation (6) is

$$V_A = |V - \omega_e \times r| \nu \quad (11)$$

The maximum deceleration and heating rate experienced by a reentry body is a function of velocity. As mentioned before, wind can change the vehicle's relative airspeed which can affect the drag or lift experienced by the vehicle. Determination of the vehicle's velocity using doppler range rate observation information is relatively accurate. Uncertainties in the radial velocity may be as low as .166 m/s [Ref. 38:p. 138].

d. Modeling Aerodynamic Lift

Lift causes the vehicle trajectory to follow a glide slope, skip path, or perturbed ballistic flight path. During hypersonic flight conditions, lift is generated by pressure forces on the lower surfaces at angles of attack caused by motion about the

center of mass. A perturbation from the nominal or zero lift flight path is the net result.

The force of aerodynamic lift is defined as [Ref. 39:p. 25]

$$L = \frac{1}{2}\rho C_L AV^2 \quad (12)$$

where

C_L = coefficient of lift

Reentry trajectories with lift reduce the thermal and structural loads on the vehicle.

During the final revolutions of orbit decay and reentry, lift is assumed or modeled to be very small or zero [Ref. 14:p. 2], [Ref. 39:p. 33]. However, an uncontrolled reentering satellite may generate a significant lift vector depending on the attitude, shape and motion of the vehicle about its center of mass. When this occurs, the lift will not be distributed equally about the nominal flight path. This may result in a deviation from the projected impact point. [Ref. 15:p. 47]

e. Reentry Equations of Motion

The reentry equations of motion can be derived by the mathematical transformation of the second-order, nonlinear, vector differential equation (4). Several analytical and semi-analytical theories describing a satellite's shallow reentry equations of motion have been developed over the last thirty five years [Refs. 14,40,41,42].

With the advent of manned space exploration and recoverable probes, it became necessary to develop accurate theories of the entry phase, during which the altitude, velocity, deceleration and the heating rate vary rapidly. [Ref. 41:p. 2]

In the derivations of these theories, several strong physical assumptions were made:

1. Spherical Symmetry--the Earth and its atmosphere are spherically symmetric.
2. Non-rotating Atmosphere--the rotation of the Earth's atmosphere which is approximately equal to the angular velocity of the planet is neglected.
3. Exponential Atmosphere--the atmospheric density decreases exponentially with altitude.
4. Gravitational Field--the gravitational field is assumed to be constant during reentry at all altitudes.
5. Coordinate System--a non-rotating two-dimensional inertial coordinate system with the origin at the center of the Earth.

(1) *Fundamental Equations of Entry Dynamics.* The exact reentry equations of motion derived by Loh, reference [40], are presented to show the basic relationship of the vehicle's force vectors along the radial and normal direction to the flight path in an inertial coordinate system as shown in Figure 10 [Ref. 40:p. 19]. This presentation serves as the foundation for the development of more sophisticated theories to be presented in Chapter III. Physical assumptions 1,3,4, and 5 were used in the derivation of these equations.

The magnitude of the relative aerodynamic velocity, V_r , does not equal the magnitude of the inertial velocity, V , due to the reentry body's trajectory through the moving atmosphere. These velocities and their geometric relationships are shown in Figure 11 [Ref. 40:p. 18] and are related by the following equation

$$V_r = V \left[\sqrt{1 - \left(\frac{V_e}{V}\right)^2 (1 - \cos \gamma_r \cos \alpha_r)} - \left(\frac{V_e}{V}\right) \cos \gamma_r \cos \alpha_r \right] \quad (13)$$

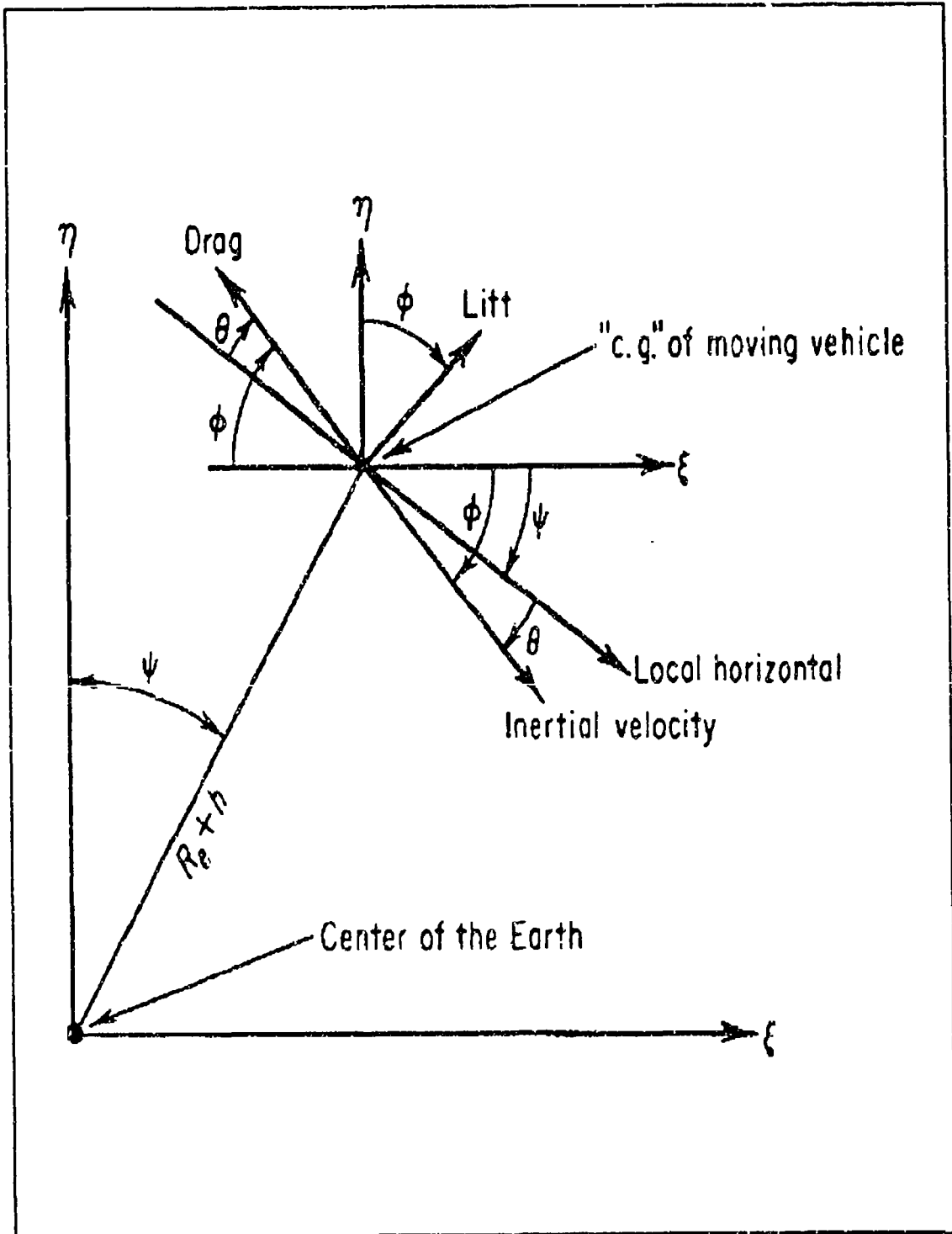


Figure 10: Inertial Coordinate System
 [Ref. 40]

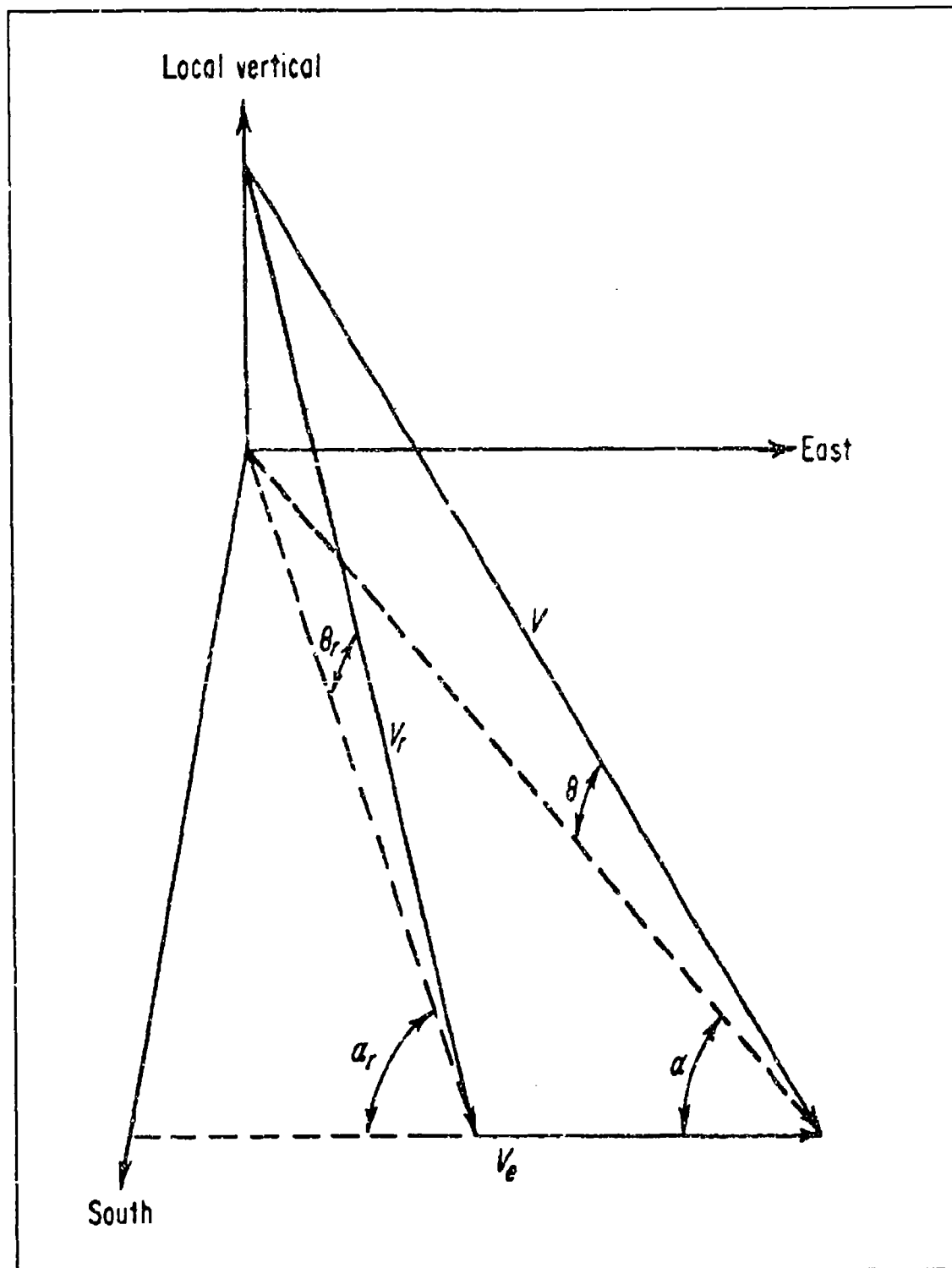


Figure 11: Relationship Between Relative And Inertial Velocity
[Ref. 40]

where

$$V_e = 1519 \cos \delta \text{ (ft/sec) (velocity of the Earth's surface at a specific latitude)}$$

$$\delta = \text{latitude angle}$$

$$\gamma = \theta \text{ (flight path angle to the local horizon from Figure 10)}$$

The force components from Figure 10 are defined as

$$F_\xi = -D \cos \phi + L \sin \phi - mg \sin \psi = m \frac{d}{dt} (V \cos \phi) \quad (14)$$

$$F_\eta = L \cos \phi + D \sin \phi - mg \cos \psi = m \frac{d}{dt} (V \sin \phi) \quad (15)$$

where

$$\phi = \gamma + \psi$$

$$V = V_r \text{ (relative velocity)}$$

By resolving equations (14) and (15) in the velocity direction, replacing L and D with equations (12) and (6) respectively, and by further rearrangement of the terms and simplification, according to Loh, the exact equations of motion are

$$\frac{d \cos \gamma}{d\rho} + \left(\frac{1}{\beta R_0} \right) \frac{\cos \gamma}{\rho} \left(\frac{g R_0}{V^2} - 1 \right) = \frac{1}{2} \left(\frac{L}{D} \right) \left(\frac{C_D A}{m \beta} \right) \quad (16)$$

$$\frac{d \left(\frac{V^2}{g R_0} \right)}{d\rho} + \left(\frac{C_D A}{m \beta} \right) \frac{\left(\frac{V^2}{g R_0} \right)}{\sin \gamma} = \left(\frac{2}{\beta R_0} \right) \frac{1}{\rho} \quad (17)$$

where

R_0 = radius of the Earth

β = inverse atmospheric scale height (Mg/RT)

M = mean molecular weight

The exact equations of motion of entry dynamics cannot be solved analytically, however, solutions can be found using numerical methods. First-order approximate analytical solutions have been developed by restricting the equations to limited regions of application. [Ref. 43:p. 25] The ability to accurately model and solve these equations depends on the knowledge of the initial conditions: the initial position, and velocity, the vehicle's area and mass, the neutral atmospheric density, and the aerodynamic coefficients.

2. Modeling Breakup

a. Reentry Body Structural Mechanics

A satellite will experience structural and thermal loads during reentry into the Earth's atmosphere. The structural response of the body during reentry may depend on the following factors: [Ref. 44]

1. Static load effects
2. Dynamic load effects
3. Thermal load effects

The coupled effect of these factors may determine when the body will experience structural failure.

b. Modeling Reentry Heating Effects

The reentry process is essentially that region of flight where the vehicle's velocity into the atmosphere is reduced and its kinetic energy is converted into thermal energy in the surrounding medium. Since breakup is determined, in large part, by when the outer surface reaches its melting point, reentry heating directly affects survivability. This will be discussed in detail in Chapter III. The conversion fraction of kinetic energy to heat energy is a function of the satellite's shape, velocity, and altitude. At very high altitudes (free-molecule flow region) the heat energy is developed almost entirely at the surface of the vehicle and up to one-half of the lost kinetic energy may be converted into heat in the vehicle body. [Ref. 43:p. 191] At low altitudes (continuum flow region) the heat energy will appear in the area between the shock wave and the body. This heat is transferred from the hot gas to the vehicle by conduction and convection through the viscous boundary layer which is adjacent to the surface of the vehicle. Radiant heating of the vehicle from the hot gas also occurs and this contribution to the surface heating is dependent upon:

1. Bluntness of the vehicle's leading edge
2. Excess orbital velocity of the vehicle

Excess orbital velocity is defined as an appreciably higher velocity than the circular orbital velocity for a given altitude. [Ref. 43:p. 192]

The rate at which the vehicle heats is not exclusively dependent upon this energy conversion fraction, it is also dependent upon the rate of kinetic energy loss by the vehicle. For the case of natural orbital decay, reentry is at small flight-path angles and the deceleration is very slow in the upper atmosphere. The surface heating rate is relatively low despite the high conversion fraction in this instance; therefore, the dominating factor is the low rate of kinetic energy loss by the vehicle. Conversely, at steep reentry angles, where deceleration occurs rapidly, the surface heating rate is high although the energy conversion fraction is low.

The total heat input into the reentry vehicle depends upon the time of heating as well as the heating rate. If the energy conversion rate were constant, the total heat input would simply be a fixed fraction of the initial energy and the type of reentry would not be of significance.

Three aspects of the aerodynamic heating process are significant, namely:
[Ref. 40:p. 181]

1. The total heat input, Q .
2. The time rate and maximum time rate of local stagnation region heat input per unit area (dH_s/dt) and $(dH_s/dt)_{max}$.
3. The time rate and maximum time rate of average heat input per unit area (dH_{av}/dt) and $(dH_{av}/dt)_{max}$.

The time rate of average heat transfer per unit area is given by equation (18) below. The average heat transfer is simply the total heat input divided by the time of input. Overall, reentry vehicle structural integrity is a function of the average heat input. [Ref. 40:p. 181] The time rate of local stagnation region heat input per unit area is given by equation (19). Local structural integrity is a function of local stagnation region heat input or the generation of local "hot spots." [Ref. 40:p. 182] The total heat input is given by equation (20).

(1) *Reentry Heat Input.* From the three previously mentioned areas of concern, the following generalized aerodynamic heating equations are given [Ref. 40:pp. 183-184]

$$\frac{dH_{av}}{dt} = \frac{1}{S} \frac{dQ}{dt} = \frac{1}{4} \rho V^3 C_F' \quad (18)$$

$$\frac{dH_s}{dt} = Kn \left[\sqrt{\mu_0} Pr^{-2} \left(\frac{\bar{\gamma}-1}{\bar{\gamma}} \right)^{\frac{1}{4}} \right] \left(\frac{\rho}{\sigma} \right)^{\frac{1}{2}} V^3 = K' \left(\frac{\rho}{\sigma} \right)^{\frac{1}{2}} V^3 \quad (19)$$

$$Q = \int \frac{dQ}{dt} dt = \frac{C_F' S}{4} \int \rho V^2 ds = \frac{C_F' S}{4} \int \frac{V^2 d\rho}{\beta \sin \theta} \quad (20)$$

where

H_{av} = average convective heat transferred per unit area, ft-lb/ft²

H_s = local stagnation region heat input per unit area

Q = convective heat transferred, ft-lb

and

$$C_F' = \frac{1}{S} \int_s \left[C_{FL} \left[\frac{\rho_l}{\rho} \right] \left[\frac{V_l}{V} \right] Pr_e^{\frac{1}{2}} \left[\frac{C_{Pl}}{C_p} \right] \right] dS \quad (21)$$

C_F' = equivalent skin-friction coefficient

V = velocity, ft/sec

ρ = atmospheric density, slugs/ft³

Kn = Knudsen number = λ/Re

Re = Reynolds number

λ = molecular mean free path

μ = coefficient of viscosity, lb-sec/ft²

Pr = Prandtl number, subscript e indicates "entry" value

γ = ratio of specific heats

σ = nose or leading edge radius, ft

K' = constant = 6.8 to 15×10^{-6}

$$K' = \left(\frac{\mu}{\mu_e} \right)^{\frac{1}{2}} \left(\frac{Pr}{Pr_e} \right)^{-\frac{2}{3}} \frac{\left[\frac{\bar{\gamma}-1}{\bar{\gamma}} \right]^{\frac{1}{4}}}{\left[\frac{\bar{\gamma}-1}{\bar{\gamma}} \right]_e^{\frac{1}{4}}} \quad (22)$$

S = surface area, ft²

θ = flight path angle, positive for descent

C_{Fl} = coefficient of friction (local conditions)

C_p = specific heat at constant pressure

C_{pi} = specific heat (local conditions)

The above equations make the following simplifying assumptions: [Ref. 40:p. 181]

1. Radiative heat transfer from the surface generally does not appreciably influence convective heat transfer to a vehicle; therefore, it is disregarded.
2. Effects of gaseous imperfections may be neglected.
3. Shock-wave boundary-layer interactions may be neglected.
4. Prandtl number is constant.
5. Reynolds analogy is applicable.

If the heat transferred to the reentry vehicle is expressed as a fraction of the total kinetic energy, then [Ref. 20:p. 138]

$$KE = \frac{1}{2}mV_E^2 \quad (23)$$

where

m = mass of reentry vehicle

V_E = reentry velocity

$$Q = \frac{2Q}{mV_E^2} \quad (24)$$

where

Q = fraction of heat transferred to the reentry vehicle

Q = total heat input

This may be rewritten as

$$Q = \frac{1}{2} \left[\frac{C_F S_w}{C_D S} \right] [1 - e^{-2a_r}] \quad (25)$$

where

C_F = coefficient of friction

C_D = coefficient of drag

S = reference area (usually nose tip)

S_w = wetted surface area

and where the trajectory parameter is defined by [Ref. 20:p.138]

$$a_E = \frac{\rho_0 C_D S H}{2m \sin \gamma_E} = \frac{\rho_0 g H}{2\beta \sin \gamma_E} \quad (26)$$

when

γ_E = reentry flight path angle

At small flight path angles, such as reentry from orbit decay, a_E will be very large,

therefore, equation (25) reduces to

$$Q = \frac{1}{2} \left[\frac{C_F S_w}{C_D S} \right] \quad (27)$$

It is now recognizable that the fraction of the initial kinetic energy, transferred to the reentry vehicle by convective heating, is one half of the ratio of the friction drag to total drag . [Ref. 20:p. 138]

In the case of ballistic reentry at small angles of reentry, both the maximum heating rate and total heat load increase as the effective mass-area ratio ($m/C_D A$) or ballistic coefficient increases [Ref. 40:p. 195].

Assuming a constant ballistic coefficient throughout the reentry process yields a different relationship [Ref. 40:p. 198]

$$Q = \frac{m}{C_D A} \quad (28)$$

$$\left(\frac{dH_s}{dt}\right)_{\max} = \sqrt{\frac{m}{C_D A}} = \frac{1}{\sqrt{\frac{L}{D}}} = \sqrt{\sin \theta} \quad (29)$$

$$Q = \sqrt{\frac{L}{D}} = \frac{1}{\sqrt{\sin \theta}} \quad (30)$$

$$\left(\frac{dH_s}{dt}\right)_{\max} = \frac{1}{Q} \quad (31)$$

Therefore, reentry at small angles of inclination reduces the maximum heating rate of the vehicle, however, the total heat load is increased. [Ref. 40:p. 198]

(2) *Reentry Heating Rate.* If the heating rate per unit time is defined

[Ref. 20:p. 135]

$$\dot{q} = \frac{dq}{dt} \quad (32)$$

then the total heat-transfer rate may be written [Ref. 20:p. 136]

$$\dot{Q} = \int_{S_w} \dot{q} ds \quad (33)$$

After some simplification it is possible to write [Ref. 20:p. 137]

$$\dot{Q} = \frac{C_F \rho S_w V^3}{4} \quad (34)$$

this assumes

$$\int_{S_w} C_F ds = C_F S_w \quad (35)$$

It is now possible to define dq/dt as the average rate of change of heat transfer per unit area

$$\dot{q} = \frac{C_F \rho V^3}{4} \quad (36)$$

It can be shown that dq/dt is a maximum when ρV^3 is a maximum. [Ref. 20:p. 137]

(3) *Ablation.* As previously discussed, the heating experienced by reentry at small flight path angles is different from that of reentry at large flight path angles. The flight duration is much longer for the first case and even with a lower maximum heating rate, the total heat input exceeds that of the larger reentry angle. The

predominant cooling mechanism of uncontrolled reentry of vehicles not designed to survive reentry is ablation. Ablation is the term which generally applies when:

...there is a removal of material (and an associated removal of heat) caused by aerodynamic heating, and therefore embraces, melting, sublimation, melting and subsequent vaporization of the liquid film, burning and depolymerization. [Ref. 15:p. 198]

Ablative materials are measured as "effective" depending on their capacity to dispose of heat (latent heat) by convection in the liquid film, and by convection in gaseous form in the boundary layer. Previous work has shown that when a material experiences a large percentage of total mass loss as vaporization, it is a more effective ablative material. Sublimation is the process whereby all the mass loss undergoes vaporization, there is no liquid film, and therefore is an excellent method for removing large amounts of heat. For these reasons, materials which undergo sublimation at reasonably high temperatures are generally more efficient at removing heat and thereby reducing the thermal load on the reentry vehicle. [Ref. 40:p. 204]

Radiative cooling is another mechanism by which heat is removed from the reentry vehicle during reentry. Radiative cooling and ablation combined are an effective pair in balancing the heating effects of reentry for a lifting body. For a non-lifting body radiative cooling is inefficient.

C. GENERAL DESCRIPTION OF THE REENTRY PHASE

A decaying satellite possesses a large amount of kinetic energy due to its velocity and potential energy because of its altitude above the Earth's surface. As the satellite encounters the atmosphere, a shock wave forms ahead of the vehicle which heats up the

atmosphere surrounding the vehicle. This enveloping layer of incandescent atmosphere causes the vehicle's temperature or thermal load to continually increase as it penetrates into an increasingly denser atmosphere. During this phase, the velocity continues to decrease as the kinetic energy is converted into heat through the atmospheric drag. If all the satellite's energy were converted into heat and contained within the vehicle, then there would be more than enough energy to vaporize the vehicle. However, this is not the case. A large part of the total energy is diverted away from the vehicle by two processes. The first process unloads a major fraction of the heat into the atmosphere by a strong shock wave mechanism. The second process involves the radiation of heat away from the hot surfaces. [Ref. 43:pp. 1-2]

The vehicle also experiences structural loads, which are a combination of aerodynamic and inertial loads [Ref. 45:p. 5]. Atmospheric drag forces usually cause a reduction in the vehicle's kinetic energy. Centrifugal and lift forces cause accelerations normal to the direction of the motion.

Aerodynamic lift and drag forces vary directly with the square of the vehicle's velocity, V^2 , and with the atmospheric density, ρ . Deceleration of the vehicle is a product of two quantities, density and velocity. As the satellite penetrates further into the atmosphere, the density increases rapidly resulting in a corresponding decrease in velocity due to drag. Initially, deceleration increases as shown in Figure 12 [Ref. 43:p. 7]. However, at some altitude the velocity begins to decrease at a faster rate than the increasing density, which results in a maximum deceleration. Additionally, the maximum heating rate, $\sim \rho V^3$, occurs at an altitude somewhat higher than the maximum

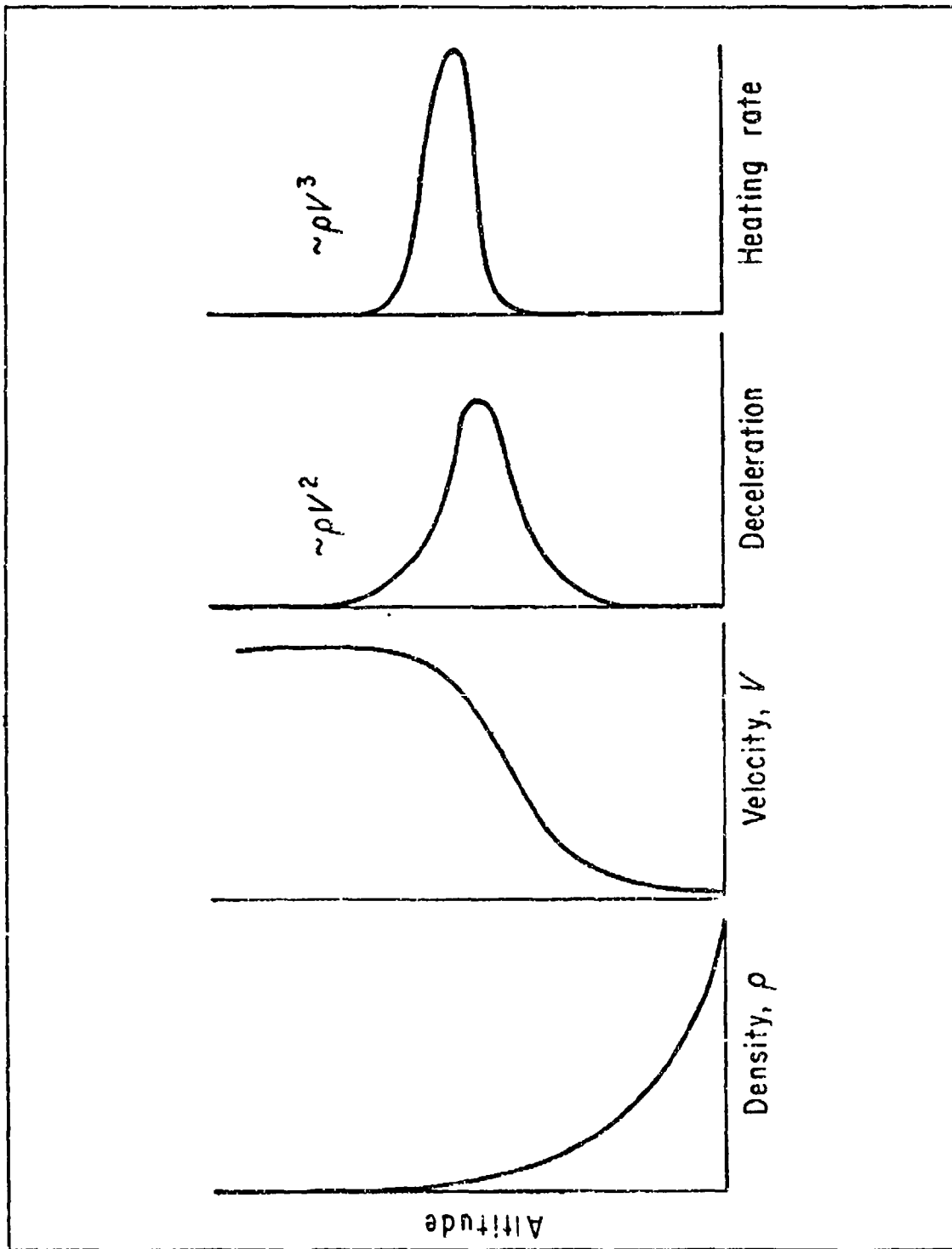


Figure 12: Changes During Atmospheric Reentry
 [Ref. 43]

deceleration [Ref. 20:p. 98], [Ref. 43:pp. 6-7]. A maximum deceleration of up to 8 g's, as shown in Figure 13, [Ref. 14:p. 30], occurs during this phase [Ref. 39:p. 36].

When the satellite's skin temperature and structural load become sufficiently high, the vehicle will start burning and breaking up. Solar panels and other projections such as antennas will separate at the earliest stage, while heavier pieces will breakup at lower altitudes. Based on predicted and observed data, satellite breakup commences at an altitude between approximately 75-120 km [Ref. 10:p. 5], [Ref. 46:p. 4], [Ref. 47:p. 39]. The resulting debris from the breakup will impact the Earth's surface provided it survives the reentry heating process.

D. CURRENT REENTRY THEORIES

Predicting reentry time and impact location relies upon observational data of the reentry vehicle. Based upon observed (measured) position and velocity, over the orbital path and ideally equally distributed over that path, an algorithm is used to calculate an elliptical orbit which best fits the observational data. If the algorithm attempts to model the physical reentry process, it will be referred to as a physical model by the authors. Another type of model to be discussed is the King-Hele or mean motion type of model which neglects certain physical aspects of the reentry process and focuses more on the observational data. The algorithm which "fits" the observational data to an elliptical orbit may also be used to propagate or predict future orbital locations as a function of time. These types of algorithms are commonly referred to as propagators.

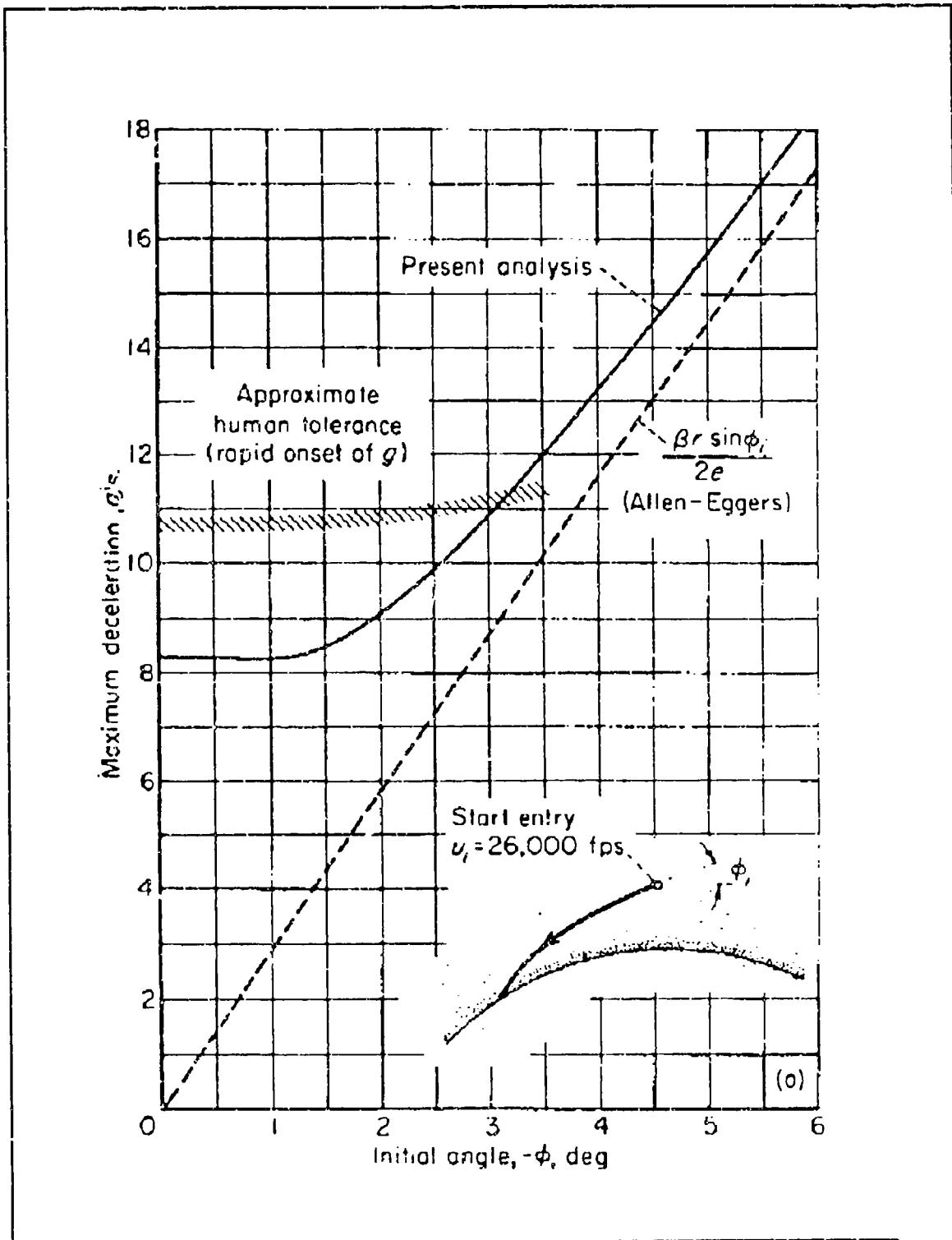


Figure 13: Maximum Deceleration vs Initial Flight Path Angle
 [Ref. 14]

1. Physical Modeling Theory

The current propagator in the United States, for reentry prediction, is the special perturbations (SP) model. This model is maintained by the Air Force Space Command and is the standard for reentry prediction in the United States.

Orbital periods of less than 87.5 minutes are defined by the Space Surveillance Center (SSC), Cheyenne Mountain Air Force Base, Colorado, as decaying orbits [Ref. 48:p. 3]. The SP model uses numerical methods to incorporate zonal, sectoral and tesseral orbital perturbations in the calculation of decaying orbit reentry predictions. Gravitational perturbations are modeled by mapping the Earth into small grids, which allows for enhanced resolution of the geopotential. Third body gravitational effects, sun, moon, and planets, may also be modeled. Third body gravitational effects are used primarily in the propagation of highly eccentric orbits with large apogee altitudes. The atmosphere is modeled using the Jacchia-Nicolet model which considers the following: [Ref. 48:p. 9]

1. Diurnal bulge
2. Solar activity
3. Geomagnetic activity
4. Semiannual variation

A technique known as differential corrections is used to "fit" the observations of the reentry vehicle into the best orbit. The differential corrections are a mathematical means of determining a single orbit path (ellipse) consistent with the observed data (the

only "known" information in the absence of active telemetry data). The need for the use of differential corrections arises from the fact that the model used to propagate the orbit into the future has inherent deficiencies. These deficiencies are then reflected as errors in the prediction of where the vehicle is supposed to be in its orbit as compared to where it is observed to be. Through a series of fitting observations to an orbit and updating the predicted orbital path, the reentry of the vehicle is calculated as a "time" when the altitude will reach a specified minimum value. This lower limit value of altitude is a function of the atmospheric density model. The impact dispersion area or footprint is calculated as ± 15 minutes of that reentry time. The sub-satellite ground trace is used to describe the impact area on the Earth's surface. Table 2 shows the format of observational data as used in the differential corrections process [Ref. 49]. Figure 14 shows the differential corrections display and Figure 15 shows the Tracking and Impact Prediction (TIP) display used at Cheyenne Mountain AFB. [Ref. 49]

It now becomes obvious that there are two extremely significant issues at hand:

1. The ± 15 minute window equates to approximately 1/3 of one complete revolution of the reentry vehicle's orbit in the decay phase.
2. The lack of observational data in the decay phase may significantly bias the predicted reentry time.

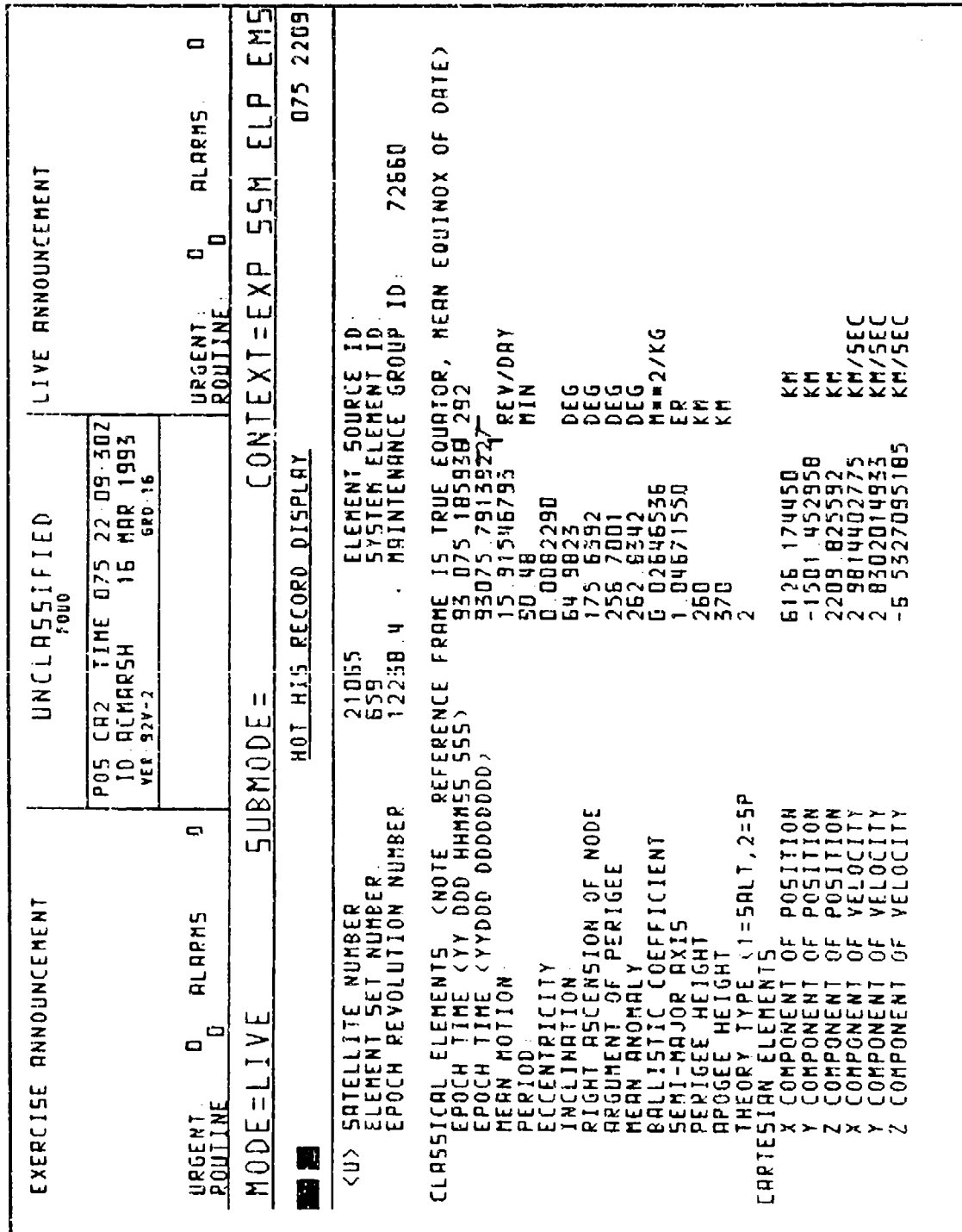


Figure 14: Differential Corrections Display
[Ref. 49]

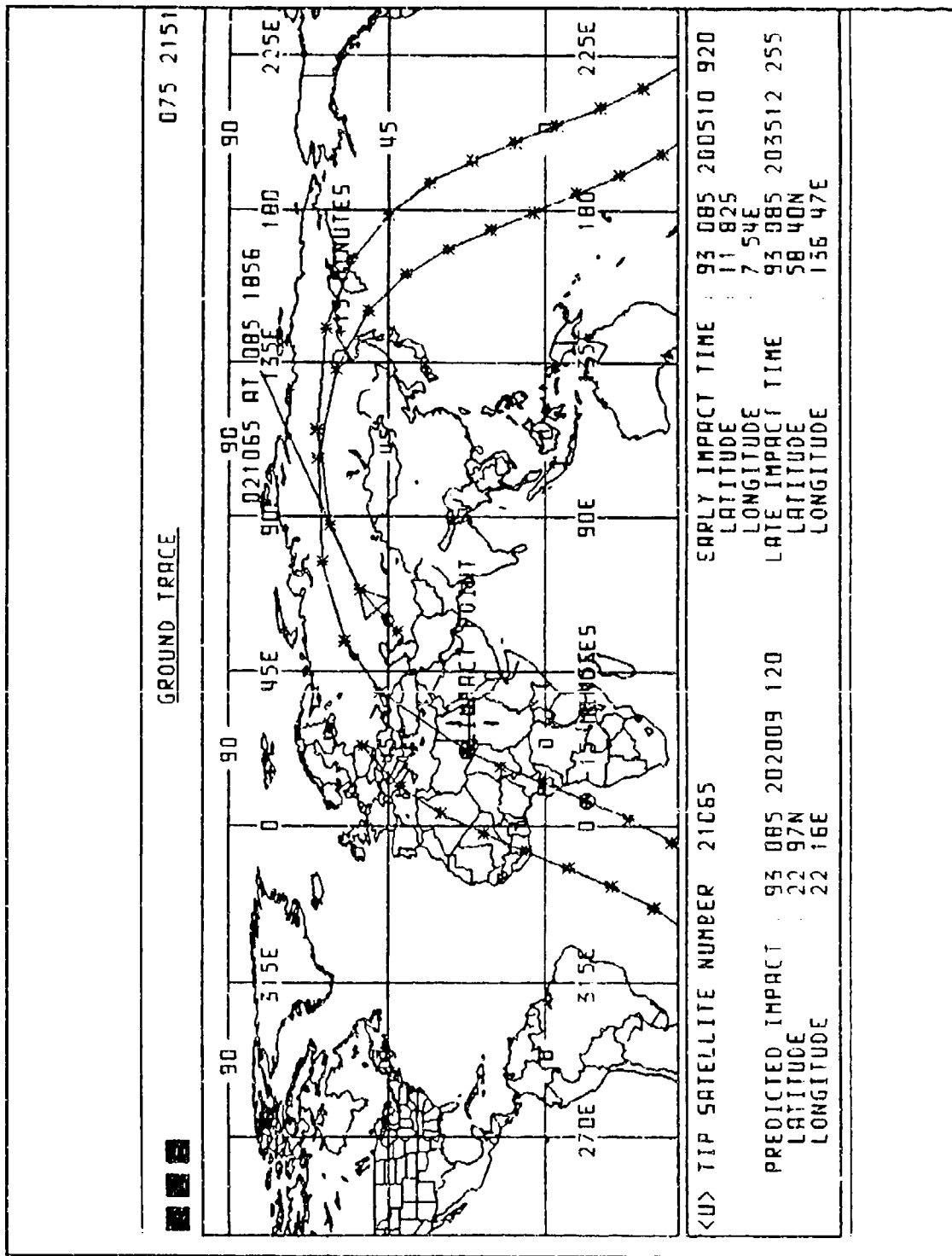


Figure 15: Tracking And Impact Prediction (TIP) Display
 [Ref. 49]

The accuracy of the reentry prediction is directly limited by the ability to observe the reentry process as well as indirectly by the inherent deficiencies in the models used to represent the physical reentry process.

2. Mean Motion Theory

In the early development of his mean motion theory of satellite lifetime prediction, King-Hele defined orbital lifetime as the time remaining until the eccentricity of the orbit reached zero [Refs. 19, 50-55]. This was a prediction of reentry based on the circularization, or contraction of the orbit, due to atmospheric drag. A principal assumption in this theory was that perigee height remained constant. When oscillations in perigee height were considered (which occurs when an oblate atmosphere is modeled), the theory had to be revised in order to take into account a zero eccentricity prior to reentry [Ref. 54]. The definition of orbital lifetime was then redefined in terms of mean motion, n , where a value of n (chosen by the user) represents an "end value" of a circular height. For example, a value of n equal to 16.5 rev/day would correspond to a circular orbit altitude of 150 km.

In the prediction of orbital lifetime, the observed rate of change of orbital period, dT/dt , was the entering argument (where T is the orbital period) [Refs. 19, 50-53]. This was equivalent to using the rate of change of mean motion, dn/dt , since the two are related by [Ref. 54:p. 5]

$$n = \frac{1}{T} \tag{37}$$

where

$$n = \text{rev/day}$$

$$T = \text{days}$$

In its simplest form, orbital lifetime is now expressed in terms of the rate of change of mean motion as

$$L = \frac{Q}{\dot{n}} \quad (38)$$

where

$$L = \text{lifetime in days}$$

$$\dot{n}/dt = \text{rev/day}^2$$

$$Q = \text{function of } e, n \text{ and } H \text{ (density scale height)}$$

and expanded by [Ref. 54:p. 8]

$$Q = \frac{3enI_0(z)}{4I_1(z)} [1 - 0.1J] \quad (39)$$

where

$$I_0, I_1 = \text{Bessel functions of the first kind, of degree 0 and 1, with argument } z$$

$$J = 0.3e_0 - 0.025$$

$$z = ae/H$$

For the circular orbit, the lifetime may be written [Ref. 54:p. 9]

$$L = \frac{3H_{-H}n(1-e^{-h/H})}{2a\dot{n}} \quad (40)$$

where

H_{-H} = scale height H km below initial altitude

h = decrease in altitude until reentry (120 km)

In this form, density scale height is the only parameter which is not directly derived from orbital data (observations). It can be shown that H is less sensitive to solar activity than a neutral density atmosphere model, therefore, uncertainties in solar activity will have less influence on the orbital lifetime prediction [Ref. 54:pp. 9-10]. Perhaps more importantly, the mean motion technique does not require any knowledge of:

1. Satellite attitude
2. Satellite size
3. Satellite shape
4. Satellite mass
5. Aerodynamic characteristics

These factors are all accounted for in the observation of mean motion and rate of change of mean motion. In summary, the mean motion theory is dependent upon five parameters: [Ref. 54:p. 12]

1. mean motion (n)
2. eccentricity (e)
3. daily solar activity index ($F_{10.7}$)
4. average solar activity index ($F_{10.7}$)
5. geomagnetic index (A_p)

The last three terms above are incorporated into the calculation of atmospheric scale height.

III. FORMULATIONS AND SOLUTIONS OF REENTRY

This chapter describes the "state-of-the-art" formulations and solutions (analytical, semi-analytical, and numerical) of decay-induced reentry as determined from the literature survey. Fundamental physical processes that were introduced in Chapter II, including reentry equations of motion, rarefied gas dynamics, reentry heating and reentry body breakup are presented.

A. ANALYTICAL REENTRY EQUATIONS OF MOTION

1. Chapman's Approximate Analytical Entry Equations of Motion

Chapman derived a nonlinear second-order differential equation by reducing equations (16) and (17) and by introducing a set of completely nondimensionalized variables [Ref. 14:pp. 3-14]. In the development of this equation, physical assumptions 1 through 3 from Chapter II were used. Additionally, two mathematical assumptions were used:

1. The fractional change from the center of the planet, dr/r , in a given increment of time is much smaller as compared to the fractional change in velocity, $d(V \cos \gamma)/V \cos \gamma$, given by the mathematical expression $|d(V \cos \gamma)/V \cos \gamma| \gg |dr/r|$.
2. The flight path angle, γ , related to the local horizon direction for lifting vehicles is sufficiently small such that the lift component in the horizontal direction is small as compared to the drag component, given by the mathematical expression, $1 \gg |(L/D) \tan \gamma|$.

It is erroneous to think that these assumptions will restrict Chapman's analysis to entry trajectories with small flight path angles and small lift-to-drag ratios as many authors have believed. On the contrary, these assumptions applied simultaneously, constitute a well balanced set of hypotheses and make Chapman's theory applicable to a large family of entry trajectories. [Ref. 42:p. 179]

As previously mentioned, Chapman introduced a set of dimensionless (independent and dependent) variables. The independent variable is

$$\bar{u} \equiv \frac{V \cos \gamma}{\sqrt{gr}} = \frac{u}{u_c} \quad (41)$$

and the dependent variable is

$$Z \equiv \frac{\rho C_r A}{2m} \sqrt{\frac{r}{\beta}} \bar{u} \quad (42)$$

Chapman's final derivation is given by

$$\left[\bar{u} \frac{d^2 Z}{d\bar{u}^2} \right] \left[- \left[\frac{dZ}{d\bar{u}} - \frac{Z}{\bar{u}} \right] \right] = \left[\frac{(1 - \bar{u}^2)}{\bar{u}Z} \cos^4 \gamma \right] \left[- \sqrt{\beta r} \frac{L}{D} \cos^3 \gamma \right] \quad (43)$$

1. 2. 3. 4.

where $\beta = Mg/RT$ and the numbers associated with the brackets in equation (43) represent the following physical quantities:

1. Vertical acceleration.
2. Vertical component of the drag force.
3. Force of gravity minus the centrifugal force.
4. Lift force.

For the specific case of the shallow reentry of a satellite from a decaying orbit where the flight path angle is very small, the Z function equation (43), can be written in the following form

$$\bar{u} \frac{d}{d\bar{u}} \left(\frac{dZ}{d\bar{u}} - \frac{Z}{\bar{u}} \right) - \frac{(1-\bar{u}^2)}{\bar{u}Z} + \sqrt{\beta r} \frac{L}{D} = 0 \quad (44)$$

with the initial conditions of

$$\bar{u}_i = 1 \quad , \quad \gamma_i = 0 \quad (45)$$

and where the corresponding boundary conditions for decaying orbits are

$$Z(1) = 0 \quad , \quad Z'(1) = 0 \quad (46)$$

Integrating equation (44) by numerical techniques for each designated initial velocity, initial flight path angle and L/D ratio generates a solution. The results of the solution are applicable to any vehicle of arbitrary dimension, size, or mass. Figure 16 shows the solution graph for a non-lifting vehicle (L/D=0) [Ref. 14]. Figure 17 shows the solution graph of various L/D values using the parameter [Ref. 14]

$$\sqrt{\beta r} \left[\frac{L}{D} \right] \quad (47)$$

The ratio u/u_c for the ordinate from Figures 16 and 17 is equal to equation (41).

Additionally, the following engineering quantities of interest during the reentry process can be calculated from the Z function:

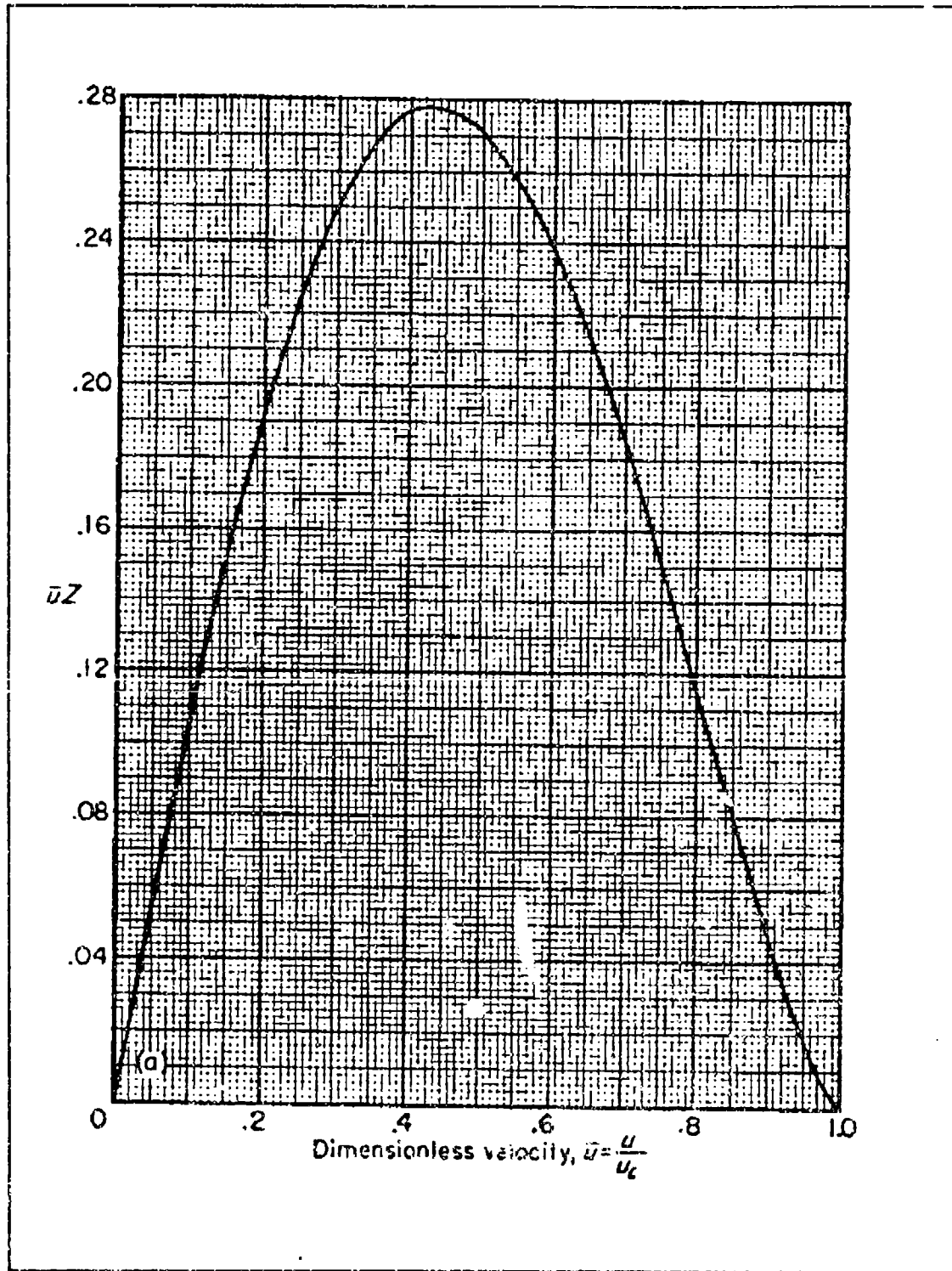


Figure 16: Z Function Solution Graph For $L/D=0$
 [Ref. 14]

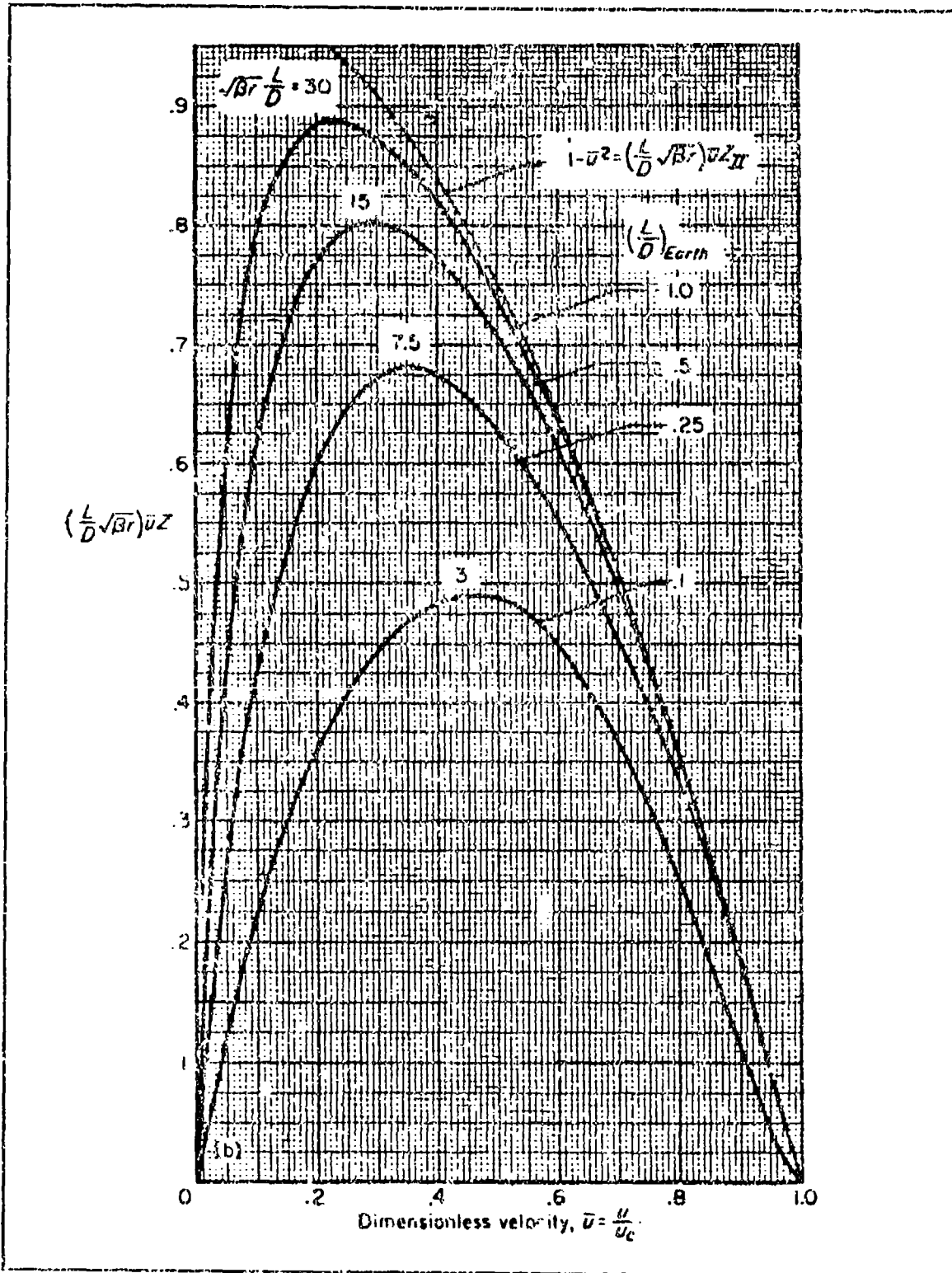


Figure 17: Z Function Solution Graph For Various L/D's
 [Ref. 14]

1. Deceleration
2. Descent angle
3. Range
4. Time
5. Density-velocity relationship
6. Dynamic pressure
7. Reynolds number
8. Heating rate
9. Total heat absorbed

2. Loh's Second Order Unified Solution of Entry Dynamics

Loh derived a general second-order solution of reentry mechanics that covers the entire range of initial flight path angles and L/D ratios [Ref. 40:pp. 25-36]. Figure 18 shows the entire range of the second-order solution as compared with several other analytical approximate solutions available in 1963, including Chapman's approximate analytical theory [Ref. 40:p. 26].

The second-order unified solution can be derived from equations (16) and (17) by using approximations, a binomial series expansion, and integration techniques for a small flight path angle, γ , and is given by the following equation

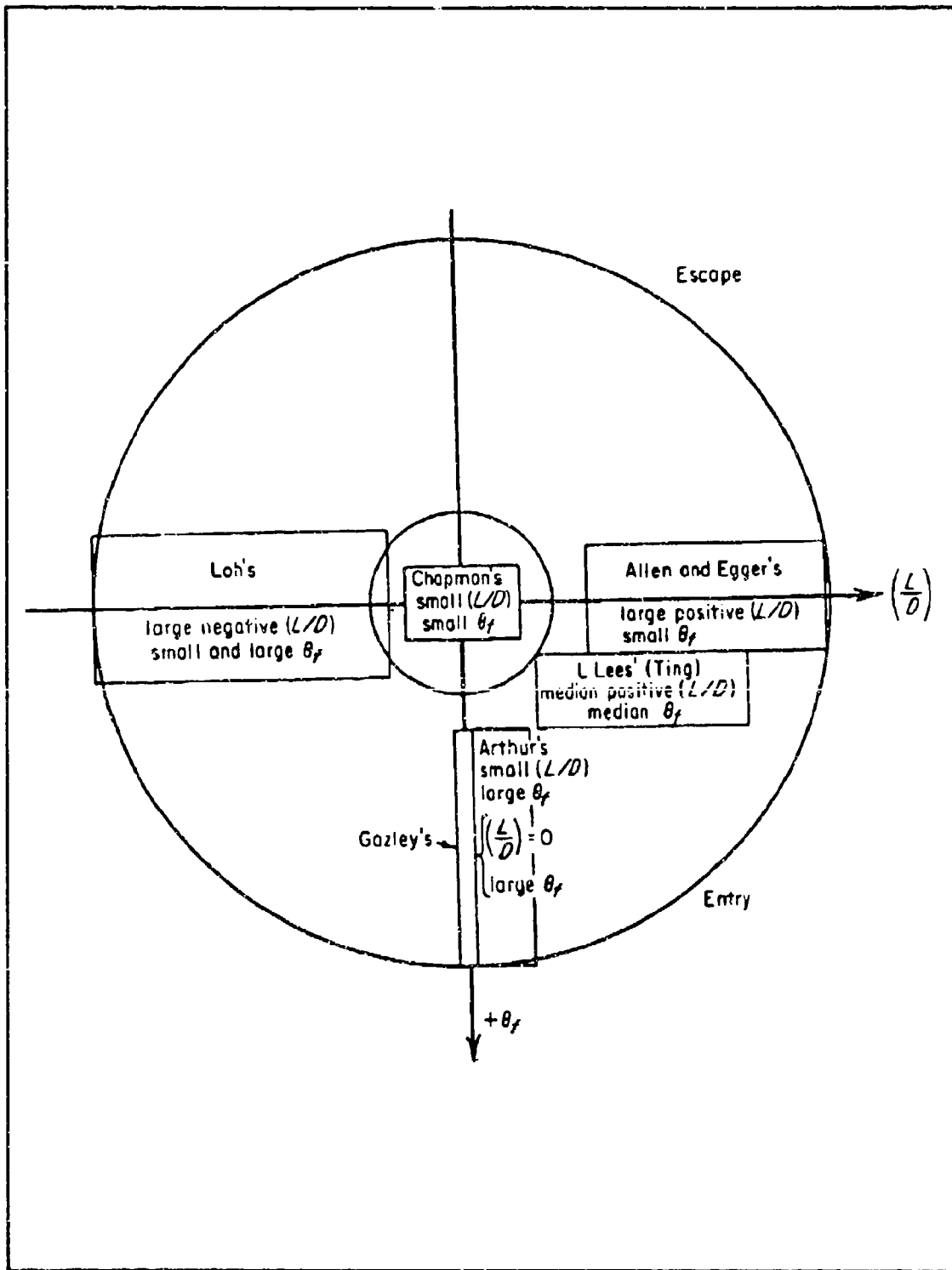


Figure 18: Loh's Second-Order Range Of Applicability
[Ref. 40]

$$\left[\frac{\chi}{\chi_f} \right] \cong \left[\left[\frac{4}{\beta R_0} \right] \left[\frac{1}{\chi_f} \right] F_1(\gamma) \right] + \left[1 - \left[\frac{4}{\beta R_0} \right] \left[\frac{1}{\chi_f} \right] F_1(\gamma_f) \right] \times \exp \left[- \frac{\left[\frac{C_D A}{m \beta} \right]}{\left[\frac{1}{\beta R_0} \right] \frac{\cos \gamma}{\rho} \left[\frac{g R_0}{V^2} - 1 \right] - \frac{1}{2} \left[\frac{L}{D} \right] \left[\frac{C_D A}{m \beta} \right]} \right] (\gamma - \gamma_f) \quad (48)$$

where

$$\chi = \left(\frac{V^2}{g R_0} \right), \quad \chi_f = \left(\frac{V_f^2}{g R_0} \right) \quad (49)$$

R_0 = radius of the Earth

f = condition at beginning of unpowered glide or ballistic entry

$$F_1(\gamma) = \left[\ln \left[\frac{\gamma}{2} \right] + (C_1 \gamma) + \frac{1}{4} (C_1 \gamma)^2 + \frac{1}{18} (C_1 \gamma)^3 \right] e^{-C_1 \gamma} - \left[\frac{(C_1 \gamma)^3}{720 C_1^4} - \frac{(C_1 \gamma)^2}{240 C_1^4} + \left[\frac{1}{120 C_1^4} + \frac{1}{12 C_1^4} \right] (C_1 \gamma) - \left[\frac{1}{120 C_1^4} + \frac{1}{12 C_1^4} \right] \right] \quad (50)$$

$$C_1 = - \left[\frac{1}{2} \left[\frac{L}{D} \right] \left[\frac{C_D A}{m \beta} \right] - \left[\frac{1}{R_0} \right] \frac{\cos \gamma}{\rho} \left[\frac{C_D A}{m} \right] \left[\frac{g R_0}{V^2} - 1 \right] \right]^{-1} \quad (51)$$

For the specific case when $L/D=0$, equation (48) can be simplified and rewritten as

$$\ln \left[\frac{\left[\frac{V_f^2}{gR_0} \right]}{\left[\frac{V^2}{gR_0} \right]} \right] = \left(\frac{C_D A}{m\beta} \right) \rho \left[1 - \frac{\rho_f}{\rho} \right] \left[\frac{\gamma - \gamma_f}{\cos \gamma_f - \cos \gamma} \right] \quad (52)$$

Figure 19 shows a comparison between Chapman's first-order solution and Loh's second-order solution for a small $L/D=0.1$ [Ref. 40:p. 63]. Both solutions offer about the same degree of accuracy.

However, the first order solution is limited by the conditions that $(L/D) \tan \gamma$ must be smaller than 1 and the initial angle of inclination γ_i must be very small; the second order solution does not suffer these particular limitations. When $L/D=0$ and $\gamma_i \equiv 0$, where the first order solution was not available previously, the second order solution offers for the first time a satisfactory solution in this region.[Ref. 40:pp. 50-51]

3. Yaroshevskii's Entry Theory

Yaroshevskii developed a semi-analytical reentry trajectory theory which was originally published in a Soviet journal, *Kosmicheskie Issledovaniya*, in 1964 [Ref. 42:pp. 158-176]. [An English translation of this article was not available to the authors.]

Using some simplifying assumptions, he derived a nonlinear second-order differential equation which can be integrated analytically by using series expansions. To some extent, Yaroshevskii's theory is a special case of a more sophisticated theory developed by Chapman. [Ref. 42:p. 158]

In the development of the theory, physical assumptions 1 through 5 apply to the basic reentry equations (16) and (17), from which the differential equation was derived. Also, for a constant angle of attack, α , the drag coefficient, C_D , and the lift coefficient, C_L , were assumed to be a function of the Mach number.

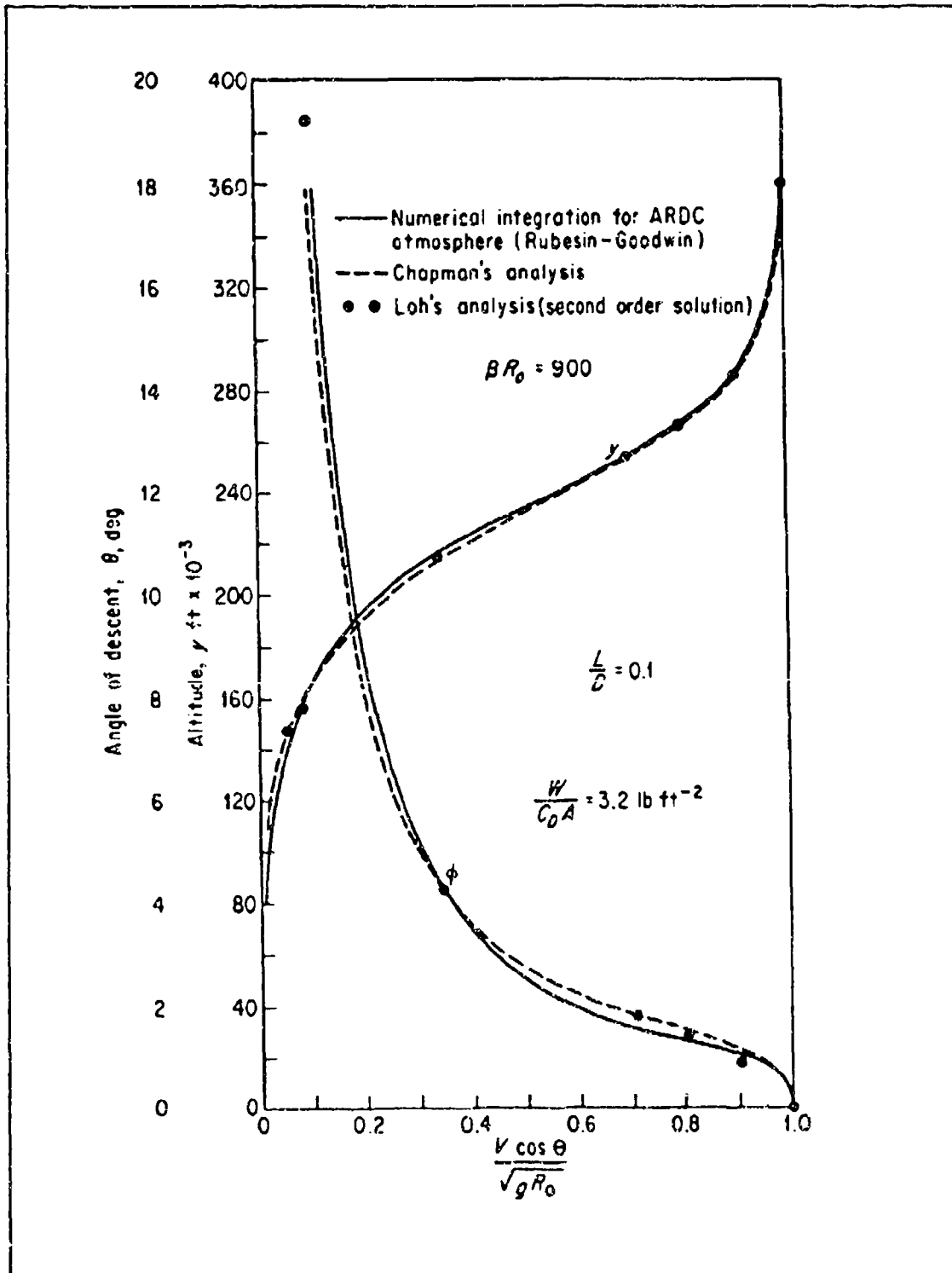


Figure 19: Loh's Second-Order vs Chapman's First-Order
 [Ref. 40]

Yaroshevskii used an independent variable, x , and a dependent variable, y , defined as

$$x \equiv - \int_1^{\nabla} \frac{C_D(1)d\nabla}{C_D(\nabla)\nabla} \quad (53)$$

and

$$y \equiv \frac{C_D(1)A}{2m} \sqrt{\frac{r_0}{\beta}} \rho \quad (54)$$

where

r_0 = radius of the planet

$$\nabla = \frac{V}{\sqrt{gr_0}} \quad (55)$$

By defining the differential relations dx and dy , using equations (53) and (54) along with the equations (16) and (17) and by eliminating the flight path angle, γ , the second-order, nonlinear differential equation is given by

$$\frac{d^2y}{dx^2} = -\sqrt{\beta R_0} \frac{C_L[\nabla(x)]}{C_D(1)} \frac{1}{y} \frac{1}{V^2(x)} \quad (56)$$

Solutions for equation (56) can be obtained by numerical integration. When C_D and C_L are independent of the Mach number, solutions can be obtained by integrating a selected series expansion of equation (54), depending on the type of reentry trajectory.

For the specific case of the shallow reentry from orbit decay, where $C_L/C_D=0$, equation (56) can be derived as

$$\frac{d^2y}{dx^2} = \frac{e^{2x}-1}{y} \quad (57)$$

with the initial conditions of

$$x_i = 0, \quad y(0) = 0, \quad \frac{dy}{dx} = 0 \quad (58)$$

By taking into account a singularity at $y=0$, the series solution to equation (57) is

$$y = \sqrt{\frac{8}{3}} x^{\frac{3}{2}} (a_0 + a_1 x + a_2 x^2 + a_3 x^3 + \dots) \quad (59)$$

where

$$a_0 = 1$$

$$a_1 = 1/6$$

$$a_2 = 1/24$$

$$a_3 = 47/4752$$

The coefficients a_k can be calculated by the recurrence formula

$$a_k = \frac{\frac{2^k}{(k+1)!} - \frac{1}{3} \sum_{m=1}^{k-1} (2m+1)(2m+3) a_m a_{k-m}}{1 + \frac{(2k+1)(2k+3)}{3}} \quad (60)$$

As in the case of Chapman's theory, several engineering quantities of interest during the reentry process can be calculated from equation (56):

1. Time of flight
2. Range
3. Deceleration
4. Heating rate
5. Heat absorbed

4. Universal Equations for Orbit Decay and Reentry

Longuski and Vinh derived a set of universal entry equations of motion for all regimes of atmospheric flight: from the free-molecule flow regime to the near free-molecule flow regime where orbital motion is perturbed by air drag, through the transition regime to the continuum flow regime where the dynamic phase of reentry occurs, and to the point of impact on the planet's surface [Ref. 41].

Rigorous mathematical techniques, such as Poincare's method of small parameters, and Lagrange's expansion are applied to obtain a highly accurate, purely analytical theory for orbit contraction and ballistic entry into planetary atmospheres. [Ref. 41:p.v]

Figures 20 and 21 [Ref. 41:pp.16-17] describe the inertial coordinate system, nomenclature and the aerodynamic forces of the equations of motion for a vehicle with a C_L/C_D ratio, defined by the following equations [Ref. 41:p.10]

$$\frac{dr}{dt} = V \sin \gamma \quad (61)$$

$$\frac{d\theta}{dt} = \frac{V \cos \gamma \cos \psi}{r \cos \phi} \quad (62)$$

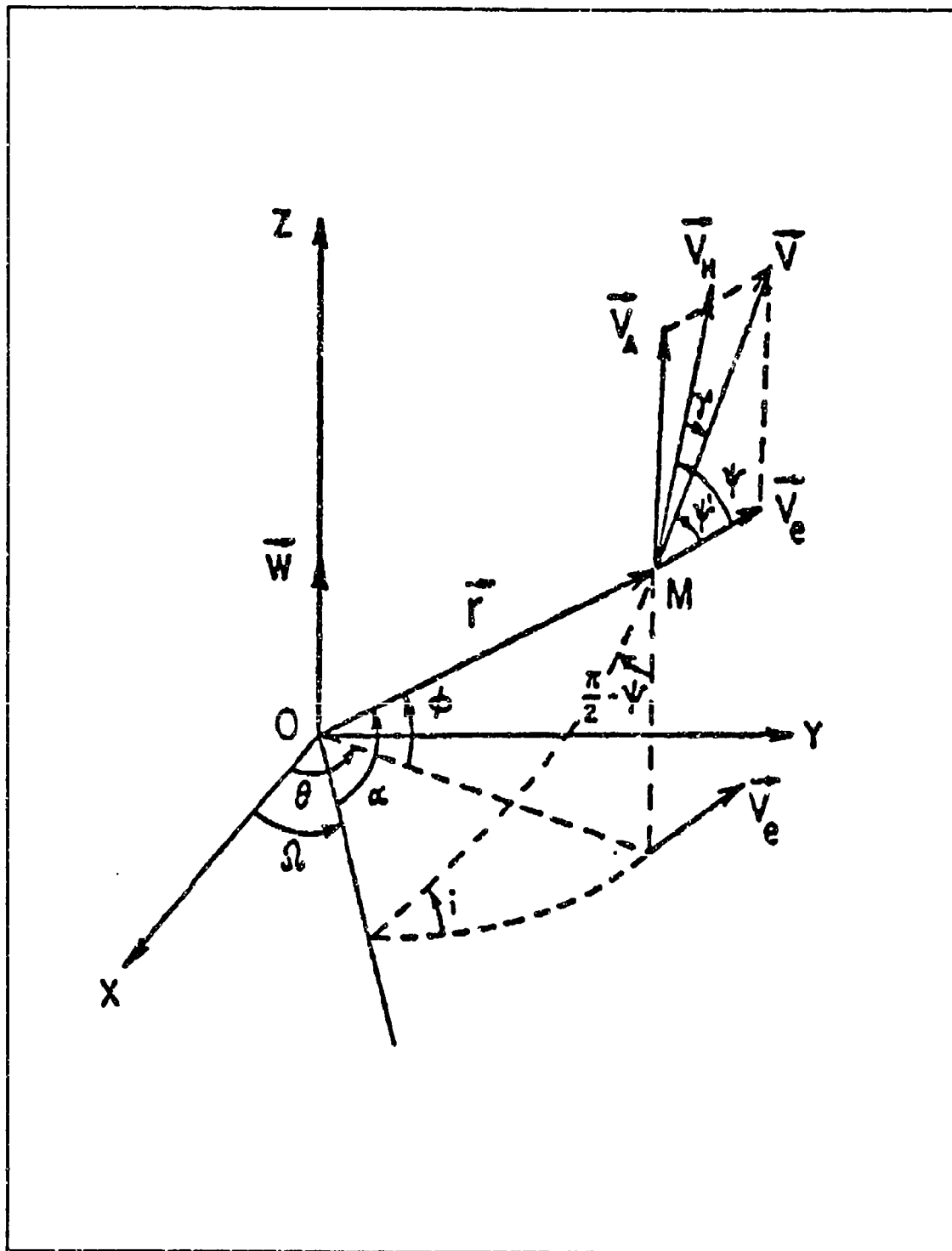


Figure 20: Coordinate System And Nomenclature
 [Ref. 41]

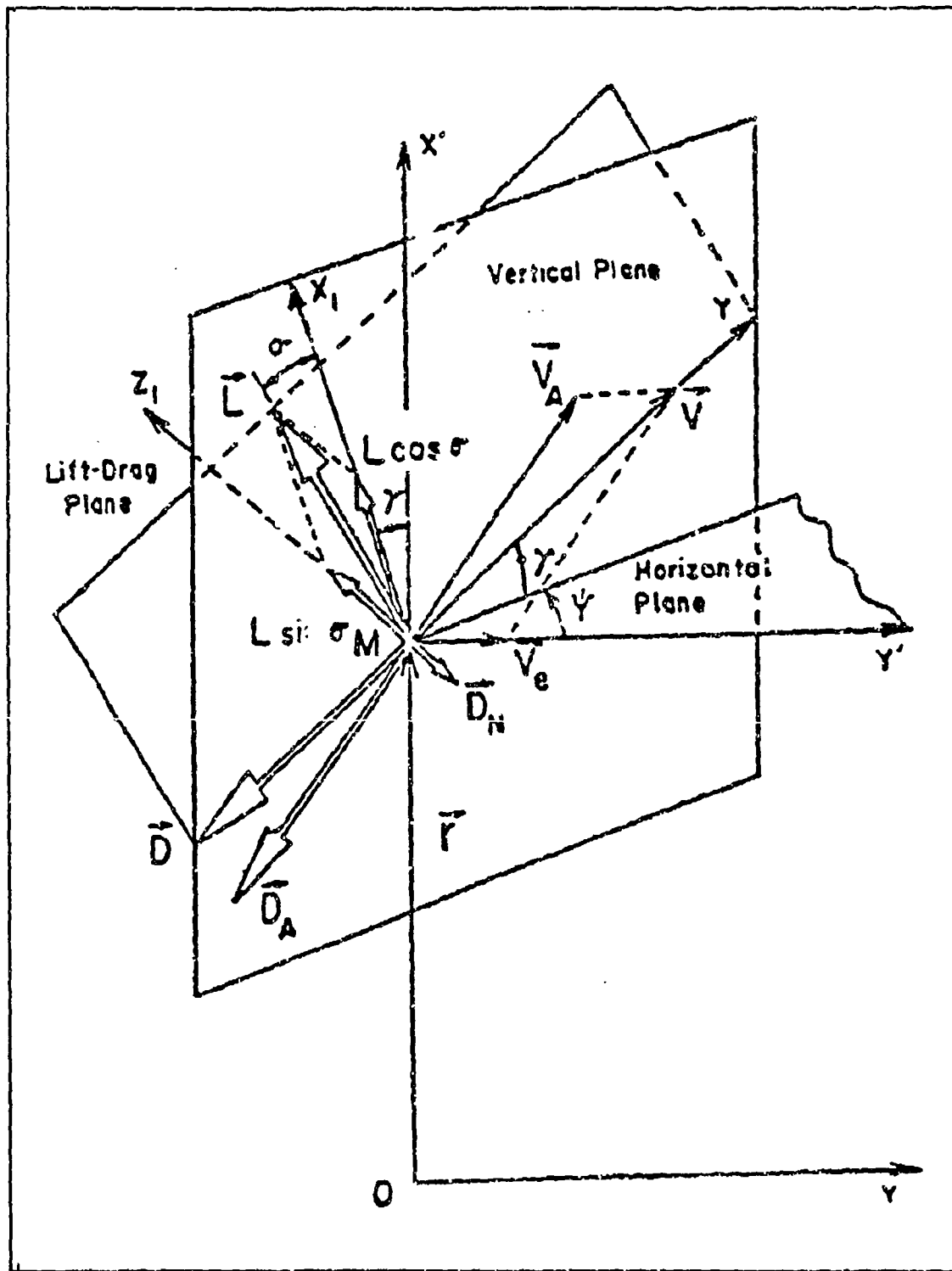


Figure 21: Aerodynamic Force Diagram
 [Ref. 41]

$$\frac{d\phi}{dt} = \frac{V \cos \gamma \sin \psi}{r} \quad (63)$$

$$\frac{dV}{dt} = - \frac{\rho A C_D V^2}{2m} - g \sin \gamma \quad (64)$$

$$V \frac{d\gamma}{dt} = \frac{\rho A C_L V^2 \cos \sigma}{2m} - \left(g - \frac{V^2}{r}\right) \cos \gamma \quad (65)$$

$$V \frac{d\psi}{dt} = \frac{\rho A C_L V^2 \cos \sigma}{2m \cos \gamma} - \frac{V^2}{r} \cos \gamma \cos \psi \tan \phi \quad (66)$$

The exact universal equations of motion for entry trajectories for a vehicle inside a rotating atmosphere can be derived from a transformation of equations (61) through (66) using the modified Chapman variables

$$u = \frac{V^2 \cos^2 \gamma}{gr} \quad (67)$$

$$Z = \frac{\rho A C_D}{2m} \sqrt{\frac{r}{\beta}} \quad (68)$$

and nondimensional independent variable

$$s = \int_0^t \left[\frac{V}{r} \right] \cos \gamma dt \quad (69)$$

The exact universal equations for entry trajectories are [Ref. 41:pp. 11-12]

$$\frac{dZ}{ds} = -\beta r \left[-\frac{1}{\beta \rho} \frac{d\rho}{dr} - \frac{1}{2\beta r} + \frac{1}{2\beta^2} \frac{d\beta}{dr} \right] Z \tan \gamma \quad (70)$$

$$\frac{du}{ds} = -\frac{2\sqrt{\beta r} Z u}{\cos \gamma} \left[1 + \frac{C_L}{C_D} \cos \sigma \tan \gamma + \frac{\sin \gamma}{2\sqrt{\beta r} Z} \right] \quad (71)$$

$$\frac{d\gamma}{ds} = \frac{\sqrt{\beta r} Z}{\cos \gamma} \left[\frac{C_L}{C_D} \cos \sigma + \frac{\cos \gamma}{\sqrt{\beta r} Z} \left[1 - \frac{\cos^2 \gamma}{u} \right] \right] \quad (72)$$

$$\frac{d\alpha}{ds} = 1 - \frac{\sqrt{\beta r} Z \sin \alpha}{\tan i \cos^2 \gamma} \left[\frac{C_L}{C_D} \right] \sin \sigma \quad (73)$$

$$\frac{d\Omega}{ds} = \frac{\sqrt{\beta r} Z \sin \alpha}{\sin i \cos^2 \gamma} \left[\frac{C_L}{C_D} \right] \sin \sigma \quad (74)$$

$$\frac{di}{ds} = \frac{\sqrt{\beta r} Z \cos \alpha}{\cos^2 \gamma} \left[\frac{C_L}{C_D} \right] \sin \sigma \quad (75)$$

where

- Ω = longitude of the ascending node of the osculating plane
- α = angle between the ascending node and the position vector
- i = inclination of the orbit
- σ = bank angle

According to the authors, the universal equations have three advantages: [Ref. 41:p.128]

1. They are exact.
2. They are free of any restrictive assumptions.
3. They contain the modified Chapman Z variable, which permits a single trajectory solution for a specified initial velocity and flight path angle that applies to any vehicle of arbitrary area, mass, or C_D .

As previously mentioned, equations (70) through (75) can be used during all phases of aerodynamic flight and are most useful for analyzing the last few revolutions and the reentry phase. The accuracy of the equations depends on the readjustment of the value of the inverse atmospheric scale height, β , for each layer of the atmosphere. [Ref. 41:p.15]

For the specific case of reentry from a circular orbit, where $C_L=0$, Longuski and Vinh derived a separate analytical theory from the exact universal equations for entry trajectories, due to the fact that:

...it does not seem possible to have a single analytic solution which is uniformly valid for all values of initial flight path angles because of the nature of the problem. In the case of atmospheric entry from circular orbit, the magnitude of the flight path angle, initially zero, rapidly increases, approaching 90° as the velocity becomes small. On the other hand, for steep angle entry, the flight path angle changes very little--of the order of tenths of a degree--as the nondimensional velocity decreases from unity to one tenth of the original value (between Mach 2 and 3). [Ref. 41:p. 85]

Under the condition of reentry from a circular orbit, equation (73) is equal to one and equations (74) and (75) are equal to zero. By using this fact and the variable

$$v = \frac{V^2}{gr} = \frac{u}{\cos^2 \gamma} \quad (76)$$

equations (70) through (73) can be written as

$$\frac{dZ}{d\alpha} = -\beta r Z \tan \gamma \quad (77)$$

$$\frac{dv}{d\alpha} = -\frac{2\sqrt{\beta r} Z v}{\cos \gamma} \left[1 - \frac{\sin \gamma}{2\sqrt{\beta r} Z} \left(1 - \frac{2}{v} \right) \right] \quad (78)$$

$$\frac{d\gamma}{d\alpha} = 1 - \frac{1}{v} \quad (79)$$

By dividing equations (77) and (79) by equation (78) to form a new set of equations, and defining the following change of variables for substitution into the new set

$$Y = 2Z \quad (80)$$

$$\Phi = -\sqrt{\beta r} \sin \gamma \quad (81)$$

$$X = -\ln v \quad (82)$$

$$\epsilon = \frac{1}{\beta r} \quad (83)$$

and then by expanding this new set of equations in one term, in ϵ , and using Poincaré's method of small parameters for integration of a system with the assumed solution form

$$\phi = \phi_0 + \epsilon \Phi_1 \quad (84)$$

$$Y = Y_0 + \epsilon Y_1 \quad (85)$$

two systems of two first-order differential equations are formed [Ref. 41:p. 89]

$$\frac{dY_0}{dX} = \Phi_0 \quad (86)$$

$$\frac{d\Phi_0}{dX} = \frac{e^X - 1}{Y_0} \quad (87)$$

$$\frac{dY_1}{dX} = \Phi_1 + \frac{\Phi_0^2}{Y_0} (2e^X - 1) \quad (88)$$

$$\frac{d\Phi_1}{dX} = \frac{e^X - 1}{Y_0} \left[\frac{\Phi_0}{Y_0} (2e^X - 1) - \Phi_0^2 - \frac{Y_1}{Y_0} \right] \quad (89)$$

Equations (86) and (87) can be written in the following second-order differential equation form

$$\frac{d^2 Y_0}{dX^2} = \frac{e^X - 1}{Y_0} \quad (90)$$

and with the initial conditions for the case of the shallow satellite reentry

$$Y_0(0) = 0, \quad \Phi_0(0) = 0 \quad (91)$$

a series solution can be obtained in the following form

$$Y_0 = \frac{2}{\sqrt{3}} X^{\frac{3}{2}} \left[1 + \frac{1}{3} \left(\frac{X}{4} \right) + \frac{1}{6} \left(\frac{X}{4} \right)^2 + \frac{47}{594} \left(\frac{X}{4} \right)^3 + \frac{20021}{605880} \left(\frac{X}{4} \right)^4 \right] \quad (92)$$

$$\Phi_0 = \sqrt{3} X^{\frac{1}{2}} \left[1 + \frac{5}{9} \left(\frac{X}{4} \right) + \frac{7}{18} \left(\frac{X}{4} \right)^2 + \frac{47}{198} \left(\frac{X}{4} \right)^3 + \frac{20021}{165240} \left(\frac{X}{4} \right)^4 \right] \quad (93)$$

Yaroshevskii's approach was used to find the first term of the series in equations (92) and (93). The same approach can be applied to equations (88) and (89) to find a solution.

Figures 22, 23, and 24 represent various solutions graphs for equations (92) and (93). The dashed line indicates the exact numerical solution while the solid line represents the analytical solution. Figure 22 shows the variations of aerodynamic deceleration, G's (g's = number \times gravitational acceleration at a radial distance r), as a function of the dimensionless velocity, v , at several initial flight path angles, γ_i , for equation (92) [Ref. 41:p.120]. Figure 23 shows the variations of $\ln (Z / Z_0) \approx (r_0 - r)/H$ = drop in altitude, in units of scale height, as a function of (v) at several (γ_i), for equation (92) [Ref. 41:p. 122]. Figure 24 shows the variation of the negative flight path angle, $-\gamma$, as a function of (v) at several (γ_i), for equation (93) [Ref. 41:p. 121].

5. Attitude Dynamics of Uncontrolled Motion During Reentry

In the previous section several analytical theories were presented describing the reentry equations of motion and their solutions. Strong physical assumptions were made in the derivations of these theories in order to describe the trajectory of the body's

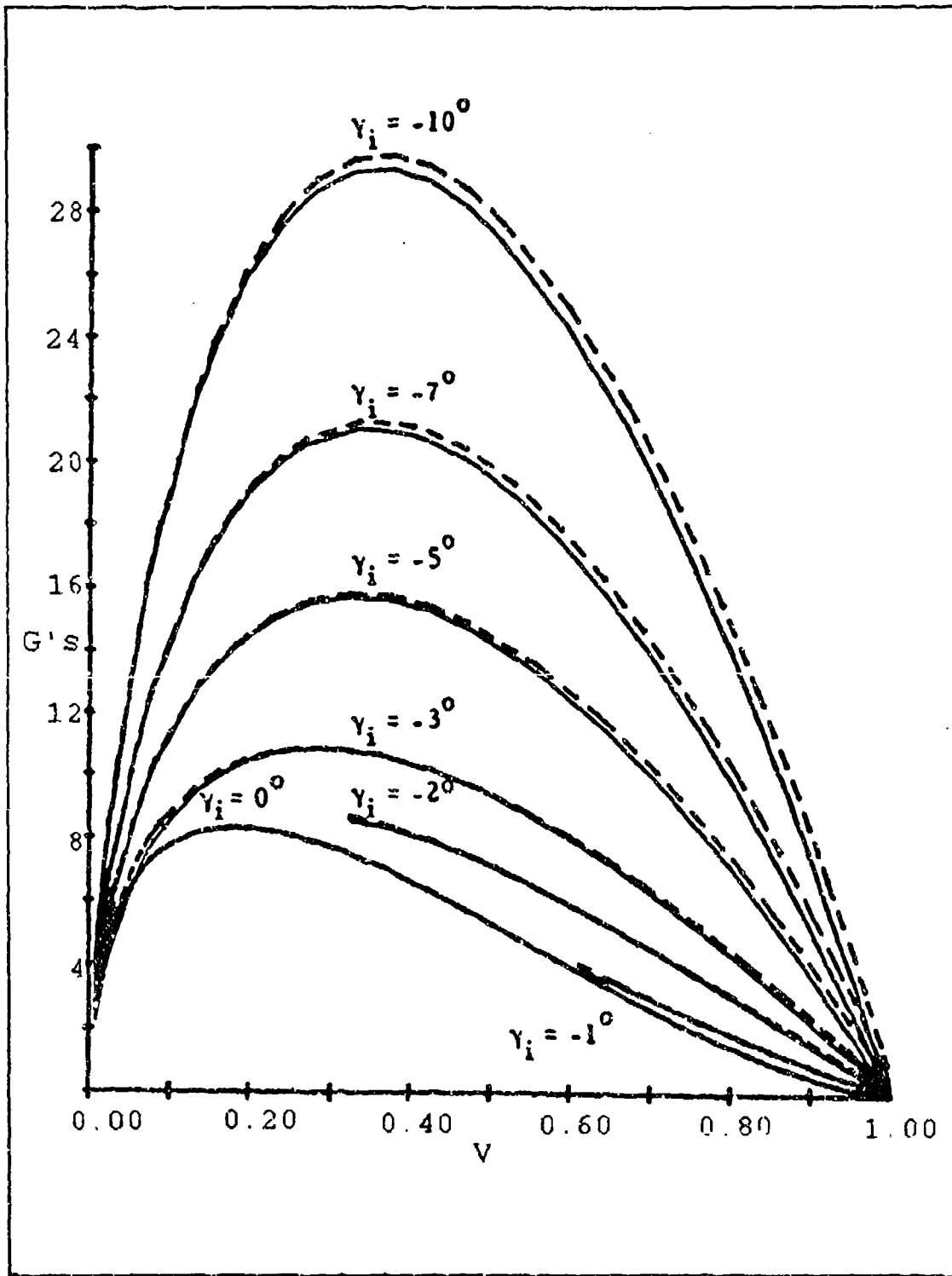


Figure 22: Variations Of γ vs The Nondimensional Velocity (v)
 [Ref. 41]

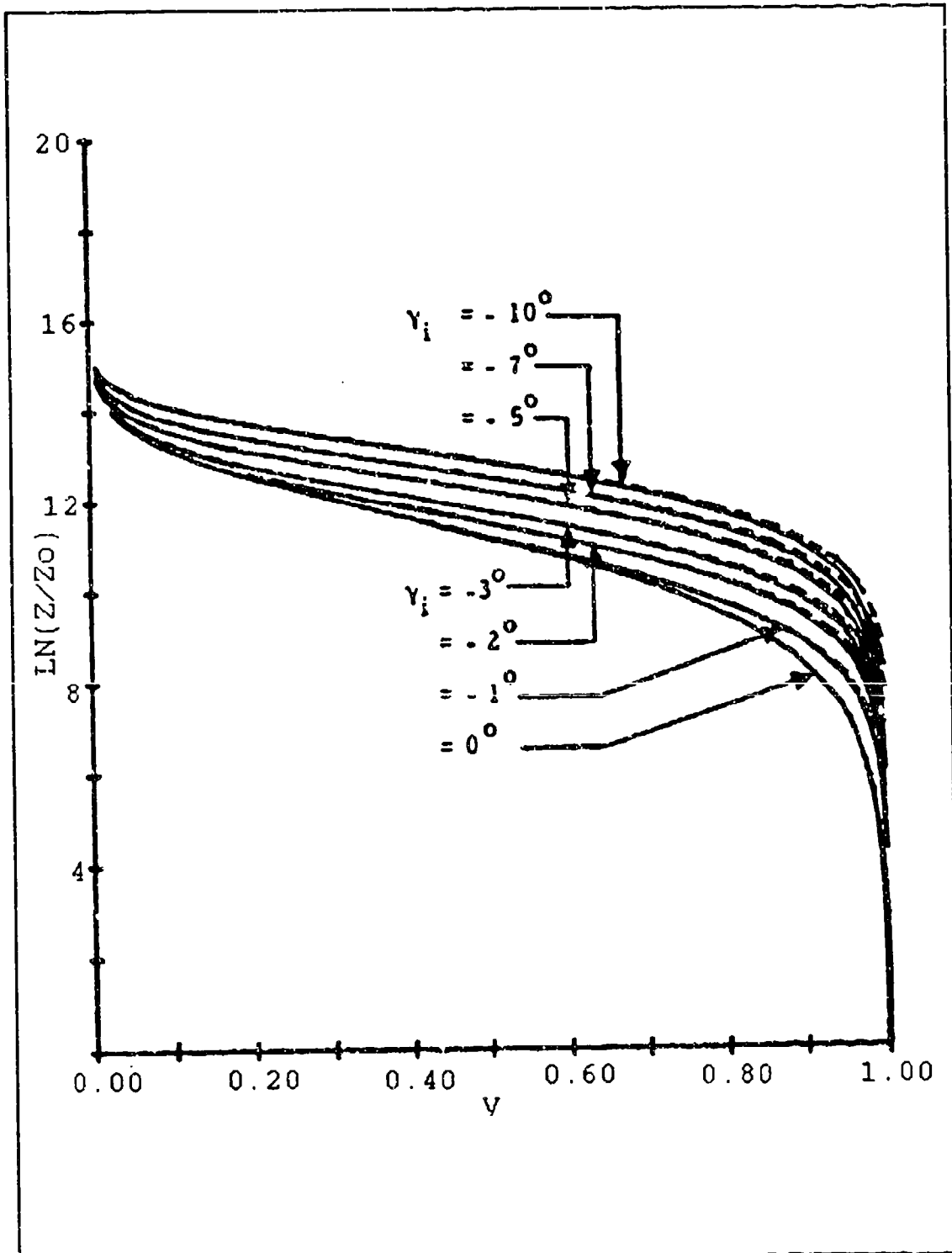


Figure 23: Variations Of $\ln(Z/Z_0)$ vs The Nondimensional Velocity (v)
 [Ref. 41]

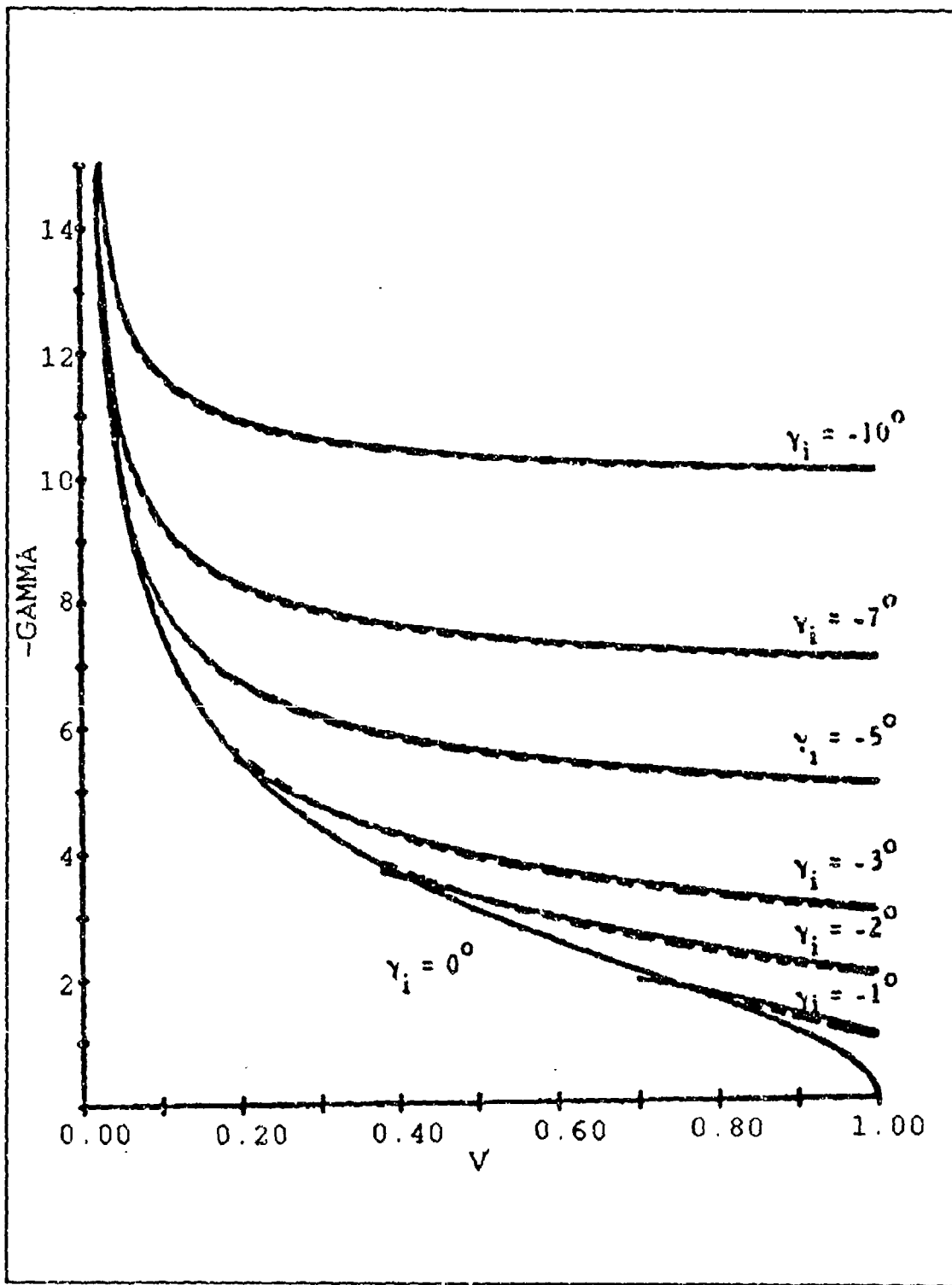


Figure 24: Variations Of G vs The Nondimensional Velocity (v)
 [Ref. 41]

center of mass or point mass. Specifically, Chapman's and Longuski and Vinh's theories used the Z variable which permits a single trajectory solution for a specified initial velocity and flight path angle that applies to any vehicle of arbitrary area, mass, or C_D . The effect of the uncontrolled motion of a body about its center of mass on the reentry trajectory was not investigated in these theories. This section will examine three analytical investigations presented by two Russian authors in this specific area.

Duzmak, in 1970, presented the first systematized explanation on the problem of the attitude dynamics of uncontrolled reentry body motion. This problem was the least developed in comparison to center of mass or point mass trajectories and aerodynamic heating [Ref. 56:p.2]

Unifying papers on the dynamics of the motion relative to the center of mass have not appeared up to the present time. [Ref. 56:p. 5]

The primary focus was the investigation and derivation of the relationship between a reentry body's parameters outside the atmosphere with the body's parameters in the dense layer of the atmosphere. Changes in the state of a reentry body's motion relative to its center of mass during the motion along its trajectory were also investigated. An asymptotic approach was used on the equations of motion to solve the problem, specifically for the cases where the characteristic time of the entry body motion relative to its center of mass is much less than the characteristic time of motion of the center of mass. Additionally, a refined asymptotic method that has a significantly wider range of applicability was developed for those cases in which the above condition was not fulfilled. This method is based on the coupling of the numerical and asymptotic

solutions of the equations of motion. Two-dimensional motion without restrictions on the shape of the body and three-dimensional motion of a body that possessed aerodynamic and dynamic axial symmetry were assumed in this investigation. [Ref. 56:pp. 1-3]

During the orbital or exoatmospheric phase, the external moments that produce the reentry body's perturbed motion about its center of mass are determined by the laws of motion of a rigid body as described by Euler. The magnitude and direction of the initial angular moment vector, H , determines the state or nature of this motion. For instance, if initial angular moment vector during the orbital phase produces two-dimensional motion, then the body rotates at a constant angular velocity, ω , about its Z or transverse axis. [Ref. 55:pp. 5-6] Figure 25 is an attitude dynamics coordinate system that shows the direction of the Z-axis relative to the body's orbit [Ref. 57:p. 113].

Regardless of the nature of the motion, the entry body's angle of attack, α , upon approaching the atmosphere can have absolutely any value at all ... Thus any complete solution of the problem of atmospheric entry can be obtained upon the necessary condition of the absence of any restrictions on the size of the angle of attack. One can say that the presence of large angle of attack is one of the main distinctive features of the problem of atmospheric entry. [Ref. 56:p. 6]

As a body with perturbed motion relative to its center of mass enters the reentry or atmospheric phase, it begins to experience a stabilizing effect that is proportional to the increase in atmospheric density. This stabilizing effect is a property of dynamical systems with variable parameters where if the stiffness of the system increases during the perturbed motion, then the vibrations dampen out. This dampening effect was described, for the case of angularly misaligned missiles during reentry, by

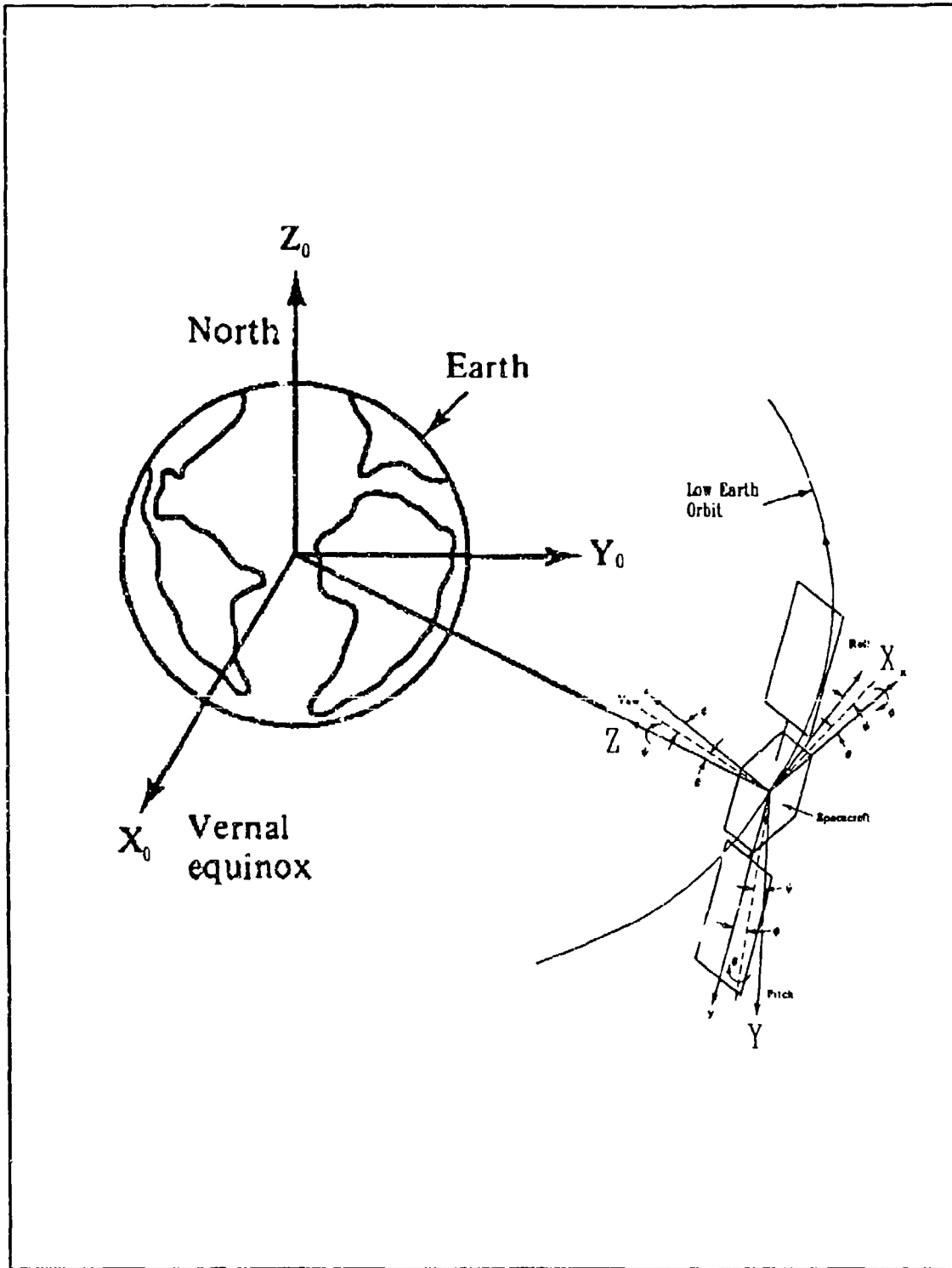


Figure 25: Attitude Dynamics Coordinate System
[Ref. 57]

Allen in 1957. [Ref. 58] The system stiffness effect during reentry is defined in the quantity

$$\frac{M_z^\alpha}{I_z} \quad (94)$$

where

M_z^α = the derivative of the dimensional aerodynamic moment with respect to the angle of attack

I_z = reentry body's moment of inertia relative to the Z-axis

Based on these facts, Duzmak states:

The value of M_z^α increases by several orders of magnitude upon the descent because of the increase in density and the indicated effect of the variation in the system's parameters is the main factor determining the damping of the oscillation ... investigating the disturbed motion upon atmospheric entry permit one conclude that a descending entry body represents a significantly nonlinear mechanical system. [Ref. 56:p. 7]

a. *Equations of Perturbed Motion*

The basic development of the equations of perturbed motion of a body about its center of mass during reentry is presented due to the uniqueness of Duzmak's work [Ref. 56:pp. 12-28]. Equations (1) through (3) describe the system of equations of motion for this problem.

The characteristic time intervals for the reentry body's motion relative to its center of mass and the motion of its center of mass are, respectively, defined as

$$t_z = \frac{1}{\Omega} \quad (95)$$

$$t_v = \frac{\Delta r}{V} \quad (96)$$

where

Ω = characteristic rotational velocity with respect to the center of mass

Δr = characteristic variation in the radius vector of the center of mass

V = characteristic velocity of its center of mass

In the development of the equations of perturbed motion, the following factors and assumptions were taken into account:

1. The interaction between the reentry body's motion with respect to its center of mass and the motion of the center of mass is neglected.
2. The hypothesis is satisfied in the upper atmosphere portion of the descent trajectory until the angles of attack becomes less than one radian because of the atmosphere's stabilizing effect.
3. The hypothesis is satisfied in the upper atmosphere portion of the descent trajectory since the body's kinetic energy of the center of mass is many times larger than the body's kinetic energy due to its motion relative to the center of mass. Due to this fact, the aerodynamic moments begin to affect the motion about the center of mass by stabilizing the body at significantly higher altitudes than the aerodynamic forces acting on the center of mass.
4. The center of mass trajectory parameters are known as a function of time.
5. The flight trajectory is two-dimensional.
6. The average rotation of the velocity vector of the reentry body's center of mass which is the curvature of the average trajectory is neglected. This effect is caused by the gravitational force and the body's rotational velocity about its center of mass.
7. The hypothesis is clearly satisfied for the sections BC and DF as shown in Figure 26 [Ref. 56:p.16], because the trajectory is nearly linear due to flight velocities of several kilometers per second. In the sections AB and FG, where

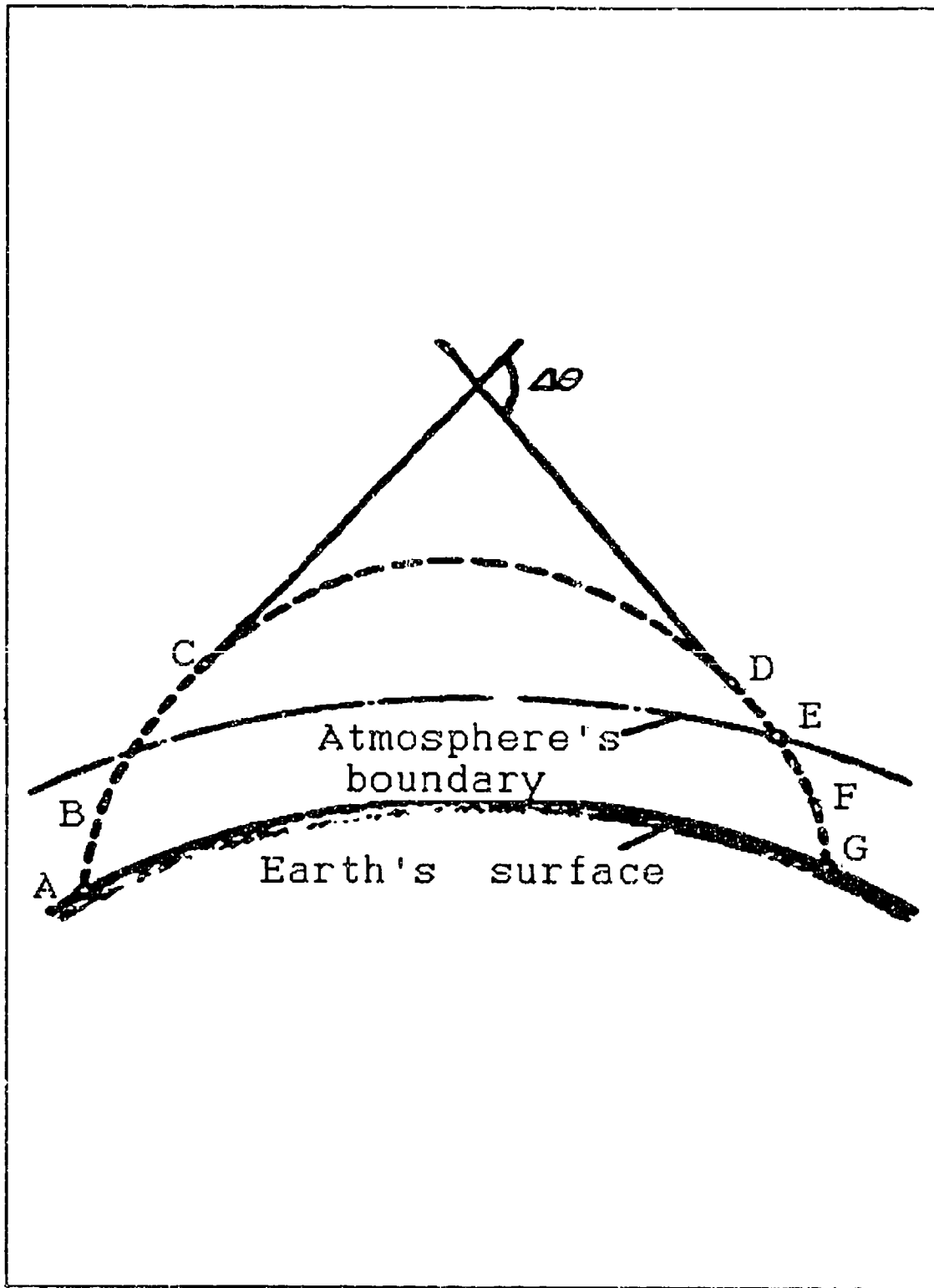


Figure 26: Trajectory Of The Reentry Body
 [Ref. 56]

the trajectory inclination angle, θ , varies significantly, the hypothesis is usually satisfied. The hypothesis is not satisfied in the exoatmospheric section CD.

8. The variation in the velocity vector orientation caused by the effect of the aerodynamic lift force is taken into account.

The reentry body coordinate system, shown in Figure 27 [Ref. 56:p. 23], has both dynamic and aerodynamic symmetry and is used for the derivation of the three-dimensional perturbed equations of motion:

1. The OXYZ right-handed coordinate system is fixed in both inertial space and relative to the reentry body.
2. The body's center of mass is denoted by, O.
3. The OXc axis is the velocity vector of the center of mass.
4. The angle, α , between the OX and OXc axis is not the three-dimensional angle of attack or nutation angle.
5. The plane containing the OXc, OX and OY axis is the angle of attack plane.
6. The motion of the body in the angle of attack plane is defined by dx/dt and is directed along the OZ axis.
7. The rotation of the angle of attack plane with respect to the velocity vector, OXc, is determined with the help of the precessional velocity, λ , which is directed along the OXc axis.
8. The body's rotation with respect to the angle of attack plane is determined using the intrinsic rotational velocity, μ , directed along the OX axis.
9. The angle, γ , between the trajectory plane and the angle of attack plane is defined by $d\gamma/dt = \lambda$.
10. The angles α and γ have the following ranges: $0 < \alpha < 180^\circ$; $0 < \gamma < \infty$.

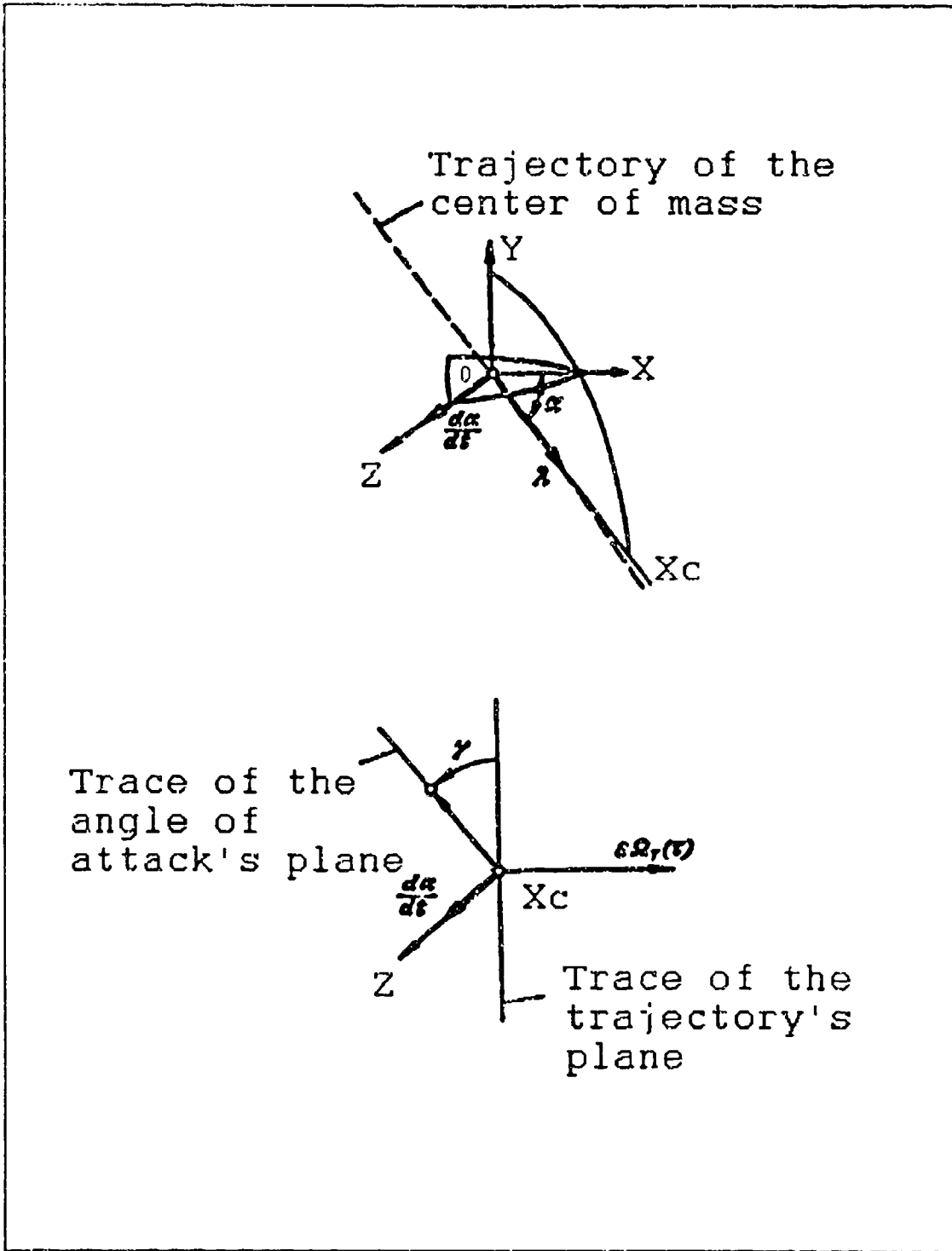


Figure 27: Reentry Body Coordinate System [Ref. 56]

This coordinate system can also be used to describe two-dimensional motion about the center of mass.

The angular velocity vector, ω , of the reentry body is the resultant of three rotations: $d\alpha/dt$; λ ; and μ . As previously mentioned, the aerodynamic lift force affects the body's velocity vector orientation. Lift acts in the angle of attack plane, creating a motion of the body's velocity vector that is in the same plane with the change of the angular velocity along the Z axis and is defined as

$$\Delta\omega_z = \epsilon \frac{L}{mV} \quad (97)$$

where

L = force of lift from equation (12)

m = mass of the body

ϵ = t_α/t_v (small parameter)

The reentry body's angular velocity vector X, Y, Z components are defined as

$$\omega_x = \mu + \lambda \cos \alpha \quad (98)$$

$$\omega_y = -\lambda \sin \alpha \quad (99)$$

$$\omega_z = \frac{d\alpha}{dt} + \epsilon \frac{L}{mV} \quad (100)$$

The reentry body's angular momentum vector, **H**, XYZ components are defined as

$$H_x = I_x \omega_x \quad (101)$$

$$H_y = I_y \omega_y \quad (102)$$

$$H_z = I_z \omega_z \quad (103)$$

where

$I_{x,y,z}$ = reentry body's moments of inertia along the X, Y, Z directions

The main moment force, M , acting on the reentry body consists of a restoring moment, $M_z(\tau, \alpha)$, and a small damping moment that can be projected in the X, Y, Z directions, is given by

$$M_z(\tau, \alpha) = m_z q A L \quad (104)$$

$$M_x^\omega(\tau, \alpha) = m_x^{\bar{\omega}} \frac{q A L^2}{V} \quad (105)$$

$$M_y^\omega(\tau, \alpha) = m_y^{\bar{\omega}} \frac{q A L^2}{V} \quad (106)$$

$$M_z^\omega(\tau, \alpha) = m_z^{\bar{\omega}} \frac{q A L^2}{V} \quad (107)$$

where

$$m_z, m_x^{\bar{\omega}}, m_y^{\bar{\omega}}, m_z^{\bar{\omega}} = \text{dimensionless aerodynamic coefficients} \quad (108)$$

$$q = \rho V^2 / 2$$

$$\tau = \epsilon t$$

By projecting $dH/dt = M$ from equation (3) on the OXYZ coordinate system and taking equations (101) through (107) into account, the reentry body's equations of perturbed motion can be written in the form

$$I_x \frac{d\omega_x}{dt} + I_z \omega_z \varpi_y - I_z \omega_y \varpi_z = \epsilon M_x^u x(\tau, \alpha) \omega_x \quad (109)$$

$$I_z \frac{d\omega_y}{dt} + I_x \omega_x \varpi_z - I_z \omega_x \varpi_x = \epsilon M_y^u y(\tau, \alpha) \omega_y \quad (110)$$

$$I_z \frac{d\omega_z}{dt} + I_z \omega_y \varpi_x - I_x \omega_x \varpi_y = M_z(\tau, \alpha) + \epsilon M_z^u z(\tau, \alpha) \omega_z \quad (111)$$

where

$$\varpi_x = \lambda \cos \alpha$$

$$\varpi_y = \omega_y$$

$$\varpi_z = \omega_z$$

Equations (109) through (111) can be rewritten by substituting in equations (99) and (100) for ω_y , ϖ_y , and ω_z and by substituting ϖ_x from above, into the following form

$$\frac{dr}{dt} + \epsilon f_x(\tau, \alpha) r = 0 \quad (112)$$

$$\frac{d\lambda}{dt} + \frac{(2\lambda \cos \alpha - r)}{\sin \alpha} \frac{d\alpha}{dt} + \epsilon \left[f_y(\tau, \alpha) - \frac{L}{mV \sin \alpha} r \right] = 0 \quad (113)$$

$$\frac{d^2\alpha}{dt^2} - \lambda^2 \sin \alpha \cos \alpha + r \lambda \sin \alpha + M(\tau, \alpha) + \epsilon f_z(\tau, \alpha) \frac{d\alpha}{dt} = 0 \quad (114)$$

where

$$r = \frac{I_x \omega_x}{I_z} \quad (115)$$

$$M(\tau, \alpha) = -\frac{M_z(\tau, \alpha)}{I_z} \quad (116)$$

$$f_x(\tau, \alpha) = -\frac{M_x^{\omega} x(\tau, \alpha)}{I_x} \quad (117)$$

$$f_y(\tau, \alpha) = -\frac{M_y^{\omega} y(\tau, \alpha)}{I_z} + \frac{L \cos \alpha}{mV \sin \alpha} \quad (118)$$

$$f_z(\tau, \alpha) = -\frac{M_z^{\omega} z(\tau, \alpha)}{I_z} + \frac{L^2}{mV} \quad (119)$$

$$L^2 = \frac{\partial L}{\partial \alpha} \quad (120)$$

Finally, the system of equations that describes the two-dimensional motion of the reentry body's center of mass is given by

$$\frac{d\theta}{dt} = \epsilon \left[\frac{C_L \cos \gamma q A}{mV} - \frac{g_T}{V} \cos \theta \left(1 - \frac{V^2}{Rg_T} \right) \right] \quad (121)$$

$$\frac{dV}{dt} = \epsilon \left[-\frac{C_D q A}{m} - g_T \sin \theta \right] \quad (122)$$

$$\frac{dH}{dt} = \epsilon V \sin \theta \quad (123)$$

$$\frac{dL}{dt} = \epsilon \frac{R_0}{R} V \cos \theta \quad (124)$$

where

g_T = gravitational acceleration of the Earth

θ = angle between the tangent to the trajectory and the local horizontal

H = altitude of the flight

R = $R_0 + H$

L = range of flight measured with respect to the Earth's surface

The investigation of equations (112) through (114) in the case of known solutions for equations (121) through (124) is the principal content of Duzmak's work.

Specifically, the following major areas were investigated:

1. The distinctive features of the two-dimensional motion that explains the interaction of the nonlinear effect with the influence of variability of parameters.
2. The distinctive features of the motion that results from the transition through the transonic velocity range.
3. The relationship of the angular momentum components with the parameters of motion in an increasingly denser atmosphere. This analysis clarifies the effect of the shape of the instantaneous characteristics, stability margin and damping.
4. The effect of the reentry body's motion parameters above the atmosphere on its motion in the denser layers of the atmosphere.
5. The case of sinusoidal dependence of the longitudinal moment on the angle of attack for three-dimensional motion.

6. The body's motion relative to its center of mass for a small angle of attack reentry (shallow angle reentry from a decaying orbit).

b. Effect of Motion Relative to the Center of Mass on the Motion of the Center of Mass

The coupled effect of the perturbed motion about the center of mass with the trajectory of the center of mass occurs because of the dependence of the aerodynamic coefficients on the angle of attack. Duzmak neglects this interaction in the development of the asymptotic solutions. This assumption is based on the fact that the atmosphere will start to influence the motion relative to the center of mass at higher altitudes than the atmosphere will start to effect the motion of the center of mass. Generally, for perturbed motion about the center of mass in a free-molecular regime, the effect of the lift force is small, since it continually acts in different directions. In the denser layer of the atmosphere, lift can also provide some additional damping of the angle of attack oscillation. [Ref. 56:p. 29]

The main effect on the trajectory is exerted by a_{drag} , equation (6). For perturbed motion at high altitudes where atmospheric density is low and $C_D(\alpha)$ varies significantly, a_{drag} has little effect on the trajectory. In many cases at lower altitudes, perturbed motion has a weak effect on the trajectory due to the fact that a reentry body is:

...able up to this instance to stabilize itself under the action of aerodynamic moments so that the variation in C_D in the case of perturbed motion becomes insignificant. [Ref. 56:p. 29]

For the case of hovering or similar motion where the oscillations do not dampen, the oscillations of the angle of attack can occur with significant amplitude. Under these conditions, it is essential to take into account the angle of attack oscillation effect on the trajectory of the center of mass. [Ref. 56:p. 317]

The determination of the range component of the scattering landing points is important. This scattering is caused by the oscillations, the angle of attack and the variation of the coefficient of drag associated with the oscillations. This quantity cannot in general be determined without taking into account the interaction of motion relative to the center of mass and the motion of the body center of mass. [Ref. 56:pp. 317-318]

In the derivation of a simple approximate method to solve this problem, the descent trajectory was divided into two sections: $H \geq H_b$ (trajectory in the atmosphere's tenuous layers) and $H \leq H_b$ (trajectory where the interaction between the motion with respect to the center of mass and the center of mass trajectory is taken into account). H_b is the limiting altitude that is calculated to be 70-80 km.. In the region, $H \leq H_b$, the refined asymptotic method breaks down. An approximate solution is derived by formulating averaged equations for the asymptotic solutions that describe the change of the slow varying components of :

1. The maximum and minimum values of the angle of attack during each oscillation
2. The instantaneous oscillation period
3. The averaged components of the center of mass trajectory

The derivation of this method is mathematically rigorous. [Ref. 56:pp. 319-336]

The direct solution to this problem can be obtained by numerically integrating the complete equations of motion given by [Ref. 56:p. 45]

$$d^2\alpha + M_{\Sigma}(x_1, x_2, \dots, \alpha) + \epsilon f_2(x_1, x_2, \dots, \alpha) \frac{d\alpha}{dt} = 0 \quad (125)$$

$$\frac{dx_i}{dt} + \epsilon X_i(x_1, x_2, \dots, \alpha) = 0 \quad (126)$$

$(i = 1, 2, \dots, 6)$

where

$$M_{\Sigma} = \frac{(G - r \cos \alpha)(r - G \cos \alpha)}{\sin^2 \alpha} + M(\tau, \alpha) \quad (127)$$

$$X_1 = f_y(\tau, \alpha)G + ([f_x(\tau, \alpha) - f_y(\tau, \alpha)] \cos \alpha - L(\tau, \alpha) \sin \alpha)r \quad (128)$$

$$X_2 = f_x(\tau, \alpha)r \quad (129)$$

$$X_3 = \frac{C_D(\alpha)qA}{m} + g_T \sin \theta \quad (130)$$

$$X_4 = \frac{g_r \cos \theta}{V} \left[1 - \frac{V^2}{Rg_T} \right] \quad (131)$$

$$X_5 = -V \sin \theta \quad (132)$$

$$X_6 = -\frac{R_0}{R} V \cos \theta \quad (133)$$

$$G = \frac{Q_x \cos \alpha - Q_y \sin \alpha}{I_z} = \lambda \sin^2 \alpha + r \cos \alpha = \text{constant} \quad (134)$$

However, in 1970, this numerical integration required an excessive amount of machine time or computer time, since the solution contains high frequency components along the trajectory.

c. Follow-on Investigations of Uncontrolled Reentry Body Motion

References [59] and [60] are extensions of Duzmak's investigation. Each paper examines a certain aspect of the uncontrolled three-dimensional motion of a reentry body relative to its center of mass.

Reference [59] investigates the three-dimensional uncontrolled motion of a spherical body relative to its center of mass with an arbitrary angle of attack. The mean differential equations are derived for rolling motion. These equations are solved in implicit form for any angle of attack by using the Van der Pol method of integration.

Reference [60] investigates the three-dimensional uncontrolled motion relative to the center of mass of a reentry body with a small geometric and dynamic asymmetry. An approximate analytical solution for the equations for unperturbed three-dimensional and the averaged equations for perturbed three-dimensional motion are derived. By imposing no limits on the initial angular velocity and the three-dimensional angle of attack or nutation angle, the averaged equations of motion computational time is reduced by a factor of approximately three as compared to the numerical integration of the complete equations of motion.

B. SIX-DEGREE-OF-FREEDOM SIMULATIONS

The foundation for six-degree-of-freedom motion has been discussed in the previous section. Several other investigators have examined the effect of motion relative to the center of mass on the trajectory of the center of mass [Refs. 61-64]. The equations of orbital decay, (121) through (124), when coupled with the equations of attitude motion, (112) through (114), will completely describe the motion of a vehicle during the final stages of life. Equations (125) and (126) are the coupled equations of six-degree-of-freedom motion written as a function of angle of attack.

Coupling these equations means: the solution of one set of equations determines the magnitude and form of the forces or moments in the other set [Ref. 62:p. 13]. For example, if the area changes due to either a loss in mass or a change in attitude, then the ballistic coefficient ($W/C_D A$) and the coefficient of drag will be affected.

References [61], [62] and [63] investigate Skylab's attitude and trajectory motion. Specifically, references [62] and [63] derive a variation of the coupled equations presented in the previous section. The authors performed a six-degree-of-freedom trajectory simulation using the coupled equations of motion. Figure 28 shows the flow chart used in their simulation [Ref. 62:p. 14]. Numerical integration of the six differential equations yielded altitude and orbital elements as a function of time. Computer run results for these simulations were extremely long and therefore the decision was made to artificially increase the magnitude of the aerodynamic damping. Subsequently, the results do not simulate the actual dynamical behavior, but they show the "possible" types of dynamical behavior for Skylab. [Ref. 62:p. 15]

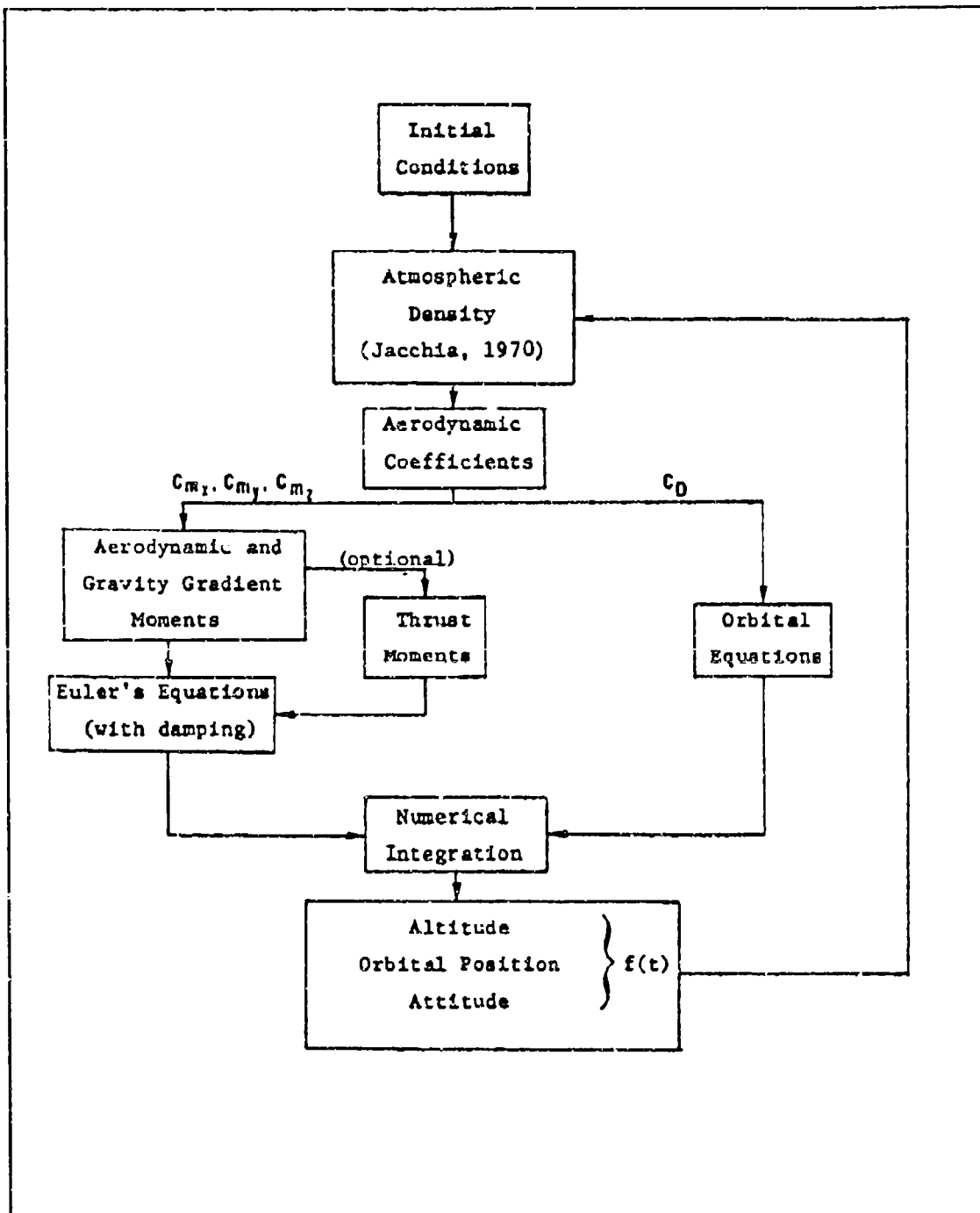


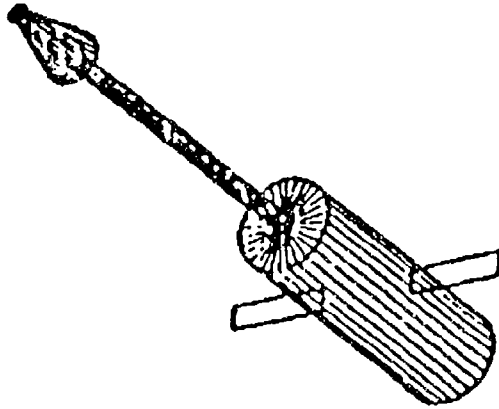
Figure 28: Six-Degree-Of-Freedom Simulation Flowchart [Ref. 62]

Reference [64] is a reentry analysis of a proposed radioisotopic thermoelectric generator (RTG) that was connected to a generic user satellite. A 3-degree-of-freedom reentry trajectory simulation was conducted that utilized aerodynamic, material property and heating characteristics.

Newtonian and free molecular drag coefficients were calculated using the Mark IV Supersonic-Hypersonic Arbitrary-Body program for the generic satellite and each of its subelements. Figure 29 shows the three-dimensional shapes of the generic spacecraft and one subelement (reactor with radiator) used by the program [Ref. 64:p. 6]. Aerodynamic blockage was neglected and a zero angle of attack was assumed in the calculations. The heat transfer methodology used in the simulation to predict the satellite's breakup during reentry, implemented a calibrated heat transfer model to closer simulate actual conditions [Ref. 64:pp. 7-12]. This will be discussed further in the section on breakup later in the chapter. The trajectory simulation was designed to change the mass properties and aerodynamic coefficients as the shape changed due to an "assumed predetermined breakup" scenario. This assumption was based on the basic geometric components or subelements of the satellite and their probable separation sequence during breakup. For example, the boom separated from the main part of the spacecraft and the reactor failed first, this was followed by the heat radiator cone, and then the other components in sequence. [Ref. 64:p.14]

Trajectory simulations were run to assess the breakup altitudes, due to reentry heating, and minimum footprint lengths, due to fuel pin release at various altitudes, which were independent of the heating effects.

GENERIC SPACECRAFT



REACTOR WITH RADIATOR

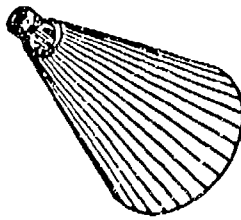


Figure 29: Simulated Generic Spacecraft And Reactor Sub-Element
[Ref. 64]

C. RAREFIED GAS DYNAMICS

Numerous authors have investigated reentry vehicle attitude, heating rates and aerodynamic coefficients in relation to the atmospheric flow regimes [Refs. 22, 56, 65-75]. As stated in Chapter II, the changes in flow regime and corresponding changes in critical parameters of the reentry trajectory or heating equations, are poorly understood in the transition from free-molecular to hypersonic continuum flow. For engineering applications the quantities of lift, drag and heat transfer are usually estimated by a "judicious faring" between regimes [Ref. 22:p. 203].

One solution to this problem is presented by Koppenwallner and Johannsmeier, reference [76]. This solution is a technique of "bridging" between the free molecular and continuum flow, based on Newtonian and free molecular theory. This technique allows the prediction of lift and drag during the hypersonic entry phase. [Ref. 76:p. 461]

Three hypersonic flow regimes, with approximate boundaries, are described as follows: [Ref. 76:p. 461]

- | | |
|-------------------------------|------------------|
| 1. Free molecular flow | $Kn > 5$ |
| 2. Rarefied transitional flow | $5 > Kn > 0.001$ |
| 3. Hypersonic continuum flow | $Kn < 0.001$ |

These boundaries are actually dependent upon reentry vehicle shape and on the aerodynamic property considered. Figure 30 shows these flow regimes in an altitude velocity graph [Ref. 76:p. 461].

The analysis of this technique is limited to flow conditions where the hypersonic Mach independence principle is applicable; therefore, blunt shaped reentry vehicles will have a lower limit of Mach 5. Figure 31 shows the typical aerodynamic data variation, for a blunt body, through the three flow regimes of interest [Ref. 76:p. 461].

The typical drag coefficient behaves such that in free molecular flow, the drag coefficient is independent of Knudsen number and the value of $C_D \approx 2$. The drag coefficient decreases throughout the transitional flow regime and again reaches a constant value in the continuum flow regime. [Ref. 76:p. 461]

The typical lift coefficient behaves such that in the free molecular flow, the lift is very small or negligible. The lift coefficient increases throughout the transitional flow regime until it reaches a hypersonic continuum flow value. [Ref. 76:p. 461]

The heat transfer Stanton number (St) is very close to a value of one in the free molecular flow regime. In the transitional flow, the heat transfer efficiency decreases and the Stanton number decreases. In the continuum flow, the Stanton number decreases continuously as a function of Reynolds number in the manner $St \sim 1/\sqrt{Re}$. [Ref. 76:p. 461]

Table III describes the bridging dependencies as modeled above. The derived transitional functions D_2 and L_2 are functions of angle of attack, vehicle shape and Knudsen number. These transitional functions must bridge the free molecular and continuum flow regimes and must degenerate, in the two limits, to the free and continuum flow values as shown in Table IV. [Ref. 76]

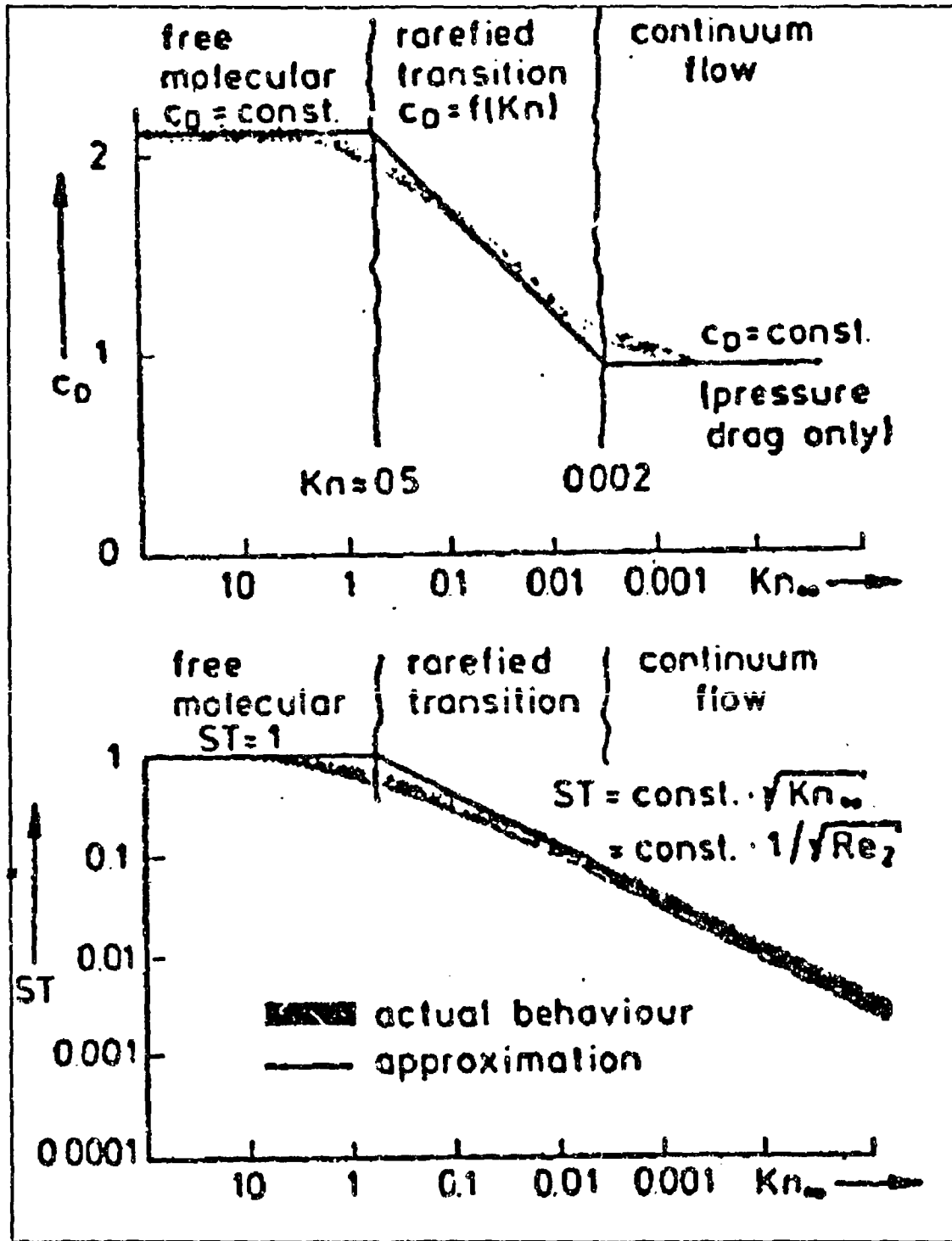


Figure 31: Aerodynamic Coefficients In The Flow Regimes
 [Ref. 76]

Table III: BRIDGING DEPENDENCIES
 [Ref. 76]

FLOW REGIME	DRAG	LIFT
Free molecular	$C_D = D_1 (\alpha, \text{shape})$	$C_L = 0$
Transitional	$C_D = D_2 (\alpha, \text{shape}, Kn)$	$C_L = L_2 (\alpha, \text{shape}, Kn)$
Hypersonic continuum	$C_D = D_3 (\alpha, \text{shape})$	$C_L = L_3 (\alpha, \text{shape})$

Table IV: TRANSITIONAL BRIDGING FUNCTIONS
 [Ref. 76]

DEGENERATE TO FREE MOLECULAR	TRANSITIONAL BRIDGING FUNCTION	DEGENERATE TO HYPERSONIC CONT.
$D_1 = (\alpha, \text{shape})$	$D_2 = (\alpha, \text{shape}, Kn)$	$D_3 = (\alpha, \text{shape})$
$L_1 = 0$	$L_2 = (\alpha, \text{shape}, Kn)$	$L_3 = (\alpha, \text{shape})$

Local flow independence exists in free molecular as well as hypersonic Newtonian flow. This means that unless "shadowing" exists, surface and shape elements will not influence each other. The shape elements of this technique are cones, spherical caps and cylindrical shells. These shape elements allow the composition of capsules, blunted cones and cone-cylinders. Figure 32 shows the shape elements and several composed bodies [Ref. 76:p. 462].

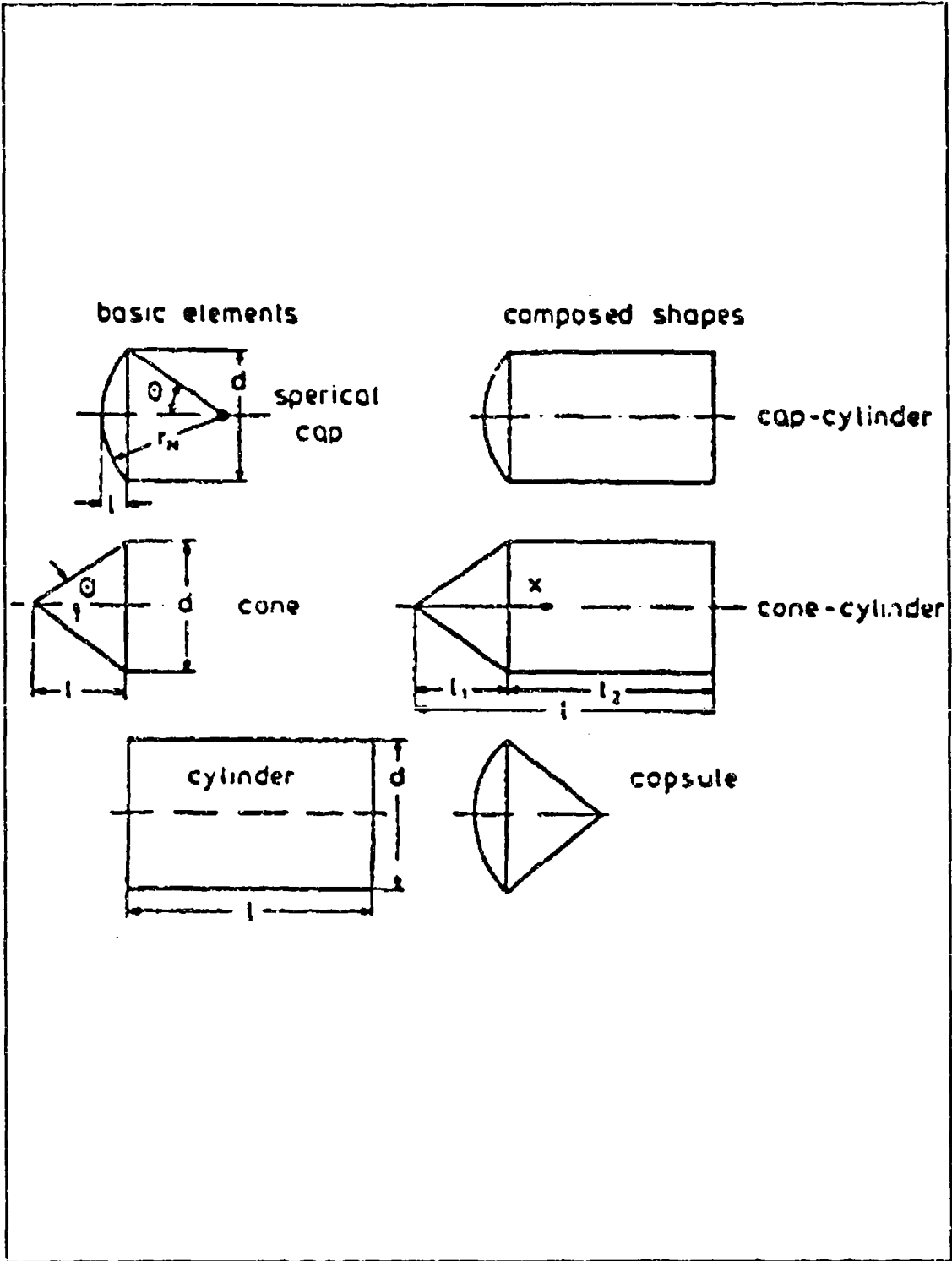


Figure 32: Shape Elements And Composed Bodies
 [Ref. 76]

1. Newtonian Aerodynamics for Hypersonic Continuum Flow

For the case of blunt bodies, it can be assumed that the main contribution to drag is pressure; therefore, the influence of viscous effects on the aerodynamic coefficients are neglected. [Ref. 76:p. 462] Using the Newtonian pressure law, the coefficients of drag and lift may be described in differential equations. The basic Newtonian relationships are as shown in Table V. [Ref. 76:p. 462]

Table V: NEWTONIAN LOCAL PRESSURE LAW
[Ref. 76]

Wetted surface	$ \theta < 90^\circ$	$p / q_\infty = k_N \cos^2 \theta$
Newtonian wake	$ \theta > 90^\circ$	$p / q_\infty = C_{D\alpha}$

where

p = pressure

q_∞ = dynamic pressure in free stream

k_N = Newton factor

θ = flow inclination against surface normal

κ = ratio of specific heats

$C_{D\alpha}$ = coefficient of drag as a function of angle of attack

and

$$k_N = 2 \quad (\text{simple Newton})$$

$$k_N = (\kappa + 3)/(\kappa + 1) \quad (\text{modified Newton})$$

In the Pike formulation, the Newtonian differential equation is given by [Ref. 71:p. 462]

$$C_{D_s}(\alpha) + C_{D_s}(\alpha)\cot(\alpha) + 12C_{D_s}(\alpha) = 6k_N \frac{A_p(\alpha)}{A_R} \quad (135)$$

$$3C_{L_s}(\alpha) = C_{D_s} \quad (136)$$

where

A_p = Flow projected area of body

A_R = Reference area ($\pi D^2/4$)

In order to determine the drag coefficient and solve the differential equations, the following approach is taken: C_D ($\alpha=0^\circ$, shape). This implies that the zero angle of attack drag is proportional to the Newton factor and to a shape dependent factor, C_s [Ref. 76:p. 462]

$$C_D(\alpha=0^\circ) = k_N C_s \quad (137)$$

Upon integration of the Newtonian pressure distribution, the following values for C_s are determined for various bodies in Table VI. [Ref. 76:p. 462]

Table VI: SHAPE FACTOR VALUES
 [Ref. 76]

Disk	$C_s = 1.0$
Sphere	$C_s = 0.5$
Cylinder	$C_s = 0.67$ (cross flow)
Cylindrical shell	$C_s = 0$ (parallel flow)
Sharp cone	$C_s = \sin^2\theta$
Spherical cap	$C_s = 1 - 1/8 \cdot (d/r_N)^2$

Figure 33 shows the shape factor as a function of the ratio (d/r_N) , diameter over nose radius [Ref. 76:p. 466].

When the shape factor or drag at zero angle of attack are known, the aerodynamic coefficients of the class are completely fixed. The following universal solutions for drag and lift are obtained from the Newtonian differential equations [Ref. 76:p. 462]

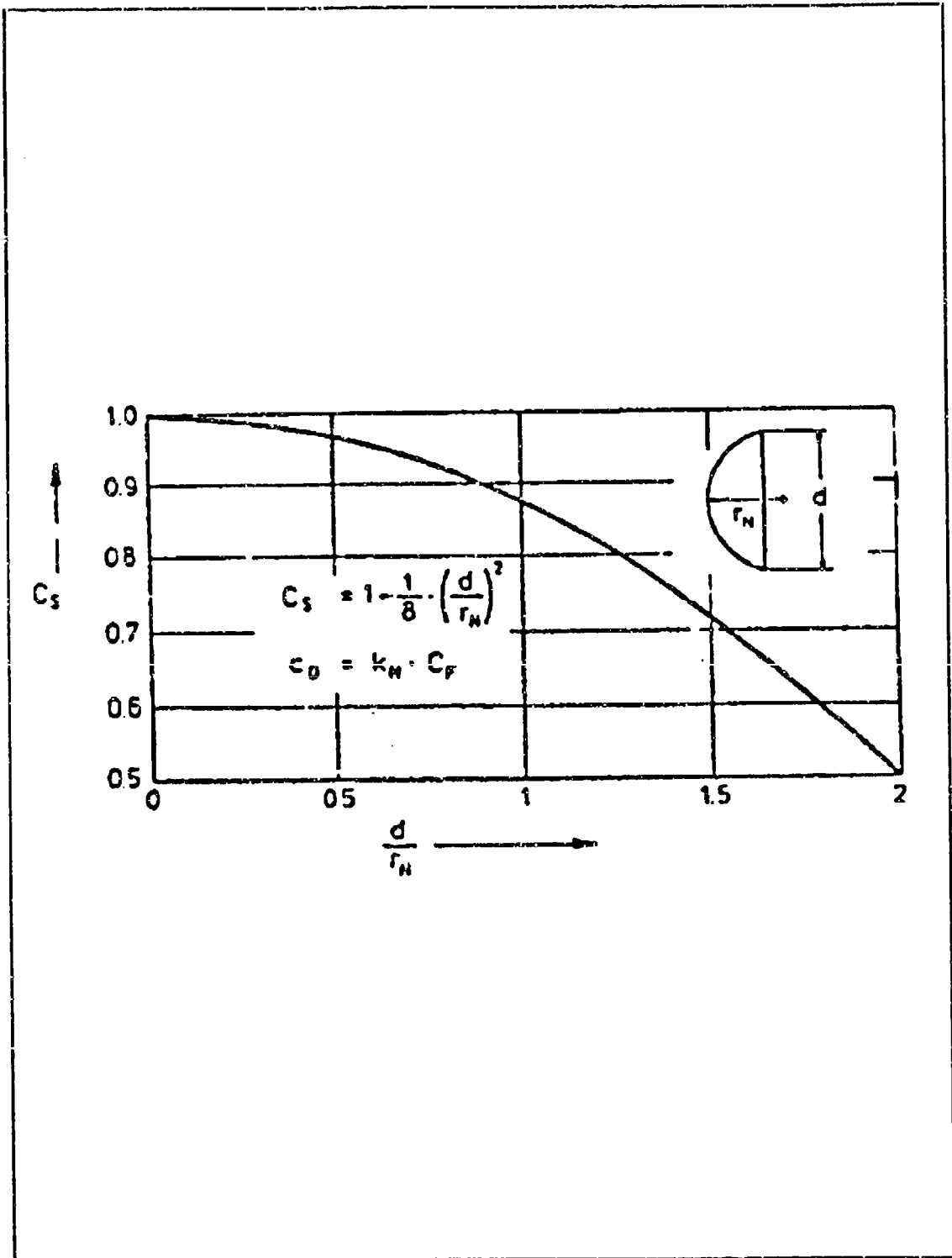


Figure 33: Shape Factor As A Function Of (d/r_N)
 [Ref. 76]

$$C_D = \frac{k_N}{2} (2C_s - (5C_s - 3) \sin^2(\alpha)) \cos\alpha \quad (138)$$

$$C_L = \frac{K_N}{2} (2(1 - 2C_s) - (5C_s - 3) \sin^2(\alpha)) \sin\alpha \quad (139)$$

These solutions are valid for $\alpha \leq \alpha_{\max}$, since at α_{\max} the wetted area decreases due to Newtonian shadowing. Figure 34 shows the universal Newtonian lift and drag functions for various angles of attack [Ref. 76:p. 466].

The shape factor at zero angle of attack serves as the critical parameter in this method. The solution is valid only under the condition that the wetted surface area remains constant for any angle of attack. [Ref. 76:p. 462]

As the geometric body bluntness increases, C_s increases and Newtonian shadowing is shifted to higher angles of attack. Table VII shows that depending upon the body shape, the lift slope at zero angle of attack may be either positive or negative. [Ref. 76:p. 462]

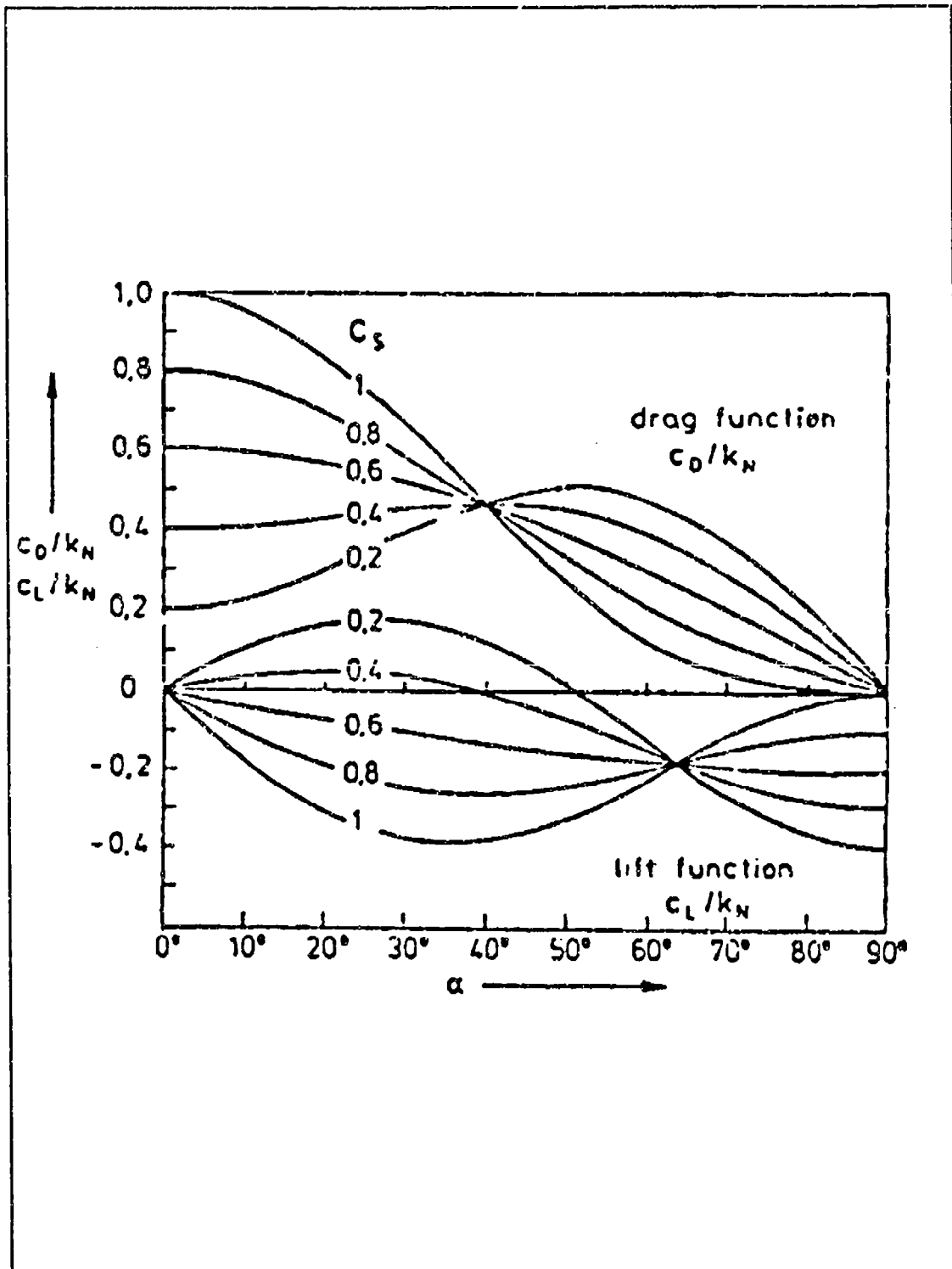


Figure 34: Newtonian Lift And Drag Functions
 [Ref. 76]

Table VII: BODY SHAPE AND LIFT SLOPE
 [Ref. 76]

C_s	Body shape	Lift slope @ $\alpha = 0$
< 0.5	slender	positive
> 0.5	blunt	negative

This demonstrates that blunt reentry bodies will experience a negative lift for a positive defined angle of attack. [Ref. 76:p. 462]

2. Free Molecular Flow Model

The technique of reference [76] also develops analytical formulas for free molecular flow. The general considerations include: [Ref. 76:p. 463]

1. Accommodation coefficient, σ
2. Finite molecular speed ratio, S
3. Wall temperature, T_w

These factors alone are insufficient thus the following simplifying assumptions are made:
 [Ref. 76:p. 463]

- | | |
|---------------------------------|------------------------------------|
| 1. Body shape | Hypersonic blunt, $Ma (d/l) \gg 2$ |
| 2. Aerodynamic cold wall | $T_w / T_\infty \ll 1$ |
| 3. Diffuse molecular reflection | $\sigma = 1$ |

From these constraints the local surface pressure and shear stress may be defined as shown in Table VIII. The aerodynamic force coefficients are also derived as shown in Table IX.

Table VIII: LOCAL SURFACE PRESSURE AND SHEAR STRESS
[Ref. 76]

Wetted surface	$ \theta < 90^\circ$	$p/q_\infty = 2 \cos^2\theta$
Unwetted surface	$ \theta < 90^\circ$	$\tau/q_\infty = \sin\theta \cdot \cos\theta$

Table IX: AERODYNAMIC FORCE COEFFICIENTS
[Ref. 76]

Drag coefficient	$C_D = 2 \cdot A_p(\alpha) / A_p(0) = \cos \alpha$
Lift coefficient	$C_L = 0$

These assumptions imply that no lift is produced and drag is proportional to the flow projected area, $A_p(\alpha)$, in the free molecular flow regime. [Ref. 76:p. 463]

In the more general free molecular flow case, where T_w/T_∞ , σ_n and σ_t are considered, an axisymmetric blunt body formulation for the force coefficients may be given by

$$C_D = 2\sigma_n \cos\alpha + \sigma_n \frac{\sqrt{\pi}}{S_\infty} \sqrt{\frac{T_w}{T_\infty}} \left[\left[C_{S1} + \frac{1}{6} \right] + \left[\frac{1}{2} - C_{S1} \right] \cos 2\alpha \right] + \frac{1}{2} (2 - \sigma_n - \sigma_t) [3(C_{S2} + 1) \cos\alpha + (5C_{S2} - 3) \cos 3\alpha] \quad (140)$$

$$C_L = \sigma_n \frac{\sqrt{\pi}}{S_\infty} \sqrt{\frac{T_w}{T_\infty}} \left[C_{S1} - \frac{1}{2} \right] \sin 2\alpha + \frac{1}{4} (2 - \sigma_n - \sigma_t) [-(C_{S2} + 1) \sin\alpha - (5C_{S2} - 3) \sin 3\alpha] \quad (141)$$

where

T_∞ = temperature, free stream

C_{S1} = shape coefficient, in front of normal shock wave

C_{S2} = shape coefficient, behind normal shock wave

The physical significance of several of the terms in equations (140) and (141)

are: [Ref. 76:p. 463]

1. The first term in C_D gives, for diffuse reflection, $\sigma=1$, the contribution of the incident flux to the aerodynamic coefficients.
2. The T_w/T_∞ term states the influence of the reentry vehicle surface wall temperature on drag and lift.
3. The $(2-\sigma_n-\sigma_t)$ term vanishes for diffuse molecular reflection.

In simple free molecular flow the equations will degenerate appropriately as $\sigma_n=1$, $\sigma_t=1$ and $T_w/T_\infty=0$. In the Newtonian formulation the equations will degenerate as $\sigma_n=1$, $\sigma_t=0$ and $T_w/T_\infty=0$. In this last case C_{S1} vanishes and C_{S2} is the Newtonian shape coefficient, C_S . [Ref. 76:p. 463]

3. Bridging Free Molecular and Continuum Flow

Several methods exist which attempt to bridge the gap between the free molecular and continuum flow regimes. [Refs. 77-79]. In the former USSR and DLR, local bridging is accomplished with a finite surface element method, [Refs. 77-78]. In the U.S., reference [79], bridging has been accomplished through an integral coefficients method. [Ref. 76:p. 463]

The method of bridging by shape element description is developed in reference [76] and is presented in the following section. The methods of references [78] and [79] may be used to derive analytical formulas for trajectory calculation. However, the basic bridging relations must be derived through experimentation. [Ref. 76:p. 463]

a. Shape Element Bridging Method.

Experimental data, presented in Figures 35 and 36 show the drag coefficient changes of a sphere and disk respectively. The data covers the the entire transitional flow regime [Ref. 76].

For a sphere, the Reynolds number, behind the normal shock (Re_2), can be related to the Knudsen number, in the free stream (Kn_1), as follows [Ref. 76:p. 463]

$$Re_2 = 1.26 \sqrt{\frac{2\kappa}{\kappa-1}} \left(\frac{1}{K_\infty} \right) \quad (142)$$

From this experimental data, an approximate formula for C_D , as a function of Reynolds number and shape, can be derived by using the "reduced" aerodynamic coefficients. [Ref. 76:p. 463]

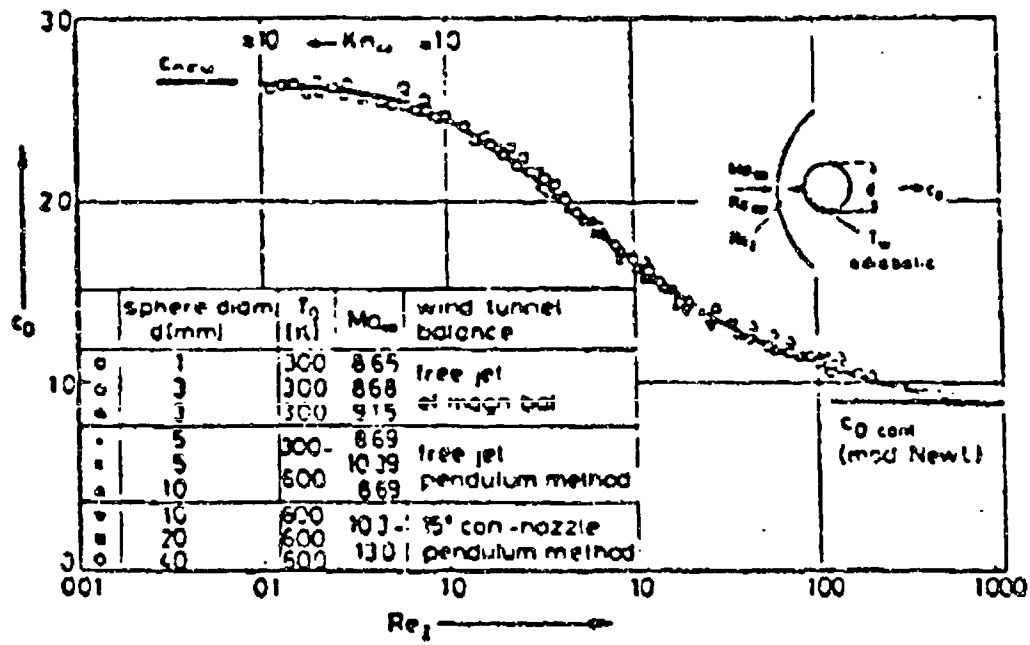


Figure 35: Sphere Drag Coefficient In Rarefied Flow
[Ref. 76]

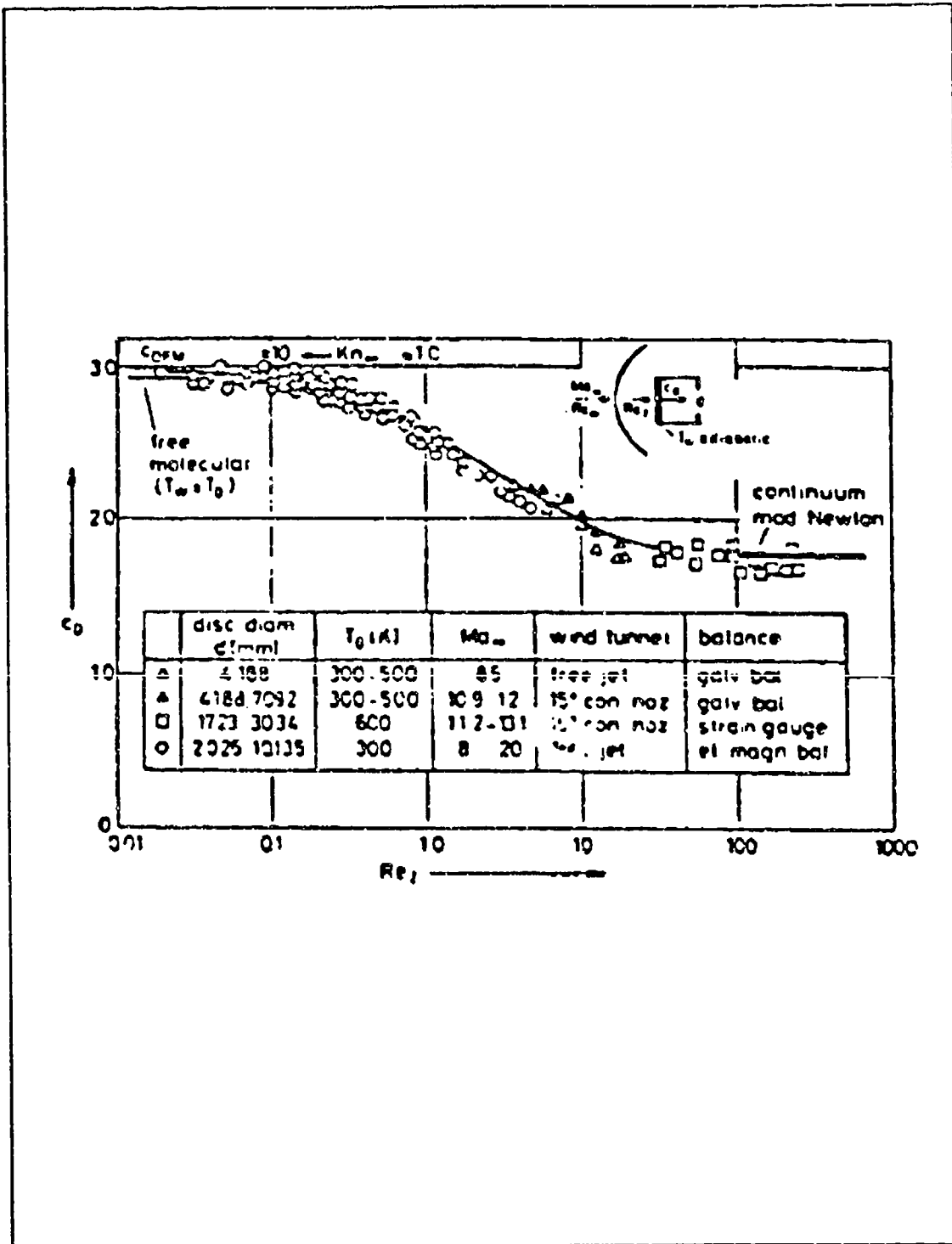


Figure 36: Disk Drag Coefficient In Rarefied Flow
 [Ref. 76]

$$\overline{C_D} = \frac{C_D(Re_2) - C_{DC}}{C_{DFM} - C_{DC}} \quad (143)$$

$$\overline{L/D} = \frac{L/D(\alpha = const., Re_2)}{L/D(\alpha = const., Continuum)} \quad (144)$$

where

C_{DC} = drag coefficient, continuum

C_{DFM} = drag coefficient, free molecular

C_D = reduced drag coefficient

L/D = reduced lift-drag ratio

Analysis of the reduced coefficients at zero angle of attack shows the following: [Ref. 76:p. 463]

1. Slope of the reduced drag coefficient is shape independent.
2. Continuum and free molecular flow boundaries are shape dependent.
3. Continuum and free molecular drag coefficients are shape dependent.

Therefore the bridging function is derived from the reduced coefficients as follows [Ref. 76:p. 464]

$$C_D = \frac{1}{5.205} (C_{DFM} - C_{DC}) \ln \frac{Re_{2c}}{Re_2} + C_{DC} \quad (145)$$

And from this, the drag coefficient may be extracted in one of two forms

$$C_D = \frac{1}{5.205} (C_{DFM} - C_{DC}) \ln \frac{K}{K_C} + C_{DC} \quad (146)$$

$$C_D = \frac{C_D(Re_2) - C_D}{C_{DFM} - C_{DC}} = \frac{1}{2.26} \ln \frac{Re_{2c}}{Re_2} \quad (147)$$

The shape dependent boundaries are defined as:

1. $Re_{2c} > Re_2 > Re_{2FM}$
2. $Kn_C < Kn > Kn_{FM}$

and the experimentally derived values are summarized in Table X below. [Ref. 76:p. 464]

Table X: SHAPE DEPENDENT BOUNDARIES
[Ref. 76]

Body Shape	d/R _N	Continuum Flow		Free Molecular Flow	
		Re _{2c}	Kn _C	Re _{2FM}	Kn _{FM}
Disk	0	28.5	0.117	0.115	21.5
Sphere	2	89.3	0.037	0.492	6.8

In summary, the technique of reference [76] allows the following conclusions to be drawn: [Ref. 76:p. 464]

1. Newtonian theory based on Pike's method for the hypersonic continuum flow is useful, as it shows the shape dependent and shape independent aerodynamic coefficients.

2. The bridging function is based on experimentally derived results for the transition flow.
3. Lift and drag bridging do not follow the same laws.

b. Local Bridging Method

Reference [78] develops a technique of "local" bridging. The differences between the shape element method, referred to as a "global" method, and local bridging are: [Ref. 78:p. 469]

1. Global bridging performs across the spectrum of aerodynamic coefficients for the complete body.
2. Global bridging is usually tailored to a specific class of shapes.
3. Global bridging techniques require new experimentally derived "fitting constants" for each new shape of interest.
4. Local bridging is a method of bridging the local pressure and shear stress coefficients. The local distribution is then integrated over the body surface which yields the global force and moment coefficients.

The common principle of all bridging techniques is the manner in which they model the transition function. The known free molecular and continuum flow limiting values for a specific aerodynamic coefficient (lift, drag or heat transfer) are weighted and applied to the bridging function. The general case is as follows

$$C(X) = C_{FM} f(X) + C_C (1 - f(X)) \quad (148)$$

where

C = aerodynamic coefficient considered

X = rarefaction-dependent flow parameter

The potential improvements of local bridging over global bridging are:

[Ref. 78:p. 470]

1. Ease of adaptation to different shapes without changing internal constants.
2. More reliable calculation of moments. These are very sensitive to rarefaction because of the varying contributions of pressure and shear in the different flow regimes.
3. Simplified method for determining reference quantities for local coefficients, such as reference length based on a local coordinate.
4. Ability to account for non-uniform flow field conditions.

The conclusion of reference [78], after examining several different bridging methods and various shapes, is that the current state of experience in applying the local bridging methods allows no definitive answer as to whether or not they can serve as an effective analysis tool in transition flow analysis.

4. Gas-Surface/Gas-Gas Interactions

Gas-surface interactions are significant in the understanding of reentry dynamics and aerothermodynamics. The primary cause of concern is that at orbital altitudes, the highly rarefied flowfield is dominated by gas-surface interactions that occur at average velocities corresponding to that of the orbiting vehicle. [Ref. 80:p. 1] Under these reentry conditions, gas-gas interactions become important and gas molecules that

reach the vehicle surface tend to have lost some of their initial translational energy. This loss of translational molecular energy is due to conversion into other forms such as heat, internal energy, etc. Figure 37 shows molecular velocity distributions in rarefied and transitional flow about a reentering sphere [Ref. 80]. The collision mechanisms by which the translational energy is converted include:

1. Chemical reactions
2. Ionization
3. Dissociation

Since the nature of the gas-surface interaction is known to be dependent upon the velocity and energy of the incident molecules, it becomes necessary to know the state of the gas molecules reaching the surface. [Ref. 80:p. 1]

Wilmoth, et al, [80] uses the technique of Direct Simulation Monte Carlo (DSMC) as developed by Bird, [Ref. 81] where the molecular velocity and energy distributions of the gas molecules are a direct result of the simulation process. Bird uses a simple engineering model of the gas-surface interactions, which accounts for diffuse and specular reflection along with other phenomena. This model can accommodate processes such as catalytic reactions and molecular recombination. A limitation of this method is that parametric studies must often be performed in order to place bounds on the predicted quantities of interest. [Ref. 80:p. 1] This also implies that the analyst must judiciously apply the model based on experience and a limited base of experimental data.

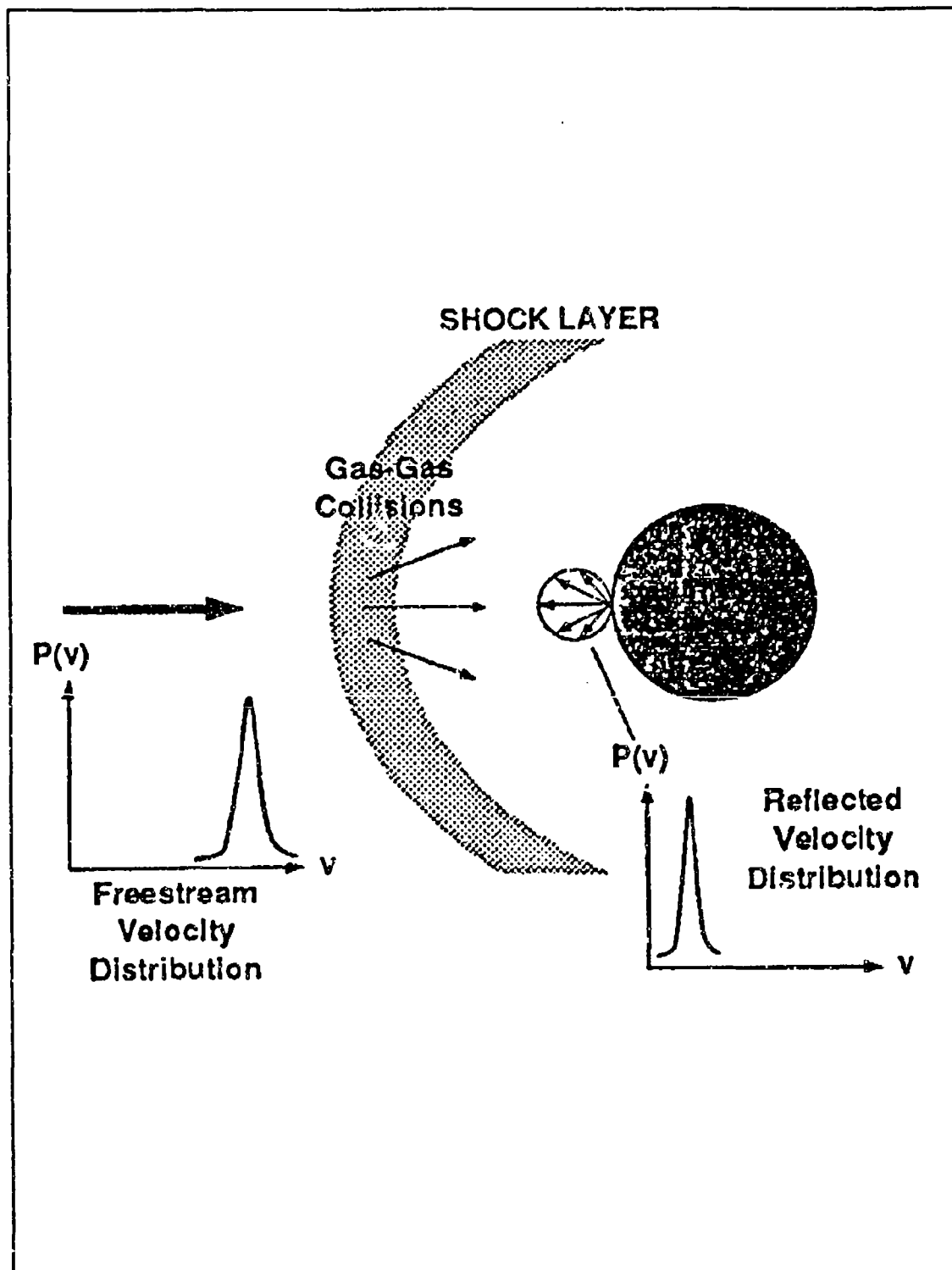


Figure 37: Molecular Velocity Distribution
[Ref. 80]

The lack of experimental data is the reason why more detailed gas-surface interaction models have not been developed. This results mainly for two reasons: [Ref. 80:p. 1]

1. It is very difficult to simulate gas-surface interactions at orbital or entry velocities in a laboratory.
2. It is difficult to characterize the surfaces used in laboratory experiments with sufficient generality that the results may have application in an engineering context.

Because of the tendency of gas molecules to decelerate after gas-gas collisions, which occur before reaching the vehicle surface, it is important to quantify the actual velocities and energies encountered in such cases.

Reference [80] studies the "typical" gas-surface interactions for transitional flow at entry velocities. The reentry vehicle was a 1.6 m diameter sphere at a free stream velocity of 7.5 km/sec over an altitude range of 90 to 130 km. [Ref. 80:p. 2] The study was conducted using the DSMC method of Bird.

The flow conditions of the DSMC simulation are given in Table XI [Ref. 80:p. 6]. The atmosphere is modeled by Jacchia, 1977, with an exospheric temperature of 1200K. The surface temperature of the sphere was assumed constant at 350K. The gas-surface interaction was assumed to be diffuse with full thermal accommodation, and the surface was non-catalytic. Five atmospheric molecular species were modeled O_2 , N_2 , O, N and NO, with 23 reaction possibilities. [Ref. 80:p. 3]

Table XI: FREESTREAM CONDITIONS
[Ref. 80]

Altitude km	ρ_∞ kg/m ³	V_∞ km/s	T_∞ K	Mole Fraction O ₂	Mole Fraction N ₂	Mole Fraction O	M g/mol	A_∞ m
90	3.43×10^{-6}	7.5	188	0.209	0.788	0.004	28.80	0.017
100	5.66×10^{-7}	7.5	194	0.177	0.784	0.040	28.24	0.100
110	9.67×10^{-8}	7.5	247	0.123	0.770	0.106	27.22	0.599
120	2.27×10^{-8}	7.5	388	0.085	0.733	0.183	26.14	2.881
130	8.23×10^{-9}	7.5	500	0.071	0.691	0.236	25.43	7.724

Wilmoth's results show the following: [Ref. 80:pp. 3-5]

1. At 130 km, a density rise of nearly 22 times the freestream value occurs over a distance of ~ 3 m. However, based on analysis of the data it is determined that very few collisions are occurring.
2. At 90 km, the density increases to well over 100 times the freestream value over a distance of ~ 0.1 m. In this altitude range collisions become very significant and there is considerable chemical activity.
3. There are significant variations in the velocity and energy of molecules reaching the surface over an altitude range of 130 to 90 km. Figure 38 shows the average translational energy per particle striking the reentry vehicle surface [Ref. 80].

D. SURFACE ROUGHNESS EFFECTS

Another important consideration in the reentry phase is the "boundary-layer transition." It is this phenomenon which is responsible for heat transfer to/from the reentry body due to atmospheric contact with the body. In the continuum flow regime viscous effects are essentially restricted to a small layer called the boundary layer. It is

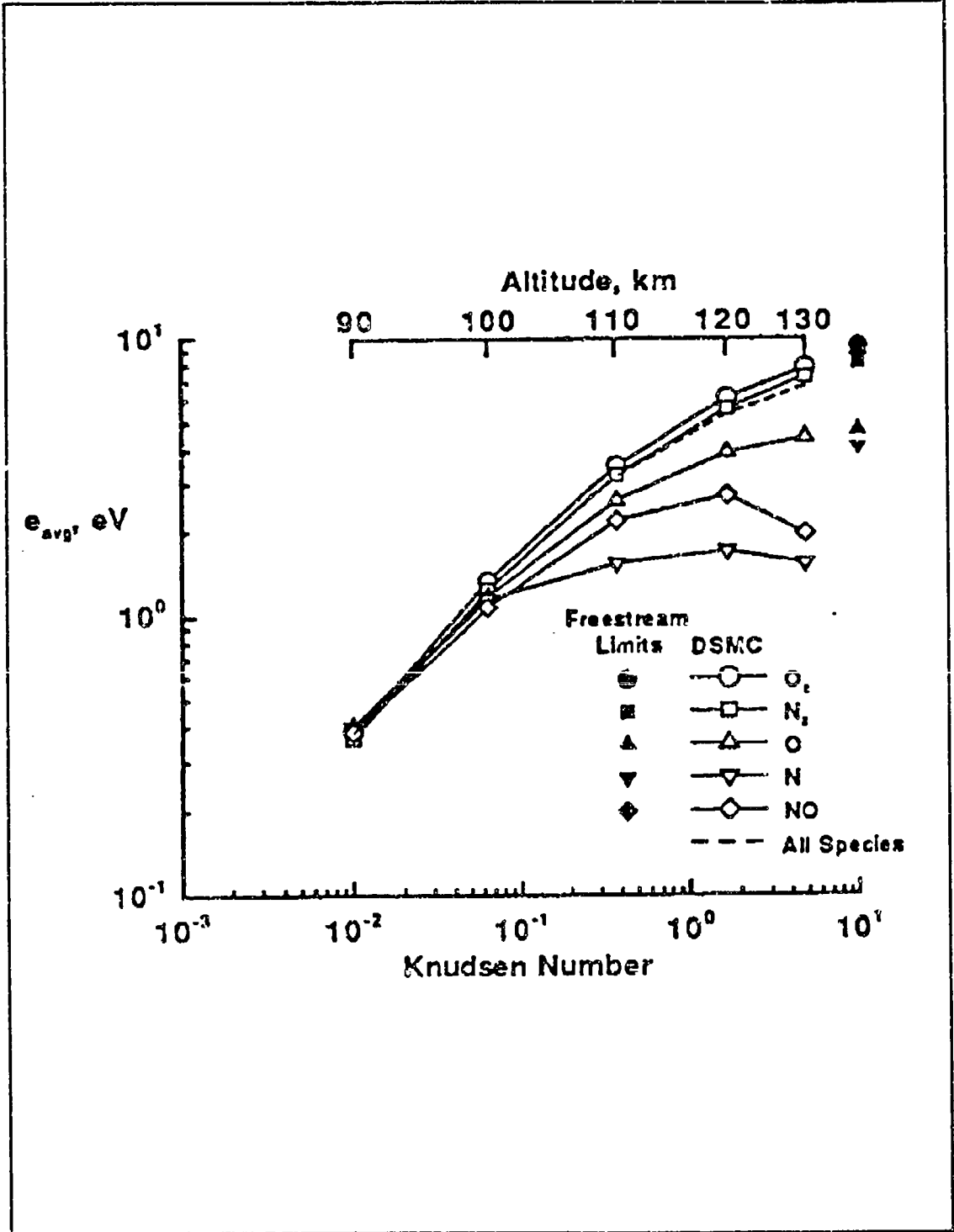


Figure 38: Average Translational Energy [Ref. 80]

within this boundary layer that the details of "fluid" motion determine the levels of skin friction and heat transfer from the flow. [Ref. 22:p. 211]

A parameter commonly used for characterizing the boundary layer is the Reynolds number. [Refs. 82-83] The Reynolds number is defined as the ratio of inertial forces to the viscous forces, as given by [Ref. 22:p. 212]

$$\frac{\text{inertia forces}}{\text{viscous forces}} = \frac{\Delta(\text{momentum})/(\text{unit time})}{(\text{shear stress})x(\text{unit area})} = Re \quad (149)$$

In order for a fluid (the atmosphere is modeled as a fluid in the continuum flow) to support a shear stress there must be relative motion between adjacent layers. This implies that there is a velocity differential within the flow layers. The following terms are defined: [Ref. 22:p. 213]

$$\tau = \text{shear stress} = \mu(dV/dy)$$

$$\mu = \text{dynamic viscosity}$$

$$y = \text{coordinate normal to direction of motion}$$

The definition of Reynolds number may now be given as [Ref. 22:p. 213]

$$Re = \frac{d(mV)/dt}{\mu(dV/dy)A} = \frac{[\rho L^3 V/(L/V)]}{\mu(V/L)L^2} = \rho \frac{VL}{\mu} = \frac{VL}{\nu} \quad (150)$$

where

$$\nu = \text{kinematic viscosity} = (\rho/\mu)$$

Now the Reynolds number may be used to characterize the boundary layer flow conditions. When the viscous forces are large enough to damp out the oscillations caused by the dynamic forces, the flow is laminar and the Reynolds number is small.

Conversely, the flow is turbulent when the dynamic forces overcome the viscous forces.

Also, the Reynolds number is large for turbulent flow. [Ref. 22:p. 212]

The velocity profiles within the laminar and turbulent boundary layers show some significant differences. The magnitude of velocity in the turbulent boundary layer is notably greater, especially near the reentry body's surface. This implies that the turbulent boundary layer yields much more energy near the surface than does a corresponding laminar flow. The velocity profile determines the skin friction on the surface and it can be expected that greater heat transfer will occur under conditions of a turbulent boundary layer [Ref. 22:p. 213]. Figure 39 shows the boundary layer types. Figure 40 shows boundary layer velocity-distance profiles. Figure 41 shows the altitude, air speed and dynamic pressure [Ref. 22:pp. 213-214].

A Reynolds stress turbulent boundary layer model which specifically accounts for surface roughness effects is described by reference [84]. In this study, surface roughness is represented by distributed "sources" and "sinks" in the various governing equations. The most significant term is a sink term in the mean momentum equation, which represents "form drag" on the roughness elements. [Ref. 84:p. 2]

A fundamental assumption of this model is that the flow around the individual roughness elements (only distributed roughness is considered) is attached to the elements. [Ref. 84:p. 3] The roughness elements provide a distributed sink, due to drag, for the momentum equation and distributed sources for mean turbulent kinetic energy and dissipation. This model also assumes that the roughness elements occupy no volume; therefore, this assumption becomes more severe as the roughness density increases. In

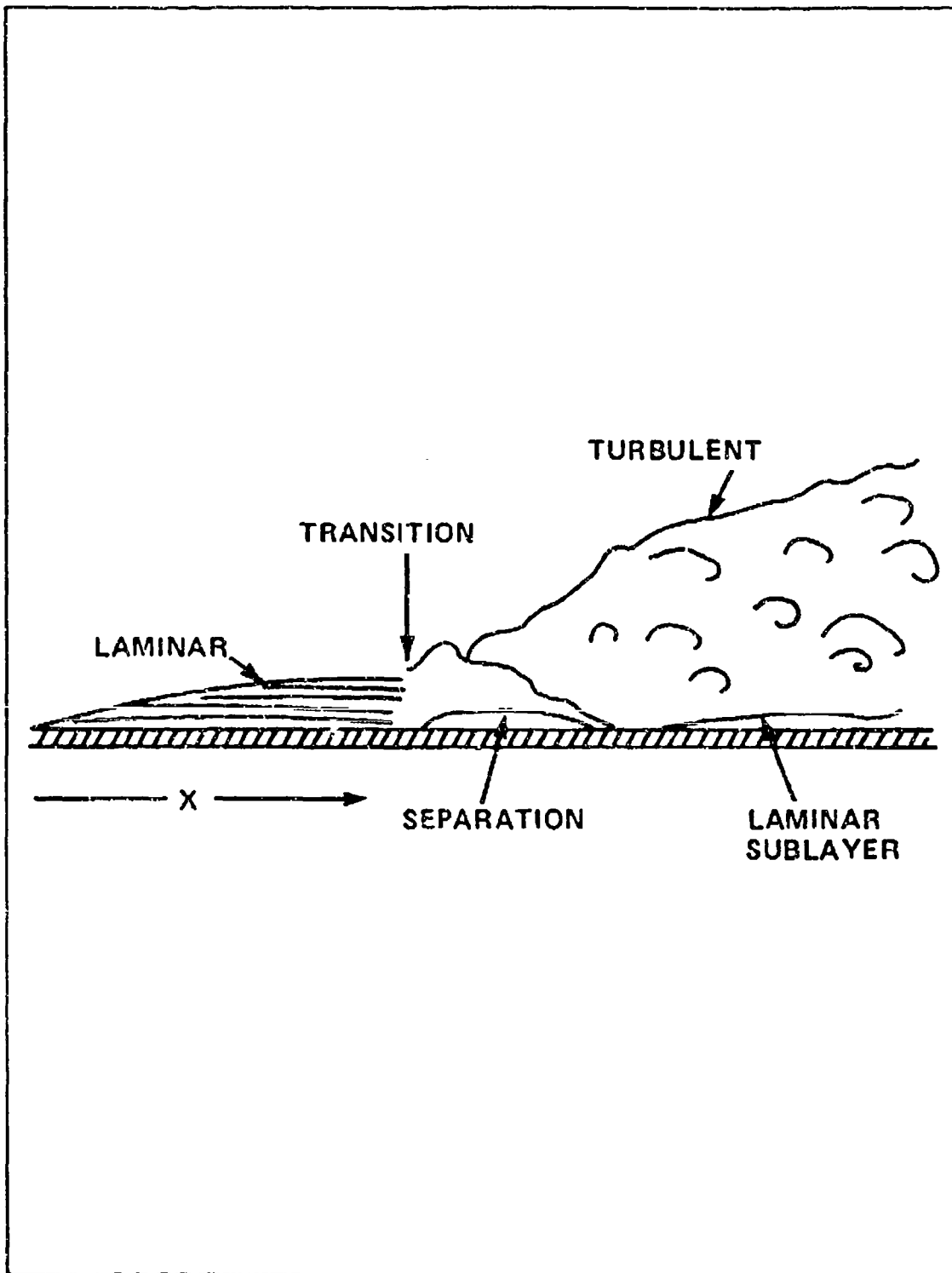


Figure 39: Boundary Layer Types
[Ref. 22]

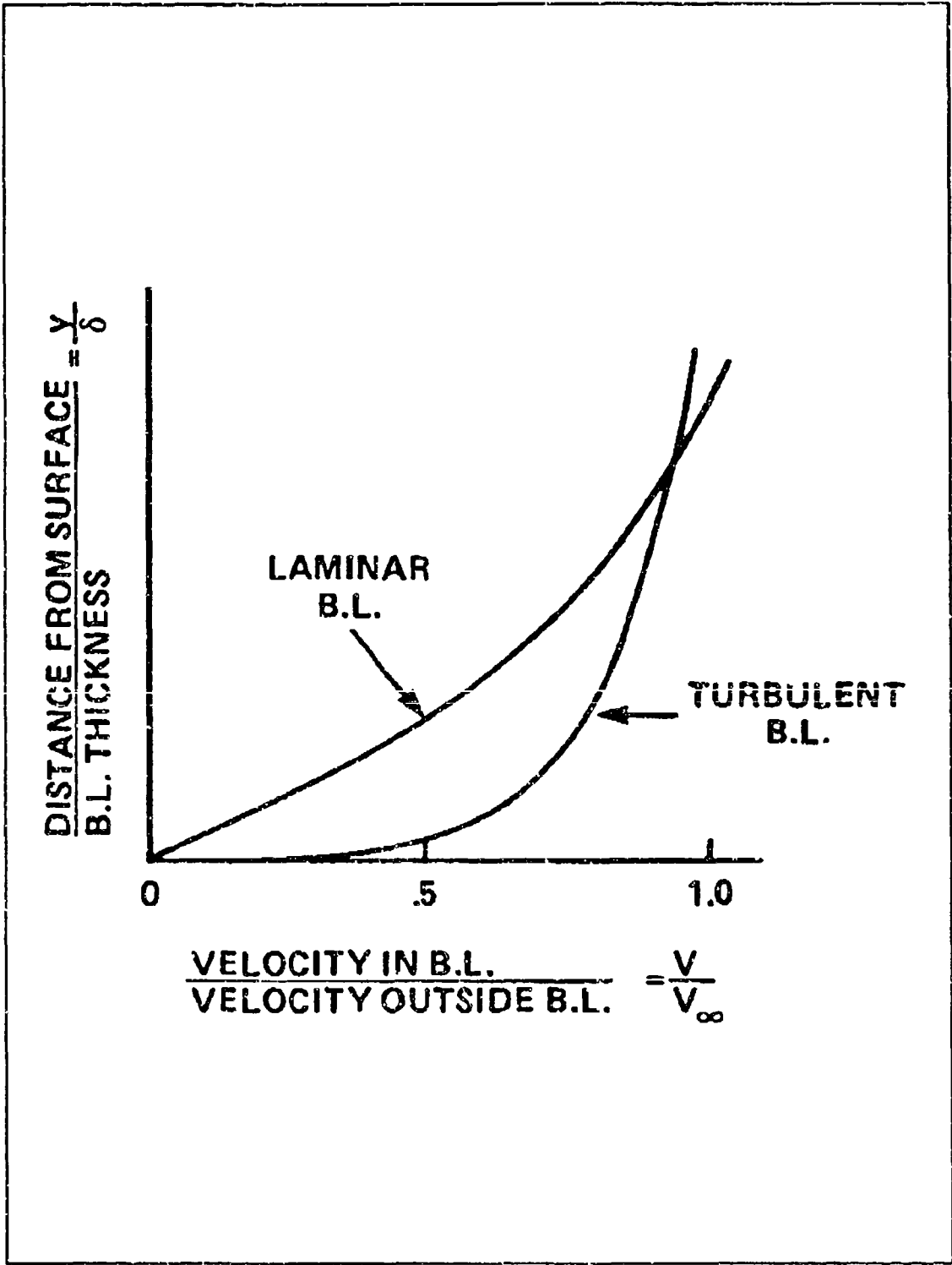


Figure 40: Boundary-Layer Velocity-Distance Profiles
 [Ref. 22]

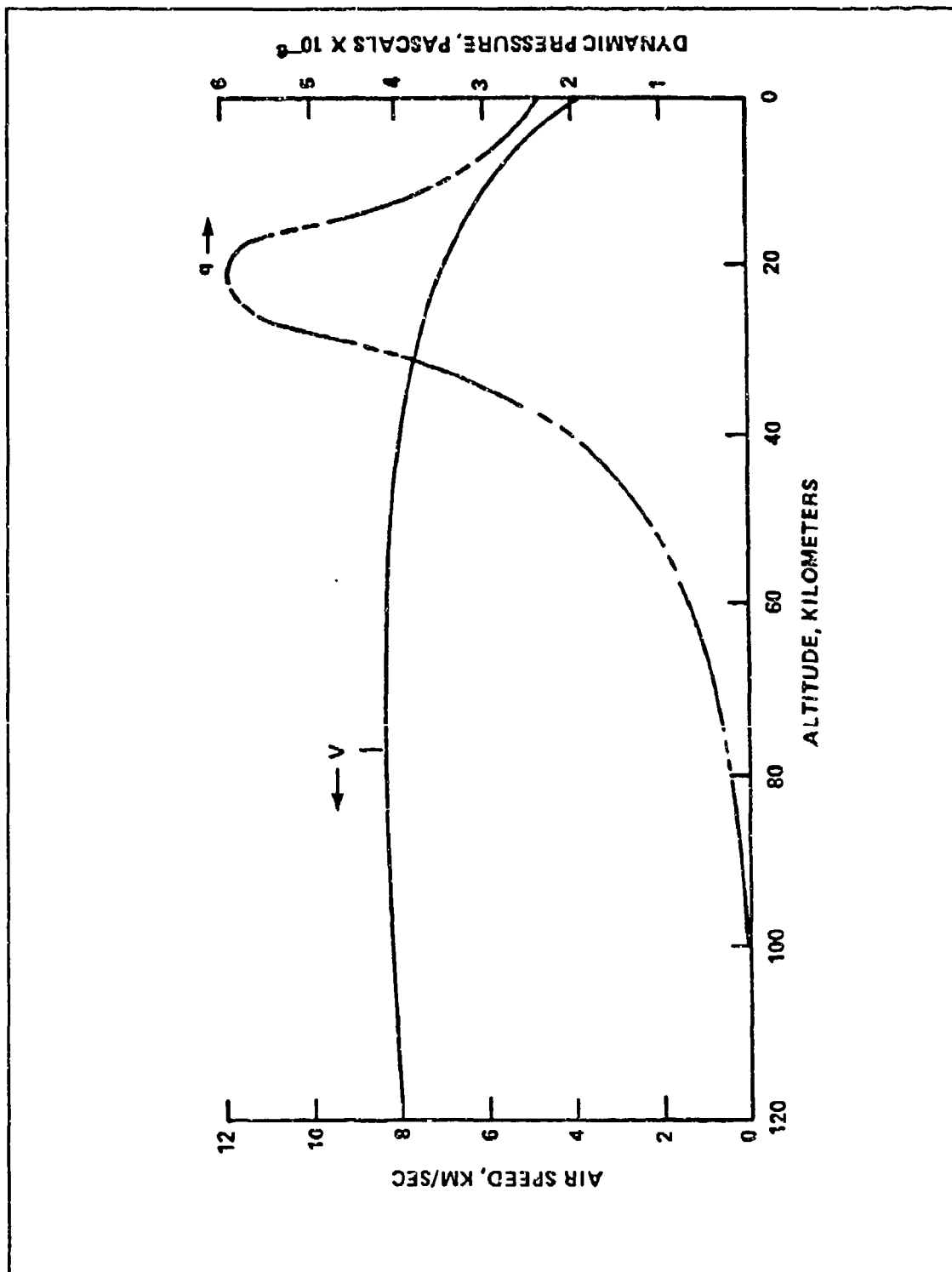


Figure 41: Altitude-Air Speed-Dynamic Pressure Relationship
 [Ref. 22]

order to compensate for this, the model has been extended to account for the blockage effect of the roughness elements. [Ref. 84:p. 4]

The mean momentum equation is given as [Ref. 84:pp. 4-5]

$$f(y) \rho U \frac{\partial U}{\partial x} + \rho V \frac{\partial U}{\partial y} = -f(y) \frac{\partial p}{\partial x} + \frac{\partial}{\partial y} \left[\mu \frac{\partial U}{\partial y} \right] - \frac{\partial}{\partial y} (\rho \overline{u'v'}) - \frac{1}{2} \rho U^2 C_D \frac{D}{l^2} \left(1 - \frac{\pi D^2}{4l^2} \right)^{-1} \quad (151)$$

The variables U, V, u/ and v/ are the reduced variables, under the boundary layer approximation, as given in reference [85]. These variables and this equation will not be derived here for the sake of brevity.

The major advantages of this model are: [Ref. 84:p. 5]

1. Solutions are obtained for both velocity and thermal variables.
2. Heat transfer is obtained directly, without invoking Reynolds analogy.
3. Finite difference solutions are obtained using the boundary conditions that fluctuating quantities are zero at the solid wall and in the free stream.

Reference [84] concludes with a comparison of a smooth wall turbulent boundary layer model and the developed rough wall model. The rough wall model is determined to show that roughness spacing is more critical than roughness height, under the conditions tested; however, the limited skin friction data obtained in the study cannot be interpreted unambiguously. [Ref. 84:p. 38]

E. REENTRY HEATING EQUATIONS

In Chapter II, the fundamentals of reentry heating were discussed as presented by the authors of references [20], [40] and [43]. Aerodynamic heating, as it applies to the reentry of space vehicles, takes its roots in the work of Allen and Eggers, reference [65]. Reentry heating becomes an important consideration of the overall reentry process for the following reasons: [Ref. 42:p. 139]

1. Structural performance of the reentry vehicle is dependent upon the dynamic pressures encountered during the reentry, which is a function of the reentry trajectory.
2. Structural strength of the vehicle is a function of the stresses induced by temperature gradients within the component materials.
3. Temperature gradients are proportional to the time rate of heat input and maximum time rate of heat input.

Therefore, the three critical parameters of the reentry trajectory are the total heat input along the trajectory, the maximum rate of aerodynamic heating and the maximum dynamic pressure. [Ref. 42:p. 139]

The mechanism of heat flow into the reentry vehicle during atmospheric entry was first described in reference [65]. Since then, numerous combinations of reentry speed regimes and aerodynamic shapes have led to the publication of numerous technical reports. However, the basic aspects of aerodynamic heating during reentry are still the same. The numerical factors for different heat transfer formulas and their ranges of validity in terms of the regime of speed are the only variation among the numerous authors. [Ref. 42:p. 139]

The basic equations of reentry heating, equations (18), (19) and (20), are developed with their simplifying assumptions as presented in Chapter II, pp. 46-48. These assumptions yield the following limitations: [Ref. 42:pp. 141-142]

1. Neglecting radiative heat transfer from the vehicle or to the vehicle from the high-temperature air between the shock wave and the vehicle surface, is based on the fact that the maximum allowable surface temperature is about the same for a variety of reentry vehicle shapes. Thus, outward radiation from the surface will be about the same. Neglecting the radiative heat transfer from the disturbed air is a qualitative simplification and therefore negates the application of the equations to very blunt and heavy shapes at reentry speeds of 3 km/sec or greater.
2. Neglecting the real-gas effects in the flow, most importantly dissociation, on convective heat transfer is a good approximation for reentry speeds of up to 3 km/sec. Nevertheless, this assumption is conservative and results in higher calculated heating rates than actual rates.
3. Neglecting the shock-wave boundary-layer interactions implies that the laminar skin-friction coefficient, on a flat plate at zero incidence, is being held constant. This assumption is not valid at reentry speeds over 6 km/sec.
4. Assuming a Reynolds analogy and holding the Prandtl number constant also restricts the validity of the equations to reentry speeds of less than 3 km/sec.

For the case of low earth orbits and naturally decaying satellites, these assumptions create severe restrictions. The circular orbital velocity may be calculated from [Ref. 17:p. 38]

$$V_c = \sqrt{\frac{\mu}{r}} \quad (152)$$

where

r = radius from center of Earth

V_c = circular velocity

Using this equation, it is possible to approximate the circular orbital radius of a satellite traveling at an altitude of near 120 km or radius of 6499 km. This is the altitude of concern for the focus of this thesis and it can be shown that the orbital velocity of interest is approximately 7.8 km/sec. The orbital radius of a satellite travelling at speeds of 3 km/sec and 6 km/sec are 44,289 km and 11,072 km respectively. This equates to circular orbital altitudes of 37,910 km and 4,694 km .

The assumptions of reference [65] which are maintained in references [14], [40] and [43] should be removed for an accurate quantitative analysis of the aerodynamic heating during the reentry of a specific vehicle. [Ref. 42:p. 142]

F. STRUCTURAL BREAKUP OF A REENTRY BODY

The previous sections of this chapter have served to develop the "state-of-the-art," as determined through the literature survey, of reentry formulations and solutions. The culmination of the uncontrolled reentry process is usually the structural breakup of the reentry body. The breakup of a reentry body is stated to be a function of surface temperature, in that, structural failure (breakup) is assumed or expected to occur when the outer structure reaches its melting temperature. [Refs. 63, 86] It has been shown previously that the maximum temperature a reentry body will experience is determined by the maximum heating rate, which is a function of ballistic coefficient. [Ref. 86:p. C-

11] Although the peak heating rate increases as the ballistic coefficient increases, average heating rate (a measure of overall survivability) and maximum local stagnation region heating (a measure of local "hot spots"), must be considered in determining where breakup occurs. [Ref. 40;pp. 181-182]

In the 1970's, the Air Force conducted reentry experiments that used optical and radar techniques to observe actual breakup events. The objective of these tests was to determine the survivability of reentry body debris. Specific findings from these tests indicate: [Ref. 86;pp. C-4--C-10]

1. Classical convective heat transfer analysis underestimates the reentry body survivability. Specifically: actual breakup is at an altitude of at least 10 nm lower than predicted; actual surface temperature is at an altitude 10 nm lower than predicted; and the effective heating rate input is a factor of four lower than predicted.
2. Consistent catastrophic failure of magnesium/aluminum structures is at an altitude of 42 nm. Figure 42 [Ref. 86] shows convergence of three ballistic coefficient lines close to the magnesium/aluminum melt zone at this approximate altitude.
3. Phenomenon of breakup process is independent of: body attitude and rates; body diameter; body shape; and entry flight path angle ($0.3^\circ > 1.5^\circ$).
4. Ballistic coefficient and material of a body determines survivability.
5. A body with low ballistic coefficient will survive reentry, as will a body with a higher melting temperature survive reentry with a higher ballistic coefficient.
6. Reentry body structural integrity is maintained until melting temperature is achieved.
7. Surface structure temperature is determined by radiation equilibrium that is based on a shallow path angle and a low thermal capacity of the outer structure.

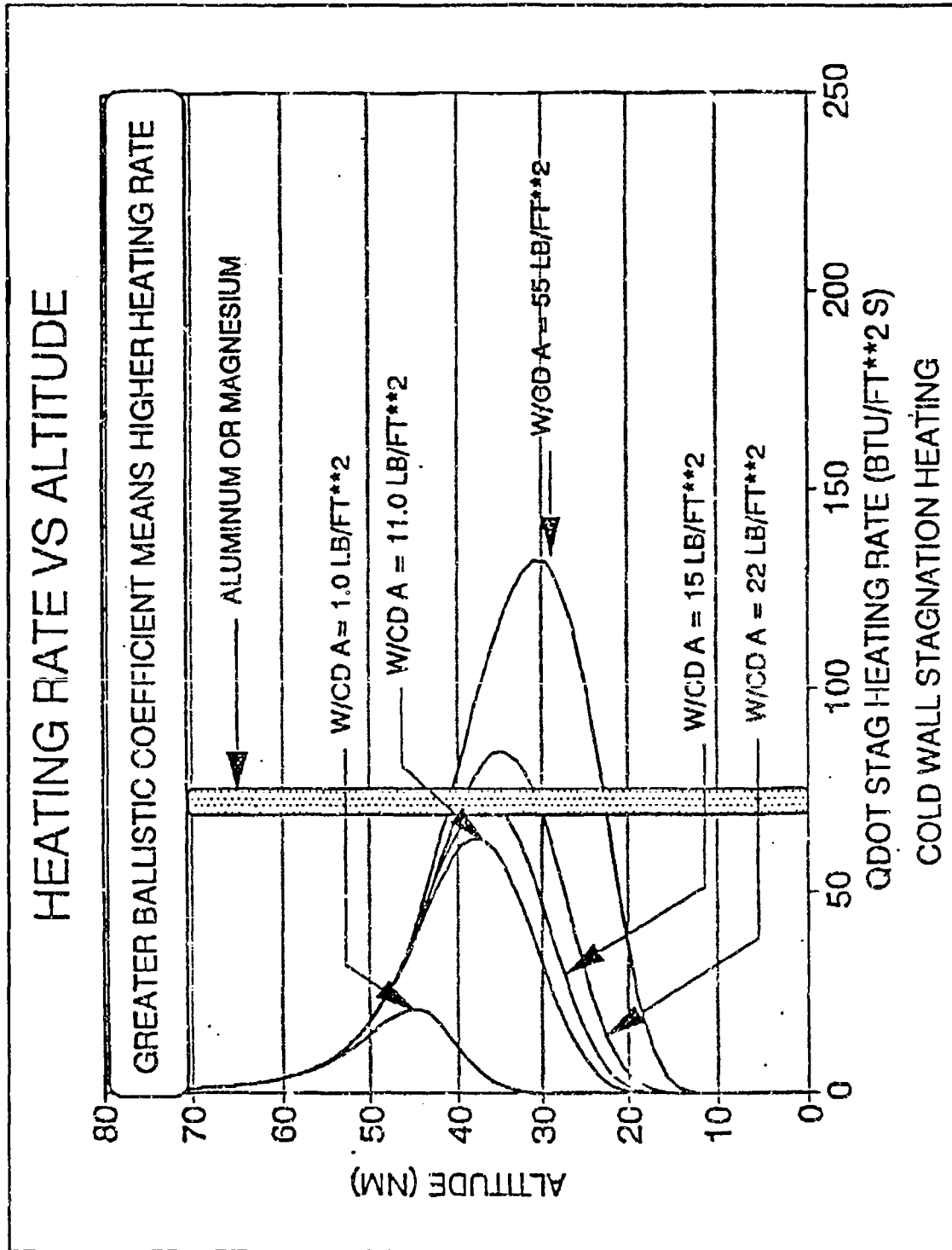


Figure 42: Structural Breakup - Heating Rate vs Altitude
 [Ref. 86]

Reference [85] concludes that classical convective heat transfer analysis in a free-molecular flow regime is not indicative of the transition/continuum flow heating which is responsible for structural breakup. This finding is in agreement with reference [42] which, as shown previously, discounts the classical reentry heating equations based on the limitations imposed by the simplifying assumptions. [Ref. 42:pp. 141-142] Reference [64] also cites the 1970's Air Force studies and indicates the deficiencies of the classical convective heat transfer analysis.

The consistent underestimation of survivability was further investigated in reference [64]. By using a calibrated heating model, the observed breakup altitude of approximately 42 nm (79.5 km) was successfully predicted for satellites with aluminum structures. Figure 43 [Ref. 64:p. 48] shows the predicted breakup altitudes for two satellite reentry simulations. [Ref. 64:pp. 7-13]

The heating model was interfaced with a trajectory simulation model in order to estimate the altitudes where possible breakup events could occur. Table XII shows the breakup analysis results of the critical elements with their associated material composition, heating rates and breakup altitudes [Ref. 64:p.59].

Since the breakup analysis was assumed with strictly aerodynamic heating for structures with low melting points, the authors recommend further investigation for the combined effect of both aerodynamic heating and aerodynamic loading on breakup. Specifically, for the case where higher melting point materials will survive to altitudes where deceleration loads are significant. [Ref. 64:p. 21]

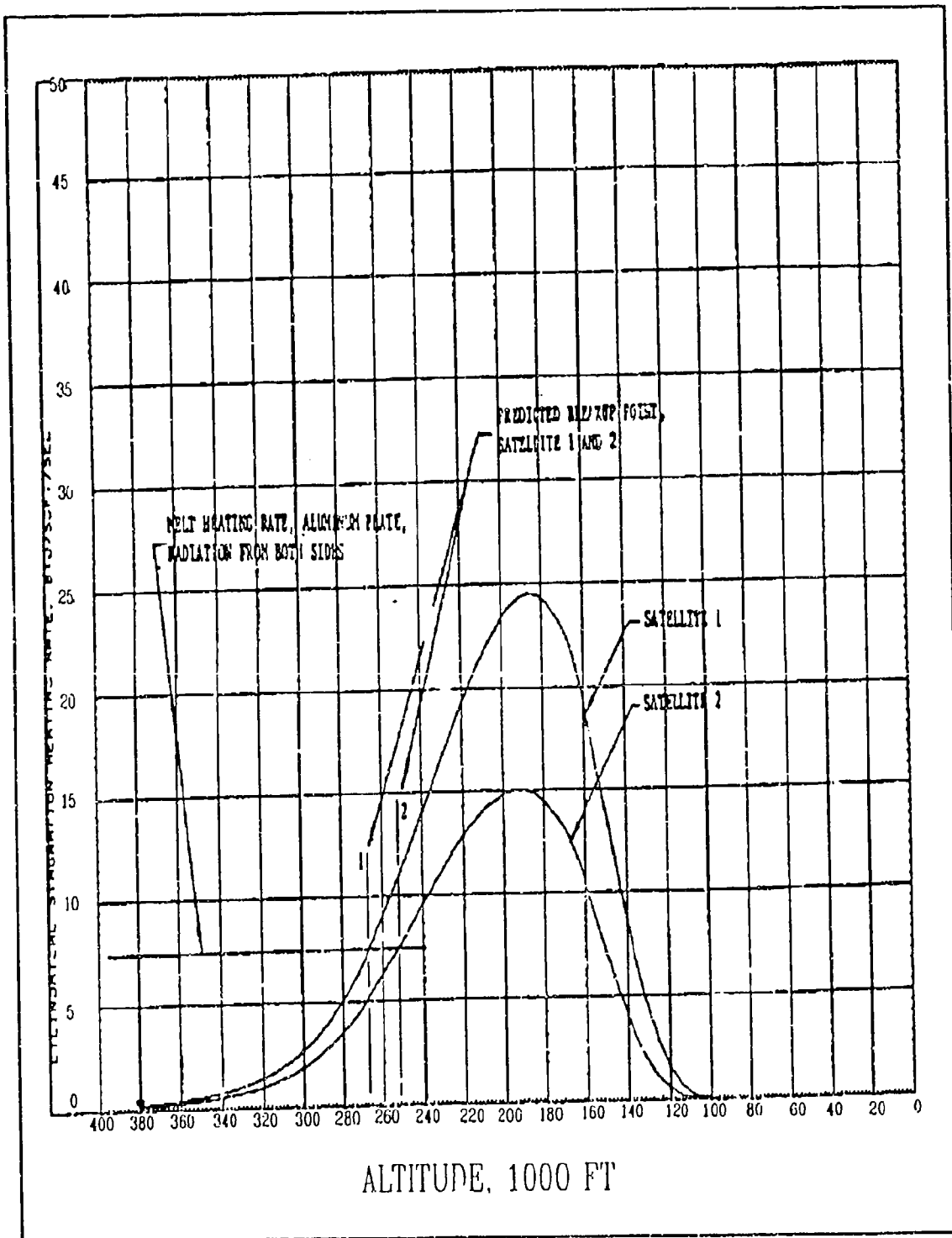


Figure 43: Breakup Altitudes For Corrected Heating Rates [Ref. 64]

Table XII: RESULTS OF BREAKUP ANALYSIS
 [Ref. 64]

Configuration	Critical Element	Candidate Construction Material(s)	$q_{req'd}$ (BTU/ft ² -s)	q_{max} (BTU/ft ² -s)	Breakup Altitude (nmi)
Spacecraft	Boom	(1) Fiberglass Epoxy	1	12 - 18	55
		(2) Metal Matrix	8	12 - 18	43
Reactor/Heat Radiator	Heat radiator	(1) Mo	688	69	-
		(2) Ti	142	69	-
		(3) Be	58	69	28
		(4) C	-	69	-
Reactor/Radiation Shield	Radiation Shield	Fe	54	80 - 104	31-32
Pressure Vessel	Wall	(1) Nb	282	165 - 255	-
		(2) Astar	-	-	-
Fuel Pin #1	Wall	Nb	282	115 - 1410	a
Fuel Pin #2	Wall	Nb	282	247 - 1185	b

a Breakup anticipated for tumbling mode, some pins may survive.

b Breakup anticipated in tumbling mode.

Another series of investigations of the breakup process are references [10] and [63]. In these studies, the reentry/breakup of Skylab was reconstructed by piecing together all available data - after the fact. Both of these reports show conclusively, through telemetry analysis, that the survivability of Skylab was underestimated. Reference [10] cites initial breakup predictions of 120 km and shows that breakup did not occur until at least 100 km. References [63] and [10] disagree on exactly where the OWS SAS (Orbital Workshop Solar Array System) separated from the main body, based on telemetry received at Ascension Island. Reference [10] states that the array was intact over Ascension Island; however, it was not generating its predicted output. Therefore, it was concluded that the array was either bent back or physically damaged.

Reference [63] concludes that the OWS SAS was completely separated from the main body prior to telemetry acquisition at Ascension Island [Ref. 63:p. 344]. Finally, reference [63] postulates a probable breakup scenario as follows: [Ref. 63:p. 344]

1. OWS SAS array (aerodynamically) off at 62 nm / 117 km.
2. ATM separates from remaining OWS at 54 nm / 102 km.
3. ATM SAS arrays separate between 50 and 54 nm / 94.5 and 102 km.
4. ATM and OWS breakup at 42 nm / 77.8 km.

Reference [10] concludes that breakup did not start until some altitude below 100 km.

IV. DETERMINISTIC REENTRY/IMPACT PREDICTION METHODS

A. CURRENT REENTRY/IMPACT PREDICTION METHOD

The following section of this chapter describes the various techniques or methods used by different countries or organizations dealing with reentry and impact prediction of naturally decaying objects. It is therefore useful to the reader to understand the current U.S. method used in reentry/impact prediction, since it is the standard by which all other methods (as determined by this literature survey) are compared.

As stated in previous chapters, the current method for predicting reentry time and impact location is that of the Space Surveillance Center (SSC) located at Cheyenne Mountain Air Force Base, or commonly referred to in the literature as NORAD. [Ref. 87] NORAD produces "element sets" which are mean values of the orbital elements that have been obtained by removing the periodic orbital variations in a particular manner. In order to use these element sets, and obtain reasonable predictions, these periodic variations must be "reconstructed" by the prediction model in precisely the same manner as they were removed by NORAD. Therefore, an input of NORAD element sets into another model (even though it may be more accurate, or even into a numerical integrator) will result in degraded predictions unless, as previously stated, the new model can "reconstruct" the periodic variations. [Ref. 87:p. 1]

NORAD element sets are generated with a general perturbations (GP) model called SGP4. SGP4 was developed by Ken Cranford in 1970. This model was a result of

simplification of the more extensive analytical theory of Lane and Cranford (1969) which uses the solution of Brouwer (1959) for its gravitational model and a power density function for its atmosphere model. [Ref. 87:p. 3] It should be emphasized that this atmosphere "model" is a static representation of density as opposed to the dynamical models discussed in Chapter II, such as those of Jacchia and others.

The gravitational model includes J_2 and J_3 harmonics; however, J_4 and J_5 were dropped in order to avoid singularities occurring at critical inclination [Ref. 88:p. 2]. Rates of change of mean motion and eccentricity are derived from the density function. The product of ballistic coefficient and a reference density, denoted B^* , is treated as a solved for parameter. Coupling between J_2 and drag is included in the argument of perigee, right ascension of the node and mean anomaly. The mean motion of SGP4 is a pure Brouwer, or two-body, mean motion. [Ref. 88:p. 3]

Reentry and impact predictions, in the U.S., are made using a special perturbations (SP) propagator with conversions between GP and SP theories handled as outlined in references [87, 89-90]. The GP theory is fast, analytical and of low-accuracy, when compared to the SP theory. SP theory uses a Gauss-Jackson, eighth-order, numerical integrator, incorporates a 6-12th order geopotential model and applies a dynamical atmospheric density model (Jacchia-65). The "conversion" between GP and SP theories is the process of performing an SP differential correction of the initial state vector as derived from the GP theory (NORAD two-line element set). These are the initial standards for GP and SP theory compatibility which must be considered in the following discussion of different reentry/impact prediction methods. [Ref. 91:p. 8]

The first TIP (Tracking and Impact Prediction) run is performed approximately 15-20 days prior to the estimated reentry date, which is initially predicted by the GP model. This is also when tasking of the observation sites is initially increased in order to support high accuracy SP processing. [Ref. 92:p. 1]

Orbit determination is accomplished through a first-order, linear, weighted, least square, curve fitting process, commonly called differential correction. Sliding fits are used to process both new and old metric data until the satellite is "no longer in orbit." The force models used are the Jacchia dynamic atmosphere (1965) and the World Geodetic System Earth gravity model (1972). The Earth gravity model is truncated to the sixth order for satellite decay predictions. [Ref. 92:p. 2]

Direct step-by-step numerical integration of the total acceleration acting on the decaying satellite is accomplished in the manner of Cowell's method. Gauss-Jackson eighth order predictor-corrector formulas, in ordinate form, are used to integrate the equations of motion. Because of computer run-time constraints, the partial derivatives necessary for differential correction are computed analytically except for the secular variations due to atmospheric drag of the orbit semi-major axis and eccentricity. These parameters are integrated numerically using a low-order (trapezoidal rule) integrator. [Ref. 92:p. 2]

Currently, the differential correction solution state consists of the equinoctial elements and satellite ballistic coefficient model parameter, B_0 . After each solution, the new state is used to predict a decay time (when altitude equals 10 km). [Ref. 92:p. 2]

B. ALTERNATE REENTRY/IMPACT PREDICTION METHODS

1. Reentry Prediction Methods At ESOC

One method used at the European Space Operations Center (ESOC) for the prediction of reentry and impact of decaying satellites is an improved and computerized version of the King-Hele technique, reference [55]. [Ref. 93] Another method used at ESOC is based in a computer program called FOCUS [Ref. 94].

The principal characteristic of FOCUS is its ability to overcome the deficiencies of the semi-analytical orbit prediction techniques at low altitudes [Ref. 94:p. 26]. Recall that in near-Earth orbits, 200-700 km, Earth oblateness (J_2) is regarded as the only first-order perturbation. Higher zonal harmonics and air drag are regarded as second-order contributions. All other effects are considered as less than second-order perturbations (less than J_2^2 in magnitude). [Ref. 94:p. 25] Eventually, the satellite passes through an altitude regime where the air drag force (caused by increasing atmospheric density) reaches a magnitude of the same order as the J_2 Earth oblateness effect. At this altitude, \approx 150 km, depending on the vehicle's ballistic coefficient, the accuracy of analytically derived drag perturbation results strongly deteriorates. [Ref. 94:p. 26]

FOCUS stops the state propagation after passing through a user-defined altitude shell ($h \approx$ 170 km specifically for the case of Salyut-7/Cosmos-1686, which is

the focus of reference [94]) and forwards a calculated osculating Keplerian state vector at epoch, together with all relevant perturbation parameters. This new set of data is then numerically integrated and the reentry trajectory is propagated until shortly before impact with the Earth. [Ref. 94:p. 26]

Several key features of the FOCUS program are: [Ref. 94:p. 26]

1. Perturbation equations:
 - (a) Cowell's formulation of the perturbed Newtonian equations written in terms of six first-order, differential equations for each component of the Cartesian state vector
 - (b) Reference frame is the mean equatorial system of date
2. Perturbation models:
 - (a) Geopotential model GEM 10B (J_2 - J_7 used)
 - (b) Atmospheric density models: MSIS-86 for altitudes ≥ 120 km, U.S. Standard Atmosphere (USSA-76) for altitudes ≤ 90 km, and a bridging function for altitudes between 90 and 120 km.
 - (c) Variable drag coefficient, $C_D = f(\text{Ma}, \text{Re}, \text{Kn})$
 - (d) Co-rotating Earth atmosphere
 - (f) Luni-solar third body attraction (point mass)
 - (g) Solar radiation pressure
3. Integrator:
 - (a) Runge-Kutta/Shanks 7/8 single step method for generation of a starting arc
 - (b) Adams-Bashforth/Adams-Moulton(AB/AM)forth-orderpredictor-corrector, multi-step method for propagation of the Cartesian state vector.

- (c) Non-regularized time (t) used as an integration variable, with constant step sizes of $\Delta t = 30$ sec.

A significant limiting feature of this program is that the reentry trajectory is terminated at 30 km altitude because the governing laws of perturbed Keplerian motion become invalid below this threshold altitude. This criterion is marked by a decrease in the orbital energy to a level, where the aerodynamic forces are essentially in balance with the zero-th order central gravitational attraction term. [Ref. 94:p. 26]

The reentry vehicle is, however, considered to be in nearly vertical fall from an altitude of 30 km and below. Thus, there is only a minor dispersion of the impact point during the final seconds of flight. This rationale leads to the conclusion that it is not necessary to perform another transition from strongly perturbed Keplerian motion to an aerodynamic flight phase for the integration to Earth impact. Thus the Center Of Impact Window (COIW) is defined as the location at which the vehicle passes through the 30 km altitude. [Ref. 94:p. 26]

The aerodynamic transition regime is defined as a computed, weighted mean of ρ_{MSIS} and ρ_{USSA} where

$$\rho_{MSIS} = f(h, \phi, \lambda, UT, \tau, t_{\sigma}, \bar{F}_{10.7}, F_{10.7}, A_p) \quad (153)$$

$$\rho_{USSA} = f(h) \quad (154)$$

which results in

$$\bar{\rho} = w_{MSIS} \rho_{MSIS} + (1 - w_{MSIS}) \rho_{USSA} \quad (155)$$

where the weighting factor

$$w_{MSIS}(h) \in [0,1] \quad (156)$$

is defined for the altitude region $h_{120} \geq h \geq h_{90}$ as

$$w_{MSIS}(h) = \frac{1}{2} \cos\left(\pi \frac{h_{120} - h}{h_{120} - h_{90}}\right) + \frac{1}{2} \quad (157)$$

where

h = geodetic altitude

Φ = geodetic latitude

λ = geographic longitude

τ = local solar time

UT = universal time

t_d = day of the year

When the altitude is high enough to maintain

$$Kn_{\omega} = \frac{\lambda_{\omega}}{d_{vc}} > 1 \quad (158)$$

where

d_{vc} = characteristic length of vehicle

then C_D is equal to a constant given by C_0^{Kn} , provided $Kn_\infty > 1$. As the altitude decreases, a transition to hypersonic continuum flow is entered, where $Kn_\infty = f(h)$ and [Ref. 94:p. 27]

$$C_D = C_1^{Kn} + C_2^{Kn} \log_e (C_3^{Kn} Kn_\infty) \quad (159)$$

provided that $0.02 \leq Kn_\infty \leq 1$. During the hypersonic continuum phase another constant C_D level is attained (about 50% less than the free molecular flow value), which is given by

$$C_D = \text{constant} = C_0^{Ma} \quad (160)$$

provided

$$Kn_\infty \leq 0.02$$

$$Ma_\infty \geq 5$$

The next phase of supersonic and transonic continuum flow can be approximated by an altitude dependent Mach number, $Ma = f(h)$, where

$$C_D = C_1^{Ma} + C_2^{Ma} (Ma_\infty - 0.4) + C_3^{Ma} \times \exp[-C_4^{Ma} (Ma_\infty - 0.4)] \quad (161)$$

provided

$$Kn_\infty \geq 0.02$$

$$0.8 \leq Ma_\infty \leq 5$$

Finally, in the subsonic phase, the drag coefficient is dependent upon viscous interactions and therefore Reynolds number, $Re = f(h)$, given by

$$C_D = C_1^{Re} (Re_\infty) ** C_2^{Re} \quad (162)$$

provided

$$Kn_\infty \leq 0.02$$

$$Ma_\infty \leq 0.8$$

These dependencies, $C_D = f(Kn, Re, Ma)$, with the underlying altitude functions $Kn(h)$, $Ma(h)$ and $Re(h)$ are from the U.S. Standard Atmosphere (USSA) and are incorporated into the numerical reentry prediction software. These model constants are limited, however, to spherical and cylindrical shapes, with their longitudinal axis perpendicular to the airflow. [Ref. 94:p. 27]

Since $Ma = V_{atm} / V_{sound}$ and $Re = V_{atm} d/v$ are functions of geodetic latitude related by $V_{sound}(h)$, kinematic viscosity, $v(h)$, and aerodynamic velocity, V_{atm} , the free fall of the reentering vehicle in the lower atmosphere may be determined by iteratively solving the following equation for the equilibrium descent velocity, V_{atm}

$$V_{atm}^2 \approx h^2 = 2 \frac{m}{A} \frac{g(h)}{\rho(h) c_D(h, V_{atm})} \quad (163)$$

where

$g(h)$ = central gravitational acceleration of the Earth

$\rho(h)$ = local air density

Using this technique, in the post-flight analysis of Salyut-7/Cosmos-1686, the following values are determined:

$$m/\bar{A} = 159.5 \text{ kg/m}^2$$

therefore V_{atm} at

$$h = 30 \text{ km, is equal to } 330 \text{ m/s}$$

$$h = 20 \text{ km, is equal to } 100 \text{ m/s}$$

$$h = 10 \text{ km, is equal to } 70 \text{ m/s}$$

Figure 44 shows the ESOC reconstruction of the Salyut-7/Cosmos-1686 final descent altitude profile. The actual reentry occurred at 0345 UCT on 7 Feb. 1991 over (39.3°S, 69.7°W) [Ref. 94:p. 29]. Table 13 shows a comparison of reentry predictions from the U.S. and various European and former Soviet sites [Ref. 94:p. 32].

The conclusions of this European Space Agency (ESA)/ESOC report indicate that there was good correlation between ESA, U.S. and former Soviet predictions. There was some difficulty in interpreting the Soviet orbit determination results at approximately 12 hours prior to reentry. Also at this time, the U.S. element sets became "time late," due to transmission delay times from the U.S. to ESOC. Therefore, the ESA/ESOC predictions could not be maintained in "real time" after this point. [Ref. 94:p. 33]

2. The LIFETIME Model

The Aerospace Corporation previously developed the LIFETIME program and it was further refined through the work of reference [95]. This program is similar in some respects to the previously discussed ESA program, FOCUS. This program offers a "fast, efficient computer tool for orbital lifetime estimation" [Ref. 95:p. 17]. An advertised major benefit of the LIFETIME program is its usefulness as a "highly accurate, real-time reentry prediction tool." [Ref. 95:p. 20] This may also have

Table XIII: SALYUT-7/COSMOS-1686 FINAL DECAY PREDICTIONS
 [Ref. 94]

Prediction Source	Re-Entry Predictions (times in UTC)	
	Received at ESOC	Re-Entry Pred. (COIW)
NASA GSFC	01-Feb 14:58	06-Feb 21:33
ESOC MAS	02-Feb 04:27	06-Feb 22:30
CNES CST	03-Feb 11:33	06-Feb 04:00
ESOC MAS	04-Feb 10:30	07-Feb 01:37
NASA GSFC	04-Feb 16:04	07-Feb 03:38
CNUCE CNR	04-Feb 19:43	07-Feb 03:17
CNES CST	05-Feb 04:27	06-Feb 18:23
ESOC MAS	05-Feb 10:00	07-Feb 02:23
NASA GSFC	05-Feb 15:05	07-Feb 03:05
ESOC MAS	06-Feb 11:33	07-Feb 03:50
RAE	06-Feb 11:38	07-Feb 04:30
CNUCE CNR	06-Feb 12:50	06-Feb 22:26
NASA GSFC	06-Feb 14:09	07-Feb 03:28
CNUCE CNR	06-Feb 15:51	07-Feb 01:24
NASA GSFC	06-Feb 16:58	07-Feb 04:14
CNES CST	06-Feb 17:00	07-Feb 05:00
ESOC MAS	06-Feb 19:47	06-Feb 04:19
CNUCE CNR	06-Feb 22:05	07-Feb 04:43
CNES CST	06-Feb 22:15	07-Feb 04:38
IKI IAM	06-Feb 23:37	07-Feb 04:40
NASA GSFC	06-Feb 23:44	07-Feb 04:05
ESOC MAS	07-Feb 01:00	07-Feb 04:50
IKI IAM	07-Feb 01:02	07-Feb 04:38
IKI MCC	07-Feb 01:02	07-Feb 04:20
CNUCE CNR	07-Feb 01:07	07-Feb 04:00
IKI MoD	07-Feb 01:57	07-Feb 04:00
IKI MCC	07-Feb 02:22	07-Feb 03:57
IKI IAM	07-Feb 04:00	07-Feb 03:37
ESOC MAS	07-Feb 04:20	07-Feb 04:29
IKI MoD *	07-Feb 04:34	07-Feb 03:47
ESOC MAS *	07-Feb 13:00	07-Feb 03:45

application as a first time modeling tool as compared to methods capable only of post flight analysis of reentry events.

The LIFETIME program uses either the Jacchia-Walker (64) or Jacchia (71) atmospheric density models for altitudes above 90 km and uses the U.S. Standard Atmosphere (1962) for altitudes below 90 km. The latest version (4.0), the subject of reference [93], also allows differential corrections of the ballistic coefficient and movement of solar panels to simulate sun tracking. [Ref. 95:pp. 18-19] Version 4.0 was designed to solve a major deficiency of version 3.0, in that, there was a built-in uncertainty in Earth impact time prediction of at least one orbital revolution. This was inherent due to the minimum step size of one revolution, which was a function of using the averaged equations of motion. [Ref. 95:p. 22]

A "unique" feature of the LIFETIME program is the differential correction of the ballistic coefficient. By using the least squares method, the following equation for differentially correcting the inverse ballistic coefficient (B^*) can be formulated [Ref. 95:pp. 28-29]

$$\Delta B^* = \frac{\sum_i^N \left(\Delta \tilde{a}_i \frac{\partial \tilde{a}_i}{\partial B^*} + \Delta e_i \frac{\partial e_i}{\partial B^*} \right)}{\left[\sum_i \left(\frac{\partial \tilde{a}_i}{\partial B^*} \right)^2 + \sum_i \left(\frac{\partial e_i}{\partial B^*} \right)^2 \right]} \quad (164)$$

where

N = number of observations

\tilde{a} = a_i/a_c

- a_i = observed semi-major axis at time i
- a_0 = semi-major axis at epoch
- e_i = observed eccentricity at time i

It can be shown that orbit decay in semi-major axis and eccentricity is directly proportional to the product of inverse ballistic coefficient and density ($B^*\rho$). This differential correction process (which absorbs the atmospheric density uncertainties) results in a "converged ballistic coefficient" through multiple iterations of equation 175. This is how LIFETIME becomes more accurate than the atmosphere model it uses. [Ref. 95:p. 29]

LIFETIME integrates the averaged equations of motion using a step size of multiples of the orbital period, until the satellite reaches a specified or default altitude. Based on [86], the default altitude chosen is 42 nm (78 km) and this is where "breakup" is said to occur. LIFETIME then backs up to the last propagation step, resets the orbital elements and time to the previous step's values. Next, the Runge-Kutta 7(8) integration routine is invoked and the satellite's orbit is propagated through breakup to impact. (The elements are converted from classical mean to classical osculating elements and finally to Cartesian elements during the numerical integration process.) [Ref. 95:pp. 32-60] Numerical integration is the preferred method for dealing with the final stages of reentry to impact since it is the "most efficient and accurate way to handle regions where a high rate of change in the equations of motion" are prevalent [Ref. 95:p. 55].

Several significant user input altitude values are: [Ref. 95:p. 59]

1. RKALT - lower limit at which LIFETIME converts to Cartesian numerical integration. Default = 0.000 km, most effective if > BRKALT.
2. BRKALT - vehicle breakup altitude. Default = 77.784 km.
3. ENDALT - perigee altitude lower limit, ends integration and propagation. Default = 10.000 km, this should be set to 0.000 km to model impact.

At the point where the satellite reaches the BRKALT, the lat/long projection of the satellite is recorded. This point is defined as the "debris heel point," or the first point along the groundtrack where debris could potentially impact. Propagation continues until ENDALT, where the lat/long is identified as the center of mass impact point. LIFETIME then resets the Cartesian elements to those at the BRKALT point, however, B is changed to 60 lb/ft^2 and the propagation to ENDALT is continued. This allows the computation of a "debris toe point," or the point of farthest travel of any breakup debris. The value of 60 lb/ft^2 for the ballistic coefficient is based on reference [86]. [Ref. 95:pp. 59-60] Figure 45 shows the debris dispersion footprint as described above [Ref. 95:p. 60]. Figure 46 shows the LIFETIME groundtrack and impact area plot as well as a sample altitude decay history [Ref. 95:p. 63]. (An item of interest not addressed by the author of reference [95] is the fact that the center of mass, in this sample plot, impacts after the "final debris impact.")

The results of impact prediction accuracy comparisons between LIFETIME 3.0 and 4.0 do not definitively show 4.0 as a significant improvement over 3.0. However, some notable improvement in accuracy for version 4.0 can be shown and

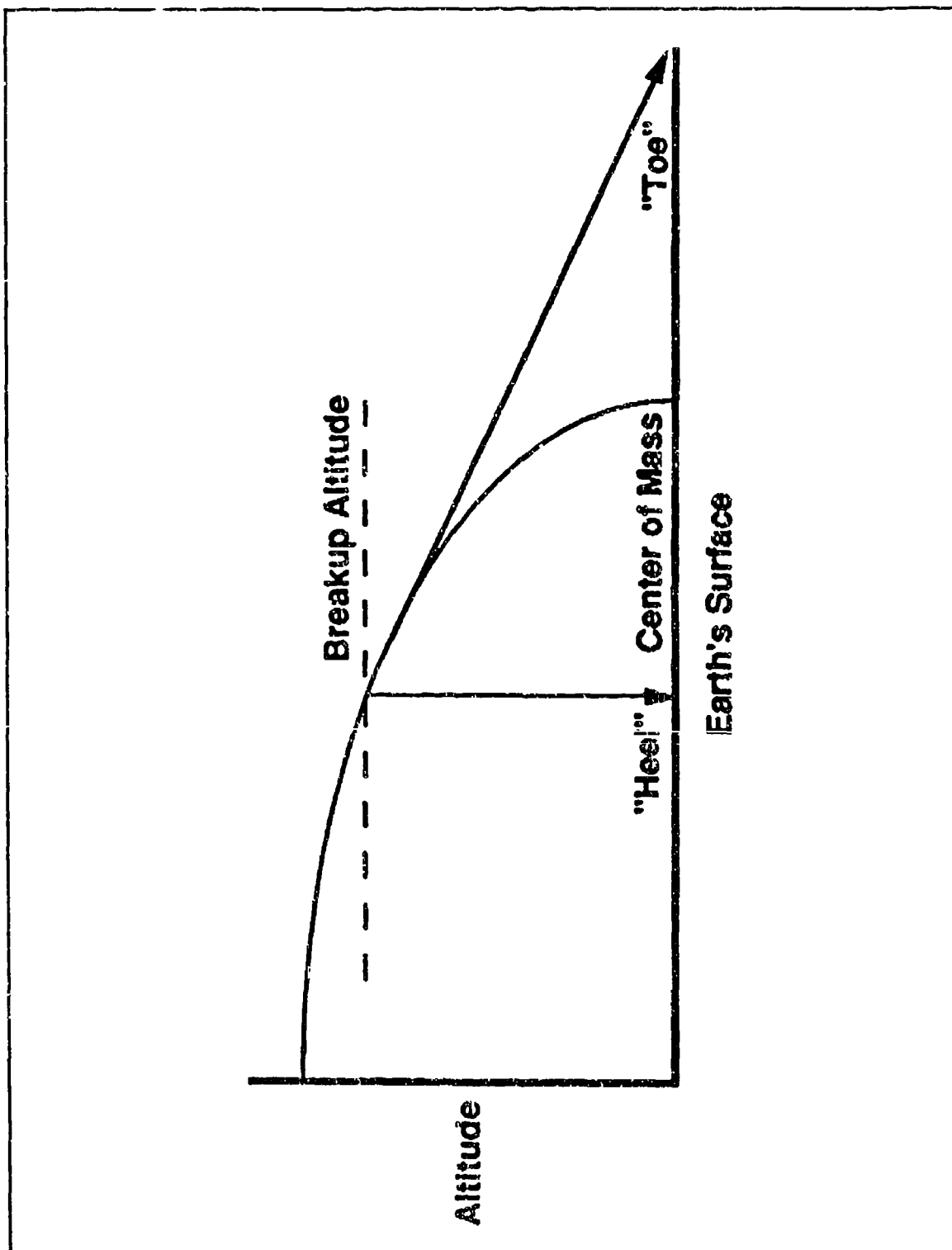


Figure 45: LIFETIME Debris Dispersion Footprint
 [Ref. 55]

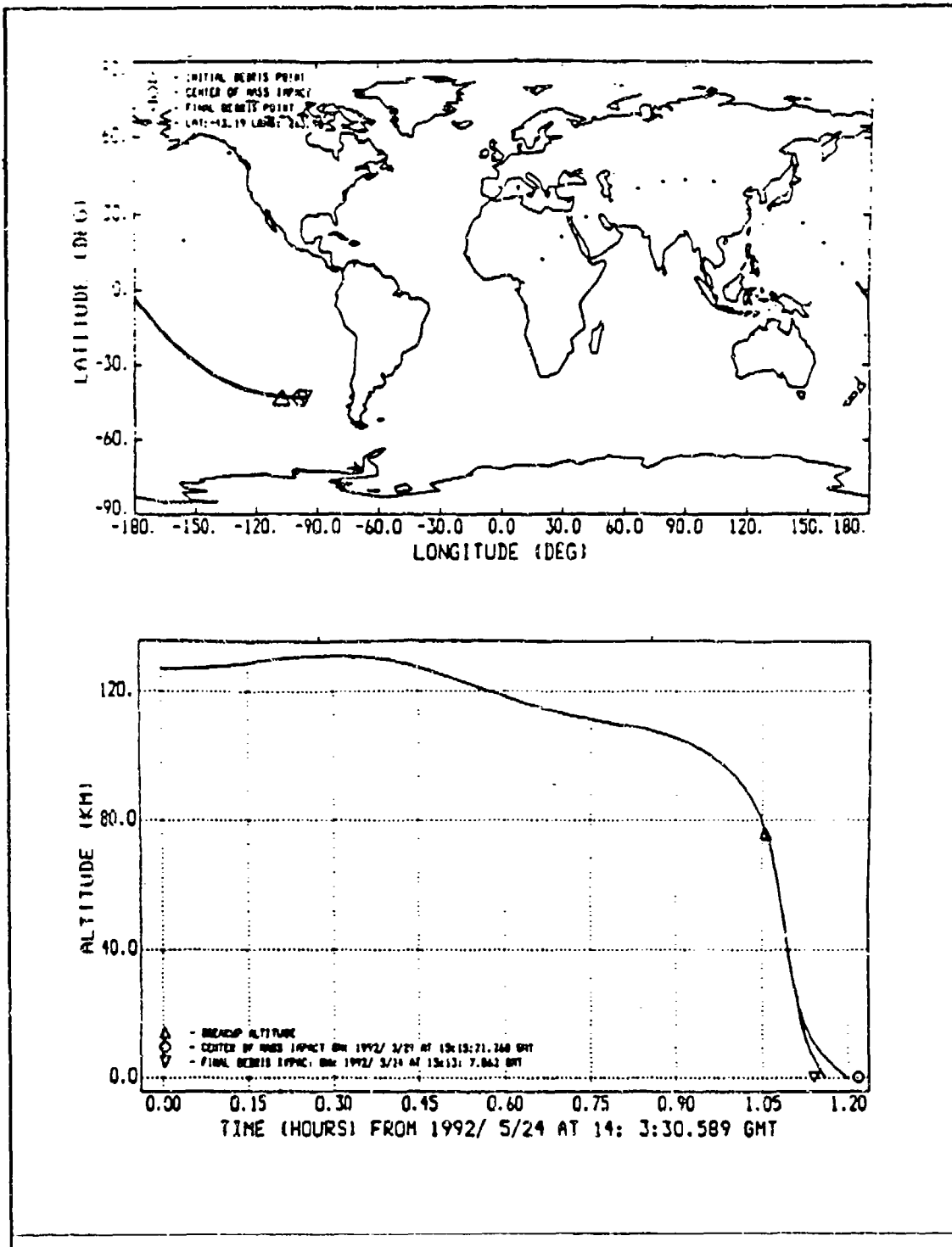


Figure 46: LIFETIME Groundtrack And Altitude Decay History
 [Ref. 95]

greater confidence is held in version 4.0's period calculations and final impact predictions. [Ref. 95:pp. 65-70]

A sensitivity study and analysis was performed in order to determine the:

1. Effects of NORAD data span on program accuracy
2. Effects of prediction span on program accuracy
3. Effects of solar conditions during differential corrections
4. Effects of solar flux on overall program sensitivity

The results of the sensitivity study and analysis are as follows: [Ref. 95:pp. 89-94]

1. NORAD data span:
 - (a) Period calculation accuracy - no strong trend for sensitivity noted
 - (b) Impact prediction accuracy - general trend for less averaged impact time error for greater time spans
2. Prediction span - impact time errors show a strong trend for increased accuracy with shorter prediction spans.
3. Solar flux - the results indicated a complex relationship between the estimated solar flux for the prediction period, the actual values of solar flux, the prediction span, and the resulting impact errors.

A general observation and conclusion is that fairly steady solar activity at modest levels provide for the most accurate impact prediction, especially when using the solar flux value of the last day on NORAD data as a constant during the prediction span. During periods of highly variable solar flux, the last day's value of NORAD data may

not give the least error, however, this conservative assumption will not result in the maximum error either. [Ref. 95:p. 92]

An appropriate concluding remark of reference [95] is that It seems there are still dynamic aspects of the final orbit decay and reentry process that warrant further study. [Ref. 95:p. 93]

3. Modeling Ballistic Coefficient

Analysis of historical data shows that in the final days prior to decay, the ballistic coefficient, B , ($C_D A/m$) exhibits a pronounced variation with time. This variation is due to one or more of several causes: [Ref. 92:p. 2]

1. Tumbling or weather vaning of the satellite
2. Loss of mass
3. Variation of the drag coefficient

Presently, none of these effects are modeled explicitly since this requires precise knowledge of the multiple variables described in Chapters II and III, such as vehicle mass, attitude and shape. Additionally, any unmodeled forces acting in the in-track direction, such as those inaccuracies in the atmospheric density model, can manifest themselves in the solution ballistic coefficient. [Ref. 92:p. 2]

Despite the lack of specific knowledge of unknown forces acting on a decaying satellite, an improvement in reentry prediction accuracy can be made by introducing a new model parameter. This parameter takes into account the fact that for many decaying satellites, the variation in B appears to be linear during the last several

days prior to reentry. This new parameter is $B_0\text{-dot}$, the time derivative of the ballistic coefficient, which is parameterized as

$$B = B_0 + \dot{B}_0(t - t_0) \quad (165)$$

where subscript 0 indicates the quantities at the solution state epoch, t_0 . [Ref. 92:p. 3]

The introduction of $B_0\text{-dot}$ requires that new semi-analytic partial derivatives for B_0 and $B_0\text{-dot}$ be calculated. These must be determined over a finite time interval using a differential correction fitting process. Several such differential corrections must be made over the course of the final days of orbit decay and reentry, with a new B_0 and $B_0\text{-dot}$ being determined for each differential correction. It is necessary to start the fitting process with close approximations of B_0 and $B_0\text{-dot}$ for the first differential correction. These initial "guesses" come from analysis of historical data. [Ref. 92:p. 3]

Reference [92] studied 264 reentry events over the time span from Jan. 1977 to Mar. 1979. All of these objects were processed as TIP reentries and historical records from the SSC were used in this investigation. In order to optimize the data, the records of 156 reentries were chosen, since these represented rocket bodies and payloads from the former USSR, which presumably would have well-known physical attributes. Table 14 shows the data distribution used throughout this investigation. [Ref. 92:pp. 3-4]

The development of the solutions for the partial derivatives of B_0 are not shown here for the sake of brevity, however, the results are as follows [Ref. 92:pp. 10-11]

Table XIV: DISTRIBUTION OF DECAYED ORBITAL OBJECTS
 [Ref. 92]

DISTRIBUTION OF 264 TIP LOG DECAYED ORBITAL OBJECTS

YEAR:	1970											
MONTH:	J	F	M	A	M	J	J	A	S	O	N	D
NUMBER:	2											

YEAR:	1977											
MONTH:	J	F	M	A	M	J	J	A	S	O	N	D
NUMBER:	8	8	11	6	15	8	8	11	14	9	8	7

YEAR:	1978											
MONTH:	J	F	M	A	M	J	J	A	S	O	N	D
NUMBER:	11	9	9	13	6	12	7	8	11	13	8	18

YEAR:	1979											
MONTH:	J	F	M	A	M	J	J	A	S	O	N	D
NUMBER:	6	10	7									

YEAR:	1983											
MONTH:	J	F	M	A	M	J	J	A	S	O	N	D
NUMBER:	1											

* Selected 156 Soviet orbitally decayed object distribution.^{6,7,8}

ROCKET BODIES			DIA(m)	LNG (m)	
21	A2	VOSTOK	(440 kg)	2.6	7.5
89	A2	VOSTOK	(2500 kg)	2.0	2.0
4	B1	COSMOS	(1500 kg)	1.65	8.0
8	C1	SKEAN	(2000 kg)	2.0	6.0
3	D1	PROTON	(1900 kg)	3.9	4.0
3	D1	PROTON	(4000 kg)	4.0	12.0
3	F1M	SCARP	(700 kg)	2.0	5.0
1	F1M	SCARP	(1500 kg)	2.5	6.0
PAYLOADS [§]					
3	NAVSAT		(875 kg)	?	?
1			(325 kg)		
1			(3640 kg)		
1			(680 kg)		
8	MILSAT		(400 kg)		
2	MIL/SCI		(550 kg)		
4	RORSAT ^x		(4500 kg)		
2	MIL		(900 kg)		
1			(1120 kg)		
1			(3800 kg)		

§ The exact size and shape of the payloads are unknown at this point.

$$B_0 \frac{\partial a_f}{\partial B_0} = B_0 a_{f0} \int_{t_0}^t \frac{1}{B} \dot{e} dt \quad (166)$$

$$B_0 \frac{\partial a_g}{\partial B_0} = B_0 a_{g0} \int_{t_0}^t \frac{1}{B} \dot{e} dt \quad (167)$$

$$B_0 \frac{\partial n}{\partial B_0} = -\frac{3}{2} B_0 \frac{n_0}{a_0} \int_{t_0}^t \frac{1}{B} \dot{a} dt \quad (168)$$

$$B_0 \frac{\partial L}{\partial B_0} = -\frac{3}{4} B_0 \frac{n_0}{a_0} (t-t_0) \int_{t_0}^t \frac{1}{B} \dot{a} dt \quad (169)$$

$$B_0 \frac{\partial X}{\partial B_0} = B_0 \frac{\partial \Psi}{\partial B_0} = 0 \quad (170)$$

where

$$a_f = e \cos (\Omega + \omega)$$

$$a_g = e \sin (\Omega + \omega)$$

\dot{e} = time rate of change of eccentricity due to drag perturbations

\dot{a} = time rate of change of semi-major axis due to drag perturbations

L = mean longitude

$$X = \tan (i/2) \sin \Omega$$

$$\Psi = \tan (i/2) \cos \Omega$$

Similarly, the partial derivatives of \dot{B}_0 are given [Ref. 92:p. 12]

$$\dot{B}_0 \frac{\partial a_f}{\partial \dot{B}_0} = \dot{B}_0 a_{f0} \int_{t_0}^t \left[(t-t_0) \frac{1}{B} \frac{\dot{e}}{e} \right] dt \quad (171)$$

$$\dot{B}_0 \frac{\partial a_g}{\partial \dot{B}_0} = \dot{B}_0 a_{g0} \int_{t_0}^t \left[(t-t_0) \frac{1}{B} \frac{\dot{e}}{e} \right] dt \quad (172)$$

$$\dot{B}_0 \frac{\partial n}{\partial \dot{B}_0} = -\frac{3}{2} \dot{B}_0 a_{g0} \int_{t_0}^t \left[(t-t_0) \frac{1}{B} \dot{a} \right] dt \quad (173)$$

$$\dot{B}_0 \frac{\partial L}{\partial \dot{B}_0} = -\frac{3}{4} \dot{B}_0 \frac{n_0}{a_0} (t-t_0) \int_{t_0}^t \left[(t-t_0) \frac{1}{B} \dot{a} \right] dt \quad (174)$$

$$\dot{B}_0 \frac{\partial \chi}{\partial \dot{B}_0} = \dot{B}_0 \frac{\partial \Psi}{\partial \dot{B}_0} = 0 \quad (175)$$

Of the 156 cases studied in the development of the new parameter and its associated partial derivatives, two case studies were chosen for the application of the new method. These cases were Cosmos-954 and Cosmos-1402, both of them being significant due to their potentially survivable nuclear reactors. [Ref. 92:p. 13]

The conclusion of this paper is that the new method is more accurate than the conventional method as evidenced by the comparison of the best fit differential correction root mean square (RMS) of residuals for each of the 25 sliding-fit runs over the last nine days of orbit for Cosmos-954. The same comparison is made for Cosmos-1402 with the

only exception that 26 vice 25 SP differential corrections were run. The results of these comparisons are shown in Figure 47 [Ref. 92:pp. 15, 17].

As stated previously, the historical data analysis of most satellites showed the linear trend in B only over the last 3-5 days prior to reentry. However, one of the two specific cases chosen for application of the new method, Cosmos-954, did not exhibit this trend until the final day prior to reentry. Table 15 shows a comparison of decay time error root mean square over the last five days of orbit (for these two case studies) as well as a similar comparison after the linear trend in B becomes apparent in both reentries. [Ref. 92:p. 18]

Another method using a correction of the ballistic coefficient comes from reference [47]. This investigation states that during the joint international effort to predict the reentry/impact of Salyut-7/Cosmos-1686, it was observed that the "most exact data" had consistently been presented by the Space Control System (SCS) of the former USSR. This was explained by the fact that:

...great attention has been given to the problem of determination and the prediction of the satellite motion in the atmosphere: for the solution of this problem they have been conducting the cycle of theoretical and experimental studies during [the last] 20 years. [Ref. 47:p. 35]

The model used by the SCS to describe satellite motion will, to a great extent, determine the "completeness" and precision of the time and area of low-orbit satellite reentry predictions. Gravitational field models in spherical functions of 36 or higher orders are not necessary, they only serve to increase the computation time. At

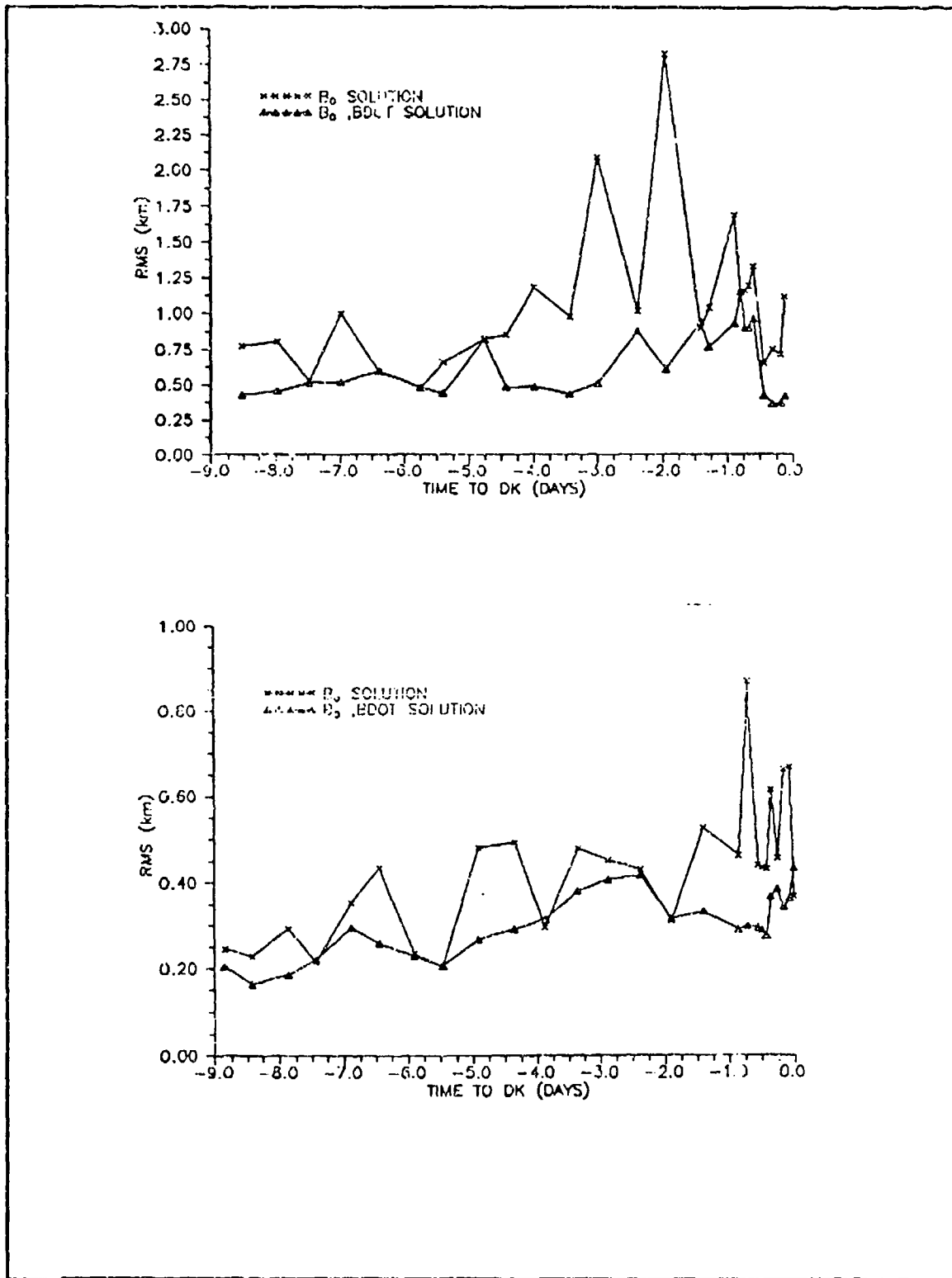


Figure 47: Best Fit DC RMS For Cosmos-954/1402
 [Ref. 92]

Table XV: DECAY TIME ERROR RMS
[Ref. 92]

DECAY TIME ERROR ROOT MEAN SQUARE (RMS) OVER LAST 5 DAYS

Satellite	Decay Error RMS(hrs)		
	B_0 Solution	B_0, \dot{B}_0 Solution, $\dot{B}_0=0.0$ for Prediction	Improvement(%)
COSMOS 954	3.51	4.11	-17.09
COSMOS 1402	1.59	1.43	10.06

DECAY TIME ERROR ROOT MEAN SQUARE (RMS) AFTER B BECOMES LINEAR

Satellite	Decay Error RMS(hrs)		
	B_0 Solution	B_0, \dot{B}_0 Solution, $\dot{B}_0=0.0$ for Prediction	Improvement(%)
COSMOS 954	1.22	0.48	60.66
COSMOS 1402	1.51	0.98	35.10

low altitudes, two to three days prior to reentry, a simple geopotential model is suitable, since it is the atmospheric resistance force which is increasing by several orders of magnitude, not gravitational forces. [Ref. 47:p. 36]

Prediction of low-orbit satellite motion is accomplished by numerical and semi-analytical integration methods. The semi-analytical methods are based on the asymptotic solutions given by Krilov-Bogoljubov, Zeipel-Brouwer averaging methods. [References given are written in Russian and the authors were unable to obtain English translations.] [Ref. 47:p. 36]

The actual method applied to a reentry event may be a variant of some numerical and semi-analytical methods. These specialized fast-acting, semi-analytical prediction algorithms for low-altitude orbits have "counting times of order 0.01 seconds" for a 24 hour prediction span. [Ref. 47:p. 36]

The reentry of the Salyut-7 complex was predicted and confirmed by observation in the range of 75-105 km. In this altitude range, it was also observed and predicted that breakup would occur. [Ref. 47:p. 39]

It was assumed that the ballistic coefficient would vary during reentry, to the same degree as it did prior to an attitude control maneuver. This assumption allowed the reentry problem to be solved by varying the initial conditions within their ranges of possible errors, with subsequent integration of motion equations up to the point of reentry. In many cases it was only the ballistic coefficient which must be varied. This sensitivity of reentry time to the ballistic coefficient is given by the following approximate formula [Ref. 47:p. 39]

$$\delta t_{reentry} = -t_i \frac{\delta k}{k} \quad (176)$$

where

t_i = time interval of motion prediction to the moment of reentry

k = ballistic coefficient = $C_D A / 2m$

Given a 1% change in ballistic coefficient, the down range travel is altered by 180 km. A 2-3% change in ballistic coefficient (as seen prior to the attempted control maneuver) alters the predicted impact point by ± 500 km. Figure 48 shows the dependence of time, latitude and longitude on the ballistic coefficient [Ref. 47:p. 40].

The approximate estimate of the probable debris fallout range, considering the errors in determining the reentry point, with the vehicle destruction occurring at 75 km altitude, is equal to ± 1000 km relative to the calculated impact point. This corresponds to the sub-satellite track crossing Chili and Argentina from the south-west to north-east. [Ref. 47:p. 40]

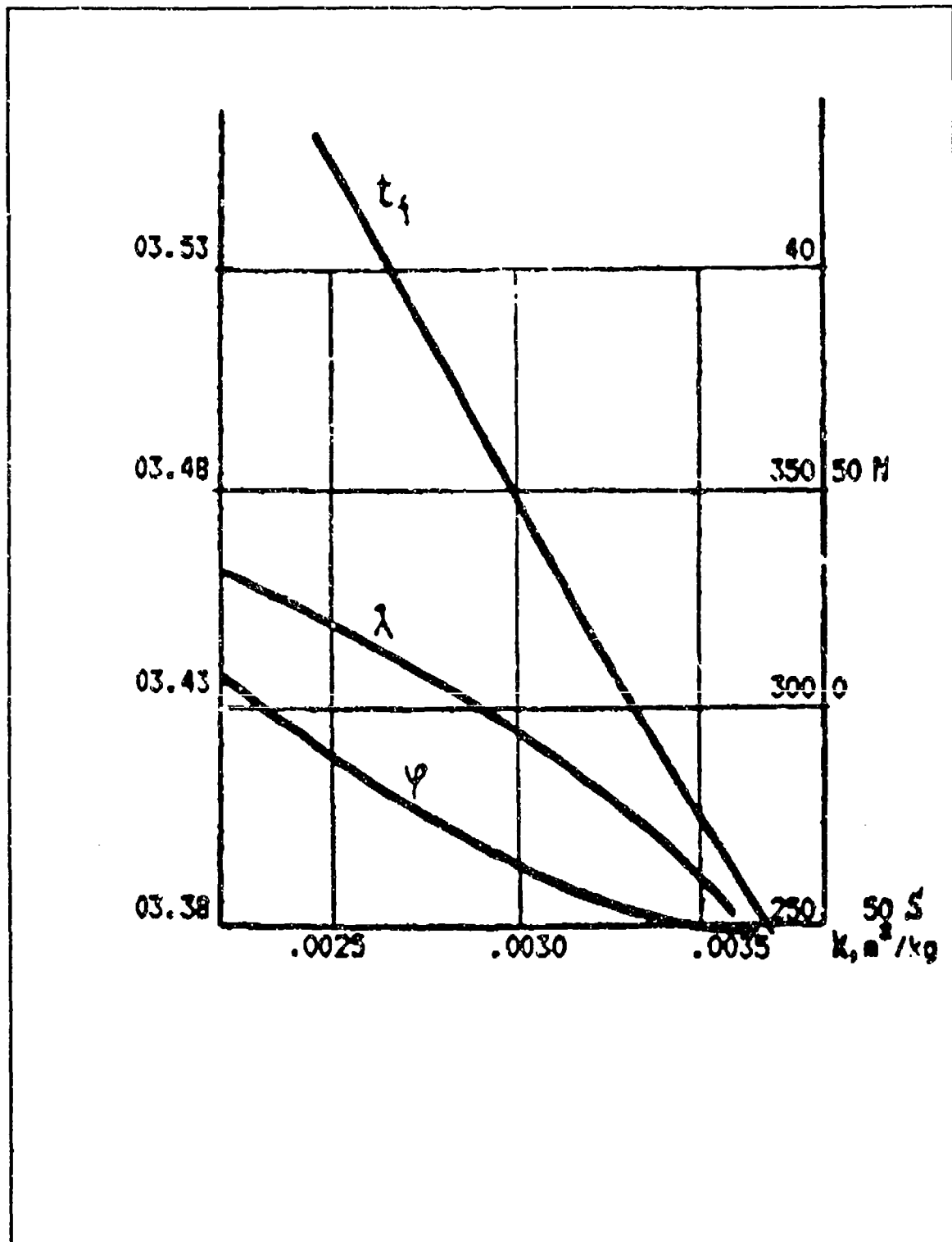


Figure 48: Dependence Of Time, Latitude And Longitude On B
 [Ref. 47]

C. FACTORS INFLUENCING REENTRY/IMPACT DISPERSION

The reentry vehicle's deceleration may be expressed in terms of "gravitational acceleration forces" (g's) as follows [Ref. 96:p. 1]

$$\frac{\text{Dynamic pressure}}{\text{Ballistic coefficient}} = \frac{\frac{1}{2} \rho V^2}{\frac{W}{C_D} A} \quad (177)$$

Assuming that density and wind velocity are the two atmospheric characteristics which most strongly influence the motion of a reentry vehicle passing through it, reference [96] states the following:

1. Reentry vehicle is non-ablative and non-maneuvering (W and A are constant)
2. Drag coefficient is dependent upon altitude (Mach dependence)
3. Drag coefficient is shape dependent

The displacement in impact point can be considered to be the sum of miss contributions from the various atmospheric layers, given by the product of influence coefficients times changes in density or wind velocity for the respective altitude layers. [Ref. 96:p. 2]

Reference [97] studies the effects of a non-spherically symmetric atmosphere on the reentry/impact location of a decaying satellite orbit. This investigation deals with two specific cases, a 90 degree and 30 degree inclined, low Earth orbit and shows the effect of the atmosphere's diurnal bulge on the impact location. It is observed that a decaying

object is "more likely" to reenter and impact the Earth at certain latitudes than at others.

[Ref. 97:p. iii]

The principal effects contributing to this impact distribution, in addition to the diurnal bulge, are the geometric oblateness of the atmosphere and the gravitational oblateness of the Earth. Also identified as important parameters, are orbital inclination and ballistic coefficient.

The results of this investigation are as follows: [Ref. 97:p. 43]

1. Polar orbit (90° inclination) reentry is most likely in the equatorial latitudes.
2. Latitudes of maximum or minimum likelihood for impact are not significantly affected by changes in ballistic coefficient.
3. Large, "balloon type" (spherical) satellites react to the diurnal bulge by causing impact on the opposite side of the Earth.
4. Smaller, heavier satellites show little influence of the diurnal bulge, but they exhibit a greater variation in impact probability with latitude.
5. The impact distribution for a given spherical satellite "flattens" as the inclination is moved from 90° to 30° . This is attributed to the fact that the extremes in Earth radius differ by only 5 km under the 30° inclined orbit as opposed to 21 km under the polar orbit.

Reference [98], a survey of satellite lifetime and orbit decay prediction, conducted in 1980, states:

...gravity perturbations cannot, by themselves, lead to orbital decay since they are conservative. But, they can induce oscillations in the orbit...drag is proportional to atmospheric density...gravity perturbations coupled with drag are more significant than when only drag is modeled. [Ref. 98:p. 3]

Also noted is the observation that non-symmetric mass distribution and shape may amplify the torques created by: [Ref. 98:p. 4]

1. Gravity gradients
2. Aerodynamic forces
3. Solar pressure forces

An interesting note, also, is that any mass loss increases the magnitude of the drag deceleration since [Ref. 98:p. 5]

$$a_{drag} \sim \frac{1}{m} \quad (178)$$

A final noteworthy observation from reference [98] is that any attempt to model satellite attitude, shape, lift, mass distribution, ablation and breakup would largely exceed the level of sophistication currently available (1980) for atmospheric density models, therefore, these non-atmospheric factors are neglected and treated as higher-order effects. [Ref. 98:p. 5]

Reference [99] was initiated after the reentry of part of Sputnik IV over Wisconsin in September 1962. [Ref. 99:p. 2] This study of factors influencing the prediction of orbit decay and impact states:

...final reentry occurs shortly after the point of minimum altitude (not coincident with perigee, because of the Earth's oblateness) [Ref. 99:p. 29]

It is possible, knowing only the initial inclination angle and reentry vehicle orbital path, to determine the points at which the minimum altitude points will occur.

Therefore, knowing where these points occur, it may be possible to predict reentry within several tenths of an orbit revolution, as opposed to ambiguities of one complete revolution as noted in reference [95] (LIFETIME v3.0), since reentry tends to follow the point of minimum altitude. [Ref. 99:p. 33]

Without such precise knowledge of the body's ballistic coefficient, the characteristics of the atmosphere, the orbital elements and their variation, only "probability estimates" can be made of impact latitude, based simply on the relative time spent by the satellite in various latitude bands. This conclusion yields the following relationships: [Ref. 99:p. 33]

1. If the initial inclination equals 50° - three times more likely to impact between $40\text{-}50^\circ$ band than $0\text{-}10^\circ$ latitude band
2. If the initial inclination equals 49° - two times more likely to impact the continental U.S. than a 65° inclined orbit

A final comment about factors influencing reentry and impact prediction from this investigation is that:

In spite of the present reentry rate of about one object a day (most of them burning up, and 2 out of 3 of Russian origin), the threat imposed on the Earth population from direct hits by debris from uncontrolled reentries of space objects can generally be regarded as minor when compared with other risks of civilization (traffic accidents, etc.). An accumulation of worst case assumptions could lead to one casualty every five years for a densely populated area of the size of the Federal Republic of Germany in case of no prior warning. In case an early warning could be issued, such casualties could most likely be avoided completely. [Ref. 100:p. 49]

Figure 49 shows the magnitude of the low Earth orbit problem purely as a function of the number of objects in orbit [Ref. 100:p. 51]. Figure 50 shows the limiting factor

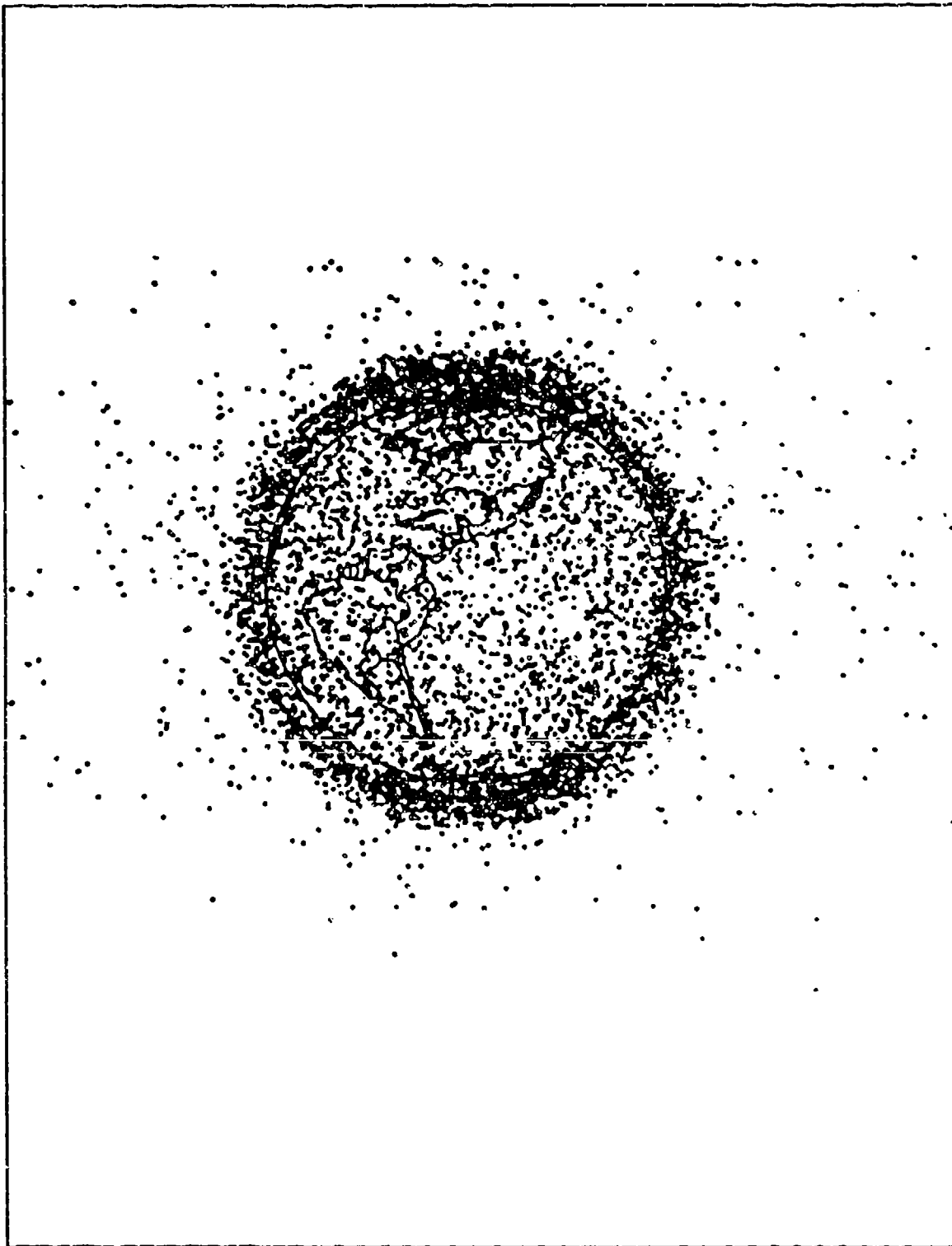


Figure 49: Near-Earth View Of All Cataloged Space Objects (1987)
[Ref. 100]

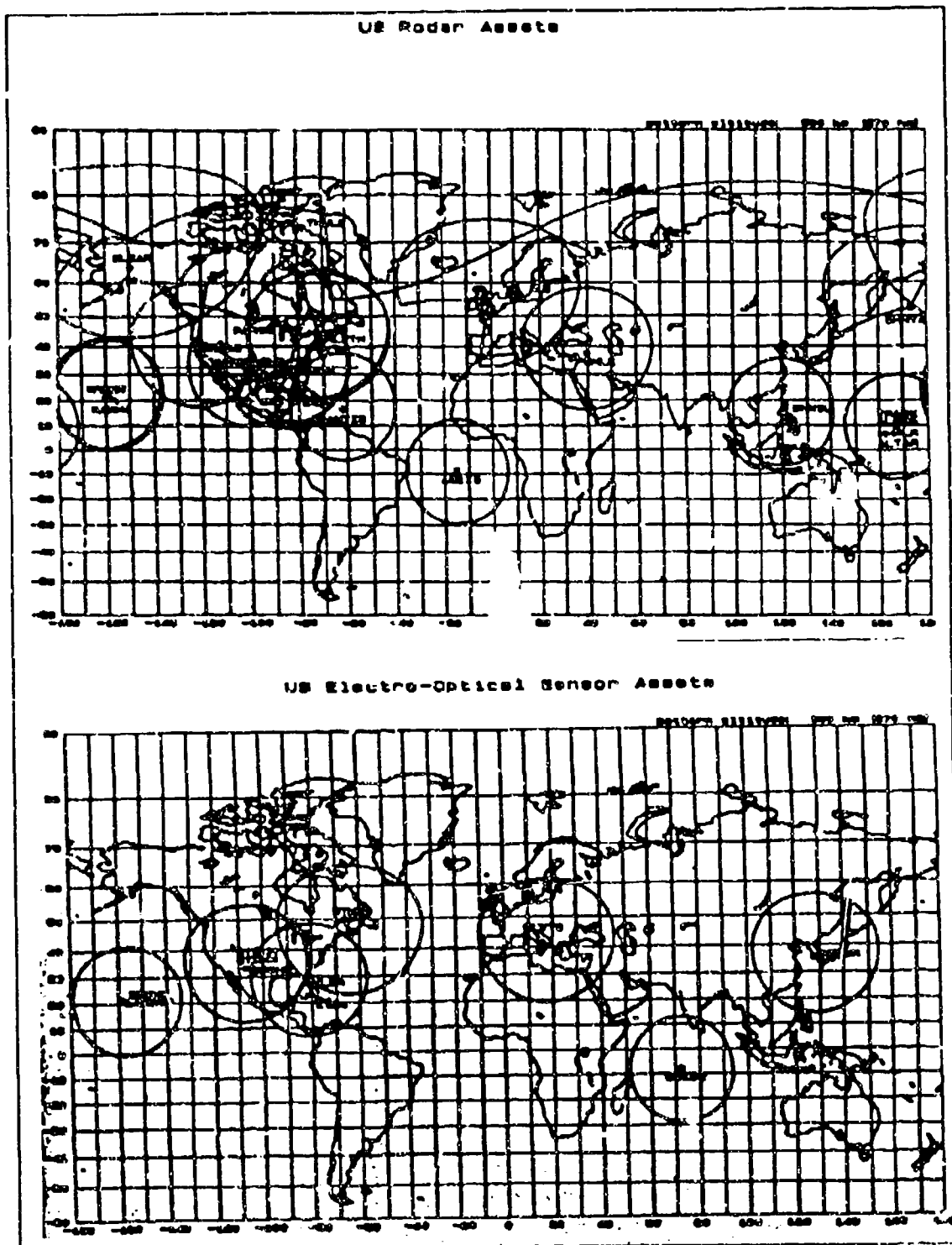


Figure 50: U.S. Radar And Electro-Optical Assets
 [Ref. 100]

of geographic location of observation sites from which data may be obtained for reentry/impact predictions [Ref. 100:pp. 5-6].

The final factor in reentry/impact prediction to be discussed here is the rotation of the orbital plane during the final phase of reentry, as presented in reference [101]. This study states that planar motion is representative of, or an adequate model for, reentry deceleration and heating rate studies. It is, however, inadequate for the study of ballistic reentry below altitudes of 60 km and ballistic coefficients in the ranges $0.001 \text{ m}^2/\text{kg} \leq B \leq 0.1 \text{ m}^2/\text{kg}$. For these values of B, the orbital plane begins to rotate at altitudes of 30 km and 60 km respectively. [Ref. 101:p. 1215] This investigation deals exclusively with the final descent from 120 km, and defines this as the "reentry phase" [Ref. 101:p. 1216].

As previously mentioned, maximum heating rates and deceleration occur at altitudes high enough, such that, rotation of the orbital plane is negligible in the calculation of these parameters. However, in the calculation of the total range traveled to Earth impact, these lower altitude effects and orbital plane rotations become significant. [Ref. 101:p. 1217]

Several initial assumptions are made: [Ref. 101:p. 1217]

1. $0.001 \text{ m}^2/\text{kg} \leq C_D A/m \leq 0.1 \text{ m}^2/\text{kg}$
2. $0 \leq \Psi_0 \leq 45^\circ$, where Ψ_0 is the initial reentry trajectory angle
3. $v_0 \leq 15 \text{ km/sec}$

As the vehicle descends, the ambient air becomes denser and the rotating atmosphere begins to force the vehicle's motion towards a direction parallel to that of the atmosphere's velocity. This effectively rotates the vehicle's orbital plane towards the direction of the atmospheric velocity vector. Figure 51 shows this rotational effect on the orbital plane [Ref. 101:p. 1219].

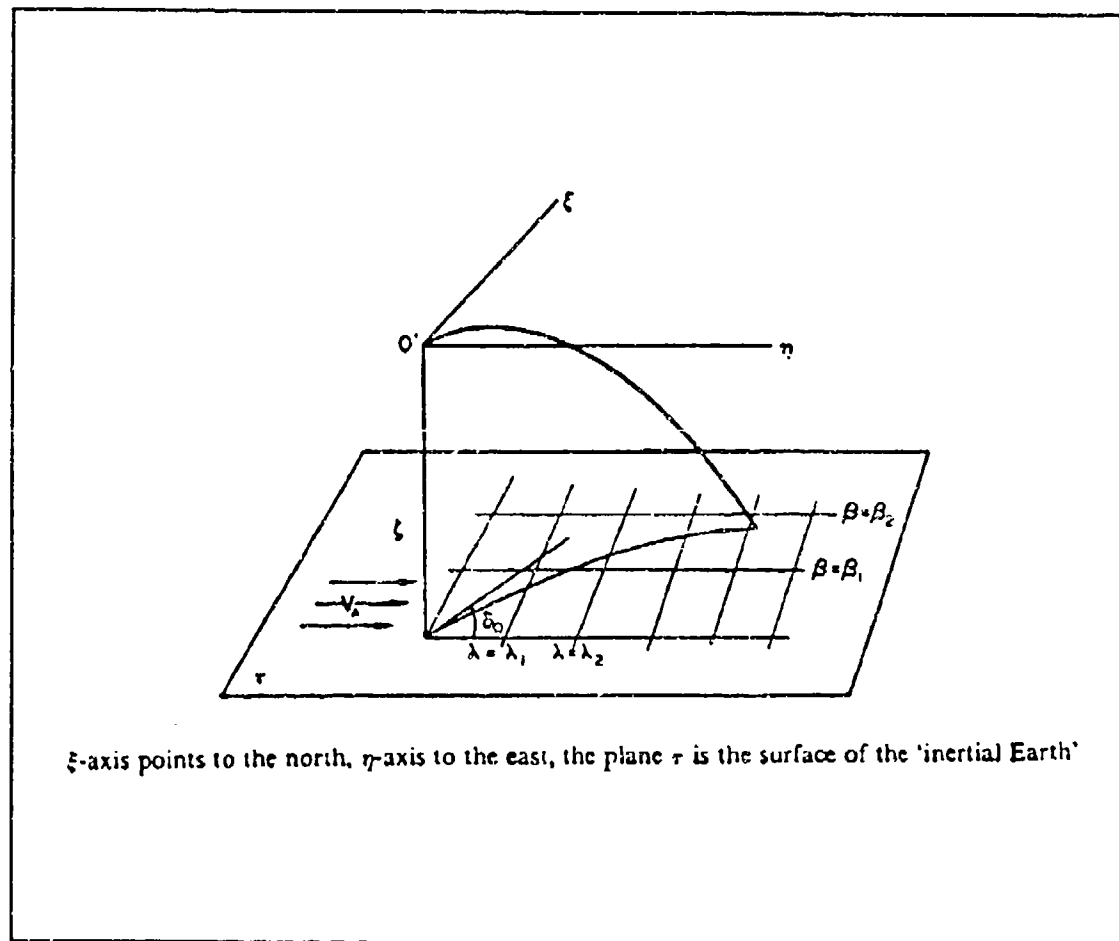


Figure 51: Orbital Plane Rotation Due To A Rotating Atmosphere [Ref. 101]

V. STOCHASTIC AND STATISTICAL PREDICTION METHODS

This chapter will describe three investigations that used stochastic and statistical techniques and methods to predict the time and impact location of decay-induced reentry. Two investigations have direct applicability to the current reentry model used by the USSPACECOM and the third investigation is a Monte Carlo simulation analysis that was used to predict the footprint dispersion area of Skylab.

A. EXTENSIONS OF THE PHYSICAL MODELING REENTRY THEORY

In Chapters II and IV, the current reentry theory used by the USSPACECOM to predict impact location and time was presented. The theory's accuracy is limited by the ability to observe the reentry process and the inherent deficiencies in the model used to represent the physical reentry process. This section will examine a Doctoral dissertation and a Master's thesis from the Air Force Institute of Technology (AFIT) which are proposed extensions or modifications of the current model. [Refs. 48,102] These investigations utilize stochastic and statistical methods and techniques to improve the predicted impact location and time.

1. Estimation of Reentry Trajectories

Reference [102] developed a linearized differential corrector technique as an extension of the existing orbital estimation technique into the reentry region to estimate the reentry trajectory. Reentry observations from a space based sensor capable of

providing infrared angular trajectory observations at fixed, discrete time intervals and large uncertainties in true reentry dynamics, were the primary engineering considerations of this problem [Ref. 102:p. 1]. The author states the following about the current deterministic model:

...the basic differential corrector with deterministic dynamics is inadequate for processing true reentry data. The deterministic dynamics and infinite memory of the basic formulation, cause the estimator to yield significantly biased solutions relative to the standard deviations of the estimator-computed covariance matrix. These occur when processing data reflecting the dynamic variations anticipated in true reentry trajectories. The use of the estimator in this form would not provide an accurate estimate of Earth impacts for satellite debris. [Ref. 102:p. 19]

Since the uncertain dynamics of the reentry process pose many difficulties for the existing deterministic model, a significant portion of the research in the dissertation was devoted to identifying limits of various estimation techniques that were considered for this problem. [Ref. 102:p. 1]

An adaptively determined, ad hoc, scalar finite memory or fading memory parameter approach was selected. The motivation of this approach is based on the fact that the existing reentry theory attempts to group all unmodeled parameters as a constant with the ballistic coefficient ($C_D A/m$) over some short trajectory span. [Ref. 102:p. 11]

In order to extend the existing orbit determination technique into the satellite reentry problem, reference [102] defined a reentry dynamics model and developed the weighted least-squares differential corrector structure currently used in the deterministic model. The estimator update and propagation equations of the differential corrector structure for an infinite memory formulation are summarized as follows:

Propagations between epochs:

State: integrate with initial conditions $x_m(t_m)$, from the epoch at t_m

$$\dot{x}(t) = f(x(t), t) \quad (179)$$

to obtain $x_m(t_{m+1})$ at epoch t_{m+1}

Covariance:

$$S_{m+1,m} = \phi(t_{m+1}, t_m) S_{m,m} \phi(t_{m+1}, t_m)^T \quad (180)$$

Update at next epoch:

State:

$$x_{m+1}(t_{m+1}) = x_m(t_{m+1}) + \sum_{i=1}^l \delta x(t_{m+1})_i \quad (181)$$

Covariance:

$$S_{m+1,m+1} = (S_{m+1,m}^{-1} + T_{(n)}^T R_{(n)}^{-1} T_{(n)})^{-1} \quad (182)$$

Recall that l is the number of iterations required to satisfy convergence and $T_{(n)}^T R_{(n)}^{-1} T_{(n)}$ is evaluated from the reference trajectory on the final iteration, l . [Ref. 102:pp. 33-34]

Equation (179) is a nonlinear dynamics model, where $f(x(t), t)$ is a deterministic function of the state variables and is a continuous function of time. The variable, $\delta x(t)$, from equation (181) is a "seeked" correction that will minimize a weighted quadratic cost function of the observation residuals. Iterations of the differential corrector continues until the observation residuals convergence criteria is satisfied. Equation (180) is the initial state covariance matrix that remains constant until the iterative process has converged. The quantity $\phi(t_{m+1}, t_m)$ from equation (180), is the state transition matrix. The final iteration in the process yields equations (181) and (182). $R_{(n)}$ and $T_{(n)}$ from equation (182) are respectively the matrices of the observation noise covariances and the observation index being processed. [Ref. 102:pp. 20-29] As previously mentioned:

Application of this batch processing algorithm to reentry estimation has often resulted in poor estimator performance. This is largely due to the more significant non-linear dynamics of reentry and the use of a deterministic and simplistic dynamics model ... in an uncertain dynamics region. [Ref. 102:p. 31]

In the development of the reentry dynamics model, the author chose an eight dimensional state vector defined as [Ref. 102:pp. 41-42]

$$\mathbf{x}(t) = \begin{array}{|l} x_1 = x \\ x_2 = \dot{x} \\ x_3 = y \\ x_4 = \dot{y} \\ x_5 = z \\ x_6 = \dot{z} \\ x_7 = B\rho_0 \\ x_8 = Q \end{array} \quad (183)$$

where

$$\dot{x}, \dot{y}, \dot{z} = \text{velocity components} \quad (184)$$

$x, y, z,$ = position components (cartesian)

B = ballistic coefficient ($C_D A/m$)

ρ_0 = sea level air density from equation (10)

Q = density scale height ($RT_0 / M_0 g_0^*$) from equation (10)

M_0 = molecular weight of air

g_0^* = acceleration of gravity at Earth surface

T_0 = atmospheric temperature at sea level

R = gas constant

H^* = altitude (g/g_0H_0) from equation (10)

g = local gravitational acceleration from the geopotential model x, y, z coordinates

g_0 = reference geoid level gravitational acceleration

H_0 = geocentric altitude ($R-R_e$)

R = local radius position relative to the Earth center $(x^2 + y^2 + z^2)^{1/2}$

R_e = $R_0 (1 - f) [1 - (2f - f^2) \cos^2 \delta]^{1/2}$

f = flattening factor of the reference geoid whose elliptical shape is consistent with J_2

δ = local latitude ($\cos^{-1}[(x^2 + y^2)^{1/2} / R_0]$)

R_0 = radius of the reference geoid at the equator

The exponential atmospheric density model, equation (10), was used in the reentry estimator because of: [Ref. 102:p. 37]

1. The reduced mathematical complexity.
2. The availability of continuous valued density and partial derivatives of the density along the reentry trajectory.

The eighth state variable, Q , was chosen since it is slowly changing at the reentry altitudes (< 100 km). For this application, the initial value, $Q = 7.0031$ km and its covariance were derived using a least squares fit to the base density values of the altitude layers from the U.S. Standard Atmosphere 1962. Also, an Earth Centered Inertial (ECI) coordinate frame was chosen to minimize the complexities of the observation noise covariance matrix, $R_{(n)}$. [Ref. 102:p.40]

Both aerodynamic and geopotential terms within the deterministic function of state variables, $f(x(t), t)$, are included in the estimator dynamics model. The dynamics equation is given in the form [Ref. 102:pp. 42-44]

$$\dot{x} = \begin{vmatrix} \dot{x}_1 = x_2 \\ \dot{x}_2 = f_{d_x} + f_{g_x} \\ \dot{x}_3 = x_4 \\ \dot{x}_4 = f_{d_y} + f_{g_y} \\ \dot{x}_5 = x_6 \\ \dot{x}_6 = f_{d_z} + f_{g_z} \\ \dot{x}_7 = 0 \\ \dot{x}_8 = 0 \end{vmatrix} \quad (185)$$

The aerodynamic acceleration x,y,z components from equation (185) are derived from equation (6)

$$f_{d_x} = -\frac{1}{2}B\rho V_A (\dot{x} + \omega y) \quad (186)$$

$$f_{d_y} = -\frac{1}{2}B\rho V_A (\dot{y} - \omega x) \quad (187)$$

$$f_{d_z} = -\frac{1}{2}B\rho V_A \dot{z} \quad (188)$$

The geopotential acceleration terms from equation (185) were derived from the Smithsonian Astrophysical Observatory SAO-III Earth Model using the model parameters and zonal and tesseral coefficients

$$f_{g_x} = \cos \alpha_s VV_x - \sin \alpha_s VV_y \quad (189)$$

$$f_{g_y} = \sin \alpha_s VV_x + \cos \alpha_s VV_y \quad (190)$$

$$f_{g_z} = VV_z \quad (191)$$

where

α_s = Right Ascension (RA) of the Greenwich Meridian

The gradient terms from equations (189) through (191) are defined as

$$VV_x = \sum_{n=0}^{\infty} \sum_{m=0}^n \left(C_{nm} \frac{\partial U_n^m}{\partial x} + S_{nm} \frac{\partial V_n^m}{\partial x} \right) \quad (192)$$

$$VV_y = \sum_{n=0}^{\infty} \sum_{m=0}^n \left(C_{nm} \frac{\partial U_n^m}{\partial y} + S_{nm} \frac{\partial V_n^m}{\partial y} \right) \quad (193)$$

$$VV_z = \sum_{n=0}^{\infty} \sum_{m=0}^n \left(C_{nm} \frac{\partial U_n^m}{\partial z} + S_{nm} \frac{\partial V_n^m}{\partial z} \right) \quad (194)$$

where

C_{nm} = zonal harmonic coefficient

S_{nm} = tesseral harmonic coefficient

$$U_n^m = \frac{GM R_0^n}{R^{n+1}} P_n^m(\delta') \cos(m\lambda) \quad (195)$$

$$V_n^m = \frac{GM R_0^n}{R^{n+1}} P_n^m(\delta') \sin(m\lambda) \quad (196)$$

G = universal gravitational constant

M = mass of Earth

R_0 = mean equatorial Earth radius

R = distance from Earth center

P_n^m = associated Legendre polynomial of degree n and order m

δ' = z/R (z = coordinate)

λ = longitude

As previously mentioned in Chapter II, in the region below 120 km, the first-order zonal harmonic, J_2 , may attain a magnitude approaching that of the atmospheric drag. Based on this fact, in the development of the actual estimator and simulation, only the central gravity, C_{00} , and Earth oblateness (J_2), C_{20} , terms were used in the reentry altitude regions.

Numerical simulations using simulated reentry data derived from a realistic "truth model" were conducted on the basic estimator structure and dynamics model to quantify its performance.

These analyses examined the effects of mismatch between the truth model and the estimator model dynamics, accuracy variations on the angular observations, multiple orbital observation locations and variations of the geometric relationships between the observing satellites and the reentry trajectory. [Ref. 102:p. 14]

A series of Monte Carlo analyses were conducted which showed the model dynamics as the most important factor impacting the estimator performance. This was accomplished by:

1. Considering the velocity estimates and mean bias of the trajectory position vs the magnitude of the standard deviations from the estimator computed state covariance matrix.
2. Comparing the magnitudes of the standard deviations from the estimator computed state covariance matrix to those derived in the Monte Carlo samples.

In the search to find possible solutions to the problems associated with the estimator performance, reference [102] reviewed and discussed the limitations of several model compensation methods that are relative to the reentry application, including: [Ref. 102:p. 15]

1. Adding a pseudo-noise compensation to the model dynamics
2. Adaptive estimation methods
3. State covariance deweighting techniques

The author developed a fading memory differential model compensation method based on the fact:

...the previous numerical results indicated, the fundamental limitation of the infinite memory estimator formulation with deterministic dynamics is the biased estimator solutions which occur when processing true reentry dynamics. With i) exact dynamics ii) an upper limit on the time span of valid linearization, and iii) a lower limit on observation accuracy (greater than or equal to 10^{-5} radians), acceptable estimator performance is available in terms of bias and $RSS/(ONE\ SIGMA)$ Ratio. [Ref. 102:p. 112]

Since the variations in global atmospheric density and the dynamic changes of the reentry body pose such a virtually intractable problem within a deterministic set, improving the linearized estimator performance is based on the impact of uncertainties within the ballistic coefficient and the atmospheric density [Ref. 102:pp. 112-113]. Improvement of the estimator was achieved by an adaptive determination of an ad hoc scalar multiplier, γ . A finite memory on the processing of earlier observations is implemented by multiplying the parameter, γ , to the terms of the state covariance matrix prior to an observation update. At each update along the trajectory, the size of the change in state variable, δx_i , is examined. Each δx_i magnitude is then compared to the magnitude of the standard deviation of their respective terms within a "deweighted" covariance matrix which is computed by the estimation algorithm. As with the infinite memory estimator model, a series of Monte Carlo analyses were conducted to assess the model's ability to estimate an anticipated true reentry dynamics trajectory. [Ref. 102:pp. 15-16]

Finally, reference [102] demonstrated the ability of the fading memory method to provide a tangent plane projection of Earth impact locations as shown in Figure 52 [Ref. 102:p. 192], by using bias magnitudes within the standard deviations of the deweighted state covariance matrix.

The standard deviation of the position error from the deweighted state covariance matrix provides a good definition of the uncertainties in the estimated Earth impact locations, thus it can be used to define a search area for recovery of satellite debris. These results illustrate the viability of the method to estimate decayed satellite impact locations and uncertainties significantly improved over existing astrodynamic applications. [Ref. 102:p. 16]

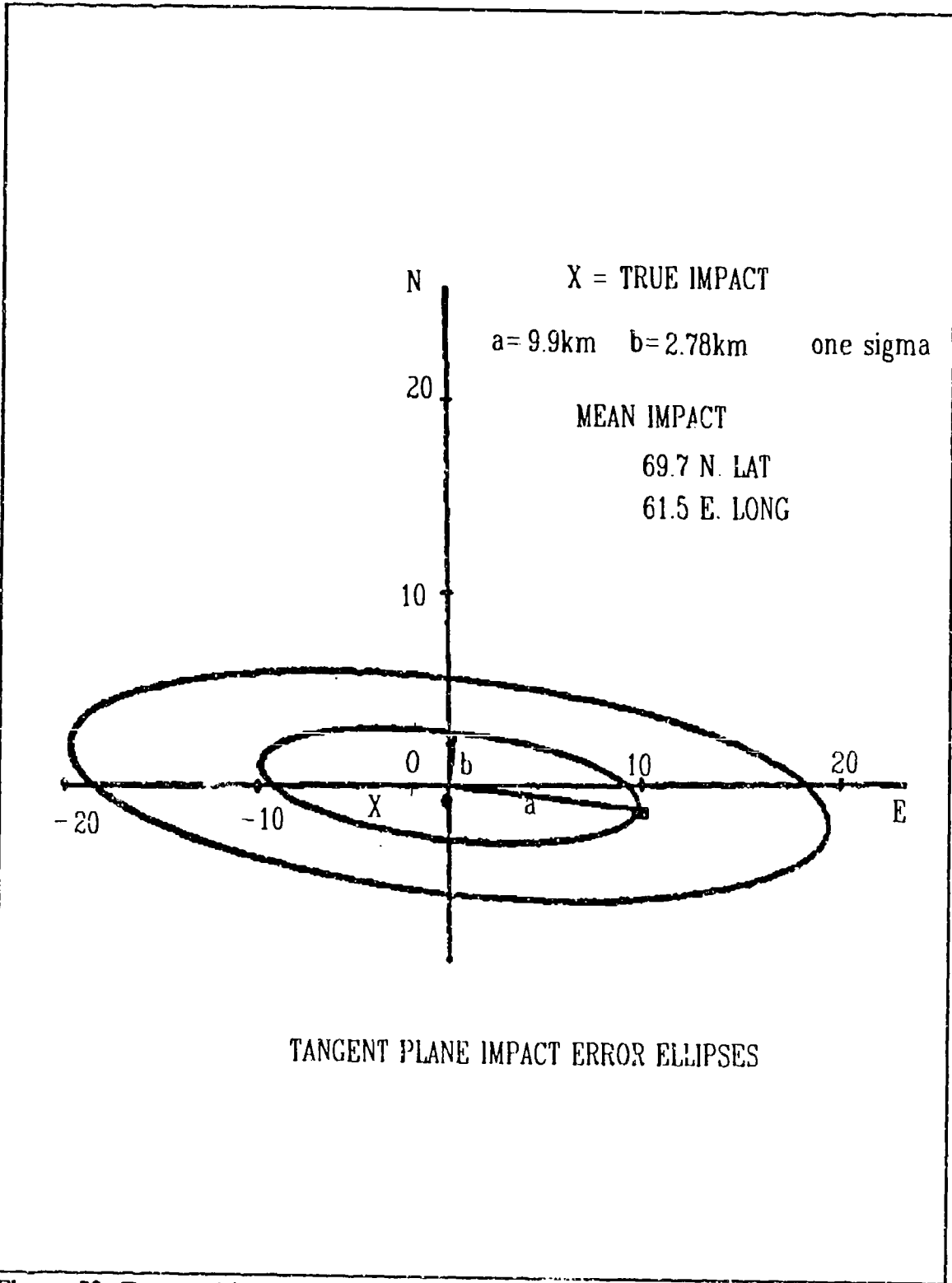


Figure 52: Tangent Plane Projection Of Earth Impact Location
 [Ref. 102]

The primary conclusions and recommendations from the dissertation are:

[Ref. 102:pp. 198-202]

1. Dynamics uncertainties of the general satellite decay trajectories significantly affect the estimator performance as shown by the Monte Carlo simulation analyses.
2. Angular observation accuracies with standard deviations less than 10^{-5} radians induce significant error in the state estimate vs the standard deviations of the state covariance matrix in deterministic dynamics models.
3. A recursive formulation of the estimator is recommended that uses a short time span between the epoch or trajectory update point and the observation(s) being processed due to the anticipated dynamics uncertainties of reentry.
5. Multiple observations from more than one the orbital source are required to improve the observability of the reentry and to provide higher data content over similar time spans in-order to achieve acceptable estimator performance in terms of bias and RSS/(ONE SIGMA) ratio.
6. An eight dimensional state vector provided superior estimation performance as compared to the seven dimensional vector used in the current deterministic models. Performance improvement is achieved through simpler mathematics in the dynamics model and continuous valued partial derivatives of the dynamics over the trajectory space for a Taylor's series linearization.
7. The adaptive, ad hoc scalar fading memory parameter is easily incorporated into the basic estimator structure.
8. A Monte Carlo derived impact covariance for the final propagation phase to impact preserves the integrity solution statistics over the non-observable final portion of the trajectory. Impact location uncertainties are on the order of one to two magnitudes smaller than those available from current operational techniques.
9. Further investigations which vary the observational data rate and the time varying character of true reentry dynamics are needed to examine the estimator performance extensions. Specifically, more accurate observations (much less than 10^{-5} radians) with higher data rates and frequency variations as well as alternative measurements, such as range or range rate.

10. Further analysis of applying the fading memory method to very high altitudes and shallow reentry angles is recommended due to the fact that violent dynamic changes under these conditions may result in divergent estimator performance.
11. Application of this estimation technique to a wide class of reentry trajectories could provide a large empirical data base to improve the estimator dynamic model. Dynamic model pseudo-noise compensation, statistical linearization, or higher order filters investigations should be pursued.

2. Analysis of Tracking and Impact Prediction (TIP)

Reference [48] analyzed the accuracy of early TIP processing (Chapter II, p.58) conducted by the USSPACECOM on 180 objects that decayed during the years 1987 through 1990. As part of the analysis, early TIPs (1 day to 3 hour predictions) were compared to the final TIP. The time error for each TIP run was calculated and compared to the $\pm 20\%$ accuracy level claimed by the SSC at Cheyenne Mountain AFB.

Results from the comparison study indicate:

1. The decay prediction accuracy is usually, but not always within the claimed accuracy level as shown in Figure 53 [Ref. 48:p. 37].
2. The existence of a positive bias which indicates early TIPs are routinely late relative to the final TIP.

The author developed six multiple linear regression models that could be incorporated into the TIP decay procedures in an attempt to model out some of the positive bias found in TIP decay prediction data. [Ref. 48:p. viii]

DECAY PREDICTION (Relative to 20 Percent Standard)

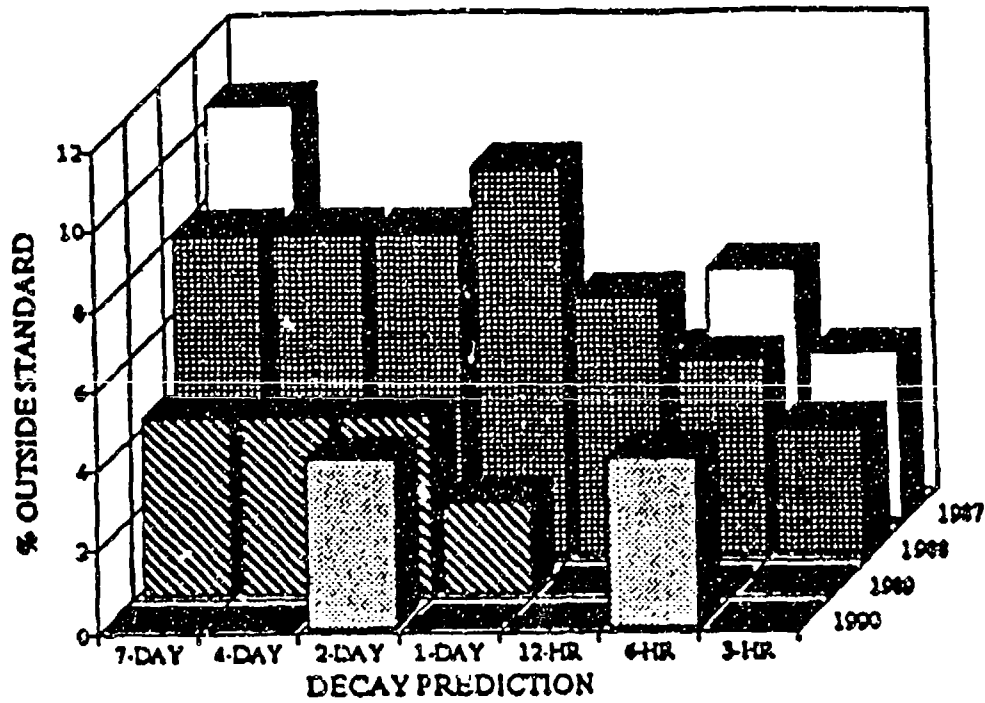


Figure 53: Decay Predicted Accuracy (By Year)
[Ref. 48]

The data used in the investigation was collected from: [Ref. 48:pp. 15-17]

1. TIP Required Item Checklist--a manually kept chronological account of each TIP processing.
2. Decay History--a computer generated log of each SP update that includes the run time, time of last observation, epoch time, epoch revolution number, B-term (ballistic coefficient), period and decay prediction.
3. Final Element Set--a listing of the final orbit parameters. The eccentricity and mean motion data from the listing were used in the investigation.

Only those objects that received the entire TIP update cycle (7 day through final run) were used to accurately analyze the effects of each successive update and prediction [Ref. 48:p. 17]. In order to assess the accuracy level claimed by the SSC, reference [48] used the data from the final decay prediction as the control by which to compare the earlier predictions.

The final prediction was chosen as the control because it uses observations which are closest to the actual impact point and is considered to be the most accurate prediction available. In order to further justify the use of the final prediction as the control, a statistical analysis was also performed to directly compare the few sighted reentry points, called *Vis Obs*, with the final prediction made by the Space Surveillance Center. [Ref. 48:p. 18]

Of the 180 objects studied, 93 were *Vis Obs*. Figure 54 shows the mean time error of the final run time vs the *Vis Obs* [Ref. 48:p.25]. The size of the final time error standard deviation decreases as shown in Figure 55 [Ref. 48:p. 26]. This decrease may be correlated to the level of solar activity during the 1987-1990 time period. Solar activity levels began to dramatically increase in 1987 and continued to increase through the solar maximum (March 1990). The rate of change increase of the sunspot activity

MEAN TIME ERROR (Final Run vs VIS OBs)

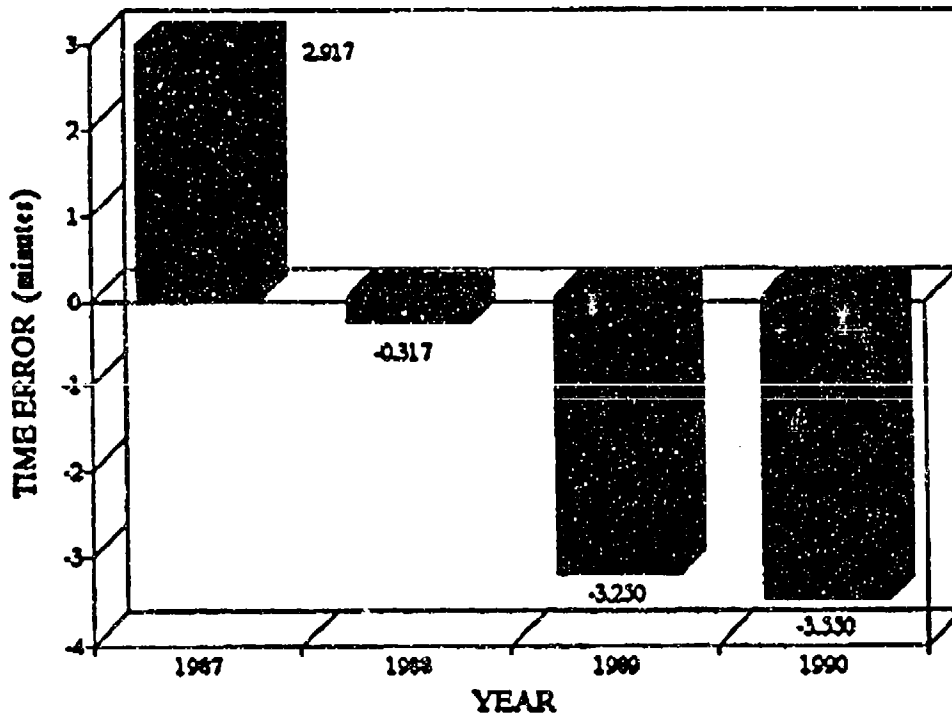


Figure 54: Final Run vs *Vis Obs* Mean Time Error
[Ref. 48]

FINAL RUN TIME ERROR (Standard Deviation)

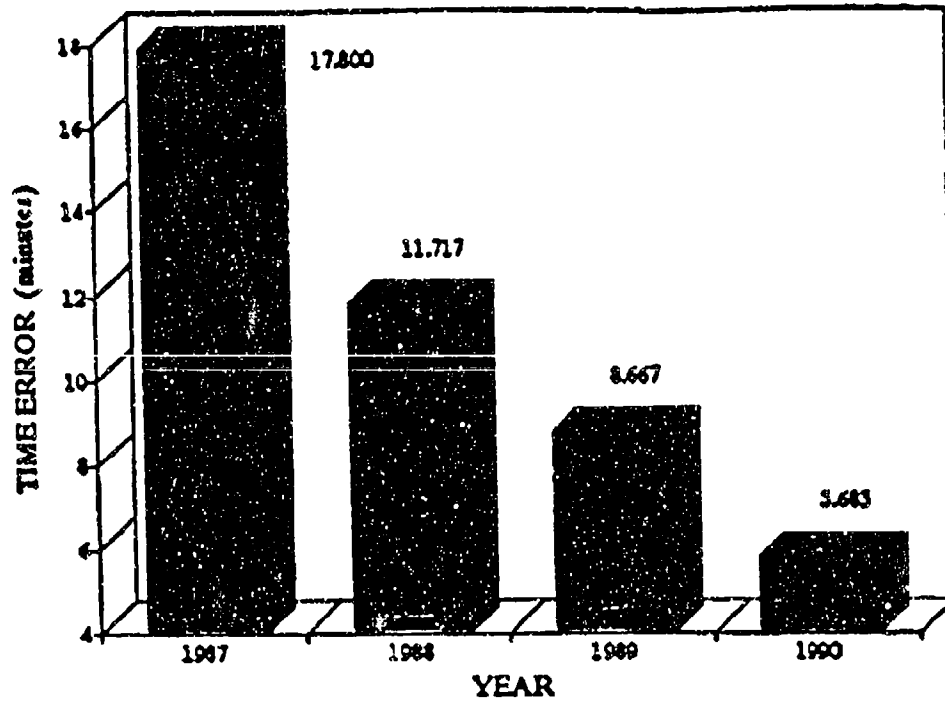


Figure 55: Final Time Error Standard Deviation
[Ref. 48]

and solar flux during 1987-1988 was greater than in period from 1989-1990. According to the author, the trend shown in Figure 55 may be related to the lesser rate of change during 1989-1990. [Ref. 48:pp. 26-28]

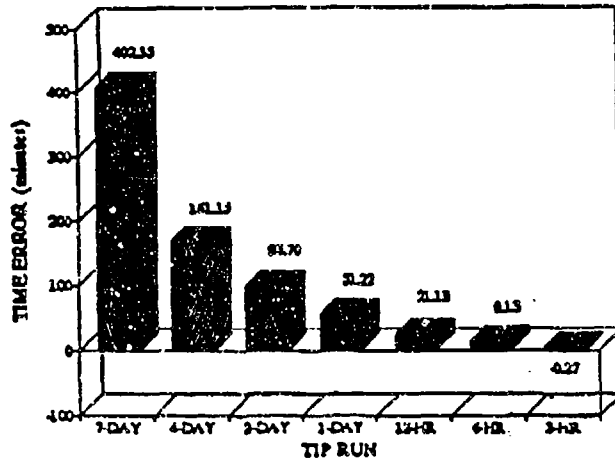
The time error for each separate TIP run was calculated as the difference between the predicted decay time for that run and the final run [Ref. 48:p. 18]. Figure 56 shows the graphic calculation results for the mean time error and time error standard deviation [Ref. 48:p. 29].

In addition to the time error calculations, the location error was calculated by taking the difference between the predicted location point for each run and the final predicted point. The method used the mean motion (n) from the Final Element Set to accurately determine the velocity for each TIP object. Since mean motion was unavailable for the early TIP runs, an approximation was made using the final mean motion value for each TIP run. This introduced an error into the calculation of the location error. However, because the location errors are very large (thousands of km), the error introduced by using the final mean motion instead of the actual mean motion for that particular TIP run was considered insignificant. The mean motion value was used to calculate the semi-major axis distance from the equation

$$a = \left(\frac{\mu}{n^2} \right)^{\frac{1}{3}} \quad (197)$$

The velocity was calculated using the semi-major axis from the equation

**MEAN TIME ERROR
(1987-1990)**



**TIME ERROR (1987-1990)
(Standard Deviation)**

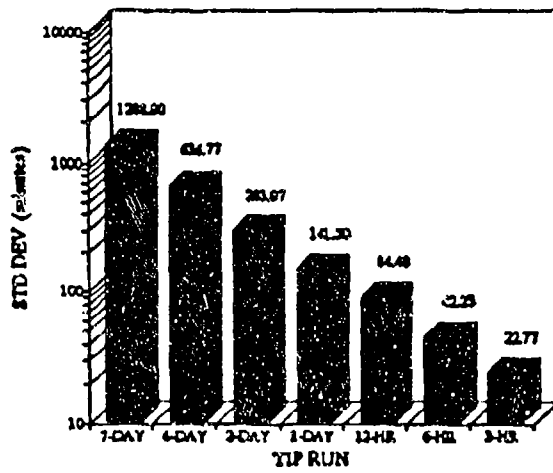


Figure 56: Mean Time Error And Standard Deviation (1987-1990)
[Ref. 48]

$$v^2 = \mu \left[\frac{2}{r} - \frac{1}{a} \right] \quad (198)$$

The object's velocity was then multiplied by the previously calculated time error in order to determine the location error (difference between the predicted location point for each run and the final predicted point). [Ref. 48:pp. 19-22] Figure 57 shows the graphic calculation results for the mean location error and location error standard deviation [Ref. 48:pp. 32-33].

Multiple linear regression describes the relationship between several independent variables and a dependent variable. The motivation for developing the multiple linear regression model to eliminate the bias found in the mean time error was based on the second objective of the investigation. This objective was to determine if it was advantageous to initiate an OPREP-3 report (used to notify higher authority of a potential reentry within 100 nm of the former Soviet Union border) earlier than the 6 hour mark. The first step in the process was to determine if the model in the form

$$E(t_f) = \beta_0 + \beta_1 t_1 + \beta_2 t_2 + \beta_3 t_3 + \beta_4 t_4 + \beta_5 t_5 + \beta_6 t_6 + \beta_7 t_7 \quad (199)$$

where

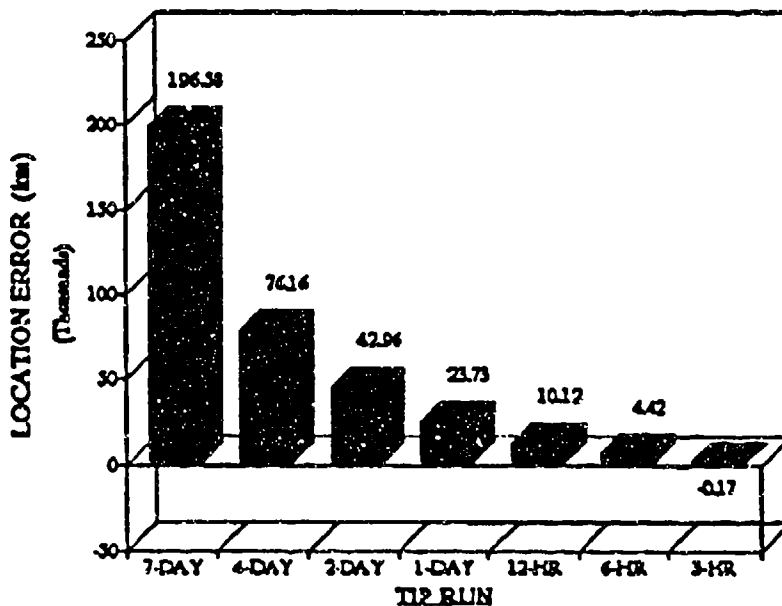
$E(t_f)$ = expected value of the final decay prediction time

t_i = early TIP decay predictions

t_f = final decay prediction time

β_i = y-intercept and coefficients to be determined

MEAN LOCATION ERROR (1987-1990)



LOCATION ERROR (1987-1990) (Standard Deviation)

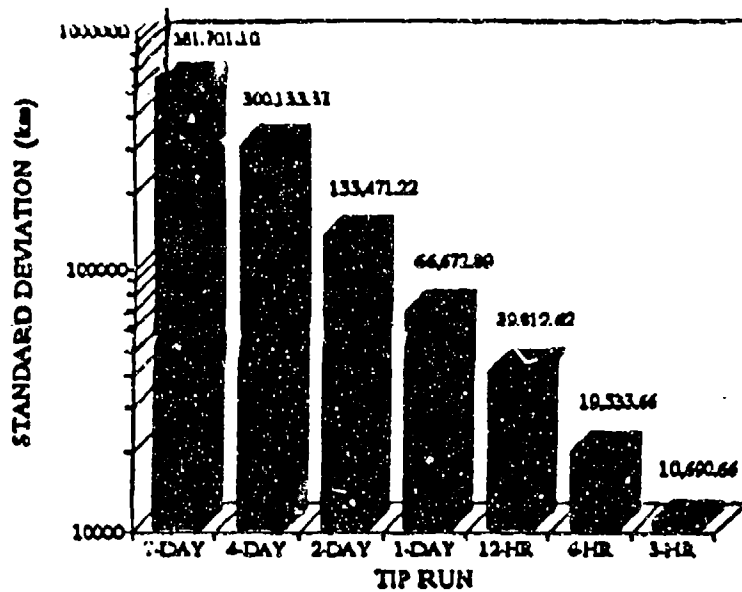


Figure 57: Mean Location Error And Standard Deviation (1987-1990)
[Ref. 48]

could be found where the early TIP data could be used to approximate the final decay prediction time. [Ref. 48:pp. 22-23] The author states the following about equation (199):

...multiple linear regression was then used to first determine if a model in the form shown...could be found to predict the final decay time. The results were an R-squared value of 1.0000 and a p-value of .0001. This means that at a significance level of .05 there exists a perfect linear relation between some of the independent variable and the dependent variable where at least two of the β terms are not zero. The variance inflation values were all extremely large, indicating the independent variables were all highly correlated and that a great deal of redundancy exists in the data. [Ref. 48:pp. 37-38]

Based on the above results, six separate linear models were developed in an effort to approximate the final TIP with greater accuracy than the current process. Specific characteristics used in the modeling include the following : [Ref.48:p. 38]

1. The first model uses only 7-day TIP data to calculate the expected value of the final decay prediction time, $E(t_f)$.
2. One additional decay prediction data point is incorporated in each subsequent model.
3. All 180 TIP objects were used in the six models to calculate $E(t_f)$.

The six models are defined as

$$E_1(t_f) = -0.116442 + 0.999064(t_1) \quad (200)$$

$$E_2(t_f) = -.0155478 + 0.49007(t_1) + 0.951197(t_2) \quad (201)$$

$$E_3(t_f) = -.0082444 + 0.41692(t_1) + 0.050001(t_2) + 0.0908343(t_3) \quad (202)$$

$$E_4(t_f) = -0.053030 + 0.007471(t_1) - 0.014395(t_2) + 0.196518(t_3) + 0.810492(t_4) \quad (203)$$

$$E_5(t_f) = -0.022322 - 0.004222(t_1) - 0.005502(t_2) + 0.046458(t_3) - 0.049000(t_4) + 1.012311(t_5) \quad (204)$$

$$E_6(t_f) = -0.008370 + 0.000553(t_1) - 0.002944(t_2) + 0.014541(t_3) - 0.009096(t_4) - 0.183413(t_5) + 1.180378(t_6) \quad (205)$$

where

- t_1 = 7-day prediction time
- t_2 = 4-day prediction time
- t_3 = 2-day prediction time
- t_4 = 1-day prediction time
- t_5 = 12-hour prediction time
- t_6 = 6-hour prediction time

Figure 58 shows the mean approximate error for the six regression models [Ref. 48:p. 40]. By comparing Figure 58 with the mean time error in Figure 56, the regression models show a better mean approximation error than the TIP runs. The conclusions and recommendations from the thesis are: [Ref. 48:p.42]

1. The decay predictions were much better in general than the reported ± 20 %.
2. The use of linear models in conjunction with the data generated by the TIP processing would allow the SSC to better predict final decay time by elimination of positive bias in the data.

MEAN APPROXIMATION ERROR (1987-1990)

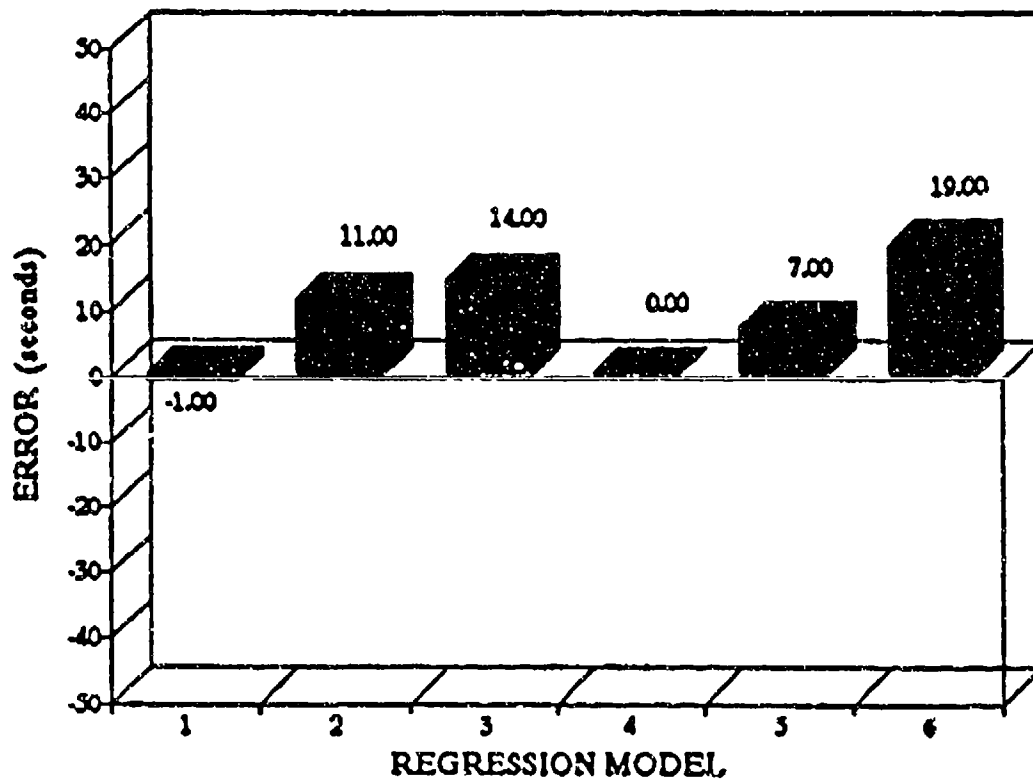


Figure 58: Regression Model Mean Approximate Error (1987-1990)
[Ref. 48]

3. The SSC should conduct a study of the current Special Perturbations model to attempt to better account for the level of solar activity and its effect on the atmosphere.

B. MONTE CARLO ANALYSIS OF SKYLAB'S IMPACT AREA

Reference [45] investigated the debris impact point dispersion area of Skylab. A combination of Monte Carlo statistical analysis and parametric methods were used to determine the three-sigma limits of the debris footprint. The investigation was conducted by Martin Marietta Aerospace during the design and development of the Teleoperator Retrieval System (TRS) for the Skylab reboost/deboost mission. The dispersion analysis was conducted to support the deboosting of Skylab to a safe oceanic impact area clear of islands and routine shipping lanes. [Ref. 45:pp. 1-2]

The Monte Carlo statistical analysis is an efficient and realistic approach that can be used to calculate the debris impact area because of the large number of input variables and nonlinearities of the problem. Impact dispersion area boundaries depend on the following factors: [Ref. 45:p. 2]

1. Entry dispersions
2. Relative flight path angle
3. Debris ballistic coefficient
4. Breakup altitude
5. Environmental conditions (wind direction/magnitude and atmospheric density)

The entry dispersions were represented by a 6×6 covariance matrix of velocity and position errors at the entry altitude. For the deboost mission, the error sources were the uncertainties associated with: [Ref. 45:p. 2]

1. Accelerometers
2. Gyros
3. Computer errors
4. Initial alignment errors
5. Vehicle performance dispersions

The covariance matrix of state variables was determined by conducting a trajectory error analysis using a 1-sigma deviation of the errors and the nominal flight trajectory. In the application of the Monte Carlo analysis the major considerations were: [Ref. 45:p. 2]

1. The simulation of perturbed trajectories.
2. The modeling of the satellite breakup.
3. The determination of impact points for each trajectory.

At the entry altitude, the Monte Carlo method required generation of random state vectors from the 6×6 covariance matrix. Because the velocity and position errors are correlated, the random error vector in an uncorrelated space was derived from a transformation to a principle axes system. This vector is given by

$$\mathbf{e}_r = [n_1 \mathbf{e}_1, n_2 \mathbf{e}_2, \dots, n_6 \mathbf{e}_6]^T \quad (206)$$

where

n_i = a set of random numbers drawn from a normal distribution of mean 0 and variance 1

e_i = the square roots of eigenvalues of the covariance matrix

The original coordinate system random state vectors were derived from the equation

$$\begin{vmatrix} R_p \\ V_p \end{vmatrix} = \begin{vmatrix} R_n \\ V_n \end{vmatrix} + |\phi| |\mathbf{e}_r| \quad (207)$$

where

ϕ = 6×6 eigenvector matrix that transforms the principle axes system into the original coordinate frame

R_p = perturbed radius vector

V_p = perturbed velocity vector

R_n = nominal radius vector

V_n = nominal velocity vector

In order to calculate the dispersion area, the Monte Carlo analysis required a large number of simulated trajectories and random perturbed state vectors at the entry point for each perturbed initial condition. [Ref. 45:pp. 2-3]

Additionally, the Monte Carlo scheme required a fast and efficient computational technique to calculate flight trajectories from several initial conditions. Analytical solutions, such as Loh's second-order theory (presented in Chapter III) were not suitable for footprint dispersion analysis because these solutions are valid for only certain portions

of the trajectory and entry conditions. The trajectory simulation used the equations of motion of a nonlifting vehicle in the form

$$\dot{V}_x = g_x - \frac{\rho V(V_x + \omega y)g}{2BP} \quad (208)$$

$$\dot{V}_y = g_y - \frac{\rho V(V_y + \omega x)g}{2BP} \quad (209)$$

$$\dot{V}_z = g_z - \frac{\rho V(V_z)g}{2BP} \quad (210)$$

where

$$V = \sqrt{(V_x + \omega y)^2 + (V_y - \omega x)^2 + (V_z)^2} \quad (\text{relative velocity}) \quad (211)$$

g_x, g_y, g_z = gravitational acceleration components

V_x, V_y, V_z = inertial velocity vector components

x, y, z = radius vector components

ω = Earth's rotation rate

BP = ballistic parameter or coefficient ($W/C_D A$)

Equations (208) through (210) were integrated several times from entry to the impact point for the Monte Carlo analysis. The integration step size used was as large as possible due to a stability consideration. The system approached a dynamic equilibrium condition which resulted in a numerical instability. This was a result of the opposing gravitational acceleration and aerodynamic deceleration during the vertical portion of the flight. A numerical search was conducted to determine the step size as a function of

satellite debris ballistic coefficient. [Ref. 45:pp. 3-4] Figure 59 shows the stable and unstable regions used for the numerical integration [Ref. 45:p. 4].

Since the Monte Carlo analysis required the simulation of a large number of trajectories, an accurate computationally fast atmospheric density model was needed. The authors chose the 1962 U.S. Standard Atmosphere that provided density values from 0 to 400,000 ft. [Ref. 45:p. 5]

Although both static and dynamic global atmospheric models accounting for diurnal, seasonal, and latitudinal variations are available, it is found that such models are not suitable for the Monte Carlo dispersion analysis of satellite footprints. A sensitivity study of density variation indicates only a second order effect on footprint dispersion. Furthermore, the results of Purcell and Barbery show the downrange impact errors resulting from atmospheric variations are slight. [Ref. 45:p. 5]

The simulation assumed one breakup altitude where all the pieces had the same initial position and velocity at breakup. By using a bounded parametric approach, the smallest and largest debris ballistic coefficients were used to determine the largest uprange and downrange footprint dispersions from the nominal impact point. Since the ballistic coefficient will vary as it passes through the atmosphere due to variations of C_D and Mach number, the program used a generalized C_D vs Mach number curve for tumbling pieces to update the ballistic coefficient at various altitudes. This curve is based on the results of a range safety study of Titan launch vehicle debris. [Ref. 45:p. 5]

For the footprint dispersion study, it is found that the transonic flow region, where C_D variation with Mach number is significant, occurs during the vertical descent of the debris with minimum effect on footprint dispersion. However, the variation of ballistic parameters with altitude affects the time of arrival of the debris on the ground. [Ref. 45:p. 5]

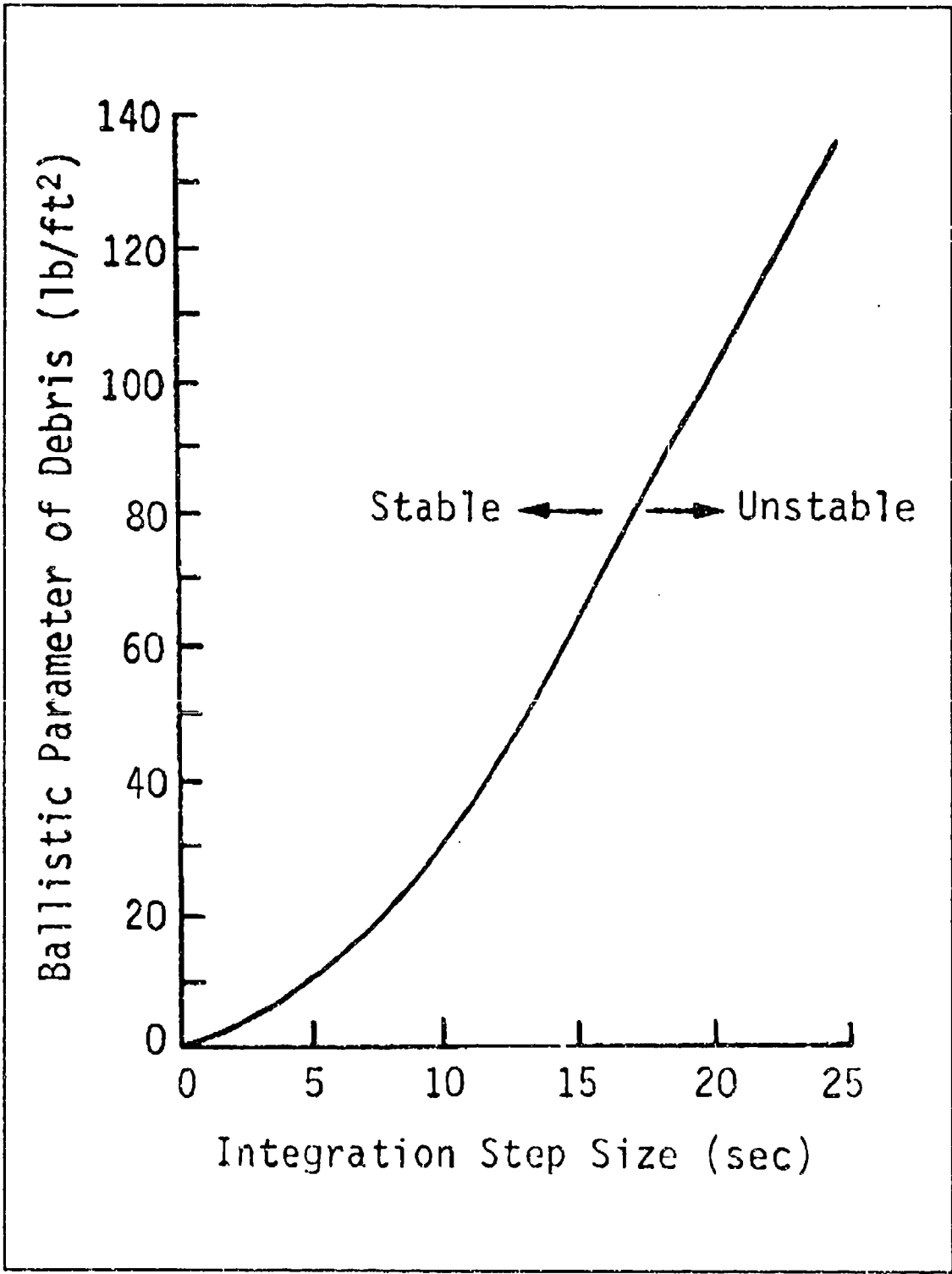


Figure 59: Numerical Stability Region
[Ref. 45]

The latitude and longitude (lat/long) impact points of the smallest and largest Skylab debris were provided by the trajectory simulation for the various initial conditions at the entry altitude. The Lat/Long impact points were statistically treated which determined a three-sigma impact area boundary. The point estimate and confidence level estimate of the impact points for any given confidence level, ϵ , and probability, α , are the fundamental statistical quantities of interest.

These statistical computations relate the calculated longitude and latitude bounds from a finite sample to their true values corresponding to an infinite sample required for the Monte Carlo technique. [Ref. 45:p. 6]

By using a normal distribution approximation given by

$$N = \frac{\alpha K_{\epsilon}^2}{(1 - \alpha)} \quad (212)$$

where K_{ϵ} is defined from the equation

$$\frac{\epsilon}{2} = (1 - \sqrt{2\pi}) \int_{K_{\epsilon}}^{\infty} e^{-\frac{t}{2}} dt \quad (213)$$

equation (212) provides the estimated number of samples required to estimate a good point. A probabilistic statement given by

$$P_r(\theta \leq \theta_{\alpha}) = \alpha \quad (214)$$

$$P_r(\phi \leq \phi_{\alpha}) = \alpha \quad (215)$$

where

ϕ = impact point latitude

θ = impact point longitude

was obtained from the frequency histogram and cumulative probability distribution of Lat/Long impact points generated from the Monte Carlo analysis. For any specified value of α , the object of the statistical analysis was the estimation of ϕ_α and θ_α . [Ref. 45:p. 6]

1. Simulation Results

During the simulation to determine the debris footprint dispersion, Skylab was deboosted from a 170 nm circular orbit. The nominal entry and corresponding impact point Lat/Long were respectively (30°S,30°W) and (49.86°S,34.92°E). The nominal entry point state vector and the lower half of a symmetrical ECI frame covariance matrix are shown in Table XVI [Ref. 45:p. 7]. By using a Gaussian distribution for the Monte Carlo analysis, the initial state vectors were randomly selected from the covariance matrix. Specifically, 500 random entry states were created by using 3000 random numbers drawn from the distribution.

To ensure that these numbers truly represent a normal distribution, their mean and variances were determined and adjusted to be 0 and 1 within stringent tolerances. The number of samples were found to be sufficient because further increase in sample size did not significantly effect the output variable distribution and probability limits. [Ref. 45:p. 8]

Figure 60 shows a scattergram of the state vectors which define the entry flight path angle [Ref. 45:p. 7]. The trajectories were then simulated from the entry points down to the breakup altitude for each randomly selected state vector. Figures 61 and 62 show the results of a nominal run used to determine the flight characteristics of Skylab [Ref. 45:pp. 8-9]. From Figure 62, the following parameters vs altitude were presented:

Table XVI: ENTRY STATE VECTOR / ERROR COVARIANCE MATRIX
 [Ref. 45]

Nominal Entry Point

$x = 17,648,032$ ft	$V_x = -3238.58$ ft/sec
$y = -5,174,810$ ft	$V_y = 21011.96$ ft/sec
$z = -10,760,572$ ft	$V_z = -14693.59$ ft/sec

ECI Error Covariance Matrix

	x	y	z	V_x	V_y	V_z
x	5.76546E8					
y	-3.95374E9	2.72016E10				
z	2.79469E9	-1.92075E10	1.35675E10			
V_x	4.86448E6	-3.34635E7	2.36298E7	4.11679E4		
V_y	-1.35955E6	9.34064E6	-6.59878E6	-1.14913E4	3.20968E3	
V_z	-3.03260E6	2.08426E7	-1.47220E7	-2.56422E4	7.16010E3	1.59759E4

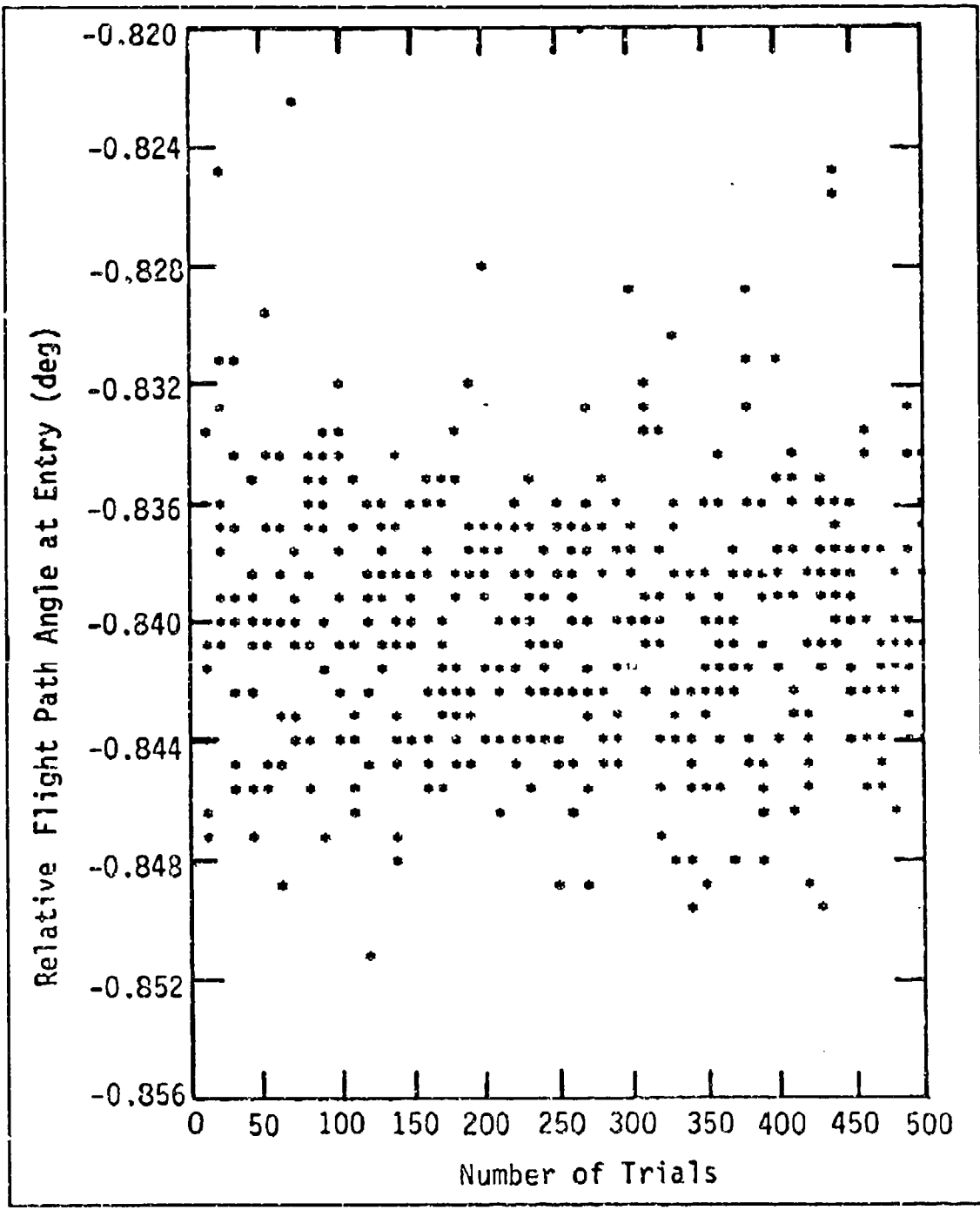


Figure 60: Relative Entry Flight Path Angle Scattergram
[Ref. 45]

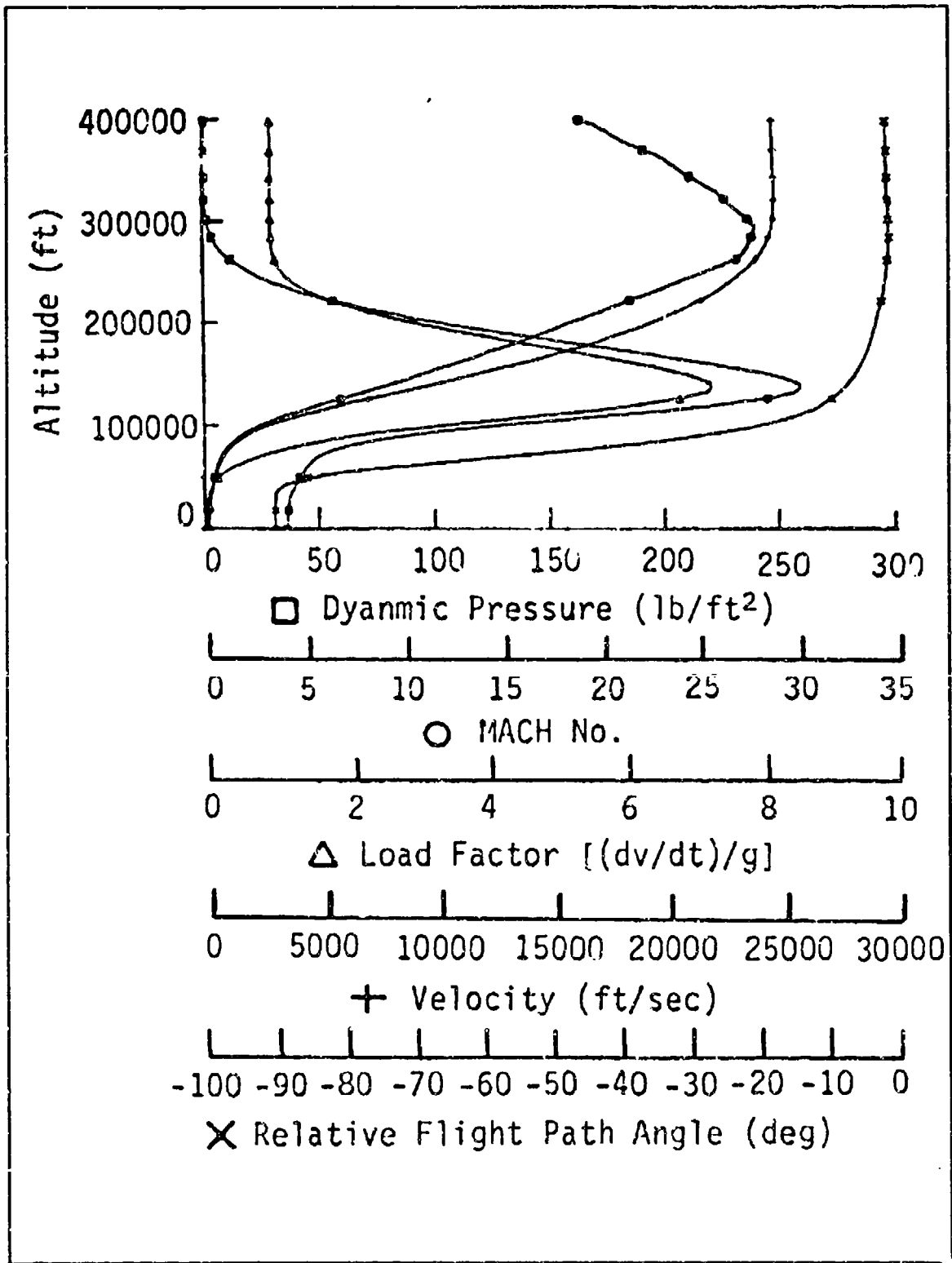


Figure 61: Skylab Nominal Flight Characteristics
[Ref. 45]

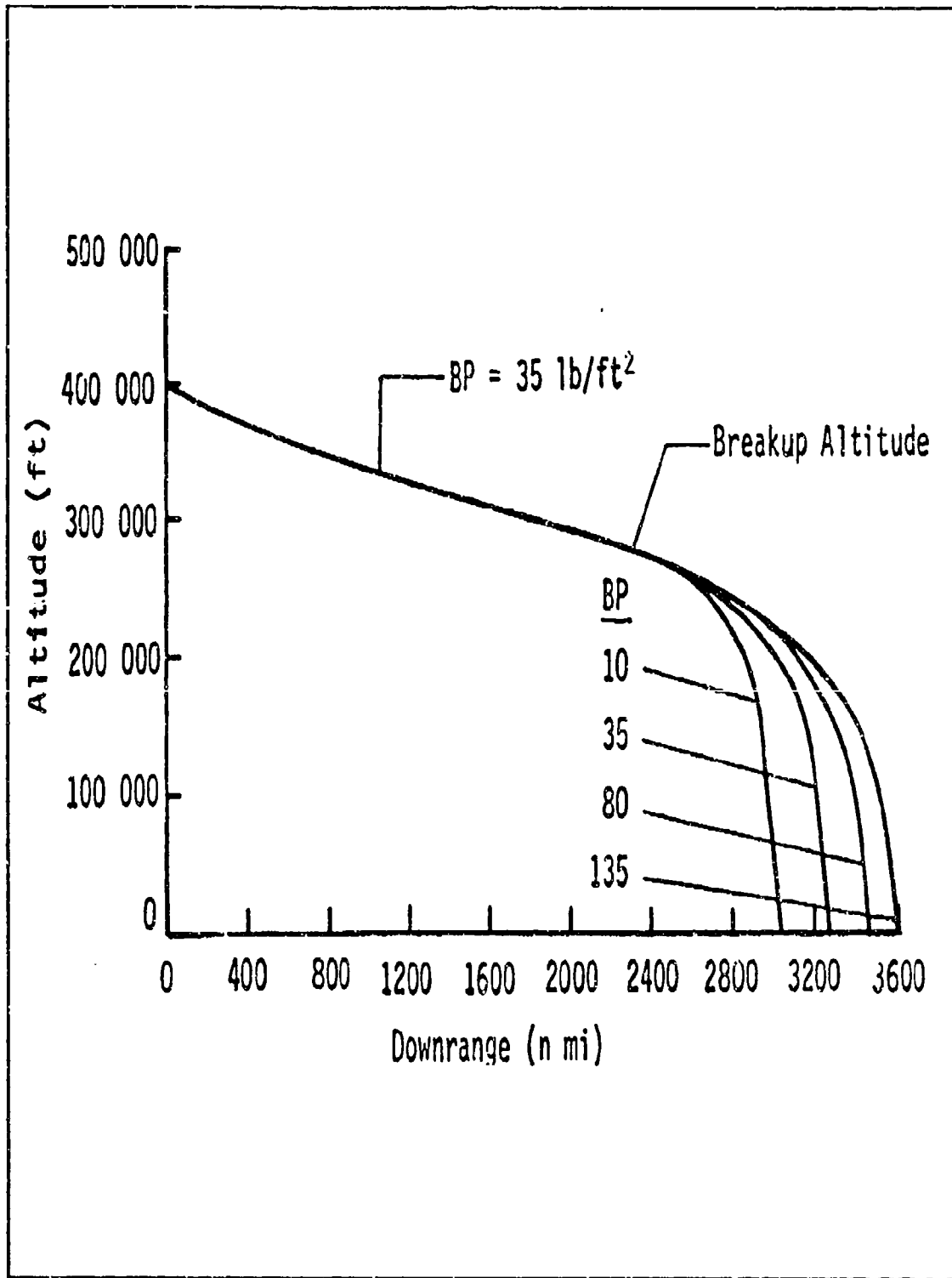


Figure 62: Downrange Impact Point Variations
 [Ref. 45]

1. Dynamic pressure
2. Mach number
3. Load factor
4. Velocity
5. Relative flight path angle

In Figure 62, the 275,000 ft (84.8 km) breakup altitude of the simulation is shown along with the downrange variations for several debris sizes (denoted by ballistic parameter or coefficient). The lat/long histogram and cumulative probability distribution diagrams respectively shown in Figures 63 and 64 [Ref. 45:pp. 11-12] indicate the two distinct regions corresponding to the largest and smallest ballistic coefficient debris. Additionally, these diagrams determine the lat/long bounds where all debris is likely to fall. [Ref. 45:pp. 7-12]

The downrange and crossrange debris impact dispersion distances were calculated using the lat/long and azimuth angles at the nominal impact point by the matrix equation [Ref. 45:p. 12]

$$\begin{vmatrix} \Delta \xi \\ \Delta \eta \\ \Delta \zeta \end{vmatrix} = \begin{vmatrix} -C\lambda S\phi_N C\theta_N - S\lambda S\theta_N & S\lambda C\theta_N - C\lambda S\phi_N S\theta_N & C\lambda C\phi_N \\ C\lambda S\theta_N - S\lambda S\phi_N C\theta_N & -S\lambda S\phi_N S\theta_N - C\lambda C\theta_N & S\lambda C\phi_N \\ C\phi_N C\theta_N & C\phi_N S\theta_N & S\phi_N \end{vmatrix} \begin{vmatrix} X_P - X_N \\ Y_P - Y_N \\ Z_P - Z_N \end{vmatrix} \quad (216)$$

where

ξ, η, ζ = orthogonal coordinate system established at the nominal point

ξ = axis tangent to the ground trace at the nominal point

η = axis along the radius vector

ζ = axis completes a right-handed triad

ϕ_N = nominal impact point latitude

θ_N = nominal impact point longitude

λ = azimuth angle ($\sin^{-1}[\cos i / \cos \phi_N]$)

X_N = $R_N C\phi_N C\theta_N$

Y_N = $R_N C\phi_N S\theta_N$

Z_N = $R_N S\phi_N$

X_P = $R_P C\phi_P C\theta_P$

Y_P = $R_P C\phi_P S\theta_P$

Z_P = $R_P S\phi_P$

S = \sin

C = \cos

N = nominal

P = perturbed

Figure 65 shows the downrange and crossrange dispersion distances from the nominal impact point calculated from equation (216) [Ref. 45:p.14]. As shown in the figure, the crossrange dispersions were relatively small as compared to the downrange dispersions.

In order to determine the effect of the breakup altitude on the dispersion area, Monte Carlo simulations were conducted at various altitudes from 200,000 to 350,000 ft (61.7-107.9 km). In this altitude range, the reentry object experiences large thermal and structural loads. Figure 66 shows three-sigma downrange and uprange dispersion for the largest and smallest debris [Ref. 45:p. 15].

This figure is useful for estimating the total footprint dispersion resulting from breakup of smaller pieces at higher altitudes and heavier pieces at lower altitudes, thereby accounting for the uncertainty in breakup altitude. [Ref. 45:p.14]

In their conclusions, the authors note significant footprint dispersion variations for breakup in the 200,000 to 350,000 ft altitude region. Furthermore, they state that the comprehensive Monte Carlo analysis is very useful and appropriate in determining impact dispersion areas of a spacecraft or discarded portions of a launch vehicle' [Ref. 45:p. 15]

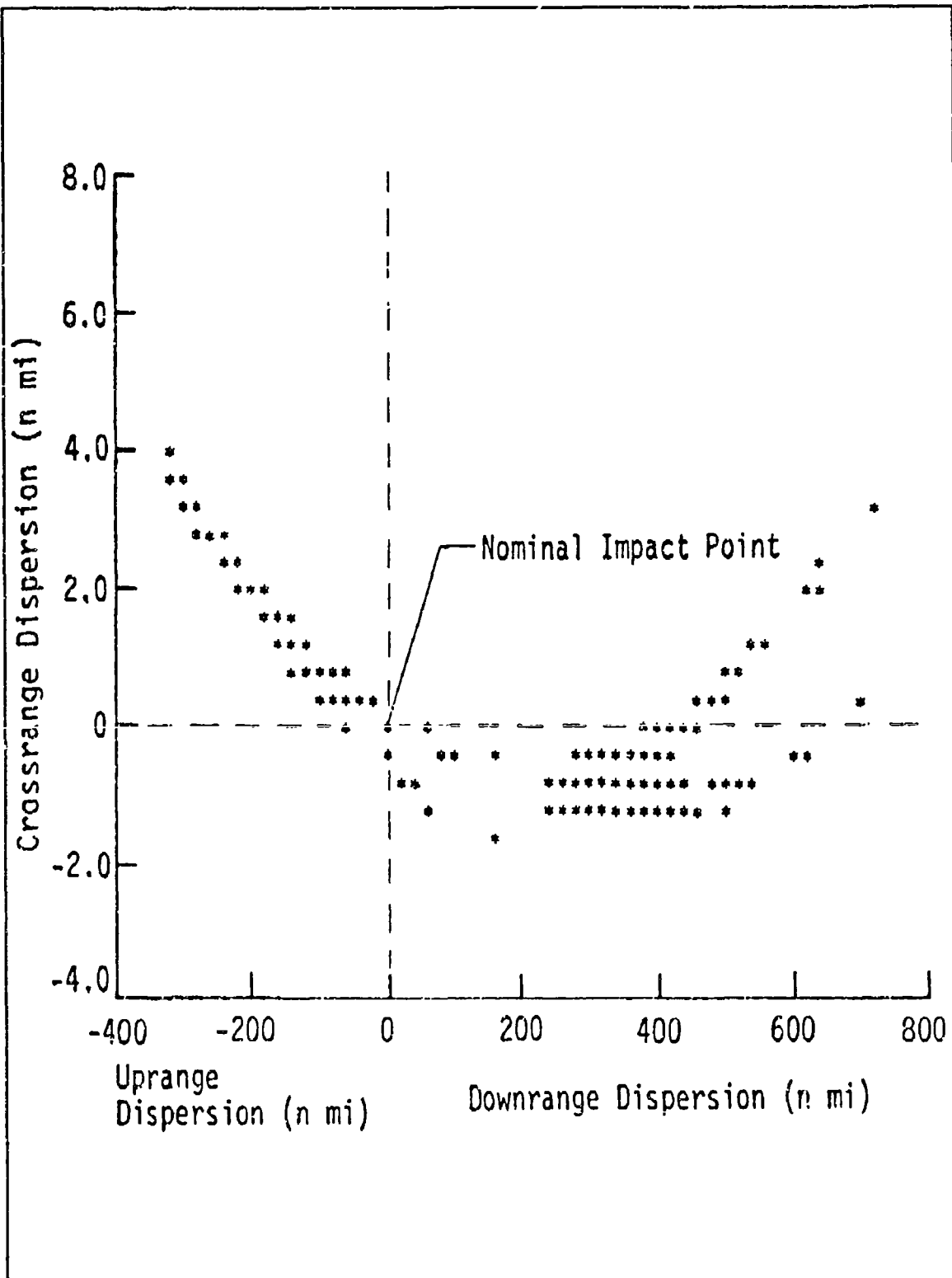


Figure 65: Down Range And Crossrange Dispersions
 [Ref. 45]

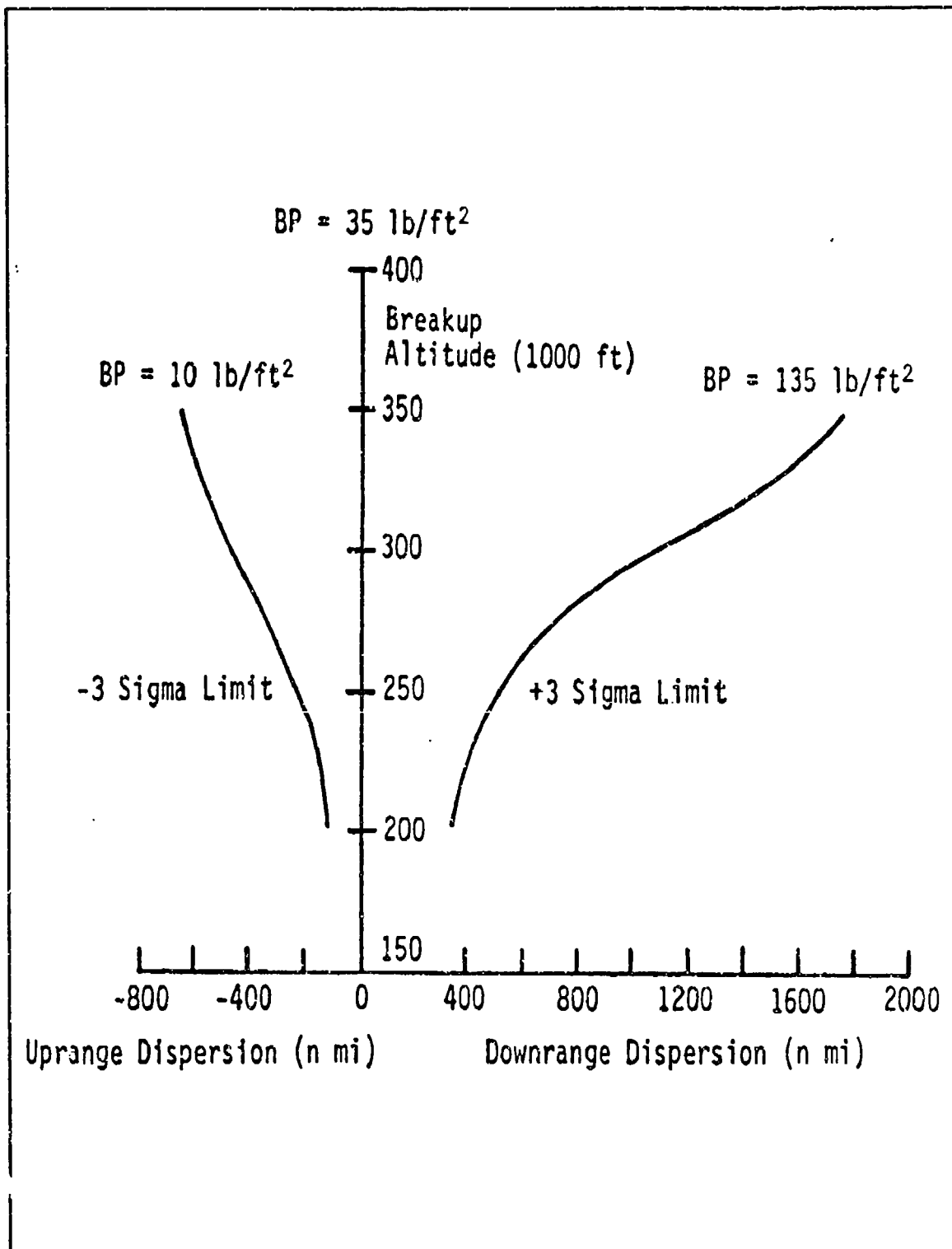


Figure 66: Downrange And Uprange Dispersions Three-Sigma Limits
 [Ref. 45]

VI. CONCLUSIONS AND RECOMMENDATIONS

A. CONCLUSIONS

The primary goal of this thesis was to identify the "state-of-the-art" of orbit-decay-induced uncontrolled reentry and impact prediction methods, with an emphasis on the physics of the final few revolutions to impact. This was accomplished through a comprehensive literature survey from the 1950's to the present of unclassified military and civil databases. The survey indicated that there is some significant foreign work being done and much of it was not available to the authors, in English translation, and thus was not included in this survey. Also, the literature survey reflects the changing scientific terminology over the course of several decades and it is especially noticeable in the different forms that the common variables take in the numerous equations presented. The authors did not make any attempt to use the standard AIAA astrodynamics nomenclature or to standardize the equations in any other way.

The principal conclusion of this thesis is that the current uncontrolled reentry and impact prediction methodology, used in the U.S. and abroad, is based on analysis which is 30 or more years old. This conclusion is based on the fact that the U.S. method takes its roots in the works of Brouwer (1959) and Allen and Eggers (1957), and that the U.S. method is the accepted international standard, as shown by the literature survey.

While conducting the literature search dating back to the 1950's, the authors noticed a definite trend, through the years, in the focus of published material related to

reentry. During the timeframe from the late 1950's until the mid 1960's, the emphasis in the literature was primarily devoted to understanding and describing the physics of reentry, specifically as it pertains to controlled ballistic reentry of Mercury and missile type vehicles. With the exception of Sputnik IV, very little of the literature surveyed during this timeframe was strictly devoted to uncontrolled reentry. However, during the derivations of their analytical reentry theories, some early pioneers such as Chapman and Loh investigated the shallow orbit-decay-induced reentry. With the physics of reentry fairly well understood, starting in the late 1960's and continuing into the 1980's, the emphasis in the literature had shifted to controlled, gliding reentry in order to support the launch of the Space Shuttle. In 1965, Eggers and Cohen stated:

Significant advances have been accomplished in the science and technology appropriate to atmosphere entry of spacecraft during the eight years since the launching of Sputnik I. This progress is illustrated by the successful entry from Earth orbit of the manned Vostok, Mercury, Voskhod, and Gemini spacecraft, for which the problems in orbital entry, such as high convective heating rate and load and communication blackout, were successfully overcome...Although the first Apollo vehicle entry has yet to be demonstrated...Much engineering work for this vehicle remains to be done; however, the fundamental research activity associated with Apollo is being reduced in favor of that associated with missions and vehicles of the more distant future. [Ref. 75:pp. 339-340]

Uncontrolled reentry briefly came back into focus in the late 1970's and early 1980's with the reentry of Cosmos-954 and Skylab and continued throughout the 1980's in varying degrees where the reentries of Cosmos-1402, 1601 and Salyut-7/Cosmos-1686 continued to spark a flurry of literature from the European Space Agency.

The literature survey of recent publications shows a strong reliance on work done in the 1950's and 1960's as a basis for "extensions" or "modifications" of pre-existing

methods used for prediction of reentry and impact. Although reliance on pre-existing methods is not in and of itself flawed, the modern works often subscribe to the same assumptions which the original authors were forced to make because of hardware or data limitations of their time. This serves to perpetuate the inherent limitations of the method's ranges of applicability and validity. For example, it has been shown [Refs. 14,16-17] that some very important work done in the 1950's, such as Allen and Eggers [Ref. 65], which is still routinely referenced in recent publications, is inherently flawed due to assumptions made under conditions of little or no data. This particular reference is especially important since it is the basis for most of the modern reentry heating work. It becomes even more significant since the literature survey has shown the coupled dependence of reentry breakup to reentry heating and dynamic load effects. Reference [42] describes the limitations imposed by these assumptions through mathematical proofs. This is further substantiated by reentry breakup observations [Ref. 86] which indicate that the classical convective heat transfer equations, when applied to breakup analysis, consistently underestimate reentry survivability.

Of the various "extensions" to the current reentry theory, of which the NORAD method is recognized as the international standard, there does not appear to be any one method which is singularly superior to the others. However, it is the opinion of the authors that the ESA FOCUS program merits special attention for further research. This conclusion is based on the fact that this program contains a very sophisticated method for dealing with the drag coefficient, C_D , and could easily incorporate other higher-order effects occurring in reentry, such as attitude generated lift, rotation of the orbital plane

(due to atmosphere rotation at attitudes < 60 km), linear variations in the ballistic coefficient in the final few days of orbit and others as mentioned previously in this thesis.

Numerous works cited in the literature survey also describe computing power and computer time constraints as critical parameters of the problem. These hardware limitations then forced one or more simplifying assumptions to be made in order to deal with the technology limitations of the day. Subsequently, much of the literature survey shows work which has limited applicability for the problem of concern.

Additionally, there is a general lack of consensus in the literature as it pertains to orbit-decay-induced uncontrolled reentry. The very definition of "reentry" remains vague and often is defined differently by investigators attempting to do similar research. Many investigators have examined various aspects of the problem; however, when surveying the literature, a common approach and standardized starting point for solving this very dynamic problem is not apparent. A good example to illustrate this point is the effect of angle of attack, α , on the ability to accurately predict uncontrolled reentry and impact. The ability to properly model the uncertainties in the reentry body configuration such as changes in area, mass, and attitude is a very difficult problem. As a result of these changes, three-dimensional angle of attack becomes an exceedingly difficult parameter to characterize especially when the reentry body is undergoing rapid configuration changes due to ablation and structural deformation. However, in order to properly model the aerodynamic coefficients for lift and drag, angle of attack must be considered. Specifically, lift as a function of angle of attack not only affects the trajectory (location of impact), but it also affects the altitude of breakup (survivability and dispersion area)

since it reduces the thermal and structural loads on the vehicle. However, in most cases where angle of attack is investigated, this coupled effect is not mentioned nor pursued. Even more likely in the literature, the reentry body is modeled as a point mass where angle of attack is not considered or lift is assumed to be zero or negligible.

Another observation from the survey is that no comprehensive sensitivity and error analysis has been conducted in order to determine quantitatively the effects of critical parameters/variables on impact prediction. For example, numerous sensitivity and error analysis studies have been conducted on atmospheric density models uncoupled from other critical parameters. However, a coupled analysis of all of the critical parameters could determine which variables contribute most significantly to the overall accuracy of the various impact prediction methods.

In addition to the author's observations and conclusions described in the previous paragraphs, a summary of specific conclusions from the literature survey are:

1. There is no clear definition of when reentry occurs. Typically 120 km or an orbital period of 87.5 minutes or less is used in the various models to define the start of reentry. However, observations and post flight analysis indicate a range of altitudes where "reentry" actually occurs.
2. There is a lack of observation data in the reentry regime due to a lack of global sensor coverage. This lack of data significantly adds to the uncertainty of the problem.
3. The current deterministic dynamics model appears to be inadequate for processing the true physics of reentry.
4. The lack of observational data coupled with the inadequate knowledge of the true physics of uncontrolled reentry significantly increases the uncertainty of the problem.

5. Reentry is most likely to occur within several tenths of a degree of the minimum altitude (height above the ground) point in the orbit, which is not necessarily the point of perigee. [Ref. 99]
6. The uncontrolled reentry is three times more likely to occur in a latitude band equaling the inclination than in an equatorial band (0 to 10 degrees), with the exception of polar orbits where an equatorial reentry is most likely to occur. [Ref. 99]
7. The impact location (downrange and crosstrack) is affected by: [Refs. 45,101]
 - (a) the rotation of the atmosphere, starting at an altitude of 30-60 km
 - (b) the debris ballistic coefficient
 - (c) the entry dispersions (velocity and position errors at the entry altitude)
 - (d) the relative flight path angle
 - (e) the breakup altitude
 - (f) the environmental conditions such as wind direction/magnitude and atmospheric density
8. There appears to be linear variations in the ballistic coefficient in the final few days prior to reentry. [Ref. 92]

B. RECOMMENDATIONS

Based on the above conclusions, the following recommendations are proposed:

1. As mentioned in Chapter I, there was no attempt made to standardize the nomenclature and variables of the equations presented in this thesis, in accordance with AIAA astrodynamics standards or any others. Based on the literature survey, there clearly exists a need for such standards, especially when dealing with work spanning the course of several decades.

2. This literature survey was conducted through unclassified sources, written in English, only. A survey of classified and foreign language sources should be conducted.
3. The primary focus of this thesis was a thorough survey of the physics of uncontrolled reentry. Throughout the survey, the authors noted several operational issues which should be addressed in follow-on research. These issues include human factors (orbit analyst experience), sensor bias and coverage, and improved international information exchanges.
4. Several reentry/impact prediction methods were presented (LIFETIME, FOCUS, and NORAD) in this thesis. A side by side comparison of these methods using historical data should be conducted in order to compare and contrast their overall accuracies and efficiencies.
5. A sensitivity and error analysis of critical parameters including atmospheric density, aerodynamic coefficients, initial conditions (vehicle area, mass, attitude, position and velocity), thermal and dynamic loads, and breakup phenomena should be conducted in order to improve the current dynamics model and to focus future research efforts.
6. In view of the lack of global sensor coverage, especially in the southern hemisphere, high priority reentry events may be better predicted through a joint cooperative effort using Navy and Air Force assets as mobile supplemental observation and tracking stations.
7. Since uncontrolled reentry is characterized by numerous rapidly changing critical parameters, which are ill-defined, stochastic and statistical methods should be applied to current reentry models to better analyze the sensitivity of the various uncertainties associated with this problem. This could serve as an "operational tool" to help improve the prediction accuracies of the current models while the physics of the reentry process is being more thoroughly investigated.
8. The authors strongly recommend future cooperative research between the Naval Postgraduate School and the AFSPACECOM/USSPACECOM in order to solve this largely unknown and highly dynamic process.

LIST OF REFERENCES

1. Fuhs, A.E., *An Analyst's Guide to Military Space*, draft copy, unpublished.
2. Trux, J., *The Space Race*, New English Library, London, 1985.
3. DeSaussure, H., "An International Right to Reorbit Earth Threatening Satellites," *Annals of Air and Space Law*, vol.3, 1978, p.383-392.
4. Doyle, S.E., "Reentering Space Objects - Facts and Fiction," *Journal of Space Law*, vol.6, no.2, 1978, p.107-117.
5. Flury, W., "The Reentry of Salyut-7/Cosmos-1686," (ESA-SP-345), *Proceedings of International Workshop ESOC, Darmstadt (D), 9 April 1991*.
6. Wilford, J.N., "Solar Max satellite plunges to Earth.," *The New York Times*, 3 Dec. 1989, p.21(N).
7. Sawyer, K., "Spacecraft's study of sun ends today: Solar Max heads for fiery reentry.," *The Washington Post*, 1 Dec. 1989, p.A3.
8. Davis, B., "If you see a shooting star Dec. 8, make a fast wish for a deep cave.," *The Wallstreet Journal*, 28 Nov. 1990, p.B1.
9. Lundquist, C.A., Vanderburgh, R.C., and Munn, W.A., "Reentry and Recovery of Fragments of Satellite 1960 ϵ 1," *SAO Special Report No. 109*, Smithsonian Institution Astrophysical Observatory, 1962.
10. Varnado, C.L., "Skylab Reentry and Impact Footprint Reconstruction," *NASA, George C. Marshall Space Flight Center, EL25-006*, Oct. 1980.
11. Borrowman, G.L., "Operation Morninglight," *Spaceflight*, vol.21, pp.302-307, 7 July 1979.
12. Martin, R.J., "Legal Ramifications of the Uncontrolled Return of Space Objects to Earth," *Journal of Air Law and Commerce*, vol.45, Winter 1980, p.457-481.

13. Heftman, K., "Proceedings of an ESA Workshop on Reentry of Space Debris," (ESA-SP-246), *Proceedings of an ESA Workshop held at the European Space Operations Center, Darmstadt, FRG, 24-25 Sept. 1985.*
14. Chapman, D.R., "An Approximate Analytical Method for Studying Entry Into Planetary Atmospheres," *Technical Report R-11*, National Aeronautics and Space Administration, 1959.
15. Anser, *Reentry Systems Analysis: Relating Subsystem Errors and Failures, External Factors and Reentry Accuracies*, Anser, Arlington, VA, 1991.
16. Griffen, M.D. and French, J.R., *Space Vehicle Design*, American Institute of Aeronautics and Astronautics, Washington, D.C., 1991.
17. Chobotov, V.A., ed., *Orbital Mechanics*, American Institute of Aeronautics and Astronautics, Washington, D.C., 1991.
18. Klinkrad, H.H., "Long-term Analytical Orbit Decay and Reentry Prediction," ESA SP-246, *Proceedings Workshop on Re-entry of Space Debris*, Darmstadt, September 1985.
19. Cook, G.E., King-Hele, D.G. and Walker, D.M.C., "The Contraction of Satellite Orbits Under the Influence of Air Drag, I. With spherically symmetrical atmosphere," *Proceedings of The Royal Society, Series A*, Vol.257, No.1289, 1960.
20. Regan, F.J., *Reentry Vehicle Dynamics*, American Institute of Aeronautics and Astronautics, New York, NY, 1984.
21. Liu, J.J.F., France, R.G. and Wackernagel, H.B., " An Analysis of the Use of Empirical Atmospheric Density Models in Orbital Mechanics," Spacetrack Report No. 4, *Project Space Track*, Space Command, USAF, Peterson AFB, CO, 1983.
22. Roble, R.G., "Global Dynamic Models of the Earth's Upper Atmosphere," AAS Paper 91-489, *AAS/ALAA Astrodynamics Specialist Conference*, Durango, CO, 1991.
23. Harris, I. and Priester, W. "Theoretical Models for the Solar-Cycle Variation of the Upper Atmosphere," *Journal of Geophysics Research*, Vol.67, 1962.
24. Jacchia, L.G., "Static Diffusion Models of the Upper Atmosphere with Empirical Temperature Profiles," *SAO Special Report No. 170*, Smithsonian Institute Astrophysical Observatory, Cambridge, MA, 1965.

25. Harris, I. and Priestler, W., "Atmospheric Structure and Its Variations in the Region From 120 to 800 km," *Cospar International Reference Atmosphere (CIRA) 1965*, Space Research IV, North Holland Publishing Company, Amsterdam, 1965.
26. Jacchia, L.G., "New Static Models of the Thermosphere and Exosphere with Empirical Temperature Profiles," *SAO Special Report No. 313*, Smithsonian Institute Astrophysical Observatory, Cambridge, MA, 1970.
27. Jacchia, L.G., "Revised Static Models of the Thermosphere and Exosphere with Empirical Temperature Profiles," *SAO Special Report No. 332*, Smithsonian Institute Astrophysical Observatory, Cambridge, MA, 1971.
28. Jacchia, L.G., "Thermospheric Temperature Density and Composition," *SAO Special Report No. 375*, Smithsonian Institute Astrophysical Observatory, Cambridge, MA, 1977.
29. Hedin, A.E., and others, "A Global Thermospheric Model Based on Mass Spectrometer and Incoherent Scatter Data, MSIS, N₂ Density and Temperature," *Journal of Geophysics Research*, Vol.82, No.16, 1977.
30. Hedin, A.E., "A Revised Thermospheric Model Based on Mass Spectrometer and Incoherent Scatter Data; MSIS-83," *Journal of Geophysics Research*, Vol.84, No.1, 1983.
31. Hedin, A.E., "MSIS-86 Thermospheric Model," *Journal of Geophysics Research*, Vol.92, 1987.
32. Coster, A.J. and Gaposchkin, E.M., "Evaluation of New Parameters for Use in Atmospheric Models," AAS Report No. 87-555, *Advances in the Astronautical Sciences, Astrodynamics 1987*, Vol.65, Part II, American Astronautical Society, 1987.
33. Coster, A.J. and Gaposchkin, E.M., "Evaluation of Recent Atmospheric Density Models," AAS Report No. 87-557, *Advances in the Astronautical Sciences, Astrodynamics 1987*, Vol.65, Part II, American Astronautical Society, 1987.
34. Marcos, F.A., "Accuracy of Atmospheric Drag Models at Low Satellite Altitudes," *Advances in Space Research*, Vol.10, No. 3-4, 1990.
35. Liu, J.J.F. and Snow, D.E., "Solar Flux, Geomagnetic Index Variations and Low Altitude Orbit Decay," Technical Note 89-4, *Directorate of Operations Analysis DCS/Operations*, Space Command, USAF, Peterson AFB, CO, 1989.

36. Interview between Mr. Frank A. Marcos, Air Force Geophysics Laboratory, Hanscom AFB, MA and the authors, 4 March 1993.
37. Crowther, R., "Space Debris: Orbit Decay and Re-entry Prediction in Theory and Practice," AAS Paper 92-183, *AAS/AIAA Spaceflight Mechanics Meeting, Colorado Springs, CO, February 24-26, 1992*.
38. Bate, B.B. , Mueller, D.D. and White, J.E., *Fundamentals of Astrodynamics*, Dover Publications, Inc., New York, NY, 1971.
39. Hankey, W.L., *Re-entry Aerodynamics*, American Institute of Aeronautics and Astronautics, Washington, D.C., 1988.
40. Loh, W.H.T., *Re-entry and Planetary Entry Physics and Technology*, Springer-Verlag New York Inc., New York, NY, 1963.
41. Longuski, J.M. and Vinh, N.X., "Analytical Theory of Orbit Contraction and Ballistic Entry Into Planetary Atmospheres," *JPL Publication* ,80-58, 1980.
42. Vinh, N.X., Buseman, A. and Culp, R.D., *Hypersonic and Planetary Entry Flight Mechanics*, The University of Michigan Press, Ann Arbor, MI, 1980.
43. Loh, W.H.T., *Re-entry and Planetary Entry Physics and Technology*, Springer-Verlag New York Inc., New York, NY, 1968.
44. Interview between Dr. I. Michael Ross, Naval Postgraduate School, Monterey, CA, and the authors, 14 May 1993.
45. Rao, P.P. and Woeste, M.A. "Monte Carlo Analysis of Satellite Debris Footprint Dispersion," AAS paper 79-171, *AAS/AIAA Astrodynamics Special Conference*, Provincetown, MA, 1979.
46. Soloman, L.H.. "Observation of the GT-5 Rocket-Body Reentry - Preliminary Analysis," *SAO Special Report Number 191*, Smithsonian Institute Astrophysical Observatory, Cambridge, MA, 1965.
47. Nazarenko, A.I., "Determination and Prediction of Satellite Motion at the End of the Lifetime," ESA Sp-345, *Proceedings International Workshop on Salyut-7/Cosmos-1686 Reentry*, Darmstadt, 1991, pp. 35-43.
48. Lefebvre, S.V., *An Analysis of Tracking and Impact Predictions*, Master's Thesis, Air Force Institute of Technology, December 1991.

49. Interview between Captain William A. Cain, USN, Chief, Theater Operations Support Division, USSFACECOM, J33S, Peterson, AFB, CO, and the authors, 16 March 1993.
- 50 Cook, G.E., King-Hele, D.G. and Walker, D.M.C., "The contraction of Satellite Orbits Under the Influence of Air Drag, II. With oblate atmosphere," *Proceedings of The Royal Society*, Series A, Vol.264, No.1316, 1961.
51. King-Hele, D.G., "The Contraction of Satellite Orbits Under the Influence of Air Drag, III. High-eccentricity orbits, *Proceedings of The Royal Society*, Series A, Vol.267, No.1331, 1962.
52. Cook, G.E. and King-Hele, D.G., "The Contraction of Satellite Orbits Under the Influence of Air Drag, IV. With scale height dependent on altitude," *Proceedings of The Royal Society*, Series A, Vol.275, No.1362, 1963.
53. Cook, G.E. and King-Hele, D.G., "The Contraction of Satellite Orbits Under the Influence of Air Drag, VI. Near-circular orbits with day-to-night variation in density," *Proceedings of The Royal Society*, Series A, Vol.303, No.1472, 1968.
54. King-Hele, D.G. and Walker, D.M.C., "The Contraction of Satellite Orbits Under the Influence of Air Drag, VIII. Orbital lifetime in an oblate atmosphere, when perigee distance is perturbed by odd zonal harmonics in the geopotential," *Royal Aircraft Establishment*, TR 86069, 1986.
55. King-Hele, D.G., "Methods for Predicting Satellite Orbital Lifetimes," *Royal Aircraft Establishment*, TR 77111, 1977.
56. Duzmak, G. Ye., *Mechanics of Space Flight. Dynamic of Uncontrolled Motion of Entry Bodies When Entering the Atmosphere*, "Nauka" Press, Main Editorial Office of Physico-Mathematical Literature, Moscow, 1970, translated by *Foreign Technology Division*, Air Force Systems Command, FTD-HC-23-161-71, 1972.
57. Agrawal, B. N., *Design of Geosynchronous Spacecraft*, Prentice-Hall, Inc., Englewood Cliffs, NJ, 1986.
58. Allen, H.J., "Motion Of A Ballistic Missile Angularly Misaligned With The Flight Path Upon Entering The Atmosphere And Its Effect Upon Aerodynamic Heating, Aerodynamic Loads, And Miss Distance," *NACA TN 4048*, Ames Aeronautical Laboratory, Moffett Field, CA, Oct. 1957.
59. Aslanov, V.S., "Spin of a Ballistic Axisymmetric Vehicle During Atmospheric Entry," Translated from *Kosmicheskie Issledovaniya*, Vol.14, No.4, pp. 491-497, 1976.

60. Aslanov, V.S., "Determination of the Amplitude of Three-Dimensional Oscillations of a Ballistic Vehicle with a Small Asymmetry During Atmospheric Entry," Translated from *Kosmicheskie Issledovaniya*, Vol.18, No.2. pp. 178-184, 1980.
61. Kaplan, M. H., Cwynar, D. J., and Alexander, S. G., "Simulation of Skylab Orbit Decay and Attitude Dynamics," AIAA Paper 78-1626, *American Institute of Aeronautics and Astronautics*, 1978.
62. Kaplan, M. H. and Alexander, S. G., "Skylab is Falling - Strategies for Reentry," AAS Paper 79-170, *AAS/AIAA Astrodynamics Specialist Conference*, Providence, MA, 1979.
63. Chudd, W. B., ed., "Skylab Reactivation Mission Report," NASA TM-78207, *NASA Marshall Space Flight Center*, AL, 1980.
64. Ailor, W. H. and others, "Analysis of SP-100 Reentry," ATR-84-80, *The Aerospace Corporation*, El Segundo, CA, 1984.
65. Allen, H.J. and Eggers, A.J., "A Study of the Motion and Aerodynamic Heating of Missiles Entering the Earth's Atmosphere at High Supersonic Speeds," *NACA TN 4047*, Washington, DC, 1957.
66. Bobbitt, P. J., "Effects of Shape on Total Radiative and Convective Heat Inputs at Hyperbolic Entry Speeds," *NASA Langley Research Center*
67. Bowman, W. A., "Atmospheric Density Models for Reentry Heating and Trajectory Applications," *Lockheed Missiles and Space Company*, Huntsville, AL
68. Karr, G. and Cranford, K., "Determination of Atmospheric Density and Gas-Surface Interaction Parameters," Analysis Memorandum 70-22, 9 Dec. 1970, *HQ FOURTEENTH AEROSPACE FORCE*, Ent AFB, CO.
69. Hoshizaki, H. and Wilson, K., "Convective and Radiative Heat Transfer During Superorbital Entry," AIAA Paper 66-106, *AIAA 3rd Aerospace Sciences Meeting*, New York, NY, 24-26 Jan. 1966.
70. Carroll, H. R., "General Heating Distributions on the Tumbling Infinite Cylinder," AIAA Paper 78-42, *AIAA 16th Aerospace Sciences Meeting*, Huntsville, AL, 16-18 Jan. 1978.
71. Crowther, R., "Re-Entry Aerodynamics Derived From Space Debris Trajectory Analysis," *Planetary and Space Science*, vol.40, no.5, 1992, pp.641-646.

72. Crowther, R. and Stark, J., "The Determination of the Gas-Surface Interaction From Satellite Orbit Analysis as Applied to ANS-1 (1975-70A), *Planetary and Space Science*, vol.39, no.5, 1991, pp. 729-736.
73. Dogra, V. K., "Aerothermodynamics of a 1.6-m-Diameter Sphere in Hypersonic Rarefied Flow," AIAA-91-0773, *AIAA 29th Aerospace Sciences Meeting, Reno, NV, 7-10 Jan. 1991*.
74. McAnally, J. V. and Engel, C. D., "Reentry Aerodynamic Heating Methods For Sounding Rocket Payloads," AIAA 79-0508.
75. Eggers, A. J., Jr. and Cohen, N. B., "Progress and Problems in Atmosphere Entry," *International Astronautical Federation, International Astronautical Congress, 16th, Athens, Greece, 13-18 Sept. 1965*, pp. 339-369.
76. Koppenwallner, G. and Johannsmeier, D., "Behavior and Modelling of the Aerothermodynamics of Ballistic Entry Vehicles in the High Altitude Flow Regimes," *Aerothermodynamics for Space Vehicles, Proceedings of the First European Symposium ESTEC, Noordwijk, The Netherlands, 28-30 May 1991*, pp. 461-467.
77. Kotov, V.M., Lychin, E.N. and Reshin, A.G., "An Approximate Method of Aerodynamic Calculation of Complex Bodies in a Transition Region," *Rarefied Gas Dynamics, vol.1*, Plenum Press, New York, 1982.
78. Boettcher, R., "Applicability of Bridging Methods to Hypersonic Rarefied Flow Aerodynamics of Reentry Vehicles," *Aerothermodynamics for Space Vehicles, Proceedings of the First European Symposium ESTEC, Noordwijk, The Netherlands, 28-30 May 1991*, pp. 469-476.
79. Potter, J.L., "Procedure for Estimating of the Aerodynamics of Three-Dimensional Bodies in Transitional Flow," *Rarefied Gas Dynamics, vol. 118*, Plenum Press, New York, 1988.
80. Wilmoth, R. G. and Moss, J. N., "Energetics of Gas-Surface Interactions in Transitional Flows at Entry Velocities," AIAA 91-1338, *AIAA 26th Thermophysics Conference, Honolulu, HI, 24-26 Jun. 1991*.
81. Bird, G. A., "Monte Carlo Simulation in an Engineering Context," *Proceedings 12th Rarefied Gas Dynamics Symposium, Progress in Astronautics and Aeronautics*, vol.74, part 1, pp. 239-255, 1988.

82. Fay, J. A., "Hypersonic Heat Transfer in the Air Laminar Boundary Layer," *The High Temperature Aspects Of Hypersonic Flow, Proceedings of the AGARD-NATO Specialists' Meeting*, Rhode-Saint-Genese, Belgium, 3-6 Apr. 1962, pp. 604-607.
83. Young, A. D., *Boundary Layers*, American Institute of Aeronautics and Astronautics, Washington, D.C., 1989.
84. Finson, M. L., Clarke, A. S. and Wu, P. K. S., "Rough Wall Reentry Heating Analysis: Final Report: Effect of Surface Roughness Character on Turbulent Boundary Layer Heating," PSI TR 204, Feb. 1980, *Physical Sciences, Inc.*, Woburn, MA.
85. Finson, M. L. and Wu, P. K. S., "Analysis of Rough Wall Turbulent Heating with Application to Blunted Flight Vehicles," PSI TR 158, 1979, *Physical Sciences, Inc.*, Woburn, MA.
86. Refling, O., Stern, R. and Pitz, C., "Review of Orbital Reentry Risk Predictions," ATR-92(2835)-1, *The Aerospace Corporation*, El Segundo, CA, 1992.
87. Hoots, F.R. and Roehrich, R.L., "Models for Propagation of NORAD Element Sets," *Project Spacetrack, Spacetrack Report No. 3, Aerospace Defense Command, USAF*, Dec. 1980
88. Kaya D. and France, R., "Stand-Alone Element Set Conversion," *General Research Corporation*, Colorado Springs, CO, Oct. 1988.
89. Spiral Decay Orbit Representation, ADC DPD 55-1-27, *Aerospace Defense Command*, May 1, 1960.
90. Wackernagel, H.B., ed, "Mathematical Foundations for SSC Astrodynamic Theory," TP SSC 8, Apr. 6, 1982.
91. Wackernagel, H.B., "Proposed Air Force Space Command Astrodynamic Standards," *Air Force Space Command, Astrodynamics Division/DOJ*, Dec. 5, 1989.
92. Barker, W.N., Eller, T.I., and Herder, L.E., "A New Approach in Treating the Ballistic Coefficient in the Differential Correction Fitting Program," (AIAA-89-374), *AAS/AIAA Astrodynamics Specialist Conference*, Stowe, VT, Aug. 7-10, 1989.
93. Lieweher, W., Peters, H.G., and Merholz, D., "Orbit Analysis and Lifetime Prediction Using Radar Data by Reentry of Salyut-7/Kosmos-1686," (ESA-SP-345), *The Reentry of Salyut-7/Kosmos-1686, Proceedings International Workshop ESOC*, Darmstadt (D), Apr. 9, 1991, pp. 9-15.

94. Klinkrad, H., "Salyut-7/Kosmos-1686 Reentry Prediction Activities at ESOC," (ESA-SP-345), *The Reentry of Salyut-7/Kosmos-1686, Proceedings International Workshop ESOC*, Darmstadt (D), Apr. 9, 1991, pp. 17-34.
95. Strizzi, J.D., "An Improved Algorithm for Satellite Orbit Decay and Reentry Prediction," Master's Thesis, Massachusetts Institute of Technology, June 1993.
96. Finke, R.G., "Reentry Vehicle Dispersion Due To Atmospheric Variations," (P-506), *Institute for Defense Analyses, Science and Technology Division*, Arlington, VA, Aug. 1969.
97. Cowley, J.R., "The Effect of the Subsolar Atmospheric Bulge on Satellite Reentry Latitudes," *Stanford University, Department of Aeronautics and Astronautics*, Oct. 1968.
98. De Lafontaine, J. and Garg, S.C., "A Review of Satellite Lifetime and Orbit Decay Prediction," *Institute for Aerospace Studies, University of Toronto, UTIAS*, Review No.43, Jun. 1980.
99. Gazley, C., Jr., Rowell, L.N., and Schilling, G.F., "On the Prediction of Satellite Orbit Decay and Impact," M-4619-PR, *The Rand Corporation*, Oct. 1965.
100. Flury, W., (Technical Coordinator), "Space Debris," (ESA-SP-1109), *A Report from the ESA Space Debris Working Group, ESA Publications Division, ESTEC*, Noordwijk, The Netherlands, Nov. 1988.
101. Arho, R., "On the Rotation of the Orbital Plane During Ballistic Reentry," *Planetary and Space Sciences*, vol.19, 1971, pp. 1215-1224.
102. Barker, R.H., Jr., *Estimation of Decayed Satellite Reentry Trajectories*, Ph.D. Dissertation, Air Force Institute of Technology, Wright Patterson AFB, OH, 1982.

INITIAL DISTRIBUTION LIST

	No. Copies
1. Defense Technical Information Center Cameron Station Alexandria VA 22304-6145	2
2. Library, Code 052 Naval Postgraduate School Monterey CA 93943-5002	2
3. Dr. Rudolph Panholzer Chairman, Space Systems Academic Group Code SP Naval Postgraduate School Monterey CA 93943-5002 (DSN) 878-2948	1
4. Dr. I. Michael Ross Code AA/RO Naval Postgraduate School Monterey CA 93943-5002 (DSN) 878-2074	15
5. Dr. Joseph Liu Chief, Astrodynamics Div./CNY HQ AFSPACECOM 150 Vandenberg St. Suite 1105 Peterson AFB CO 80194-4025 (DSN) 692-5467	1
6. Director, Navy Space Systems Division (N63) Space and Electronic Warfare Directorate Chief of Naval Operations Washington DC 20350-2000	1

7. CAPT William A. Cain 1
Chief, Theater Operations Support Division
HQ USSPACECOM/J33S
250 S. Peterson Blvd.
Suite 116
Peterson AFB CO 80914-3040
(DSN) 692-5943
8. Dr. Sam H. Parry 1
Code OR/PY
Naval Postgraduate School
Monterey CA 93942-5002
(408) 656-2779
9. Dr. Ed Euler 1
Code SP
Naval Postgraduate School
Monterey CA 93942-5002
10. Mr. Frank Marcos 1
PL/GPIM
29 Randolph Blvd.
Hanscom AFB MA 01731-3010
(DSN) 478-3037
11. LCDR Brian D. Neuenfeldt 2
NAVSPACECOM DET COLORADO SPRINGS CO
250 S. Peterson Blvd.
Peterson AFB CO 80914-3040
(DSN) 692-3973
12. LT William K. Henderson 2
VS-33
FPO AP 96601-6509
(DSN) 735-7077